



City Research Online

City, University of London Institutional Repository

Citation: Allday, A. W. (2004). Detection capabilities of energy dispersive X-Ray diffraction with respect to in-vitro trabecular bone mineral loss. (Unpublished Doctoral thesis, City, University of London)

This is the accepted version of the paper.

This version of the publication may differ from the final published version.

Permanent repository link: <https://openaccess.city.ac.uk/id/eprint/30147/>

Link to published version:

Copyright: City Research Online aims to make research outputs of City, University of London available to a wider audience. Copyright and Moral Rights remain with the author(s) and/or copyright holders. URLs from City Research Online may be freely distributed and linked to.

Reuse: Copies of full items can be used for personal research or study, educational, or not-for-profit purposes without prior permission or charge. Provided that the authors, title and full bibliographic details are credited, a hyperlink and/or URL is given for the original metadata page and the content is not changed in any way.

City Research Online:

<http://openaccess.city.ac.uk/>

publications@city.ac.uk

**DETECTION CAPABILITIES OF
ENERGY DISPERSIVE X-RAY DIFFRACTION
WITH RESPECT TO IN-VITRO
TRABECULAR BONE MINERAL LOSS**

Ph.D. THESIS

ALLAN WILLIAM ALLDAY

Submitted for

The Degree of Doctor of Philosophy

City University, London

Department of Radiography

May 2004

Copyright © 2004 by Allan Allday

All rights reserved

Version 2 (post *viva voce*), May 2004

To mum and dad

The fate of specialists in any one area of science is to focus more and more narrowly on their special topic, learning more and more about less and less, until eventually they end up knowing everything about nothing.

John Gribbin, *Almost Everyone's Guide to Science: The Universe, Life and Everything*

CONTENTS

	CONTENTS	v
	LIST OF TABLES	xiii
	LIST OF FIGURES	xvii
	ACKNOWLEDGEMENTS	xxv
	ABSTRACT	xxvii
	ABBREVIATIONS	xxix
<i>Chapter 1</i>	INTRODUCTION	3
1.1	Bone	8
1.1.1	Components and Synthesis of Bone	9
1.1.2	Cortical and Trabecular Bone	10
1.2	Biomechanics of Bone	11
1.2.1	Mechanical Functions of Bone	11
1.2.2	The Proximal Femur	13
1.2.3	Force, Displacement, Stress, Strain and Elastic Modulus	16
1.3	Bone Density	18

1.3.1	Factors Affecting Bone Density	20
1.3.2	Diseases Affecting Bone Density	21
1.4	X-ray Photon Interactions with Matter	23
1.4.1	Coherent Scattering	26
1.4.2	Photoelectric Absorption	29
1.4.3	Compton Scattering	31
1.5	Bone Mineral Density Measurement	32
1.5.1	Radiographic Methods	32
1.5.2	Photon Absorptiometry Methods	34
1.5.3	Computed Tomography	37
1.5.4	Photon Scattering Methods	38
1.5.5	Neutron Activation Analysis	39
1.5.6	Radiation Free Methods	40
1.6	Radiation Dosimetry	40
1.6.1	Radiation Dose Quantities and Units	41
1.6.2	Thermoluminescent Dosimetry	42
1.7	X-ray Diffraction	44
1.7.1	Bragg Diffraction	44
1.7.2	X-ray Powder Diffraction	46
1.8	Energy Dispersive X-ray Diffraction	47
1.8.1	An EDXRD Diffractometer	48
1.8.2	Measuring Bone Density using EDXRD	50

PART 1	PREPARATION	
<i>Chapter 2</i>	PHOTON SOURCE AND DETECTION COMPONENTS OF THE EDXRD SYSTEM	57
2.1	X-ray Tube Characterisation	57
2.1.1	Stability of the X-ray Tube Output	58
2.1.2	Mapping the X-ray Tube Output	59
2.1.3	X-ray Tube Alignment using Focal Spot Imaging	61
2.2	Detector Characterisation	62
2.2.1	Detection System Calibration	63
2.2.2	Detection System Energy Resolution	65
2.2.3	Mapping Detector Effective Size	66
 <i>Chapter 3</i>	 EDXRD EXPERIMENTAL GEOMETRY AND BONE PHANTOM PREPARATION	 69
3.1	EDXRD Diffractometer Geometry	70
3.1.1	Diffractometer Scattering Volume	70
3.2	Bone Phantom Construction	73
 <i>Chapter 4</i>	 INITIAL BONE DENSITY MEASUREMENTS USING PHANTOMS	 77
4.1	EDXRD Experiments	77
4.2	DEXA Experiments	83
4.3	Comparing EDXRD and DEXA Results	86
4.3.1	EDXRD and DEXA Sensitivity	87

<i>Chapter 5</i>	TRABECULAR BONE SAMPLE PREPARATION AND DEMINERALISATION	89
5.1	Study Sample from Within the Femoral Head	89
5.2	Cleaning the Trabecular Bone Samples	91
5.3	Simulating Bone Mineral Density Loss	93
5.4	Demineralisation Homogeneity Assessment using Microdensitometry	97
5.5	Bone Sample Cube Density Correction	104
5.6	Introduction of Marrow Substitute into Sample Trabecular Spaces	106
 <i>Chapter 6</i>	 A FIXED PARAMETER DIFFRACTOMETER AND ATTENUATION CORRECTION	 109
6.1	The Fixed Parameter EDXRD Assembly	112
6.2	Assessing the Attenuation Correction Technique	115
PART 2		
STUDY		
 <i>Chapter 7</i>	 EDXRD AND DEXA INVESTIGATION INTO ONE COMPONENT TRABECULAR BONE DENSITY MEASUREMENT	 127
7.1	EDXRD Bone Density Measurements using a One Component Sample System	128
7.1.1	Calibrated One Component EDXRD Analysis	133
7.1.2	Demineralised One Component EDXRD Analysis	142
7.2	DEXA Bone Density Measurements using a One Component Sample System	147

	7.2.1	Calibrated One Component DEXA Analysis	149
	7.2.2	Demineralised One Component DEXA Analysis	154
	7.3	Comparison of EDXRD and DEXA Results	158
	7.3.1	Comparison of Calibrated One Component Results	158
	7.3.2	Comparison of Demineralised One Component Results	160
<i>Chapter 8</i>		EDXRD AND DEXA INVESTIGATION INTO TWO COMPONENT TRABECULAR BONE DENSITY MEASUREMENT	163
	8.1	EDXRD Bone Density Measurements using a Two Component Sample System	164
	8.1.1	Calibrated Two Component EDXRD Analysis	168
	8.1.2	Calibrated Two Component EDXRD Analysis using Peak Fitting	187
	8.2	DEXA Bone Density Measurements using a Two Component Sample System	196
	8.2.1	Calibrated Two Component DEXA Analysis	197
	8.3	Comparison of EDXRD and DEXA Results	200
	8.3.1	Comparison of Calibrated Two Component Results	201
<i>Chapter 9</i>		DOSE MEASUREMENTS FROM THE EDXRD EXPERIMENT	205
	9.1	EDXRD Dose Estimation Experiment	205
<i>Chapter 10</i>		AN INVESTIGATION INTO BONE SAMPLE STRENGTH	215
	10.1	Trabecular Bone Sample Compression	215

11.3.6	Compression Tests	245
11.4	Final Conclusions for the Project	245

APPENDICES

<i>Appendix A</i>	FORMULAE DERIVATIONS	251
A.1	Momentum Transfer	251
A.2	Scattering Volume Formulae	253
 <i>Appendix B</i>	 TECHNICAL DRAWINGS	 257
B.1	Bone Cutting Chucks	257
B.2	Fixed Parameter EDXRD Diffractometer Blocks	257
 <i>Appendix C</i>	 POWDER DIFFRACTION FILE DATA	 263
C.1	Hydroxyapatite	263
 <i>Appendix D</i>	 RADIATION DOSIMETRY WEIGHTING FACTORS	 265
D.1	Radiation Weighting Factors	265
D.2	Tissue Weighting Factors	266
 <i>Appendix E</i>	 SOFTWARE	 267
E.1	Converting Maestro CHN Files: AttenCHN	267
E.2	Other Software for Data Analysis	302
E.3	The PGM Image File Format	303

REFERENCES	305
-------------------	-----

BIBLIOGRAPHY	313
---------------------	-----

Radiation Physics and Detection	313
---------------------------------	-----

Anatomy, Physiology and Pathology	313
-----------------------------------	-----

Bone Density Measurement	314
--------------------------	-----

LIST OF TABLES

<i>Chapter 1</i>		
1-1	Some variations in bone density definitions.	19
<i>Chapter 2</i>		
2-1	FWHM measurements for each energy peak of Americium-241.	66
<i>Chapter 3</i>		
3-1	Optimum EDXRD ribbon beam diffractometer geometry ranges for bone densitometry.	70
3-2	Scattering volume lengths for various experimental geometries.	72
3-3	Quantity details of the phantoms produced.	75
<i>Chapter 5</i>		
5-1	Parameters for the fitted EDTA demineralisation curves.	97
5-2	Comparison of measured densities of trabecular bone sample cubes with calculated region of interest densities.	102
<i>Chapter 6</i>		
6-1	Chart showing attenuation correction ratios calculated for this experiment.	118
6-2	Attenuation correction results expressed in terms of total spectrum photon count reduction.	121

Chapter 7

7-1	Summary of the number of experimental variations that each generated an EDXRD scattered spectrum.	131
7-2	Variation between repeated measurements of attenuation corrected EDXRD scattered spectra photon count regions.	133
7-3	Parameters for the one component sample system error fits.	136
7-4	Results from the EDXRD one component sample system calibrated experiments.	139
7-5	Results from the EDXRD one component sample system demineralisation experiments.	145
7-6	Summary of the number of experimental variations used to generate DEXA scans.	149
7-7	Results from the DEXA one component sample system calibrated experiments.	153
7-8	Results from the DEXA one component sample system demineralisation experiments.	157
7-9	Summary of the best case condition impressiveness factors.	159
7-10	Summary of the best case condition demineralisation results.	161

Chapter 8

8-1	Quantities of aluminium and Perspex used for each clinical site simulation.	166
8-2	Summary of the number of experimental variations that each generated an EDXRD scattered spectrum.	167
8-3	Summary of the analysis methods performed.	169
8-4	Parameters for the two component sample system error fits.	177
8-5	Results from the EDXRD two component sample system calibrated experiments (no additional attenuation).	178

8-6a	Results from the EDXRD two component sample system calibrated experiments with added attenuation for calcaneus simulation.	183
8-6b	Results from the EDXRD two component sample system calibrated experiments with added attenuation for radius simulation.	184
8-6c	Results from the EDXRD two component sample system calibrated experiments with added attenuation for femoral neck simulation.	185
8-7	Parameters for the peak fitted two component sample system error fits.	192
8-8	Results from the EDXRD two component sample system calibrated experiments (no additional attenuation) with fitted peaks.	193
8-9	Summary of the number of experimental variations used to generate DEXA scans.	196
8-10	Results from the DEXA one component sample system calibrated experiments with added attenuation for calcaneus, radius and femoral neck simulation.	199
8-11	Summary of the best case condition impressiveness factors.	201
8-12	Impressiveness factor performance deviation from expected best case condition.	202
<i>Chapter 9</i>		
9-1	Results from the EDXRD two component sample system dose estimation experiments.	209
9-2	Effective dose estimates for each clinical simulation, dose measurement site and tube current \times scanning time.	210
9-3	Effective dose and effective dose equivalent estimates.	211

Appendix C

C-1	Hydroxyapatite interplanar spacings from the JCPDS table 9-432.	263
-----	---	-----

Appendix D

D-1	Radiation weighting factors for equivalent dose calculation.	265
D-2	Tissue weighting factors for effective dose calculation.	266

Appendix E

E-1	MatLab M-files developed for data processing for this project.	302
E-2	General format of the PGM file header.	303

LIST OF FIGURES

Chapter 1

1-1	A comparison of transmission and scattering bone densitometry techniques.	4
1-2	External landmarks of the proximal femur.	13
1-3	Sketch of the proximal femur demonstrating Ward's trabecular systems.	14
1-4	Internal structures of the proximal femur.	Plate 1
1-5	Typical load-displacement and stress-strain curves.	17
1-6	Illustration of osteoporosis.	Plate 2
1-7	Simple exponential attenuation of a narrow beam monoenergetic photon beam.	24
1-8	Coherent scattering.	27
1-9	Photoelectric absorption.	30
1-10	Compton scattering.	31
1-11	Proximal femora diagrams showing the range of trabecular system degradation for Singh classification.	33
1-12	An illustration of dual photon absorptiometry.	36
1-13	An illustration of fluorescence, phosphorescence and thermoluminescence.	43
1-14	A selection of the numerous crystal plane families of a simple cubic lattice.	45
1-15	A two-dimensional representation of Bragg diffraction.	45
1-16	Recording a powder diffraction pattern using the Debye-Scherrer method.	47
1-17	An experimental system for EDXRD measurement.	48
1-18	EDXRD bone spectra.	52

1-19	EDXRD spectra generated using bone and marrow mixtures.	53
 <i>Chapter 2</i>		
2-1	X-ray tube output stability of the MXR-160.	59
2-2	X-ray tube output map of the MXR-160.	60
2-3	Radiographic image of the focal spot of the MXR-160.	61
2-4	Aligning the tube using focal spot imaging.	Plate 3
2-5	Schematic diagram of the multichannel analyser based spectroscopy system.	63
2-6	Americium-241 spectrum measured by the detection system.	64
2-7	The experimental geometry used to map the active area of the detector.	67
2-8	Map of the detector active area.	68
 <i>Chapter 3</i>		
3-1	Plan views of the experimental scattering volume.	71
3-2	Perspex supporting structure for the phantoms.	73
 <i>Chapter 4</i>		
4-1	Parameters of the experimental EDXRD diffractometer (variable version).	78
4-2	Illustration of a bone + marrow spectrum showing the region of interest.	80
4-3	EDXRD normalised bone peak photon counts for the phantom set.	81

4-4	An illustration of the reasoning behind the calculation of precision.	81
4-5	Phantom arrangement for the DEXA experiments.	84
4-6	DEXA bone density measurement results for the phantom set.	85
4-7	Sensitivity comparison of EDXRD and DEXA results by normalising to unity.	87
 <i>Chapter 5</i>		
5-1	Diagram of the proximal femur showing sample site selection.	91
5-2	Percentage reduction of bone sample mass as a function of exposure time to EDTA.	96
5-3	Region of interest of a bone sample cube.	99
5-4	Example of a stepwedge optical density plot with fitted exponential function.	100
5-5	Digitised radiographs of a trabecular bone sample cube before and after demineralisation, using microdensitometry.	Plate 4
5-6	Calibration line for determining mean bone density from microdensitometry.	101
5-7	Images of two trabecular bone sample cube slices generated from data acquired using MRI	Plate 5
 <i>Chapter 6</i>		
6-1	Examples of conditions that result in differing attenuation of scattered spectra from a defined scattering volume of equal density.	110
6-2	Spectra generated using a single marrow free trabecular bone cube.	111

6-3	Schematic illustrating the geometry for the measurement of scattering and transmission spectra.	112
6-4	The fixed parameter EDXRD diffractometer assembly.	113
6-5	Parameters of the experimental EDXRD diffractometer (fixed version).	114
6-6	Transmitted spectra measured to correct for attenuation.	117
6-7	The EDXRD spectra as corrected for attenuation.	119
 <i>Chapter 7</i>		
7-1	Histogram illustrating the density range and distribution of the 58 trabecular bone sample cube set.	129
7-2	Example of a one component sample system EDXRD scattered spectrum, corrected for attenuation.	132
7-3	One component sample system calibration model.	134
7-4	One component sample system errors as a function of \log_{10} (mAs).	135
7-5	Examples of measured one component samples processed using the calibration formula.	137
7-6	One component EDXRD impressiveness factors.	140
7-7	Example scatter plot of one component EDXRD bone density reduction measurements.	143
7-8	Example scatter plots of one component EDXRD bone density reduction measurements.	144
7-9	Density reduction detection failure points for each measurement condition.	146
7-10	Configuration of trabecular bone sample and added attenuation for the DEXA experiments in this chapter.	148
7-11	Example of DEXA reference set measurements.	150
7-12	DEXA measurement one component sample set results.	152

7-13	Example scatter plot of one component DEXA bone density reduction measurements.	154
7-14	Scatter plots of the one component DEXA bone density reduction measurements.	156
 <i>Chapter 8</i>		
8-1	Configuration of trabecular bone sample and added attenuation for all experiments in this chapter.	166
8-2	EDXRD spectrum analysis area selection for the two component sample system.	170
8-3	Two component sample system calibration models.	172
8-4	Examples of measured two component samples with no added attenuation, processed using the calibration formulae.	175
8-5	Two component sample system errors as a function of \log_{10} (mAs).	176
8-6	Two component EDXRD impressiveness factors for measurements with no additional attenuation.	179
8-7	Examples of measured two component samples processed using the unity normalisation calibration formula.	181
8-8	Examples of peak fitted two component sample system spectra.	189
8-9	Peak fitted two component sample system errors as a function of \log_{10} (mAs).	191
8-10	Improvements in two component EDXRD impressiveness factors by using peak fitting.	194
8-11	DEXA measurement two component sample set results.	198

Chapter 9

- 9-1 Positioning of the TLD devices at various points within a 207
 clinical site simulation.

Chapter 10

- 10-1 Diagrams showing how bone sample cube orientation 217
 relates to the original location within the femoral head.
- 10-2 Stress-strain plot examples for two trabecular bone sample 219
 cubes.
- 10-3 Plots of Young's moduli against the measured density. 220

Chapter 11

- 11-1 Images of a bone cube slice, reconstructed from data Plate 6
 collected using microtomographic apparatus.
- 11-2 Illustration of a possible method of decreasing patient dose 244
 by measuring multiple spectra.

Appendix A

- A-1 A diagrammatic representation of momentum transfer. 251
- A-2 Plan view of the scattering volume showing the scattering 254
 length and the total length.
- A-3 Plan view of the scattering volume showing dimensions 254
 used for formulae calculations.

Appendix B

- B-1 Drawing of the first of two additional bone cutting chucks. 258
- B-2 Drawing of the second of two additional bone cutting 259
 chucks.

List of Figures

B-3	Drawing of the primary block of the fixed parameter EDXRD diffractometer.	260
B-4	Drawing of the secondary block of the fixed parameter EDXRD diffractometer.	261
 <i>Appendix E</i>		
E-1	Image generated using the PGM file example.	304

ACKNOWLEDGEMENTS

I would like to express my thanks to the following, for their support during this work:

My supervisor, Michael Farquharson, and my other colleagues at the laboratory: Andrew Bagshaw, Tina Geraki, Marios Yiannakas, Tarjani Patel and Elaine Ryan.

Roger Hicks and Jennifer Edie and their staff at the Department of Radiography, including Delia Hayes (radiation dose measurement), Martin Benwell and Gay Canning.

Tom Rose of the Department of Engineering and Mathematical Sciences (bone sample strength) and Richard Reynolds (work with the original diffractometer assembly).

Robert Speller and Gary Royle of University College, London, for allowing me to sit in on their medical physics lectures.

Ian Cullum of University College Hospital for DEXA.

Russell Luggar and Paul Jenneson of Surrey University for their work with the microtomographic method of measuring bone sample demineralisation homogeneity.

Mark Stanton and Denzil Booth for making, respectively, the trabecular bone cutting jig and fixed angle EDXRD diffractometer block.

Mr. Goldie and the staff of the Orthopaedic Department at Whipps Cross Hospital, London.

Mr. Marston and the staff of the Orthopaedic Department at St. Mary's Hospital, London.

Mr. Grange and the staff of the Orthopaedic Department at the Royal London Hospital.

Selina Blades of the Rheumatology Department at the Middlesex Hospital, London.

The staff of the Orthopaedic Department at the Chelsea and Westminster Hospital, London.

The Engineering and Physical Sciences Research Council (EPSRC) and the City University Department of Radiography for funding facilities for the project.

Thanks to my family and friends, many of whom are included in the above list. Especial thanks to Anne, Bill, Jill, Sam and Zoë, Paul and Ute, Maureen and to John Loram for his immense help with how this report reads. Much love to all.

I grant powers of discretion to the University Librarian to allow this thesis to be copied in whole or in part without further reference to me. This permission covers only single copies made for study purposes, subject to normal conditions of acknowledgement.

ABSTRACT

This study concerns the measurement of bone density pertaining to the management of osteoporosis. Bone density measurements may be absolute quantities for comparison to population norms or comparative measurements over time to ascertain bone loss rate. They provide important data to help physicians develop therapy programmes, determine fracture risk and to advise on preventative measures to those in higher risk groups.

This report primarily describes an investigation into bone mineral measurement utilising scattered x-radiation known as energy dispersive x-ray diffraction (EDXRD). Osteoporosis typically manifests itself in regions of trabecular bone to a greater extent than cortical bone and, as such, osteoporosis levels may be determined with greater accuracy by measuring trabecular bone density in isolation. EDXRD was used to accomplish this by defining a scattering volume within a region of trabecular bone.

The first part of this work is concerned with characterisations of the x-ray tube and detection system, which were found to be suitable for the EDXRD experiments. Then follows the calculation of EDXRD experimental geometry with respect to the bone samples used, and construction of bone + marrow mix phantoms. Sample and phantom material dimensions were set at $15 \times 15 \times 15 \text{ mm}^3$. Initial EDXRD and dual energy x-ray diffraction (DEXA) experiments using these phantoms are then described. Methods for the preparation and use of trabecular bone cubes for the main densitometry study were developed. This included the location of sample extraction from excised femoral heads (involving the medial trabecular region); the removal of sample marrow lipid (using a sequence of detergent and ethanol); a technique to simulate bone mineral density loss (using ethylenediaminetetra-acetic acid (EDTA)); a method to assess demineralisation homogeneity (microdensitometry of sample radiographs); a method of calculating the density of EDXRD scanned volumes from within the bone cube samples (microdensitometry); and a procedure to introduce bone marrow substitute into the samples (using a vacuum pump and magnetic resonance imaging to determine success). The EDXRD diffractometer used for the main study is described, followed by a method to correct measured EDXRD scattered spectra for attenuation by the samples and any additional attenuation added to simulate clinical sites. This correction was achieved using ratios of transmitted spectra with and without the attenuating material in place.

Following this preparatory work, two EDXRD and DEXA studies are presented that involved trabecular bone sample cubes. Precision, accuracy and correlation of each modality was investigated. The first study used bone density measurements of one component bone sample systems (trabecular bone only with no marrow). With a potential maximum of 1.000, best case results for EDXRD were found to be 0.9510 (for precision), 0.9573 (volume measurement accuracy) and 0.8659 (correlation), and for DEXA, 0.9703 (precision), 0.6186 (volume measurement accuracy) and 0.9797 (correlation). Additional attenuation was detrimental to EDXRD precision (0.8909) and volume measurement accuracy (0.8044), with slight improvement to correlation (0.8799), whereas DEXA precision was marginally improved (0.9764), volume measurement accuracy deteriorated significantly (0.1688) and correlation deteriorated marginally (0.9685). This study was then extended by using demineralised one component bone samples.

The second study consisted of two component bone sample system measurements (trabecular bone with marrow substitute in the trabecular spaces), along with additional attenuation to simulate typical calcaneus, radius and femoral head measurement sites.

Best case calcaneus results for EDXRD were 0.9692 (precision), 0.9156 (volume measurement accuracy) and 0.9469 (correlation), and for DEXA, 0.9782 (precision), 0.4761 (volume measurement accuracy) and 0.9785 (correlation). Best case radius results for EDXRD were 0.9357 (precision), 0.8584 (volume measurement accuracy) and 0.9356 (correlation), and for DEXA, 0.9776 (precision), 0.1541 (volume measurement accuracy) and 0.9837 (correlation). Best case femoral head results for EDXRD were 0.9357 (precision), 0.5888 (volume measurement accuracy) and 0.9464 (correlation), and for DEXA, 0.9866 (precision) and 0.9785 (correlation). DEXA volume measurement accuracy for the femoral head simulation was too low to calculate. DEXA precision (which was fairly consistent for each attenuation condition) outperformed that of EDXRD (which deteriorated with increased attenuation). DEXA correlation (fairly consistent for each attenuation condition) outperformed that of EDXRD (also fairly consistent). EDXRD volume measurement accuracy (which deteriorates with increased attenuation) clearly outperforms that of DEXA. (DEXA accuracy is presented here in terms of measuring specific bone volumes, which the method is unable to achieve and should not therefore be considered a failure of DEXA.)

An investigation into radiation effective dose necessary for useful EDXRD results was performed using thermoluminescent dosimetry (TLD), based on the method employed in this project for the two component bone sample system. Results suggest an EDXRD effective dose (568 μSv at 70 kV_p, 800 mAs) of around 142 times that of DEXA (4 μSv from typical published data).

An examination of bone sample strength using the one component bone samples concluded the main study. Elastic moduli were calculated from results of cube compression in all three orientations. Trabecular bone cube orientation was shown to have a differing influence on elastic modulus for different samples, suggesting bone strength is determined by trabecular architecture in addition to density. R² correlation between measured bone densities and elastic moduli in the medial trabecular region direction (0.0814) was found to be approximately half of that for the other two orientations (0.1698 and 0.1568).

The above results suggest that EDXRD is most suited to the measurement of absolute bone density values for specific bone volumes but that DEXA demonstrates better results in terms of precision and correlation. This, along with a greatly reduced dose cost, makes DEXA much more suited to the clinical environment. However suggestions are offered which include EDXRD dose reduction methods for potential clinical applications.

ABBREVIATIONS

AA	Added Attenuation
ALARA	As Low As Reasonably Achievable
BD	Bone Density
BDCC	Bone Density Calculated from Calibration
BMD	Bone Mineral Density
BR	Bone Region Analysis
BUA	Broadband Ultrasonic Attenuation
CHN	Channel (file type)
CS	Calcaneus Simulation
CT	Computed Tomography
CZT	Cadmium Zinc Telluride
DBDR	DEXA Bone Density Reduction
DBMD	DEXA Bone Mineral Density
DEF	Demineralisation Evenness Factor (of trabecular bone)
DEXA	Dual Energy X-ray Absorptiometry
DPA	Dual Photon Absorptiometry
DPI	Dots Per Inch (scanner pixels per inch)
EBDR	EDXRD Bone Density Reduction
EDTA	Ethylenediaminetetra-acetic Acid
EDXRD	Energy Dispersive X-ray Diffraction
EPSRC	Engineering and Physical Sciences Research Council
FFD	Focus Film Distance
FHD	Femoral Head Demineralisation (bone sample)
FS	Femoral Neck Simulation

Abbreviations

FWHM	Full Width at Half Maximum (of a Gaussian peak)
HPGe	High Purity Germanium
ICRP	International Commission on Radiological Protection
ICRU	International Commission on Radiation and Units
IF	Impressiveness Factor
JCPDS	Joint Committee on Powder Diffraction Standards
LAX	Low Angle X-ray Scattering
MAD	Measured 'Area Density'
MCA	Multichannel Analyser
MD	Measured Density
MRI	Magnetic Resonance Imaging
NAA	No Added Attenuation
NCRP	National Council on Radiation Protection and Measurements
PC	Personal Computer
PDR	Percentage Density Reduction
PGM	Portable Greymap (file type)
PTH	Parathyroid Hormone
QCT	Quantitative Computerised Tomography
RA	Radiographic Absorptiometry
RF	Radio Frequency
ROI	Region of Interest
RS	Radius Simulation
SD	Standard Deviation
SDR	Sample Density Reduction
SI	Système International
SPA	Single Photon Absorptiometry

Abbreviations

SVBD	Scatter Volume Bone Density
TLD	Thermoluminescent Dosimetry
TTP	Time-Temperature Profile
UN	Unity Normalisation Analysis
WHO	World Health Organisation

**DETECTION CAPABILITIES OF
ENERGY DISPERSIVE X-RAY DIFFRACTION
WITH RESPECT TO IN-VITRO
TRABECULAR BONE MINERAL LOSS**

Chapter 1

INTRODUCTION

This study is concerned primarily with the measurement of bone density. A reduction in bone density from the norm is an important factor that directly affects bone strength. The resulting increase in skeletal porosity leaves the bones more susceptible to fractures which, in turn, often lead to further complications. With frail patients, the shock following such a fracture can be fatal.

The increased rate of fractures resulting from bone density decrease requires expensive treatment. Osteoporosis affects an estimated 75 million people in the United States, Europe and Japan, including one in three postmenopausal women (World Health Organisation, 2002). According to the International Osteoporosis Foundation, someone in the European Union has a fracture as a result of osteoporosis every 30 seconds. Annual direct medical costs to treat 2.3 million osteoporosis fractures in Europe and the USA are of the order of US\$ 27,000 million (World Health Organisation, 1999).

It is clearly important to have effective means of determining the mineral content of bone. Significant bone density reduction must be diagnosed as early as possible in order to maximise the effectiveness of treatment and so minimise fracture risk. There are a variety of methods employed in clinical bone density measurement today, discussed later in this chapter. Each has its own merits but none have proven to be entirely satisfactory.

This report outlines the progress of an investigation into the effectiveness of a method of bone density measurement not (as yet) employed in the clinical environment. It is known as energy dispersive x-ray diffraction (EDXRD) or low angle x-ray scattering (LAX). EDXRD utilises the coherent scattering of x-ray photons by the regular crystalline structure of a sample material to produce a spectrum of scattered photon energies. If the scattered x-ray photons are detected at a precise angle, a spectrum may be recorded that is unique to the material type being measured. Crucially, this spectrum 'signature' also provides an indication to the quantities of material present.

Bone may be classified as one of two forms, either cortical bone (a dense outer shell that forms the exterior structure) or trabecular bone (a porous region of bony struts usually

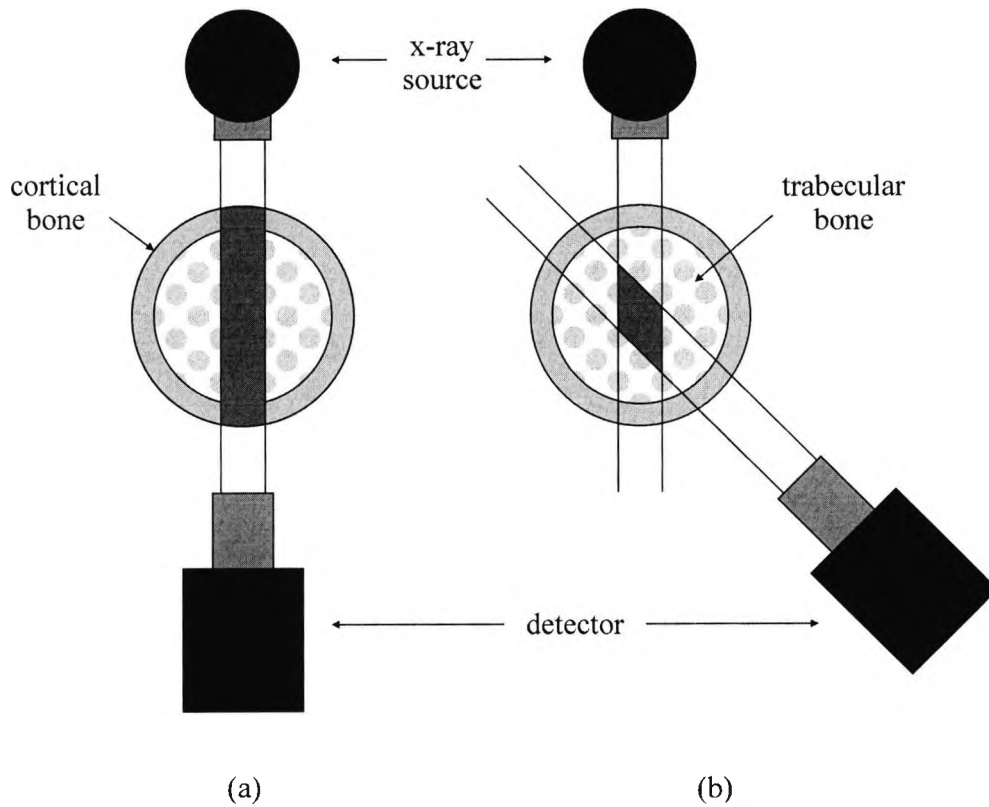


Figure 1-1. A comparison of transmission (a) and scattering (b) bone densitometry techniques. Information from both trabecular and cortical bone is detected by the transmission method whereas information from the defined volume of trabecular bone only is detected using the scattering method.

contained within a cortical surround). Trabecular and cortical bone are discussed in section 1.1.2.

It has been shown that osteoporosis levels may be determined with greater accuracy by measuring trabecular bone in isolation from cortical bone (Leichter *et al.*, 1987). Photon scattering methods such as EDXRD offer such a capability (figure 1-1b). In the clinical environment, the density of bone is most commonly measured using dual energy x-ray absorptiometry (DEXA), a photon transmission method which cannot isolate specific bone volumes (figure 1-1a). This results in a measure of both cortical and trabecular bone. For the EDXRD bone density experiments discussed in the following chapters, the geometry was arranged to position the scattering volume within a region of trabecular bone, thus reducing the influence of cortical bone.

This work concentrates on the determination of the minimum limits of detection that can be achieved using an EDXRD system. If a change in bone density may be detected with a precision comparable or better than that of the contemporary clinical methods, EDXRD may be a clinically viable alternative. It may offer bone densitometry diagnosis in aspects not available using current methods, such as the accurate determination of the bone density of specific volumes of trabecular bone.

If it can be shown that EDXRD is a useful and convenient diagnosis tool for the determination of bone density offering information not available using current methods, the onset of osteoporosis in a patient might be detected earlier. Thus a treatment programme may be started sooner, reducing the risk of debilitating fractures that are also expensive to treat.

The general aims of this project are:

- To develop techniques for bone sample preparation and demineralisation to simulate *in-vivo* bone density loss.
- To accurately measure the density of bone + marrow volumes to determine the minimum detectable limits of EDXRD as compared to those of DEXA.
- To assess the viability of the EDXRD method for clinical use with respect to radiation dose ramifications.
- To demonstrate that structure has an important role in determining the strength of trabecular bone, not density alone.

In order to fulfil these aims, the work of this project is discussed in the following chapters:

- | | |
|---------------|---|
| Chapter One | The remainder of this introduction is a discussion of the theory upon which the various aspects of the project are based, including comments on related research and literature. |
| Chapter Two | Preliminary characterisations of the x-ray tube and detection system used for all the EDXRD experiments of the project. |
| Chapter Three | The first part of this chapter discusses the calculation of EDXRD experimental geometry with respect to the bone samples used. The second part describes the construction of bone + marrow mix phantoms (masses of solid or liquid medium designed to simulate the attenuating properties of a human body or region therein). These |

- phantoms, constructed to have various bone densities, were used in initial EDXRD and DEXA experiments.
- Chapter Four A description of initial EDXRD and DEXA experiments using the bone + marrow phantoms. The EDXRD apparatus featured many variable parameters that enabled optimum geometry to be determined for a largely fixed parameter EDXRD diffractometer. Initial minimum detectable limits for EDXRD and DEXA were determined.
- Chapter Five This chapter describes various aspects of the trabecular bone sample cubes used for the experiments of the remainder of this project. The location of sample extraction from excised femoral heads is discussed, along with the removal of sample marrow lipid. A technique to simulate bone mineral density loss using EDTA is described, followed by a method to assess demineralisation homogeneity. A method of calculating the density of EDXRD scanned volumes from within the bone cube samples and a procedure to replace bone marrow substitute into the samples are also presented.
- Chapter Six The EDXRD diffractometer with largely fixed parameters is described, followed by a method to correct measured EDXRD scattered spectra for attenuation by the samples and any additional attenuation added to simulate clinical sites.
- Chapter Seven The first of two chapters describing the main EDXRD and DEXA studies using the trabecular bone sample cubes. This chapter discusses studies using one component bone sample systems (trabecular bone only with no marrow), including calibrated results (absolute bone density measurement) and comparative results (comparing measurements before and after bone density reduction). A variety of additional attenuation is also employed.
- Chapter Eight This second chapter describes further EDXRD and DEXA studies using the trabecular bone sample cubes. This chapter discusses studies using two component bone sample systems (trabecular bone with marrow substitute in the trabecular spaces), including calibrated results (absolute bone density measurement). The EDXRD method is further refined using peak fitting to smooth scattered spectra. A

	variety of additional attenuation is also employed to simulate clinical sites.
Chapter Nine	An investigation into radiation dose necessary for EDXRD measurements of varying effectiveness. Dose measurements are compared to those from studies of radiation dose resulting from other density measurement modalities, notably DEXA.
Chapter Ten	An investigation into bone sample strength, designed to illustrate that strength (and therefore fracture risk) is influenced not only by bone density but also by trabecular architecture.
Chapter Eleven	This chapter summarises the conclusions from the preparatory work and the main study. Suggestions for further work are offered and final project conclusions are made.
Appendices	A collection of useful information pertinent to this project, including formulae derivations, technical drawings, data tables and software (especially useful for the formats of file types).
Bibliography	Offers a selection of useful texts encountered during the course of this project.

- o 0 o -

The following sections of this introduction provide a discussion of the variety of background theory upon which aspects of this project are based. Extensive referencing to related research and literature are included.

Section 1.1	An introduction to the anatomy and physiology of bone, including the mineral element (properties of which are exploited by the EDXRD technique) and definitions of cortical and trabecular bone.
Section 1.2	A discussion of various aspects of bone biomechanics. The mechanical function of bone is reviewed, along with an introduction to the proximal femur (project sample source and biomechanical example) and definitions of the physical quantities used for determining bone strength
Section 1.3	A discussion of various aspects of bone density, including definitions of density relating to various states of bone. Factors and diseases

affecting bone density are introduced.

- Section 1.4 A review of x-ray photon interactions with matter pertinent to this study. These include transmission, scattering and absorption, further discussed in sections on coherent scattering, photoelectric absorption and Compton scattering.
- Section 1.5 A review of various methods of bone densitometry including radiographic methods (radiogrammetry, radiographic photodensitometry and the Singh index), photon absorptiometry (single photon, dual photon and DEXA), computed tomography, photon scattering methods, neutron activation and radiation free methods (ultrasound and magnetic resonance imaging).
- Section 1.6 Radiation dosimetry is discussed in this section, including definitions of some of the radiation dose quantities in use and the theory of thermoluminescent dosimetry.
- Section 1.7 X-ray diffraction is introduced, forming the basis of EDXRD. The discussion is then refined to aspects of diffraction pertinent to this study, being Bragg diffraction and x-ray powder diffraction.
- Section 1.8 The discussion of diffraction is developed into the EDXRD method, a description of a practical diffractometer and how this might be applied to the measurement of bone density.

1.1

BONE

Bone is a connective tissue of a highly vascular nature, its functions many and varied. It is required for supporting the soft tissues of the body and for providing attachment for skeletal muscles. It is also necessary as a protective barrier for delicate internal organs, such as the rib cage surrounding the heart and lungs and the skull enclosing the brain. The skeleton is essential for the movement of the body, the attached muscles contracting to move bones. Minerals important to body function are stored as part of bone structure, mainly calcium and phosphorous (minerals required for muscle and nerve activity). If levels decrease in the body, minerals are released from bone into the blood for distribution around the body in order to maintain the critical balance.

Red bone marrow is found within the medullary cavities of some adult bones (and all infant bones), important for the production of red and white blood cells and platelets. As

infants develop, much of the red bone marrow becomes yellow marrow, the cells of which store lipids – an important chemical energy store.

Bone is a dynamic, living tissue. The bones of adults are continuously being broken down and remodelled by dedicated cells called osteoclasts and osteoblasts. The function of osteoclasts is to break down the bone matrix, removing minerals and collagen. Osteoblast cells deposit new minerals and collagen, the actions of the two cell types combining in a delicate homeostasis. If osteoblast activity significantly lags that of the osteoclasts, bone substance decreases, weakening bones and compromising bone function. Should osteoblast activity become significantly advanced beyond that of the osteoclasts, bones become abnormally dense, leading to impaired function such as reduction of joint movement.

1.1.1 Components and Synthesis of Bone

In terms of histology, bone may be considered to be composed of three components, being the organic matrix (collagenous and non- collagenous), the mineral content and bone cells.

Approximately one-fifth of the weight of mature bone consists of matrix water. Between 30 and 40 percent of the dry weight of bone is made up of an organic protein matrix, of which 90 to 95 percent forms a system of collagenous fibres. This structure provides resilience and a certain amount of flexibility. The remaining 60 to 70 percent consists of complex mineral salts, impregnated in the protein fibres to provide strength and weight bearing capabilities. (Soames, 1995.) Bone cells are also present in the mineralised protein matrix.

The bone salts form the inorganic component of bone. A variety of techniques, such as colourimetry, atomic absorption spectrometry and x-ray diffraction have been employed to investigate the nature of these salts (Hukins, 1989). Constituent bone salt ions have been found to be mainly calcium (Ca^{2+}), magnesium (Mg^{2+}), phosphate (PO_4^{3-}), carbonate (CO_3^{2-}), hydroxyl (OH^-), chloride (Cl^-), fluoride (F^-) and citrate ($\text{C}_6\text{H}_5\text{O}_7^{3-}$) (Williams and Warwick, 1980).

Some of these bone salts form structured crystals and some are amorphous. Studies using x-ray diffraction have shown that the principle crystal is (or most closely resembles) hydroxyapatite ($\text{Ca}_5(\text{PO}_4)_3(\text{OH})$), sometimes known as tricalcium phosphate), with some calcium carbonate (CaCO_3). Hydroxyapatite forms needle shaped crystals of

20 to 40 nm length, 3 to 6 nm width (Williams and Warwick, 1980). Usually, the long axis of the crystal lies parallel to the collagen fibres, the crystal being partly embedded within them.

Human bones do not become fully rigid until growth stops during late adolescence. The embryonic skeleton consists of fibrous connective tissue membrane (derived from embryonic connective tissue called mesenchyme) and pieces of hyaline cartilage which form an initial bone shape. Bone is formed by the ossification of these supporting structures. Ossification begins around the sixth or seventh week of embryonic life and continues throughout adult life.

Bone synthesis is under the control of cells known as osteoblasts, which initially replace the pre-existing connective tissue with bone during its formation. Bone remodelling continues throughout life, whereby bone is absorbed by osteoclasts and replaced by cells called osteoblasts. The rate of remodelling differs dramatically throughout the skeleton. A variation of this phenomenon, known as bone modelling, is demonstrated when (for example) bone trabeculae are encountered with osteoblasts on one side and osteoclasts on the other. The trabecular shape is changed as bone deposition occurs on one side and absorption on the other. This process is thought to accommodate altered stresses acting throughout the bone, perhaps following injury (Freemont, 1989). It is particularly important during bone formation.

1.1.2 Cortical and Trabecular Bone

Throughout the body, relative quantities of bone and bone structure vary significantly, reflecting shape, function and location. The arrangement of cavities and bone microstructure provides an optimum mass to strength ratio. It is therefore useful to classify differing bone types in order to compare them. Bone may be classified as one of two forms, either *cortical bone* (also known as compact bone) or *trabecular bone* (also known as cancellous or spongy bone).

Cortical bone is the dense outer shell that forms the exterior structure that, in most cases, surrounds the porous honeycomb of trabecular bone. It is covered in a membranous periosteum layer, except for the articulating surfaces, which are covered with a tougher cartilage layer.

Volumes contained within the cortex (the outer layer of cortical bone) are either hollow or include regions of bony struts, known as trabecular bone. Spaces between trabecular

bone (or hollow medullary cavities where there are no trabeculae) are filled with bone marrow. The fine inner trabecular structures collectively contribute to the overall strength of the bone and divide some of the marrow areas. Trabecular bone is, in general, enclosed in the hard cortical bone shell. However there are some exceptions, such as parts of the calcaneus and vertebral bodies, where trabecular bone exists without a complete cortical surround. Trabecular bone is essentially a compromise, maximising strength while minimising size and weight to maintain its local function.

Blood vessels enter the bone at various points, to provide nutrition. Also there are some nerves associated with bone, primarily associated with pain.

Cortical and trabecular bone are both porous but differ from each other in their relative amount of solid matter and in the size and number of their integral spaces. Cortical bone has a relatively high amount of solid matter and a small amount of spaces, the converse being true for trabecular bone.

1.2 BIOMECHANICS OF BONE

Adult bone appears at first to be a simple, immobile tissue, but has a variety of important physiological roles (as described in section 1.1). The mechanical functions of bone are served by the important properties of hardness and moderate elasticity, along with minimal plasticity and brittleness. These properties are essential for the efficient mechanical roles of bone – standing, moving, muscle insertion and operation (establishment of lever systems to transform muscle contraction to movement) and soft tissue and organ protection (Bonucci, 2000).

1.2.1 Mechanical Functions of Bone

Comparisons are often made between the mechanical properties of man made structures and those of the macro structure of bone and internal trabecular structure. Bone structure and the mix of cortical and trabecular bone has evolved in response to the nature of the local forces the bone has to withstand. This has long been recognised, F. O. Ward having studied trabecular patterns in the femoral head in the 19th century (quoted in Soames, 1995). Trabecular systems are observed that have adapted to specific forces at work on the bone. This includes, for example, the attachment of tendons at the greater trochanter (part of the proximal femur). The external feature of the bone is pronounced, there is a thicker cortex and the trabeculae are more condensed. Adaptation is also evident in the

structure of long bone. The mid part of the tubular cortical shaft of a long bone has the thickest region of cortex, in order to withstand torsion and bending stresses. There are few or no trabecular. The articulating extremities of long bones have a markedly different structure, generally adapted to withstand compression forces. The extremities have a thin cortex that contains a volume filled with trabecular bone.

Bone strength, including the strength of trabecular bone, cannot be assessed by studying bone density alone. The structure of bones is an important factor and must therefore be considered in any study of bone strength. There is strong evidence (Maquet, 1985) that trabecular architecture plays an important role in bone strength and therefore in determining risk of fracture. Although yet to be conclusively proved, it is thought that structured trabecular patterns coincide with routes of stress. Very complex situations are involved and so it is difficult to apply absolute models, close approximations often being the most achievable (Whitehouse and Dyson, 1974). Isolation of sample areas or model simplification makes testing and analysis easier but inevitably causes the model to become more remote from the true situation.

In general terms, the study of mechanics assesses the effects of forces applied to objects. Bone mechanics may be studied with respect to whole bone units or isolated samples, designed to test particular structural components.

There have been numerous studies of bone mechanics forming a large body of knowledge in its own right. Bone architecture is considered to be organised in a hierarchical fashion, depending on the magnification employed in its study (Hoffler *et al.*, 2000). It is thought that bone mechanical properties at one such level are defined by the properties of more microscopic levels (Hoffler *et al.*, 2000). For example, compression testing of trabecular bone cubes (the investigation employed in this study) may be considered with respect to the modulus of the whole specimen. It may also be considered with respect to the trabecular structure within the cube (finite element studies) or trabecular microstructure.

The hierarchy defined by Hoffler *et al.* (2000), with some examples of bone work, is:

1. *Whole-bone level*: an investigation determining a relationship between regional bone density and vertebral properties (McCubbrey *et al.*, 1995).
2. *Architectural level* (cortical or trabecular specimens): an investigation into the compression properties of trabecular bone cubes in three orientations taken from various locations showed high variability (Ciarelli *et al.*, 1991).

3. *Tissue level* (single trabeculae, osteons or cortical microbeams): an investigation into the fatigue behaviour of human cortical and trabecular tissue showed that cortical tissue had a higher modulus and fatigue strength than trabecular tissue (Choi and Goldstein, 1992).
4. *Lamellar level* (unit layers, concentric as part of Haversian system, or central spongiosa).
5. *Ultrastructure level* (molecular and mineral components): an investigation into the contributions of collagen and mineral to elastic and plastic behaviour (Burstein *et al.*, 1975).

1.2.2

The Proximal Femur

The proximal femur is discussed here as a typical example of bone biomechanics and because the bone specimens used throughout this work were obtained from femoral heads. The whole femur is the longest and strongest bone in the body, being required to withstand large forces from body weight and muscular attachment. Figure 1-2 shows the femur with its important landmarks.

The proximal femur features a rounded articular head that forms more than two thirds of a sphere. It is smooth, except for a small, roughened depression for ligament attachment, called the fovea. The neck is a narrow portion about 50 mm long that connects the head to the shaft. It lies at an approximate angle of 125° to the shaft (this angle is less obtuse in males than in females (Gunn, 1996)). The greater trochanter lies on the lateral aspect of the proximal femur, providing an insertion for the gluteus and

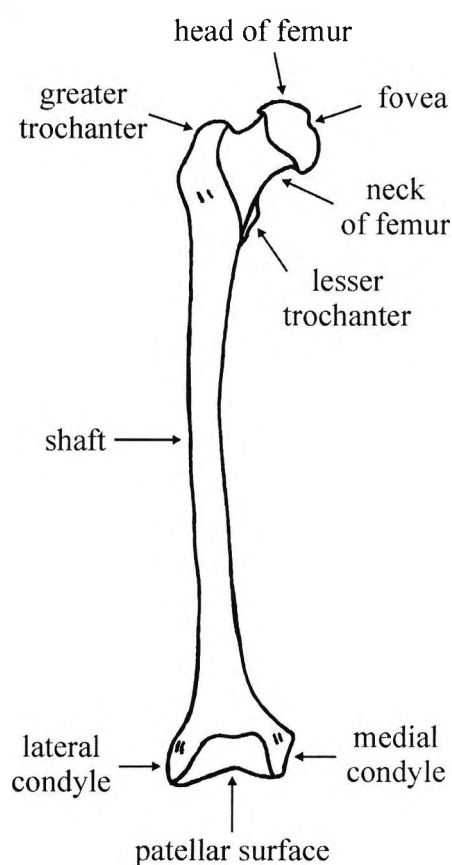


Figure 1-2: External landmarks of the femur. (After Gunn, 1996.)

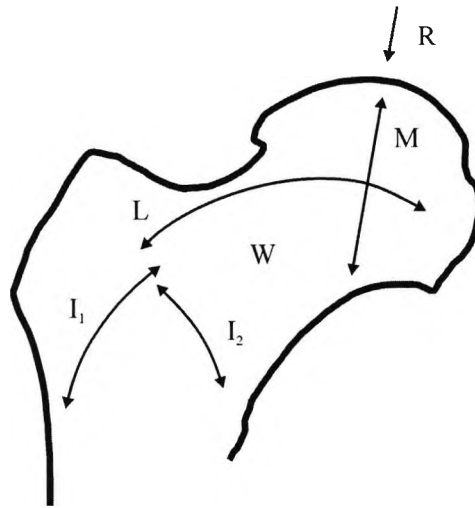


Figure 1-3. Sketch of the proximal femur demonstrating Ward's trabecular systems. (After Whitehouse and Dyson, 1974.)

piriformis muscles. The lesser trochanter lies inferiorly on the junction between the neck and the shaft, providing an insertion for the ilio-psoas muscle.

Internally, there is considerable diversity in trabecular architecture of the proximal femur, even in closely neighbouring regions. Trabecular widths vary between 50 μm and 400 μm (Soames, 1995). Even in an apparently uniform region of the trabecular pattern, measured characteristics are found to vary by as much as 20% between adjacent 5 mm \times 5 mm areas (Whitehouse and Dyson, 1974).

Trabeculae in the proximal end of the femur appear to be arranged along lines of greatest compression and stress (approximately). Whitehouse and Dyson comprehensively examined trabecular bone in this region, in their important paper of 1974. The trabecular systems observed in the proximal femur, first described by Ward in 1838, are shown in figures 1-3 and 1-4, using terminology by R. S. Garden (Soames, 1995).

The medial group (M) is the system that can be most satisfactorily described in terms of function. It consists of a column of very dense and highly organised trabeculae, its upper end arranged in a dense wedge at right angles to articular surface of the head (supported by strong trabeculae extending to the sides of neck). This system can be clearly identified on the radiographic image in figure 1-4a. It extends in a gentle curve to the strong cortical bone of the upper part of the femoral shaft. The system is surrounded by a

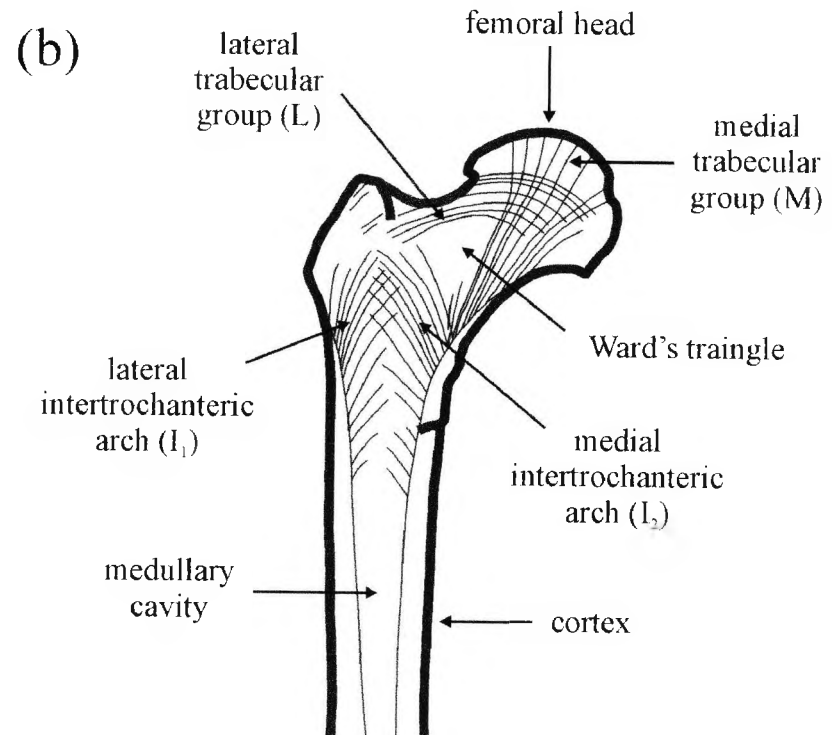
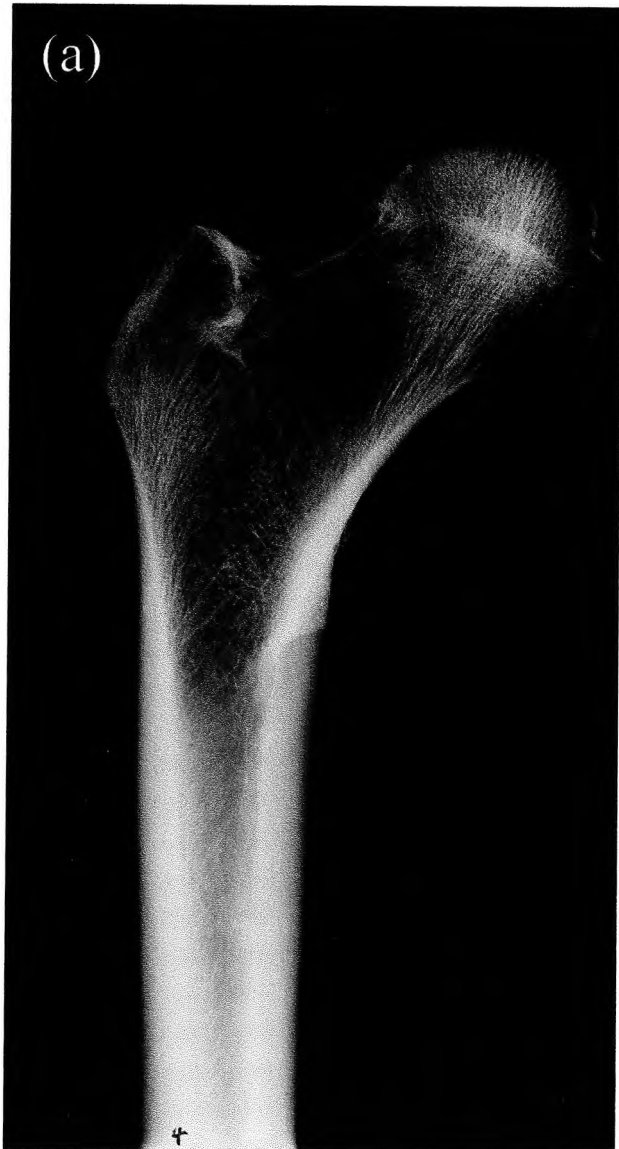


Figure 1-4: Internal structures of the proximal femur. A radiograph of an archaeological proximal femur (a) clearly demonstrates the features shown in the key (b).

complete or almost complete ring of lighter trabeculae bone, which underlies areas where the cortex is thin (and therefore not designed to transmit stress). This demonstrates the importance of the medial trabecular group. Forces applied to the femoral head are transmitted by the medial system to the junction of the femoral neck with the shaft. The system is in line with the main direction of stress, R (which is not quite vertical), transmitted from the acetabulum (of the hipbone) in the standing position (figure 1-3). Heavy and strongly orientated trabeculae are observed in the inferior portion of the medial group with less orientation in the superior portion. There is also a structural discontinuity called the epiphyseal scar (not shown), which is located at the site of the epiphyseal line (present during bone formation). There is no marked change in bone density at the scar but disruption of the trabecular pattern is observed (Whitehouse and Dyson, 1974).

The lateral group (L), also identifiable in figure 1-4a, lies below the greater trochanter and upper surface of the neck. It is plausible that the function of this group is to withstand tension and as such is often referred to as the tensile group (Whitehouse and Dyson, 1974). The group is usually described as decussating with the medial group (M), forming two sets of mutually perpendicular members, one withstanding compression and one withstanding tension. The idea that there are two systems of trabeculae (M and L) in the region of decussation is controversial (Whitehouse and Dyson, 1974).

The trabeculae vary in character throughout the lateral group. There is little apparent orientation and similarities in different areas. This leads to greater difficulty in describing the function of structure fully, perhaps indicating that the group is not composed of a single system, due to the complex variety of forces that are at work (Whitehouse and Dyson, 1974).

There are two further groups, the intertrochanteric arches (I_1 and I_2), that originate from lateral and medial cortical bone. These two groups form the upper layers of a series of arches which extend between sides of the shaft, transmitting forces applied to the upper end of the femur.

Ward's triangle (W) is a region containing less trabeculae than neighbouring areas. It is framed by the M, L and I_2 groups. Ward's triangle is less prominent in younger subjects. As with other areas of lightly constructed bone, it also exhibits trabeculae with less order. This region of the femoral neck is therefore the most at risk from fracture in subjects with low bone density.

1.2.3 Force, Displacement, Stress, Strain and Elastic Modulus

In mechanics, force is a measurable vector with magnitude and direction (and point of contact). There are three main types of force that may be considered in bone strength mechanics – compressive, tensile and shearing. Since the samples under test are static, the effect of force is to change the sample shape (not its velocity – a dynamic condition). Force magnitude is expressed in SI units of newtons (N).

The mechanical element of work in this project is limited to an architectural level study of sample cube compression strength in three orientations. It is designed to complement the densitometry work to illustrate that bone strength is a function of both bone density and structure, not density alone.

Under normal conditions, bone behaves in a similar manner to that of an elastic material (An *et al.*, 2000a). Beyond elastic limits, bone material exhibits plastic properties and material failure presents as bone fracture. While a sample is being loaded, a load-displacement curve may be generated, which defines the deformation of the sample in the direction of the applied force. An example is shown in figure 1-5a.

In order to compare different materials, or similar materials with different dimensions, a method of standardisation is required. Force and displacement are normalised to stress and strain using the dimensions of the sample. The load-displacement curve is therefore converted to a stress-strain curve (figure 1-5b).

Stress (σ) is defined as force per unit area, calculated by dividing the magnitude of the force by the surface area over which it is applied:

$$\sigma = \text{force} / \text{area} \quad [1.1]$$

Stress may be normal (tensional or compressive), bulk (volume) or shear. The SI unit of stress is the pascal (Pa), one newton per square meter. However, for this study, specimens are generally $15 \times 15 \times 15 \text{ mm}^3$ and so stress is usually quoted in N/mm^2 .

Strain (ϵ) is defined as the dimensional change (linear, volume (bulk) or shear) of a body under the influence of force(s). Linear strain is the change in length (ΔL) per unit length (L):

$$\epsilon = \Delta L / L \quad [1.2]$$

Strain is a ratio and therefore has no units. Strictly speaking, if a material is compressed, strain is negative. However for this study, it is generally expressed as a positive value.

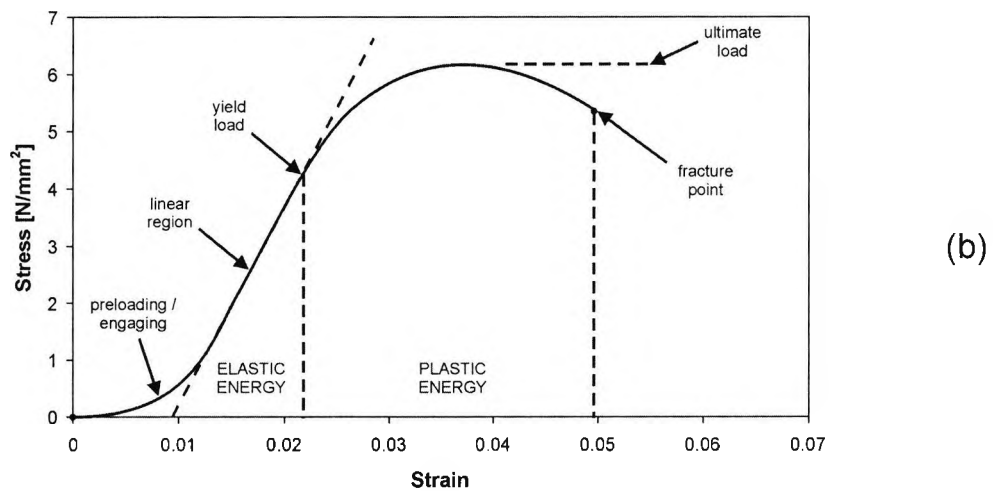
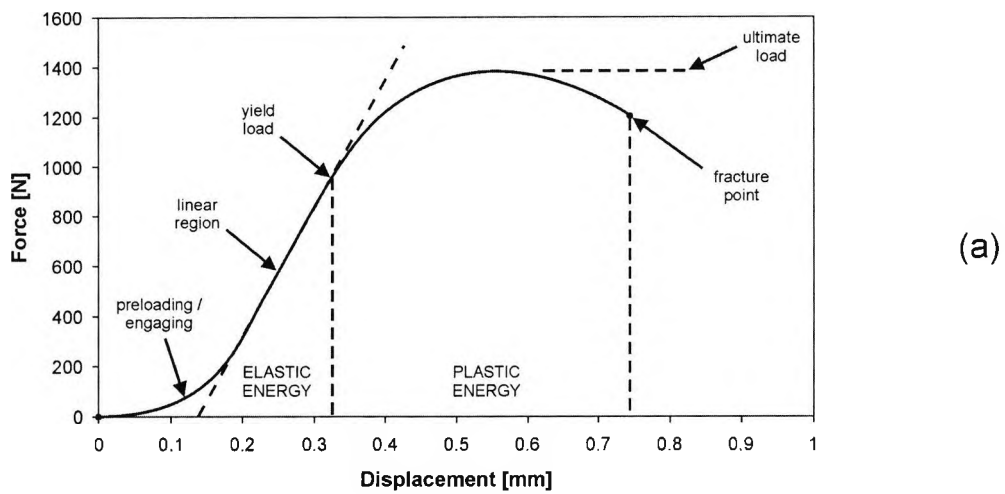


Figure 1-5: Typical load-displacement (a) and stress-strain (b) curves. The load-displacement curve was generated from data recorded from the compression of a $15 \times 15 \times 15 \text{ mm}^3$ trabecular bone sample. The stress-strain curve was created by normalising the data from the load-displacement curve (a). (After An *et al.*, 2000a.)

The elastic modulus is the ratio of stress to strain of an elastic material. It is only valid over the elastic (linear) region of the stress-strain curve i.e. whilst the material obeys Hooke's law (for a certain range of stresses, the strain produced is proportional to the stress applied; the stress disappears completely on removal of the stress). There are several elastic moduli depending on the strain applied (normal, bulk or shear). When

normal stress is applied, the elastic modulus is known as Young's modulus (E) and is defined as:

$$E = \frac{\text{applied load per unit area of cross section}}{\text{change in length per unit length}} \quad [1.3]$$

Since strain is a ratio and therefore dimensionless, elastic moduli have the same units as stress (force / area).

The elastic modulus may be determined by measuring the gradient of the curve in the elastic region.

1.3 BONE DENSITY

The term 'bone density' is not particularly meaningful without further qualification. Bone density must be defined with respect to given conditions and may also vary depending on a modality used for measurement.

The *material density* of bone is defined as the wet weight (bone matrix fully hydrated) of a specimen divided by its volume (bone material but not marrow space). Cortical bone material density ranges between 1.7 and 2.0 g/cm³ and trabecular bone material density between 1.6 and 1.9 g/cm³ (An *et al.*, 2000b), cortical and trabecular being similar in value.

$$\text{material density} = \text{wet weight} / \text{material volume} \quad [1.4]$$

The *apparent density* of bone is defined as the wet weight per unit structural volume (including bone and marrow space with no marrow). The bone matrix is fully hydrated, but the pores or voids are free of water and marrow. It may also be known as *structural density*. Cortical bone has an average apparent density of 1.9 g/cm³ (An, 2000), basically the same as material density since porosity is minimal (no marrow space). The term '*cortical bone density*' is therefore often used as a general description. Trabecular bone has an average apparent density of 0.62 g/cm³ (0.14 to 1.10 g/cm³) (An, 2000).

$$\text{apparent density} = \text{wet weight} / \text{sample volume} \quad [1.5]$$

Bone mineral density (BMD) is defined as bone mineral mass per unit bone volume. If an ashing method is used to obtain this measurement, it may also be called the *ash density*. Ash density is approximately 60% of the value of apparent density (An, 2000).

$$\text{ash density} = \text{ash weight} / \text{sample volume} \quad [1.6]$$

Term	Evaluation Method	Unit	Definition
Material density	Weighing	g/cm ³	Wet weight per unit material volume (bone material but not marrow space).
Apparent density	Weighing	g/cm ³	Wet weight per unit structural volume (bone material and marrow space but not marrow).
Bone mineral density (BMD)	Weighing	g/cm ³	Bone mineral mass per unit bone volume (ash density if an ashing method is used).
	Two-dimensional imaging (such as x-ray images)	grey scale	Intensity of image portion due to mineral content to a defined sample thickness.
	Radiographic absorptiometry (RA)	grey scale	Percentage difference to a standard (normal) number.
	Single-photon absorptiometry (SPA)	g/cm ²	Bone mass per measured area.
	Dual energy x-ray absorptiometry (DEXA)	g/cm ²	Bone mass per measured area.
	Quantitative computed tomography (QCT)	g/cm ³	Bone mass per measured volume.
Bone mineral content (BMC)	Weighing	%	Ratio of mineral portion unit weight to dry bone unit weight.
	Single-photon absorptiometry (SPA)	g/cm ²	Bone mass.
	Dual energy x-ray absorptiometry (DEXA)	g/cm ²	Bone mass per unit length.
	Quantitative computed tomography (QCT)	g/cm ³	Bone mass per measured length.

Table 1-1. Some variations in 'bone density' definitions (from An *et al.*, 2000b, Wong and Sartoris, 1996 and Van der Perre and Lowet, 1994). Methods of evaluation are described in section 1.5.

Bone mineral content (BMC) is defined as the ratio of the unit weight of the mineral portion to dry bone unit weight. This ratio is often given as a percentage. If an ashing method is used to obtain this measurement, it may also be called the *ash content*. Ash content is calculated as a ratio of ash weight to dry weight:

$$\text{ash content} = (\text{ash weight} / \text{dry weight}) \times 100\% \quad [1.7]$$

Dry weight is the dehydrated equivalent of wet weight (assessed by alternating sequences of sample drying and weighing until the mass remains unchanged). Ash weight is determined by burning off all material except for the bone mineral in a furnace.

For many of these terms there is some variation in the definition and expression of bone density, usually depending on the method used to determine it. These variations are summarised in table 1-1.

1.3.1 Factors Affecting Bone Density

There are many factors that influence the density of bone. These include nutrition (minerals, vitamins, etc.), hormone levels in the body, lack of exercise, smoking and alcoholism (Shane, 1988).

The dietary intake of calcium is a key factor that affects bone mineral density. If calcium intake in adolescents is below that which is required during the rapid period of bone growth, peak bone mass will be stunted. Other mineral deficiencies affect bone mineral density significantly. For example, a deficiency of magnesium will inhibit the action of the osteoblasts. Boron may be required to inhibit calcium loss and to increase levels of oestrogens. (Tortora and Grabowski, 1996.)

Vitamin C is necessary for the maintenance of the bone matrix. Deficiency leads to decreased collagen production (organic bone matrix), inhibiting bone growth and delaying fracture repair (Tortora and Grabowski, 1996). Calcium salts tend to accumulate at the metaphyseal end of long bones creating an area of increased density and leaving the rest of the bone deficient (Cotran *et al.*, 1994). Vitamin A is important in the activity, distribution and co-ordination of osteoblasts and osteoclasts (Tortora and Grabowski, 1996).

Parathyroid hormone (PTH), secreted by the parathyroid glands, promotes bone absorption. The number and activity of osteoclasts is increased by enhancing the

recovery of calcium from urine and by promoting the formation of the active form of vitamin D (calcitriol). PTH is an important hormone for the regulation of calcium exchange between the blood and bone. If PTH is present in excess, the increased activity of osteoclasts results in rarefaction of bones. Calcitonin, secreted by the thyroid gland, promotes bone formation by inhibiting the activity of osteoclasts, speeding up calcium absorption from the blood and accelerating calcium deposit in bones. (Tortora and Grabowski, 1996.)

Reduced physical activity has been shown to increase bone loss. This is striking with losses observed in immobilised or paralysed limbs and in the skeletons of astronauts exposed to prolonged periods in a gravity-free environment. Higher bone densities are observed in athletes when compared with individuals with a less active lifestyle. (Cotran *et al.*, 1994.)

Weight bearing exercises help to build thicker and stronger bones and to retard the loss of bone mass that occurs as people age. When placed under these additional stresses, bone tissue becomes stronger with time, through increased deposition of mineral salts and production of collagen fibres. Calcitonin production is also increased, inhibiting bone re-absorption. Bones are remodelled (by the osteoblasts and osteoclasts) according to the changing stresses and strains imposed upon them. Trabeculae arrangement corresponds to the direction of the lines of force and realign if the force lines change, perhaps due to an injury. This is known as Wolf's Law (see also section 1.1.1). Ligament grooves also follow this law. Without mechanical stress, bone re-absorption outstrips bone formation. Removal of mechanical stress weakens bone through demineralisation and collagen reduction. If a person is bedridden or has a fractured bone in a cast, the strength of the unstressed bone diminishes.

1.3.2 Diseases Affecting Bone Density

Osteoporosis is a skeletal disease characterised by low bone density and general deterioration of bone tissue. Bone loss may be localised to certain bones (or areas of bone), perhaps resulting from the disuse of a limb, or it may involve the entire skeleton due to the manifestation of a metabolic bone disease. Three major fracture sites in osteoporosis are the hip, vertebrae and distal radius. Fracture can follow from minor trauma in the frail and elderly, the shock from which can be fatal.

Although the whole skeleton may be affected, osteoporosis manifests itself in certain regions to a greater extent than in others. Trabecular regions have a far greater surface

area for a given bone mineral density and are known to be three to four times more metabolically active than regions of cortical bone (Pacifci and Avioli, 1993). Trabecular bone loss begins approximately a decade earlier than in cortical bone, for both men and women (Mazess, 1982). As such, trabecular regions of bones, such as those of the vertebral bodies or femur, are far more likely to show a significant manifestation of osteoporosis. This increased porosity is strikingly illustrated by figure 1-6. The measurement of bone mineral density with a view to detecting the onset of osteoporosis might therefore be improved if the density of trabecular bone were measured in isolation from that of cortical bone.

The primary (postmenopausal or senile) form of osteoporosis includes those forms of the disorder in which the cause is idiopathic (unknown). It occurs with ageing, particularly among postmenopausal women. Little is known of the underlying pathological processes that result in this bone loss but it has been suggested that this is related generally to the age related dysfunction of bone cells (Pacifci and Avioli, 1993). The deficiency of oestrogen is thought to be the major factor, starting a chain of events that stimulates greater osteoclast activity and therefore the reduction in bone mass. The osteoblast bone forming cells have a reduced ability to make bone matter and essential proteins deposited from the bone matrix become less effective. These age related changes in bone cells and the bone matrix have an effect on the remodelling balance.

Secondary osteoporosis is associated with conditions other than age or menopause. It may be caused by certain drugs or diseases, such as rheumatoid arthritis, or it may be genetically inherited (Shane, 1988).

Peak bone mass is achieved during young adulthood, the magnitude of which is predominantly determined by hereditary factors, with physical activity, muscle strength, diet and hormonal activity also being contributing factors (section 1.3.1). After this peak, the remodelling cycle becomes less effective and a small deficit of bone mass between resorption and formation develops. This bone density loss typically begins after 60 years in men and 30 years in women (accelerating between the ages of 40 to 45). As much as 30% of calcium is lost by the age of 70 (Tortora and Grabowski, 1996). Age related bone loss can average at 0.7% per year (Cotran *et al.*, 1994), affecting each sex to the same degree but white people more than black people. Up to 2% of the mass of cortical bone and up to 9% of the mass of trabecular bone may be lost in the 10 years following the menopause (Cotran *et al.*, 1994).

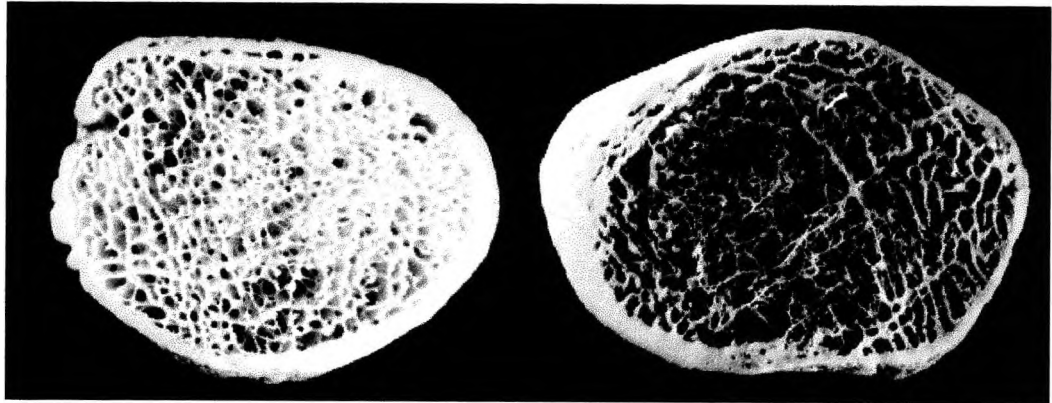


Figure 1-6: Illustration of osteoporosis. This photograph shows slices through two femoral necks. The slice on the left illustrates healthy bone and the slice on the right illustrates bone with a significant degree of bone density loss. Note that although the cortex does display some bone loss, the majority is from the trabecular region. (Image courtesy of M. Farquharson.)

Although osteoporosis is the primary cause of adverse bone density condition, there are a number of other diseases that affect bone. These include osteomalacia and rickets (an insufficient mineralisation of the skeleton), Paget's disease (destruction and repair of bone resulting in the weakening, deformity and thickening of bone) and osteopetrosis (a rare failure of the absorption mechanism, resulting in an increase in bone density).

1.4 X-RAY PHOTON INTERACTIONS WITH MATTER

A number of photon interactions may occur as x-rays pass through matter. Since these interactions are important to many of the bone density measurement techniques discussed in section 1.5, they are briefly discussed here. Further details for this section, including origins of formulae, may be found in standard texts such as Johns and Cunningham (1983).

As a photon passes through matter, it may be transmitted, scattered or absorbed. A transmitted photon passes through material without interacting with any of its atoms, and is unaffected. However, if the photon interacts with the atoms by being scattered or absorbed, the primary photon beam intensity is reduced and so attenuated.

The simple exponential attenuation of a large number of photons (I) may initially be described by considering an attenuating material of infinitesimal thickness dx (figure 1-7a). If μ is the probability that an individual photon interacts in a unit thickness of material, the probability of an interaction within dx is μdx . μ may be considered as a constant of proportionality (with units of length^{-1} , often expressed in cm^{-1}).

If I photons are incident upon dx , the change dI in I is given by:

$$dI = -\mu I dx \quad [1.8]$$

So attenuation of a photon beam in the direction of incidence is related to the thickness of the material with which it may interact. In other words, the number of photons removed from a primary beam is proportional to the thickness of the material through which it passes.

The fractional change in I due to the attenuation is:

$$dI/I = -\mu dx \quad [1.9]$$

Integrating equation 1.9 over the whole depth of attenuating material, x (figure 1-7b), results in equation 1.10, the law of exponential attenuation:

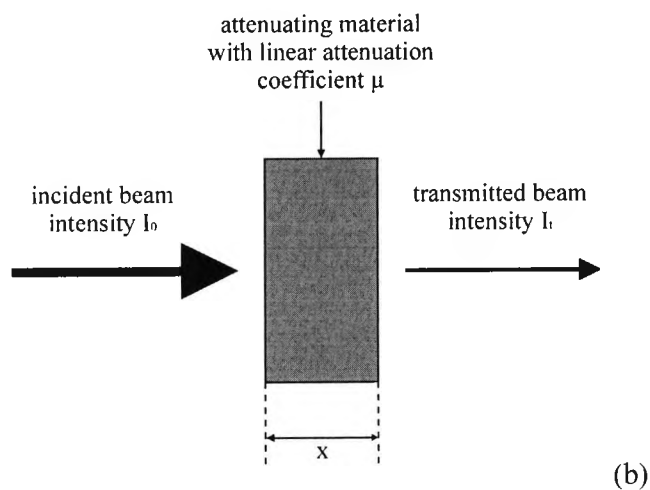
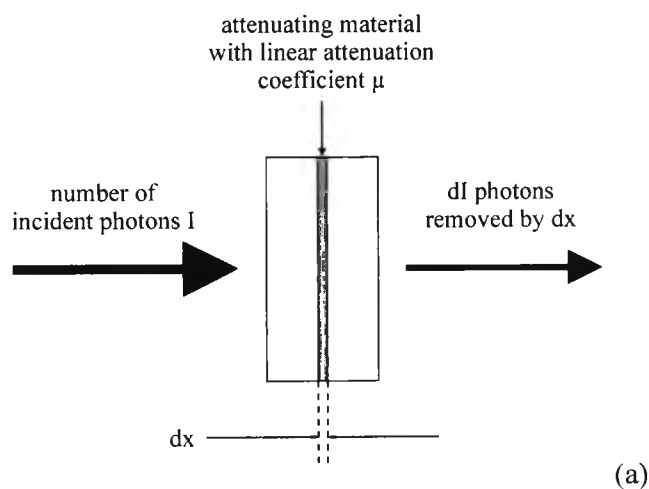


Figure 1-7. Simple exponential attenuation of a narrow beam monoenergetic photon beam by a material of infinitesimal thickness dx (a), illustrating equation 1.8, and by a material of thickness x (b), illustrating equation 1.10.

$$I_t = I_0 e^{-\mu x} \quad [1.10]$$

where I_t is the intensity of transmitted photons, attenuated by material of thickness x , I_0 is the original intensity of photon beam (i.e. at thickness $x = 0$) and μ is the total linear attenuation coefficient (the fraction of photons that interact per unit thickness of

attenuator), which is characteristic for a given material. This law provides a means of calculating attenuation by any thickness of material.

The exponential relationship is only valid for a monoenergetic photon beam, since μ is dependent on photon energy. The total linear attenuation coefficient also changes depending on the attenuating material and also on its physical state. The latter dependency can be overcome by dividing the total linear attenuation coefficient by the density of the attenuating material, ρ , resulting in the more fundamental total mass attenuation coefficient, μ_m (equation 1.11). It is the fraction of photons removed from a beam of unit cross-sectional area by unit mass of the material.

$$\mu_m = \frac{\mu}{\rho} \quad [1.11]$$

The probability of a photon interacting with a material depends on a number of factors, including the atomic number of the material (Z) and the energy of the photon (E). This probability is related to the effective area of an atom or molecule interacting with the photon, known as the cross section (per atom or molecule). Defining σ as the total effective cross section per scatterer for the removal of photons from the primary beam, the total linear attenuation coefficient, μ , is given by:

$$\mu = N\sigma \quad [1.12]$$

where N is the number of attenuating sites per unit volume.

If an x-ray photon interacts with an atom of a material and loses all of its energy, it is said to have been absorbed. An absorption process involves the transfer of energy from the photon to the atom of the material.

Scattering of an x-ray photon by the atoms of a material results in the photon being deflected from its path. The photon may or may not lose energy, depending on the nature of the scattering (inelastic or elastic, respectively).

Attenuation is the removal of photons from the primary beam by absorption or scatter processes, so the total attenuation coefficients (and therefore the total cross section) consist of individual attenuation coefficients resulting from any one of four predominant (or other) attenuating processes. These processes mainly consist of coherent scattering, photoelectric absorption, Compton scattering and electron-positron pair production. Total linear attenuation therefore consists of the sum of the individual linear attenuation coefficients for each of these reactions:

$$\mu = \sigma_{\text{coh}} + \tau_{\text{PE}} + \sigma_{\text{Com}} + \pi_{\text{PP}} + \text{others} \quad [1.13]$$

where σ_{coh} is the linear attenuation coefficient due to coherent scattering, τ_{PE} is the linear attenuation coefficient due to photoelectric absorption, σ_{Com} is the linear attenuation coefficient due to Compton scattering and π_{PP} is the linear attenuation coefficient due to pair production. Again this may be expressed in terms of mass attenuation coefficients by dividing by density, ρ :

$$\frac{\mu}{\rho} = \frac{\sigma_{\text{coh}}}{\rho} + \frac{\tau_{\text{PE}}}{\rho} + \frac{\sigma_{\text{Com}}}{\rho} + \frac{\pi_{\text{PP}}}{\rho} + \text{others} \quad [1.14]$$

The probability of any of these interactions occurring is given by the cross section for each interaction.

Pair production can only occur if the energy of the incoming photon is at least 1.02 MeV (the rest mass energy of an electron plus that of a positron). Since the photon energies used throughout this study do not approach 1.02 MeV, pair production is not discussed here. The remaining three interactions may occur and so are described in the following sections.

1.4.1 Coherent Scattering

Coherent scattering (also known as Rayleigh or elastic scattering) results in no permanent energy transfer from the photon to the atoms of the material. Since energy is conserved by the photon, no absorption occurs. Coherent scattering occurs when the photon energy is low compared to binding energies of the orbiting electrons of the material.

An incoming photon passes close enough to an electron to interact with it and raise its energy, but not sufficiently to ionise the atom. The electron then returns to its original energy level and a photon is emitted of equal energy to the original photon. This photon is emitted in a different direction to the path of the original photon (the basis of all scattering mechanisms) resulting in an effect known as Thomson (or classical) scattering.

Elastic scattering from a single free electron into the angular range θ to $\theta + d\theta$ can be determined from the differential scattering cross section per unit angle:

$$\frac{d\sigma_0}{d\theta} = \frac{r_0^2}{2} (1 + \cos^2\theta) 2\pi \sin\theta \quad [1.15]$$

where r_0 is the classical radius of electron ($2.817\ 94 \times 10^{-15}$ m).

The total cross section for this scattering event, σ_0 , known as the Thomson classical scattering coefficient, is given by integrating equation 1.15 between 0° and 180° (equation 1.16). It has the same value for all photon energies.

$$\sigma_0 = \frac{8\pi}{3} r_0^2 \quad [1.16]$$

Thomson scattering describes the process of scattering when considering a single electron. For coherent scattering, the effect of the whole atom is taken into account. The photon is an electromagnetic wave with wavelength λ and energy $h\nu$ (where h is Planck's constant and ν is frequency). The oscillating electric field of the photon sets the atomic electrons into momentary vibration, creating an electric dipole. The oscillating electrons emit electromagnetic radiation with the same wavelength (and therefore the same energy) as the incident photon. These scattered waves combine to form the final scattered photon, hence the term coherent scattering (a co-operative phenomenon). All the electrons of the atom are involved (figure 1-8).

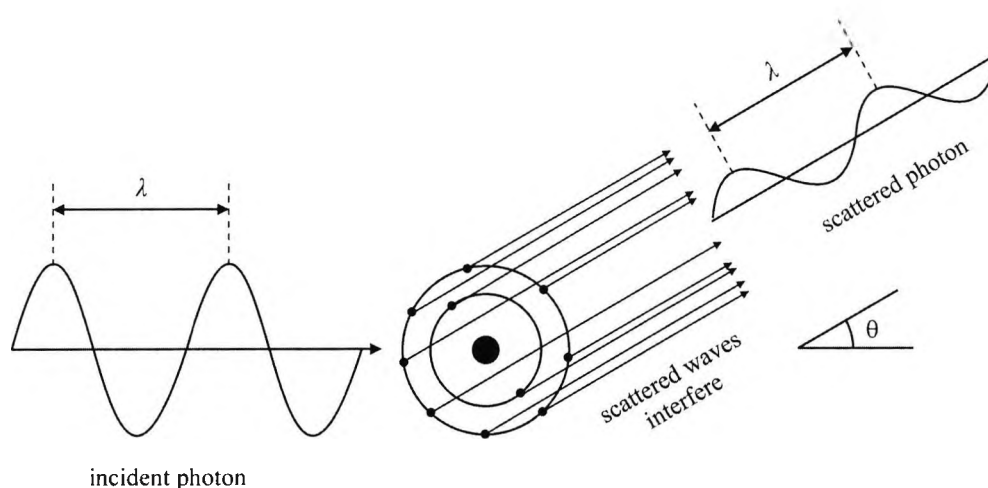


Figure 1-8. Coherent scattering, involving all the atomic electrons of the electron cloud. No energy is permanently transferred to the material. (After Johns and Cunningham, 1983.)

Coherently scattered photons are predominantly scattered through small angles. At larger angles, interference effects between photons scattered from different electrons of the same atom become more destructive, reducing the amplitude of the emitted photon. The change of the linear attenuation coefficient due to coherent scattering (σ_{coh}) with respect to the change of scattering angle is represented by differential equation 1.17:

$$\frac{d\sigma_{\text{coh}}}{d\theta} = \frac{r_0^2}{2} (1 + \cos^2\theta) [F(x, Z)]^2 2\pi \sin\theta \quad [1.17]$$

where x is given by equation 1.18 and $F[x, Z]$ is the atomic form factor.

Equation 1.17 is adapted from equation 1.15 with the inclusion of the atomic form factor which describes the loss of amplitude with coherent scattering as a function of x and Z , the atomic number of the scattering material. The parameter x , sometimes known as momentum transfer, is defined as the momentum transferred to a coherently scattered photon such that it is deflected through an angle θ (appendix A.1). It is given by:

$$x = \frac{1}{\lambda} \sin\left(\frac{\theta}{2}\right) \quad [1.18]$$

A form factor may be described as the ratio of scattered photon amplitude by an atom to the scattered photon amplitude of a free electron. For large values of scatter angle θ , this relationship tends towards zero. For smaller values, it approaches Z , the atomic number of the material. Thus form factors decrease with increasing θ for a given wavelength.

Atomic form factors are available as tables for various materials (for example Hubbell *et al.*, 1975). Molecular form factors have also been tabulated, values largely obtained experimentally.

The cross section for coherent scattering (σ_{coh}) decreases with increasing photon energy, becoming negligible at energies around 100 keV for materials with low atomic number.

A further phenomenon occurs as the scattering angle θ tends towards zero. According to equation 1.17, as θ decreases, the differential cross section increases, becoming highly forward peaked, resulting in a higher probability of coherent scattering taking place. However, an experimental study by Johns and Yaffe (1983) has shown that as θ approaches zero, the differential cross section tends towards zero due to the almost completely destructive interference of photons. This does not theoretically occur if a scattering molecule is considered in isolation, the differential cross section approaching

a maximum at $\theta = 0^\circ$. However interference between the scattered photons from electrons of other molecules of the material result in the high level of destructive interference at very low scatter angles. The maximum probability of coherent scattering therefore occurs at a low, but non-zero, angle. This maximum is dependent on the scattering material and the photon energy. For example, for pure water, maximum probabilities have been shown to occur at 11.3° for 20 keV photons, at 3.8° for 60 keV photons and at 2.2° for 100 keV photons (Johns and Yaffe, 1983).

Attenuation by this interaction may be represented by the mass attenuation coefficient for coherent scattering ($\sigma_{\text{coh}} / \rho$), demonstrating a dependency on the square of the atomic number of the material, Z , and the inverse of photon energy, E . Integrating equation 1.17 over θ gives:

$$\frac{\sigma_{\text{coh}}}{\rho} \propto \frac{Z^2}{E} \quad [1.19]$$

where ρ is the density of the scattering material.

It is the coherent elastic scattering of photons from a crystalline array of atoms that provide the basis of the energy dispersive x-ray diffraction (EDXRD) bone density measurement method. The Bragg diffraction exploited by EDXRD requires scattered photons that have not had their energy modified (see sections 1.7 and 1.8).

1.4.2 Photoelectric Absorption

Photoelectric absorption is an inelastic event since the incoming photon interacts with an orbiting atomic electron and gives up all its energy (figure 1-9). For this event to occur, the photon energy must be equal to or greater than the binding energy of the electron. The electron is ejected from the atom and the photon is absorbed. Any excess energy that the photon has above the binding energy is passed to the electron as kinetic energy. Since total absorption of the incoming photon occurs with this interaction, no scattering of this photon takes place.

An electron from a higher energy level of the atom quickly fills the vacancy left by the ejected electron. The difference in energy through which the electron passes to fill the vacancy is radiated as a characteristic photon. Alternatively, this photon may energise an outer shell electron sufficiently for it to be ejected as an Auger electron.

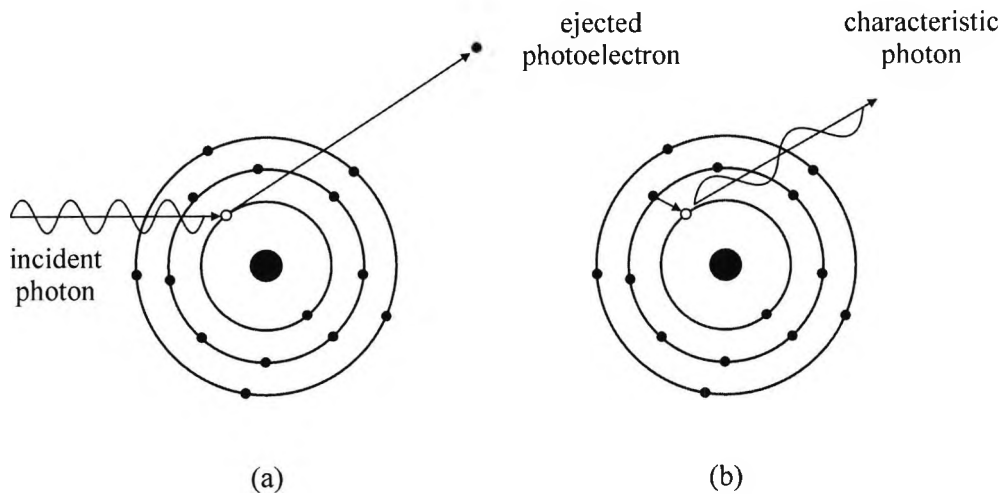


Figure 1-9. Photoelectric absorption. An incoming photon ejects an electron from its shell (a), which is replaced by an electron from a shell of higher energy, radiating a characteristic photon (b).

Attenuation by this interaction may be represented by the mass attenuation coefficient for photoelectric absorption (τ / ρ). It is approximately related to the cube of the material atomic number, Z , and the inverse of the cube of the photon energy, E :

$$\frac{\tau}{\rho} \propto \frac{Z^3}{E^3} \quad [1.20]$$

As the photon energy exceeds (approximately) 200 keV, the E^3 term becomes E^2 and, as energy increases further, eventually E .

For low Z materials (such as water), a plot of τ / ρ against energy demonstrates a smooth relationship. For higher Z materials (such as lead), this relationship becomes more complicated. Sudden increases in τ / ρ occur at the binding energies of each electron shell (K, L, etc.). As photon energy increases above a binding energy, the electrons of this shell are suddenly available for photoelectric absorption resulting in an abrupt increase in the mass attenuation coefficient. (These absorption edges do occur for lower Z materials but at lower energies that are usually not significant.)

1.4.3 Compton Scattering

If the energy of an incoming photon is much higher than the binding energy of an electron with which it interacts, Compton scattering may occur, in which some scattering and partial absorption occurs (figure 1-10). For this event, the interaction electron is regarded as free (i.e. not bound to an atom). The incident photon of energy E_1 (or $h\nu_1$) imparts some of this energy to the electron, which is scattered in a forward direction. The energy of the scattered photon is reduced to E_2 (or $h\nu_2$).

The total energy E_1 is conserved in the scattering process. The division of incident photon energy between the electron and the scattered photon is dependent on E_1 and the photon scattering angle θ . For energy and momentum to be preserved:

$$\lambda_2 - \lambda_1 = \frac{h(1 - \cos\theta)}{mc} \quad [1.21]$$

where $\lambda_2 - \lambda_1$ is the Compton wavelength shift, h is Planck's constant, m is the mass of the electron and c is the velocity of light.

In order to calculate photon energy reduction, it is useful to express equation 1.21 in terms of the energy shift of the photon:

$$\frac{1}{E_2} - \frac{1}{E_1} = \frac{(1 - \cos\theta)}{511} \quad [1.22]$$

providing E_1 and E_2 are in keV. Equation 1.22 proves to be useful for a method of

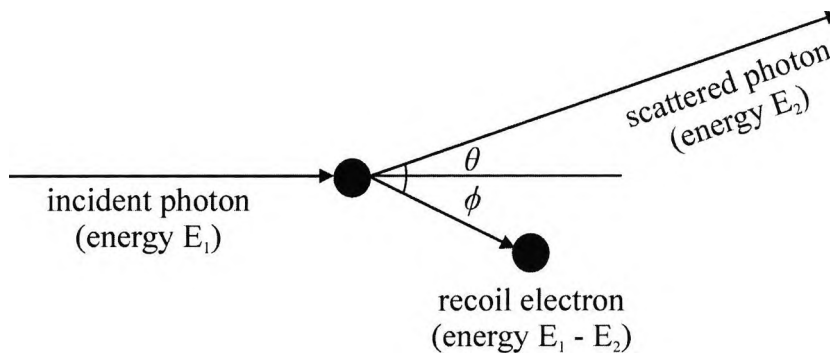


Figure 1-10. Compton scattering. The energy of the incident photon (E_1) is shared between the scattered photon (E_2) and the recoil electron ($E_1 - E_2$). (After Johns and Cunningham, 1983.)

attenuation correction described in chapter six, section 6.2.

Compton scattering is an *inelastic* process since the wavelength of the scattered photon is greater than that of the incident photon. After Compton scattering, the electron can only travel in a forward direction relative to the incident photon. Thus θ may be any value while ϕ must lie between $\pm 90^\circ$. The scattering of photons with low energy (up to about 100 keV) is fairly isotropic whereas photons with high energy (> 1 MeV) are more likely to be scattered in a forward direction (i.e. θ is low).

Attenuation by this interaction may be represented by the mass attenuation coefficient for Compton scattering ($\sigma_{\text{Compton}} / \rho$), which is dependent on the inverse of photon energy, E:

$$\frac{\sigma_{\text{Compton}}}{\rho} \propto \frac{1}{E} \quad [1.23]$$

It is apparent from equation 1.23 that Compton scattering is independent of the atomic number of the material, Z.

Compton scattering contributes to the background signal and is therefore detrimental to the measured EDXRD spectra (examples in section 1.8.2). It is important to shield the sensitive detector from this photon scattering as far as possible, to minimise its effect, and as such, careful consideration must be made during the experimental design.

1.5 BONE MINERAL DENSITY MEASUREMENT

There are numerous techniques that have been used to measure the density of bone. Many diverse methods are based on a variety of different aspects of radiation physics. The key methods are noted briefly.

1.5.1 Radiographic Methods

The oldest procedures to estimate *in-vivo* bone mineral density are those that employ the use of radiographs. A series of radiographs of sites from the appendicular skeleton are taken over a period of time to allow for comparisons that indicate bone density change.

For *radiogrammetry*, the thickness of the cortical bone is measured from each radiograph, usually of the hands. The subsequent radiographs may show a decreasing thickness of cortical bone, indicating a loss in bone mass.

For *radiographic photodensitometry* (also known as *radiographic absorptiometry* or RA), optical densities are measured from the radiographs to determine mineral density, via a calibration phantom. The radiograph is taken, usually of the forearm, including a reference step wedge in the image. The simultaneous exposure of a step wedge alongside the measurement site may be used to minimise the effects of variations in geometry, exposure parameters, film characteristics and processing. The arm and wedge are usually immersed in water in order to eliminate soft tissue variation effects (water has similar density and attenuation properties to soft tissue (Speller *et al.*, 1989)). The surrounding water maintains a constant transmission thickness. An indication of trabecular bone mineral density is provided via an image optical density to equivalent thickness of step wedge material to bone density calibration.

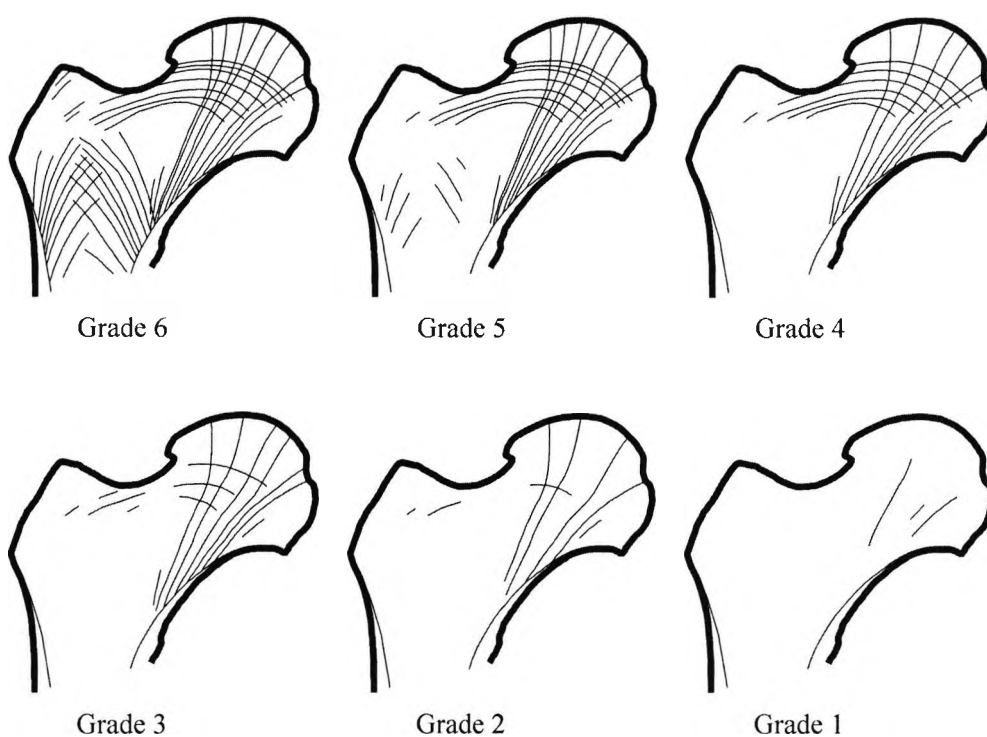


Figure 1-11. Proximal femora diagrams showing the range of trabecular system degradation for Singh classification. The grading is grade 6: all normal groups of trabeculae visible; grade 5: principle groups (M and L) more prominent; grade 4: complete resorption of I_1 and I_2 (secondary) groups; grade 3: lateral group L discontinuous; grade 2: only principle medial group M prominent; grade 1: no group prominent. (After Singh *et al.*, 1970.)

It is suggested that Ward's trabecular systems (section 1.2.2) can be examined to provide an indication of the osteoporotic state of a patient. The state of the systems are categorised using a radiograph of the proximal femur, and graded between six and one using the criteria illustrated by figure 1-11 to determine the *Singh index* (Singh *et al.*, 1970).

There is a great deal of ambiguity and controversy surrounding the generation and use of the Singh index. Koot *et al.* (1996) question the viability of the method after their study using radiographs shown to various observers who were asked to determine the Singh Index. Grading variations between observers were significant and Singh Indices were found to have no correlation with dual energy x-ray absorptiometry (DEXA) bone density measurements.

However it is possible that the observer subjectivity problem may be some way to being overcome by using computed methods to select the grade (Smyth *et al.*, 1997). It has been used, with reservations, in digital image processing analysis methods, developed to investigate the relationship of trabecular pattern to the risk of hip fractures (Geraets *et al.*, 1998).

1.5.2 Photon Absorptiometry Methods

A measure of bone density may be obtained by employing photon absorptiometry methods. In its simplest form, a collimated monoenergetic photon beam from an isotope source of radiation is directed through the site of interest, replacing the x-ray beam with its temporal and spatial non-uniformity and beam hardening problems. A scintillation detector replaces the x-ray film, eliminating the non-uniformity of film sensitivity and processing and minimising scattering effects (Tohill, 1989). The subsequently measured photon attenuation is related to bone density.

Single-photon absorptiometry (SPA), introduced by Cameron and Sorenson (1963), employs the collimated source of radiation from an isotope, which is commonly iodine-125 (emitting near-monoenergetic photons with an energy of 27.4 keV (Speller *et al.*, 1989) – ideal for forearm measurement). The beam is passed through the site to be measured, which must be immersed in water to eliminate the variation effects of the soft tissue surrounding the bone. The transmitted intensity of the beam is measured with the detector and compared with its initial intensity to arrive at a measure of beam attenuation, which is related to bone density.

Bone mineral mass per unit area, m_B (in g/cm^2), is given by:

$$m_B = \frac{\rho_B \ln\left(\frac{I_0}{I_1}\right)}{\mu_{mB}\rho_B - \mu_{mS}\rho_S} \quad [1.24]$$

where I_0 is the transmitted photon beam intensity through soft tissue only, I_1 is the transmitted photon beam intensity through bone and soft tissue, μ_m is the mass attenuation coefficient (see equations 1.11 and 1.14), ρ is density and subscripts B and S represent bone and soft tissue.

The SPA technique requires that only two components are present in the measuring site, being bone and homogeneous soft tissue. This limits the method to simple measurement sites and errors may be introduced by non-uniform soft tissue.

Dual photon absorptiometry (DPA), introduced by Reed (1966), is illustrated by figure 1-12. The technique employs two monoenergetic photon beams of differing energy. The absorption of the lower energy photons is particularly sensitive to the atomic number, absorption by bone mineral dominating when the method is used for such densitometry assessment. The absorption of the higher energy photons is less sensitive to atomic number and as such is determined by the mass of material in the beam path. A comparison of the two transmissions may therefore be utilised to provide a measure of bone mineral present in the irradiated area. (Reed, 1966.) Optimum photon energies depend on bone and soft tissue thicknesses. A trunk thickness of 20 cm, including bone with a mineral density of $1 \text{ g}/\text{cm}^2$, typically requires a lower photon energy of 40 keV and a higher photon energy greater than 100 keV for optimum results (Tohill, 1989). For example, gadolinium-153 provides useful photon emissions at energies of 44 keV and 100 keV (Speller *et al.*, 1989).

DPA uses data from areas adjacent to the bones to determine a soft tissue baseline, which is assumed to be equal to the soft tissue component in the data measured from the bone sites. Different soft tissue thicknesses are allowed for, removing the necessity for water bath immersion to maintain a constant measurement thickness. Sites are no longer limited to the peripheral skeleton where trabecular bone component is low. Also areas of unknown void in the body (such as variable gut gas) are accounted for, allowing sites such as the spine and hip to be measured.

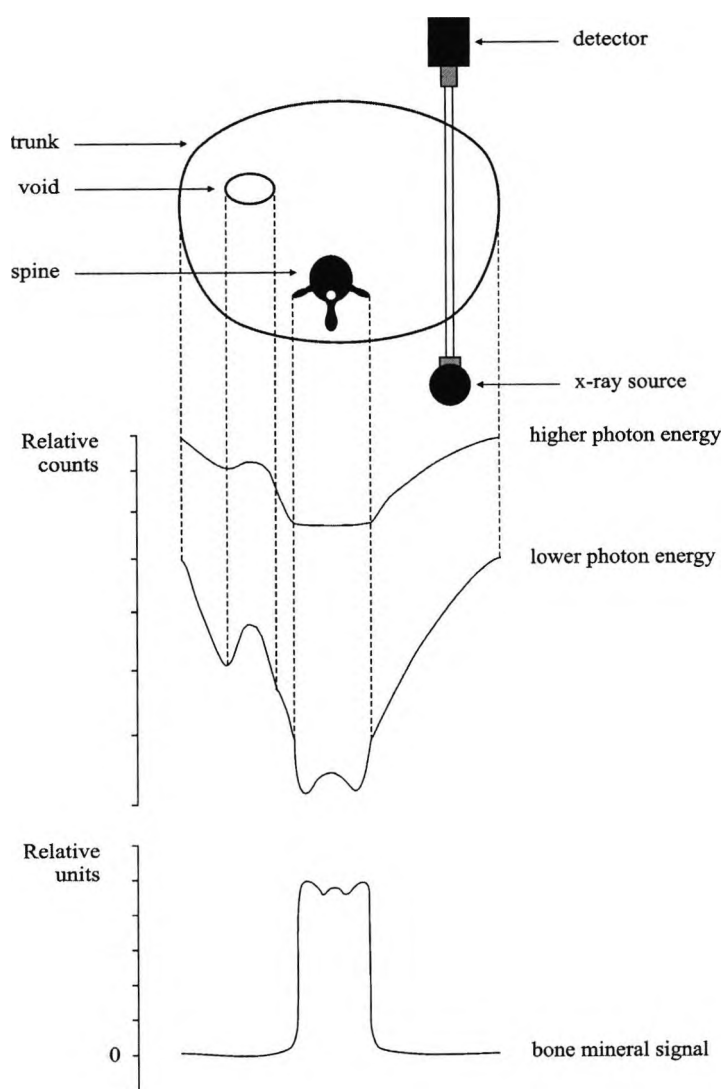


Figure 1-12. An illustration of dual photon absorptiometry. The relationship between two distinct monoenergetic photon beams may be compared to produce a signal for bone mineral in isolation from soft tissue and voids. (After Tothill, 1989.)

Bone mineral mass per unit area, M_B (in g/cm^2), is given by:

$$M_B = \frac{\ln\left(\frac{I_{0L}}{I_{1L}}\right) - \left(\frac{\mu_{mSL}}{\mu_{mSH}}\right) \ln\left(\frac{I_{0H}}{I_{1H}}\right)}{\mu_{mBL} - \mu_{mSL} \left(\frac{\mu_{mBH}}{\mu_{mSH}}\right)} \quad [1.25]$$

where the symbols are the same as for SPA (equation 1.24), with additional subscripts L and H representing the low and high photon energies. Note that this calculation is independent of densities (ρ).

The DPA technique also requires that only two components are present in the measuring site, being bone and soft tissue. However fat forms a third component, which becomes important with some DPA measurement sites (fat has attenuation properties that differ from water and soft tissue). Non-uniform fat distributions do introduce some error. Tothill, Pye and Teper showed this error to range between 3 to 9% in the lumbar spine region (quoted in Tothill, 1989).

Dual energy x-ray absorptiometry (DEXA) is a further development of the DPA technique. The same principles as DPA apply but an x-ray generator replaces the isotope source. The generator is used to generate beams of two different energies, either by energy switching or by dividing the beam into two major components using a K-edge filter. This results in a higher photon flux than DPA, reducing scanning time to between four and five minutes (spine or hip measurement). The photon beam may be more collimated, the scan image is sharper and precision is improved (Hassager and Christiansen, 1995).

DEXA is a convenient, rapid and precise clinical method of obtaining a value for bone density, resulting in a relatively low radiation dose to the patient. However, as a photon transmission method (figure 1-1), it is not able to measure specific bone volumes. For example, the density of trabecular bone cannot be accurately determined in isolation from cortical bone since information from all material in the photon beam path is included.

DEXA is currently established as the main clinical method for the measurement of bone density and as such forms an important part of this study.

1.5.3 Computed Tomography

Data from *quantitative computerised tomography* (QCT) images, reconstructed from x-ray profiles of the site of interest, can be related directly to bone density. It is thought that the ability to isolate the QCT response of trabecular bone may offer an improvement in accuracy. This offers a significant difference from the previous techniques, which measure total bone mass only. Since osteoporosis manifests itself more readily in

trabecular bone, removing the effect of cortical bone may increase the sensitivity of the detection.

X-ray profiles are taken at a number of orientations around the patient. The trabecular bone regions of vertebra are considered by many to provide the most relevant measurement of bone density (Tothill, 1989). The mean CT (Hounsfield) number for the region is calculated from:

$$H = 1000 (\mu_T - \mu_W) / \mu_W \quad [1.26]$$

where μ_T is the linear attenuation coefficient for the tissue under examination and μ_W is the linear attenuation coefficient for water. H is approximately 2000 for cortical bone (Tothill, 1989) (c/w H = 0 for water). This CT data is related to bone mineral density by comparing it to phantoms of known density.

An image may be reconstructed from these profiles using algorithms such as filtered back projection.

Radiation dose to the patient is high, although this can be minimised with the use of selected peripheral sites such as the forearm.

1.5.4 Photon Scattering Methods

The measurement of specific sample sites, such as trabecular regions of bone, may also be achieved by utilising photon scattering techniques. In most radiological examinations, scatter is considered as detrimental to the technique. For example, a radiographic image recorded on film will suffer from a certain level of degradation from x-ray scattering. This imaging method therefore incorporates measures to minimise this scattering to produce an optimum image. However, scattering properties may be utilised for some techniques. Since scattering changes the photon direction, a measurement volume may be defined in a specific sample region by careful collimation.

Compton scattering densitometry methods have been developed that rely on the relationship between the intensity of scattered photons, the density of scattering material and the original energy of the incoming photons. Since Compton scattering is not dependent on the atomic number of the material, the measurement is greatly simplified.

A collimated narrow beam of monoenergetic x-ray photons is incident on the region of interest. A collimated detector (usually a scintillation counter) is arranged at a specific angle, the path intersection with the incident beam defining the measurement volume.

The photons detected will only be those scattered through this angle and therefore the energy shift is known. The detected intensity would be proportional to material density but for attenuation of the primary and scattered photons by the scattering medium and surrounding tissues. This necessitates a method of correction, commonly achieved by adding a second source-detector pair to form a cross shaped photon path geometry. The arrangement mirrors the original pair in such a way that transmission measurements are taken along with scattering measurements, in all source-detector combinations. A variation of this correction technique was employed for this study (chapter six). Making the assumption that attenuation of the transmitted and scattered paths are similar, density is given by:

$$\rho = k\sqrt{S_1S_2/T_1T_2} \quad [1.27]$$

where k is a calibration constant, S and T are the number of photons detected by scattering and transmission respectively, while the subscripts represent photon source 1 and 2.

This method was first introduced by Clarke and Van Dyk (1973).

Coherent scattering forms the basis of the energy dispersive x-ray diffraction method of this project and is described later in this chapter (sections 1.7 and 1.8).

A combined *coherent-Compton scattering* method has been investigated, which is based on ratios of peaks generated from the two scattering mechanisms (described by Speller *et al.*, 1989). The method is engineered such that photons from each scattering mechanism are subject to the same attenuating material path and the energy difference between the coherent and Compton peaks is small. Therefore attenuation effects may be cancelled by using the peak ratio.

1.5.5 Neutron Activation Analysis

Neutron activation analysis can be used to determine the absolute quantity of a particular element within the site of interest by measuring the quantity of γ -rays generated from n, γ reactions. The patient is irradiated with a uniform beam of fast neutrons that induce reactions such as $^{48}\text{Ca}(n, \gamma)^{49}\text{Ca}$, among many others (Speller *et al.*, 1989). Once irradiation has been completed, a whole body counter is used to detect the emitted γ -rays.

Since 99% of calcium in the body is found in the skeleton (Tothill, 1989), this method can be used to obtain a measure of total calcium content (and therefore skeletal mass), but the dose to the patient needed to obtain this is high.

1.5.6 Radiation Free Methods

There are some methods for bone density measurement that are not based on radiation techniques, notably ultrasonic attenuation and magnetic resonance imaging.

Ultrasound waves are attenuated when directed through tissue and so tissue composition may be determined by the degree of attenuation. Bone with a lower mineral density will attenuate the ultrasonic waves to a lesser degree than healthy bone, providing information on bone density status. *Broadband ultrasonic attenuation* (BUA) is based on the reasonably linear relationship between the ultrasonic frequency of a beam and its attenuation when directed through bone. A gradient of ultrasonic frequency for healthy bone provides a reference to which the attenuation of a wide frequency range (broadband) measurement may be compared.

There is no radiation dose to the patient but the method may suffer from inherent inaccuracies. Ultrasonic densitometry devices have been developed for use in the clinical environment.

Some work has been performed to investigate the viability of using *magnetic resonance imaging* (MRI) techniques to assess bone density. It is based on the measurement of marrow within trabecular bone spaces to produce images of the bone structure. From this, a bone volume fraction (ratio of bone to marrow) may be calculated that provides an indication of bone density.

1.6 RADIATION DOSIMETRY

Medical radiation dosimetry is concerned with the measurement of the amount of ionising radiation received by a patient. The energy transferred from this radiation to the cells of a patient produces a risk of damage due to the ionisation of cellular material, which may lead to abnormal cell behaviour.

Radiation received from medical procedures provides the greatest contribution to artificially produced radiation dose. The balance between risk to the patient and potential benefits of a procedure (risk-benefit) must be carefully considered. A radiological examination should therefore only be performed if there is an expectation that benefits to

the patient outweigh any risks. For example, a new diagnostic technique may improve on results from previous methods but the increase in radiation dose to achieve this improvement may be too great to justify its use.

In radiotherapy, targeted cellular damage is desirable for the reduction of tumour cells, but for diagnostic methods, damage risk must be minimised. Thus, for any investigation using radiation, the ALARA (As Low As Reasonably Achievable) principle should be adopted. This concept was introduced by the International Commission on Radiological Protection (ICRP, 1977), which concerns the practical balance between the desirability of low radiation doses and the difficulty and cost of achieving them.

1.6.1 Radiation Dose Quantities and Units

Conventions for the quantification of radiation dose have developed over time as understanding of the effects of various radiation types on different body tissues has improved. Current definitions by the International Commission on Radiological Protection (ICRP, 1991) and the National Council on Radiation Protection and Measurements (NCRP, 1993) are used in this study, being absorbed dose, equivalent dose and effective dose.

Absorbed dose, D , is defined as the energy absorbed, ΔE_D , per unit mass, Δm :

$$D = \frac{\Delta E_D}{\Delta m} \quad [1.28]$$

Units are joules per kilogram (J/kg), which, as absorbed dose, has a special unit name of gray (Gy). This is the basic quantity of radiation dose that may be measured and may be subsequently weighted to produce the equivalent dose and the effective dose.

Equivalent dose, $H_{T,R}$, for a given radiation type, R , is based on an average absorbed dose in the designated tissue, T . It is calculated by weighting the absorbed dose (from this radiation), D_R , with the radiation weighting factor, w_R :

$$H_{T,R} = D_R w_R \quad [1.29]$$

This is summed for multiple radiation types and energies to produce an equivalent dose to the designated tissue:

$$H_T = \sum_R w_R D_{T,R} \quad [1.30]$$

Providing the absorbed dose is given in grays, the special unit for equivalent dose is the sievert (Sv, being $w_R \times \text{Gy}$).

Radiation weighting factors for equivalent dose calculations adopted by the ICRP (1991) and the NCRP (1993) by radiation and energy, are tabulated in appendix D, section D.1.

Effective dose, E , is weighted so the resultant value is proportional to the probability of cancer or genetic effects occurring as a result of the radiation received by the designated tissue. It is calculated by weighting the equivalent dose (for tissue T), H_T , with the tissue weighting factor, w_T :

$$E = \sum_T w_T H_T \quad [1.31]$$

The resulting value, again in sieverts (Sv), provides an estimation of risk from stochastic effects, whether the body was irradiated uniformly or to specific sites.

Tissue weighting factors for effective dose calculations adopted by the NCRP (1993) are tabulated in appendix D, section D.2.

1.6.2 Thermoluminescent Dosimetry

There are a number of methods by which radiation dose received may be measured, including the use of ionisation chambers, Geiger-Müller counters, photographic film, scintillation and semiconductor detectors. For this study, the thermoluminescent dosimetry (TLD) technique was adopted and so is briefly discussed here.

A material that emits visible light when irradiated by x-ray photons is said to exhibit the property of luminescence, which is known as fluorescence if the production of light ceases within 10^{-8} seconds after the radiation source is removed. Fluorescence will only take place as a result of a number of physical stages after a suitable material is initially irradiated. The x-ray photons initially undergo photoelectric interactions in the material and the subsequently ejected electron, and others which it excites, are raised to the conduction band of the irradiated material. A hole is left in the valence band. Fluorescence occurs if the excited electrons fall to lower energy levels that happen (or, with the addition of impurities, are designed) to have a quantum energy that corresponds to photons with a wavelength within the visible range (400-700 nm).

Efficiency may be increased with the addition of impurities (activators) to form

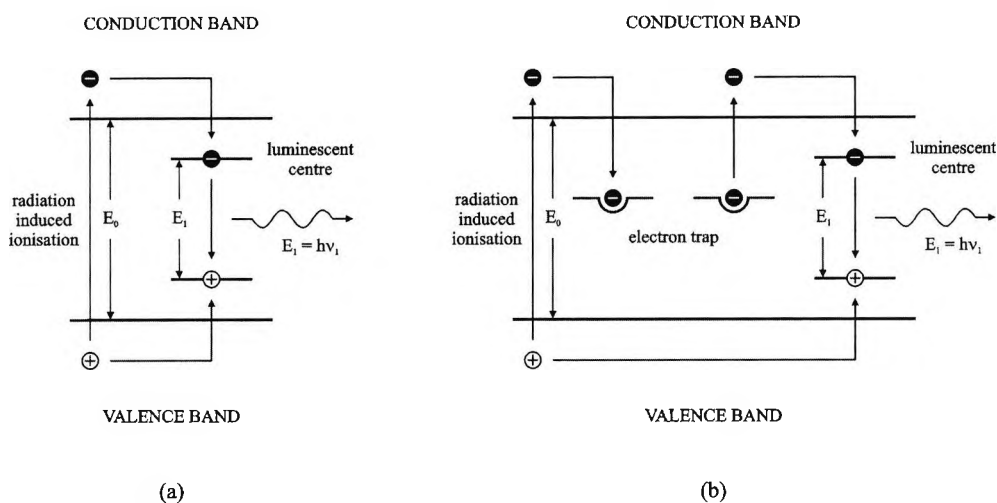


Figure 1-13. An illustration of fluorescence, phosphorescence and thermoluminescence. Fluorescence occurs when electrons (-) promoted to the conduction band (energy E_0) subsequently fall through the energy quantum (E_1) of the luminescence centre (a). A light photon is emitted with a wavelength (ν_1) in the visible range. Phosphorescent light photon emission is delayed since electrons are temporarily caught in electron traps, subsequently released as a result of thermal agitation (b). If the energy difference between the electron trap and conduction band is too great for thermal agitation to release the electron but additional heating provides sufficient energy, the process is known as thermoluminescence (b). (After Attix (1986) and Graham (1996).)

luminescent centres within the material that have the required quantum energy for fluorescence. Conduction band electrons lose small amounts of energy to fall to the higher energy of the luminescent centre and valence band holes gain small amounts to raise them to the lower energy. The final quantum energy change to the electron is then determined by that of the luminescence centre (figure 1-13a).

If the emission of visible light photons is delayed until after the radiation source is removed, this luminescence is known as phosphorescence (sometimes called 'afterglow'). This phenomenon occurs if excited electrons are caught in electron traps (activators) below the conduction band and are subsequently released with additional energy due to thermal agitation (figure 1-13b).

The material is said to be thermoluminescent if trapped electrons that would otherwise not be released by natural thermal agitation (the electron trap energy is too far removed from that of the conduction band) may be promoted to the conduction band by the

application of heat (figure 1-13b). These materials therefore require suitable activators to form both luminescence centres and electron traps. Light intensity is proportional to the quantity of radiation originally incident on the device and so may be used for thermoluminescent dosimetry (TLD).

A useful TLD material, adopted for the dosimetry of this project (chapter nine), is lithium fluoride (LiF) activated with magnesium (Mg) and titanium (Ti). The most common form, TLD-100, have a wide useful dose range, from a few times 10^{-5} Gy up to 10 Gy linearly (with dose) and 10-100 Gy supralinearly (Attix, 1986). They may be formed into small chips that are easily positioned at significant locations and also have an effective atomic number of 8.2, close to that of tissue (being 7.5 (Graham, 1996)). Thus the TLD devices may be positioned with minimal interference to the measurement of the applied radiation.

Once irradiated, the TLD devices are placed in a suitable reader, which heats the TLD phosphor and measures the light emitted. Suitable calibration using TLD devices irradiated by a known amount allow estimation of absorbed radiation dose. This procedure is applied in chapter nine.

1.7 X-RAY DIFFRACTION

Diffraction is defined as the interference effects that occur when waves interfere with each other. Diffraction patterns may be demonstrated by the interference of photons (or the wave function of particles) to produce a series of dark and light bands (or high and low intensities).

X-ray diffraction is an important tool for the investigation of crystalline materials. Interference patterns are formed when the x-rays are scattered from the atoms in a crystal lattice. Since x-rays are electromagnetic waves and the atoms of crystalline materials are arranged in regular patterns, the scattering of x-ray photons by such materials result in a unique interference pattern. X-ray diffraction by three-dimensional crystalline structures is known as Bragg diffraction.

1.7.1 Bragg Diffraction

Regular three-dimensional crystal lattices provide many scattering planes for diffraction, as illustrated by figure 1-14 for a simple cubic lattice. Incident x-rays are diffracted by

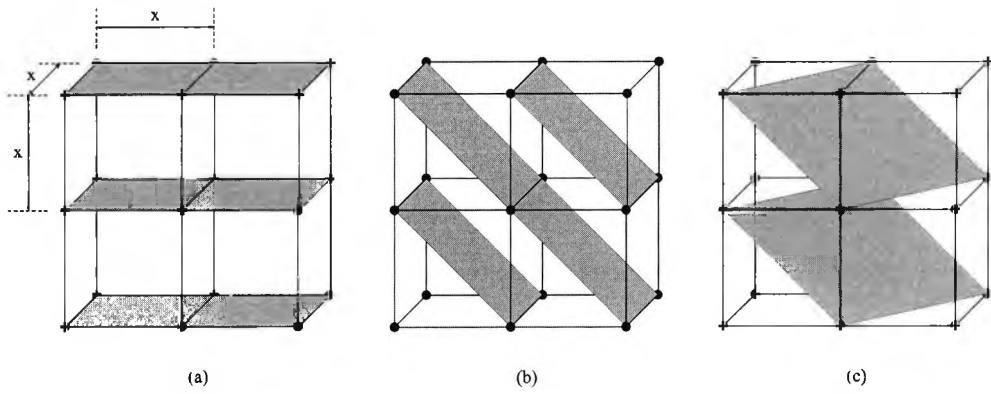


Figure 1-14. A selection of the numerous crystal plane families of a simple cubic lattice, with equal atomic spacings, x . The spacing of the planes in (a) is x , in (b) is $x/\sqrt{2}$ and in (c) is $x/\sqrt{3}$.

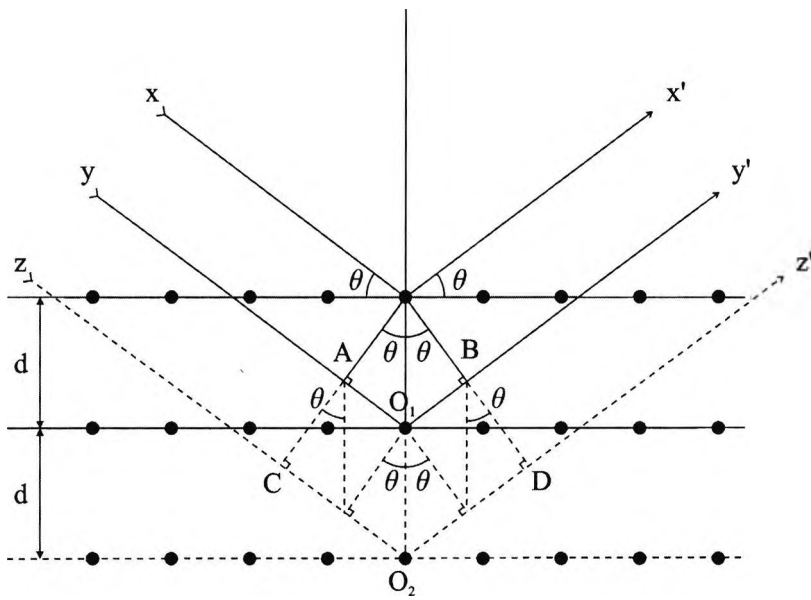


Figure 1-15. A two-dimensional representation of Bragg diffraction (see text for discussion).

the scattering planes, resulting in an interference pattern related to the material. This pattern is formed from combinations of constructive and destructive interference.

Bragg's law describes the conditions under which constructive interference of x-ray photons occur, with respect to one family of scattering planes:

$$n\lambda = 2d \sin \theta \quad [1.32]$$

where λ is the wavelength of the photons, d is the spacing between the scattering planes, θ is the Bragg scattering angle (glancing angle) and n is the order of diffraction.

Constructive interference of the incident photons occurs when the order of diffraction, n , is a positive integer. Figure 1-15 illustrates this for a given Bragg scattering angle θ and scatter plane spacing d (a two-dimensional representation of the three-dimensional condition).

The scatter planes, three of which are illustrated, are formed by the ordered molecular structure of the material. Molecules are represented by the small circles in the diagram. The incidental photon wavefront x, y and z is scattered by the planes to x', y' and z' .

Distance AO_1 equals $d \sin \theta$ and so AO_1B equals $2d \sin \theta$. The Bragg condition is satisfied if the distance AO_1B is a whole integer multiple of the photon wavelength. Distance CO_2D is twice that of AO_1B , and also satisfies the Bragg condition.

1.7.2 X-ray Powder Diffraction

A common application of Bragg's law is x-ray powder diffraction, used extensively to detect and identify crystalline materials. Figure 1-16 illustrates a method using film to record the interference pattern generated by exposing a powdered crystalline sample to a monoenergetic x-ray beam.

The experiment geometry is used to calculate the experimental scattering angle, 2θ , of a scatter ring generated from constructive photon interference. The corresponding scattering plane separation, d , is then calculated from a knowledge of the photon wavelength, λ , by rearranging formula 1.32 (and by setting order of diffraction $n = 1$):

$$d = \frac{\lambda}{2 \sin \theta} \quad [1.33]$$

The calculation for one value of θ provides the separation, d , for one set of parallel

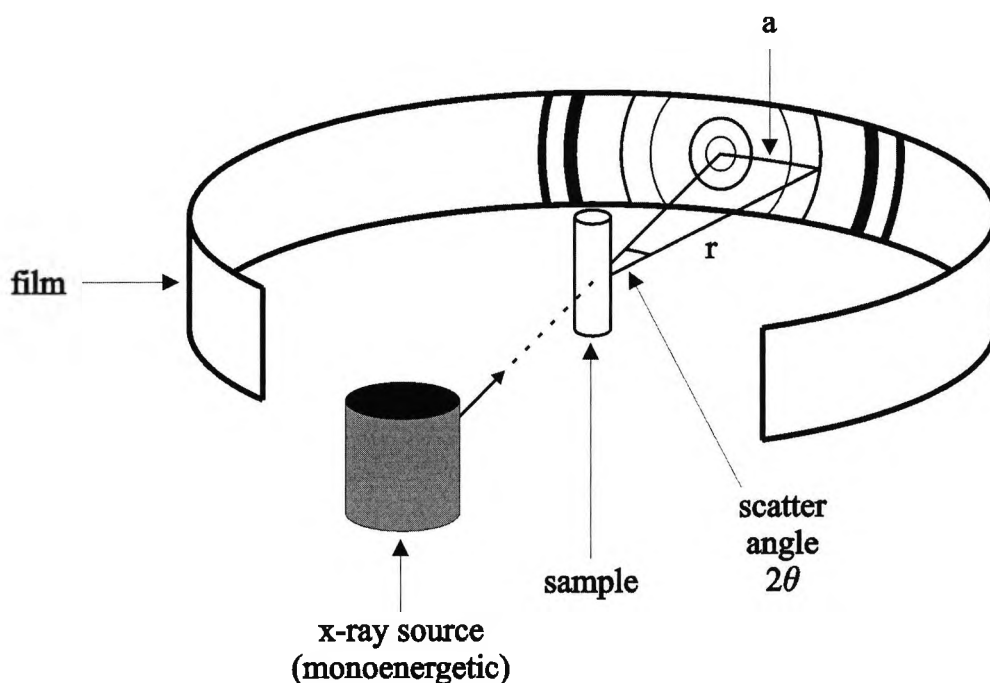


Figure 1-16. Recording a powder diffraction pattern using the Debye-Scherrer method. For a peak scattering intensity (maximum constructive photon interference), angle θ may be calculated from film radius (r) and arc (a) by using $\theta = a / 2r$ (in radians). (After Hukins, 1989.)

planes. There are many such plane sets (with corresponding d separations) for a given crystal structure. They may be described in terms of a unit crystal lattice cell and Miller indices. Once the scattering plane separation d is obtained for each plane set, the crystal unit cell dimensions may be calculated. In practice, the scattering material may be identified directly by comparing with reference scattering patterns.

Detection of the scattered x-rays by using a diffractometer system is an alternative to the use of film strips. The experiment geometry is the same but the film is replaced with a counting detector that measures photon intensity directly, around the same arc.

1.8 ENERGY DISPERSIVE X-RAY DIFFRACTION

The powder diffraction method uses Bragg's law by fixing the x-ray photon wavelength parameter to a known value (for example, 0.154 nm from copper K_{α} emissions) and using the experiment to record the resultant constructive scattering angles. This angular

dispersion is used to calculate the set of scattering plane spacings d . A variation on this theme is to fix the scattering angle to a suitable value and expose the sample to a spectrum of x-ray photon energies. Since the energy is now the variable parameter, the technique is known as energy dispersive x-ray diffraction (EDXRD). Some photon wavelengths from the energy range of the incident spectrum will satisfy Bragg's Law for constructive interference (for a particular value of d).

1.8.1 An EDXRD Diffractometer

An EDXRD experimental system is shown schematically in figure 1-17. As configured for this project, a polyenergetic source of x-ray photons was generated using an x-ray tube. These photons were collimated into a ribbon beam using a primary slit collimator, which was arranged to be incident on the sample under investigation. Within the sample, coherent scattering takes place, predominantly at low experimental scatter angles ($2\theta < 12^\circ$). A secondary collimator was arranged at such an angle so that only photons scattered at this chosen angle reach the detector. This arrangement defined the scattering volume in the same way as the Compton scattering methods described in section 1.5.4. The final beam generated with this geometry was detected with an energy dispersive

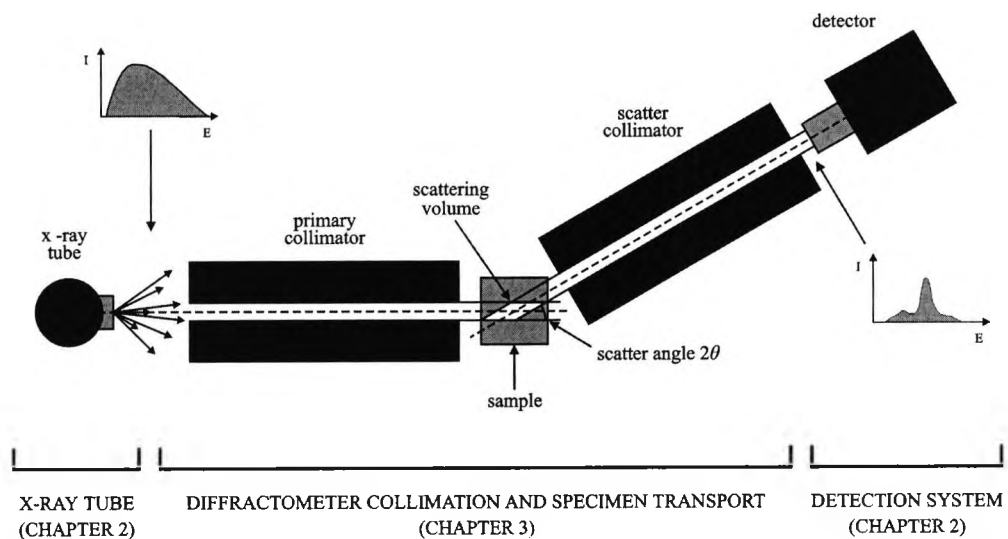


Figure 1-17. An experimental system for EDXRD measurement. Three distinct components are shown - x-ray source, collimation and detection systems. The chapter numbers refer to studies designed to optimise an EDXRD diffractometer system for this bone density project.

high purity germanium detector and then processed using a multichannel analyser (MCA).

The optimum experimental scatter angle, 2θ , will depend on the molecular structure of the sample material under investigation and the wavelength (energy) of the incident photons. This leads to the detection of a spectrum of photon energies that will have a unique 'signature' shape, related to the material under investigation. This signature spectrum will change for a dissimilar material because the d spacings will be different. The peaks and troughs of the signature spectrum will be at energies that correspond with materials present within the scattering volume. The intensity of each peak can be related to the quantity of each material.

Farquharson (1996) has extensively modelled EDXRD diffractometer parameters for bone density measurement. This modelling included the effect on spectra resulting from the following EDXRD considerations:

1. Angular blurring.
2. Coherent scattering (energy dependence).
3. Compton scattering (contribution to the background of the detected spectrum).
4. The incident spectrum (polyenergetic range from 0 keV to a maximum energy, kV_p).
5. Attenuation of the incident and scattered photons by the sample material.
6. Detector resolution.

Angular blurring (and to some extent detector resolution) is responsible for additional spread of each peak. It is derived from the geometry of the diffractometer collimation and affects the ability of the diffractometer to resolve different peaks in the spectrum. Ideal diffractometer collimation will only allow photons of the primary beam to pass in a parallel manner, reaching the sample with no angular deviation. Likewise, the secondary collimation of the scattered photons will only allow photons to reach the detector that are scattered at the angle defined. However this is not the case in a practical system.

The collimators have a defined separation width and channel length. This finite width and length are in essence a compromise. To obtain a good resolution between different elements within a detected spectrum, the photon beam width must be as narrow as possible and the length of the collimation channels must be as long as possible. This narrows the angle of photons presented to the sample, absorbing photons that diverge from this angle. As collimation is reduced, photons diffracted at a wider range of angles

are detected, therefore reducing spectral resolution. A variety of models have been formulated in order to quantify the effect of geometry on angular blurring (for example, Luggar *et al.*, 1996).

By reducing the angles presented by tighter collimation, photon flux is also reduced. Sufficient primary and secondary photon flux must be allowed so a statistically valid photon count may be detected within a given measurement time.

The type of collimation will also effect the resolution and photon flux. The ideal collimation to maximise resolution is a narrow pencil beam (in place of the ribbon beam arrangement used throughout this study). However photon flux is reduced to impractical levels for this study method (Farquharson, 1996), counting times necessary to obtain good quality spectra unreasonably increased.

1.8.2 Measuring Bone Density using EDXRD

EDXRD has been used in a wide range of applications. Examples include the identification of explosive materials (Luggar *et al.*, 1997), archaeological bone densitometry (Farquharson *et al.*, 1997b), the analysis of breast tissue (Royle *et al.*, 1999) and inspection in the oil and food industries (Luggar and Gilboy, 1999). This project is primarily concerned with continuing the work of investigators such as Royle and Speller (1995) and Farquharson and Speller (1998) into measuring bone density using EDXRD techniques.

Since bone mineral, predominantly hydroxyapatite, has a crystalline structure, techniques based upon Bragg's law may be successfully applied for identification and quantification. This, in combination with the ability to define a scattering volume, suggests that the EDXRD method might be ideal for the measurement of bone density.

In the clinical environment, the density of bone is most commonly measured using DEXA. This results in a measure of both cortical and trabecular bone. For the EDXRD bone density experiments discussed in the following chapters, the geometry was arranged to position the scattering volume within a region of trabecular bone, thus reducing the influence of cortical bone.

A selection of illustrative EDXRD scatter spectra are presented here to show the various effects that may be used in the determination of bone density (figure 1-18). Each spectrum is normalised to unity (by dividing each energy channel by the total spectral photon count) to allow direct comparison. The energy axes are converted to momentum

transfer (appendix A.1) except for figure 1-18b, which is presented as energy to allow the spectra to be compared.

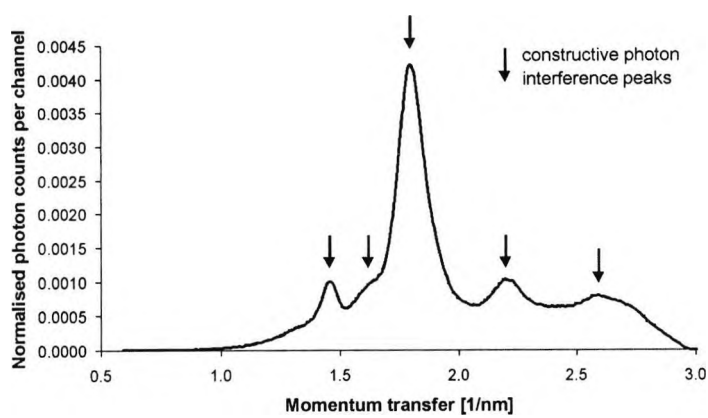
An EDXRD spectrum for a bone phantom (chapter three) is shown in figure 1-18a. The phantom consisted of cleaned, ground trabecular bone. The spectrum was produced using the experiment described in chapter four. Prominent bone peaks are indicated by the arrows, which are in reality amalgams of peaks that cannot be resolved by this experiment.

The spectra shown in figures 1-18a and 1-18c were recorded at an experimental angle of 6° . Figure 1-18b demonstrates the effect of altering the experimental scatter angle. The spectra were generated using angles of 5° , 6° and 7° . Note how the spectrum has been shifted with respect to energy, due to the effect of Bragg's law (equation 1.32). As part of the experiment discussed in chapter four, measurements were made to show the optimum scatter angle required for effective bone density measurement. Farquharson (1996) has shown that the optimum experimental scattering angle lies between 5° and 6° for a incident x-ray photon spectrum with a peak energy of 70 kV_p .

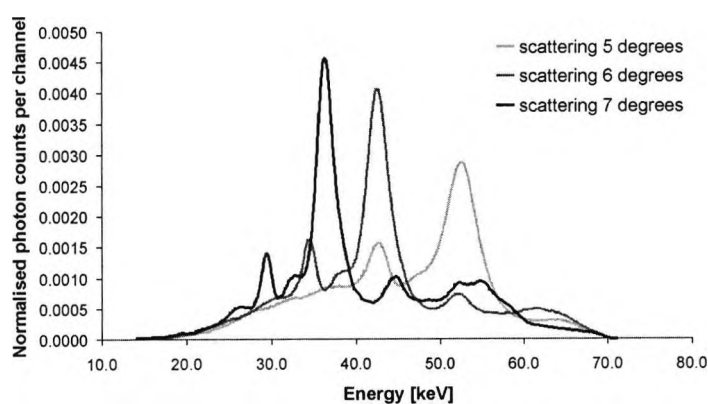
Figure 1-18c includes an EDXRD spectrum for a marrow only phantom. In this example, there is one large peak at momentum transfer 1.1 nm^{-1} , consisting of a number of unresolved peaks. These peaks have a wide momentum transfer range because the fat does not have the regular crystalline structure of bone.

An EDXRD spectrum from a phantom representing a healthy mix of bone and marrow (ratio by volume of 20% bone to 80% marrow – see chapter three) is shown in figure 1-19. The phantom consisted of cleaned, ground bone and fat, which together simulate *in vivo* bone and marrow. The large marrow peak at approximate momentum transfer of 1.1 nm^{-1} can be clearly distinguished from the main hydroxyapatite bone peak at approximately 1.7 nm^{-1} . A smaller hydroxyapatite peak at approximately 1.4 nm^{-1} is also just apparent on this spectrum.

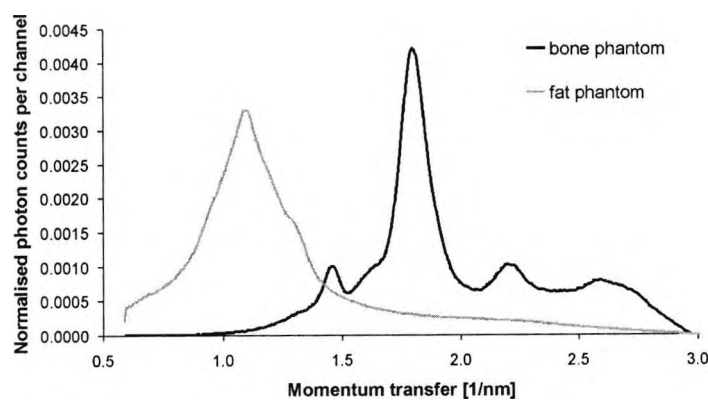
Figure 1-19 also shows the effect of reducing the bone content of the phantom. Two spectra are shown here, one generated from the phantom representing the healthy ratio of bone and marrow and the other (shown in grey) representing a 35% reduction in bone content. The hydroxyapatite peaks have been significantly reduced in intensity in the latter spectrum. It is this change in photon counts that is exploited by the EDXRD method of bone density measurement. The intensities of the peaks for bone material are analysed to provide a measure of bone mineral density within the scatter volume.



(a)



(b)



(c)

Figure 1-18. EDXRD bone spectra. Spectrum (a) was generated using powdered bone (incident spectrum 70 kV_p, experimental scattering angle $2\theta = 6^\circ$). Spectra (b) demonstrate the effect of different 2θ values (here 5° , 6° and 7°), shifting the scattered spectrum energies (despite the incident spectrum remaining unchanged at 70 kV_p). Spectra (c) are the bone spectrum with a marrow spectrum added for comparison (70 kV_p, $2\theta = 6^\circ$). Fat is used as a substitute for bone marrow.

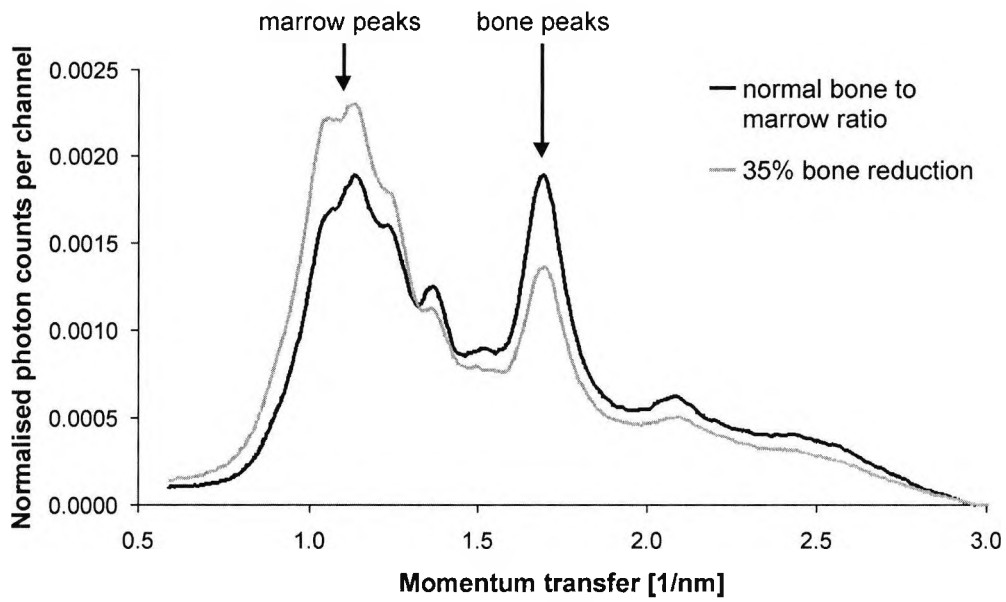


Figure 1-19. EDXRD spectra generated using bone and marrow mixtures. The bone and marrow scattering effects combine into one bone + marrow spectrum (c/w figure 1-18c). Here two such spectra are shown, one representing the bone + marrow proportions of healthy bone and the second with reduced bone content (70 kV_p , $2\theta = 6^\circ$).

Note how the marrow peak is increased in intensity, due to the increased amount of fat in the phantom taking up the space of the missing bone. In chapter eight, this increase is investigated in order to improve the sensitivity of the EDXRD method by analysing the bone and marrow peak ratios.

Part One

PREPARATION

Chapter 2

PHOTON SOURCE AND DETECTION COMPONENTS OF THE EDXRD SYSTEM

Throughout this project, two EDXRD diffractometers were used to generate bone density scattering data. The first had options for continuous adjustment of many of the EDXRD parameters, such as scattering angle and collimation channel width. It was initially designed by Farquharson (1996) and was used in this study for initial experiments to optimise EDXRD parameters (chapter four). These refined parameters were incorporated into the second EDXRD diffractometer for the final study measurements (chapters six, seven and eight). This diffractometer featured fixed optimised EDXRD parameters to improve repeatability.

This and the following two chapters discuss the components of both diffractometers and describe initial investigations into optimal assembly and performance. An EDXRD diffractometer schematic is shown in figure 1-17 (chapter one, section 1.8.1), with its three major components.

This chapter comprises:

- Section 2.1 Characterisation of the x-ray tube used for all the EDXRD experiments of the project. Output stability, mapping and alignment are discussed.
- Section 2.2 Characterisation of the detection system used for all the EDXRD experiments of the project. Calibration, energy resolution and mapping are discussed.

2.1 X-RAY TUBE CHARACTERISATION

There were three preparatory investigations involving the x-ray tube. The first was designed to ensure that photon flux was sufficiently stable over operation time. The second mapped the tube output over the area of its aperture to ascertain the point of maximum photon flux and the third used focal spot imaging as a means to align the photon beam.

Throughout this project the x-ray tube was a Comet MXR-160/0.4-3.0 (tungsten target, 3.0 mm focal spot, 1 mm beryllium inherent filtration, 40° radiation coverage) with a Gulmay CP160/2 generator and Gulmay AGO HS MP1 controller.

2.1.1 Stability of the X-ray Tube Output

It is important that x-ray tube photon flux is stable throughout periods of operation. Ideally, with tube parameters unchanged, exposures of the same duration should result in the same number of incident photons. Measurements of different times should result in photon counts of the same proportion. This is particularly important when comparing spectra that cannot be normalised to negate the effects of tube output instability (chapter seven). In reality there will be some statistical variation in photon flux. Providing the x-ray tube output is sufficiently stable, these variations become less significant for longer measurement times.

Method

The x-ray tube output was collimated to a diameter of 5 mm by fixing an aluminium-strengthened lead aperture. A 15 cc ionisation chamber with Keithley 35050A dosimeter was positioned perpendicularly and centrally to the tube output, 100 mm from the tube output plate (approximately 200 mm from the tube target). With the dosimeter set to measure in mC/kg/s and with a tube current of 15 mA, the tube output was recorded over 200 minutes at 300 second intervals from a cold start. Time zero was taken to start at the maximum output after the initial rise from switch on. This experiment was repeated for kV_p settings of 30 keV, 70 keV and 120 keV.

Results

The recorded tube outputs at the three energies were normalised by dividing by the initial (maximum) measurement to form a relative output. These normalised outputs were plotted over 200 minutes, as shown in figure 2-1.

Conclusions

Stability at all three kV_p settings is good, 30 and 70 keV being within 99% of the initial output and 120 keV being within 98%. Each result set was recorded from a cold tube start, so these results include an element of warming up. Under usual measurement

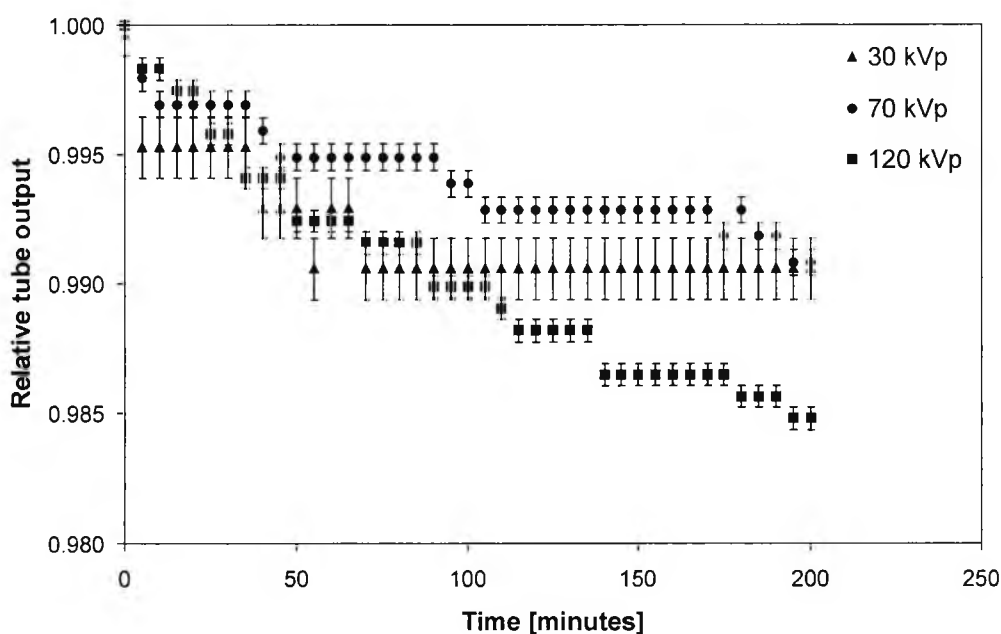


Figure 2-1. X-ray tube output stability of the Comet MXR-160/0.4-3.0 with Gulmay CP160/2 generator. Errors are derived from the accuracy of the Keithley 35050A dosimeter.

conditions throughout this project, a kV_p of 70 keV was used following a tube warm up cycle (approximately 13 minutes) for maximum stability, which is therefore expected to be better than 99%.

2.1.2 Mapping the X-ray Tube Output

X-ray photon flux will vary depending on the positioning of an output aperture with respect to the x-ray tube flux. For best efficiency, an experiment will be set for maximum flux for a given tube exposure setting. If the tube is well set up and maintained, maximum flux is expected to be at the centre of the tube output aperture. This experiment is designed to locate this point of maximum flux.

Method

This experiment used the same apparatus set as for the tube stability experiment (section 2.1.1) with the exception of the fixed aperture. The x-ray tube output was collimated to a

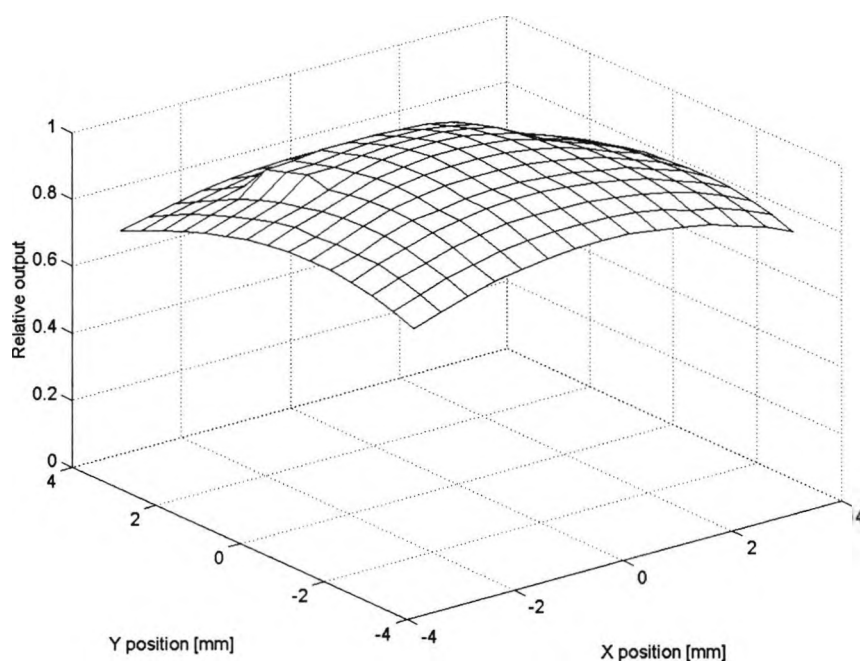


Figure 2-2. X-ray tube output map of the Comet MXR-160/0.4-3.0 with Gulmay CP160/2 generator. X position refers to horizontal aperture co-ordinates and Y position to vertical aperture co-ordinates.

diameter of 1 mm by fixing an aluminium strengthened lead aperture. This aperture was fixed to the tube output plate by mounting on two translators, one fixed vertically and one horizontally. Using this arrangement, the 1 mm aperture was mapped perpendicularly to the x-ray photon beam, starting at the centre and measuring in 0.5 mm steps to ± 3.5 mm horizontally and vertically. The tube output was recorded at each position after allowing the reading to stabilise. The dosimeter was set to measure in $\mu\text{C}/\text{kg}/\text{s}$ and the tube exposure was set to 70 kV_p and 15 mA.

Results

The mapped tube outputs were normalised by dividing by the maximum measurement to form a relative output. The results are shown plotted in figure 2-2. The maximum x-ray tube photon flux was found to be at the centre (0,0 position) of the tube output aperture.

Conclusions

The maximum photon flux was found to be at the centre of the tube output aperture. Therefore for maximum efficiency, an experiment should be aligned to this centre.

2.1.3 X-ray Tube Alignment using Focal Spot Imaging

Another consideration for photon flux optimisation is the alignment of the x-ray beam through the EDXRD diffractometer collimation channels, parallel to the system in both the horizontal and vertical planes. Since the diffractometer experiments are mounted on an optical table, the beam must be the same distance from the table along the length of the diffractometer and passing in the same direction as the primary collimator.

Knowledge of the path of the photon beam was achieved by imaging the focal spot on x-ray film at the far end of the table. One such image is shown in figure 2-3. Note the two lobes of the image, which are formed as a result of electron beam focusing on the tungsten target in the tube.

Method

For this investigation, an x-ray film (in a cassette) was exposed twice, once for film position information and once to image the focal spot. The portion of film for the focal spot image was shielded from the first exposure.

A general purpose Kodak T_MAT L/RA x-ray film with Kodak Min-R 2 cassette (Min-R 2000 screen) was positioned at the far end of the optical table in the path of the x-ray beam. A portion of the film was shielded by being positioned below the level of

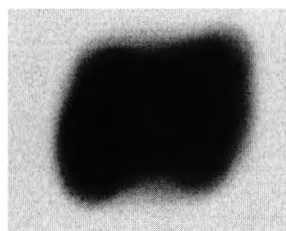


Figure 2-3. Radiographic image of the focal spot of the MXR-160/0.4-3.0 (exposure factors 15 kV_p, 2 mA, 10 seconds, FFD 1507 mm, tube aperture 1 mm, film-screen combination Kodak T_MAT L/RA film, Kodak Min-R 2000 screen).

the table and the target area of the film was shielded with lead to provide an area of the film for the focal spot image. A centre marker was also added. The film was exposed for the first time (exposure factors 20 kV_p, 20 mA, 20 seconds, FFD 1507 mm) with no added aperture reduction, so when developed the unshielded area was blackened. For the second exposure, the lead was removed from the target area and the x-ray tube set for focal spot imaging (1 mm diameter aperture added, exposure factors 15 kV_p, 2 mA, 10 seconds, FFD 1507 mm). Once developed, the centre of the focal spot image was used to determine the path of the beam. A removable laser fixed to the tube was aligned with the beam path.

Results

Figure 2-4 shows the result of the exposure from which the path of the photon beam in the horizontal and vertical planes was determined.

Conclusions

The laser, when fixed to the tube, indicates the x-ray beam path and was used when aligning experiments.

2.2 DETECTOR CHARACTERISATION

A schematic of the EDXRD detection system used throughout this project is shown in figure 2-5. It consists of an EG&G Ortec GLP Series High Purity Germanium (HPGe) Planar Photon Detector (GLP-25300/13-P Pop Top), the output of which drives an multichannel analyser (MCA) system. The MCA system includes an EG&G Ortec 659 bias supply, an EG&G Ortec 672 spectroscopy amplifier and an EG&G Ortec 921E Ethernim high rate multichannel buffer (which incorporates an analogue to digital converter). These three units are mounted in an EG&G Ortec 4001A modular system bin, which also supplies the units with power.

Liquid nitrogen cooling of the detector (typically 70°K) is required to bring thermal noise down to acceptable levels. The detector bias supply is required so charge carriers created within the depletion region of the detector can be quickly and efficiently collected, increasing the signal to noise ratio.

Detected data is stored and processed using a PC linked to the multichannel buffer, which produces a CHN spectrum file using EG&G Maestro-32 software. This file

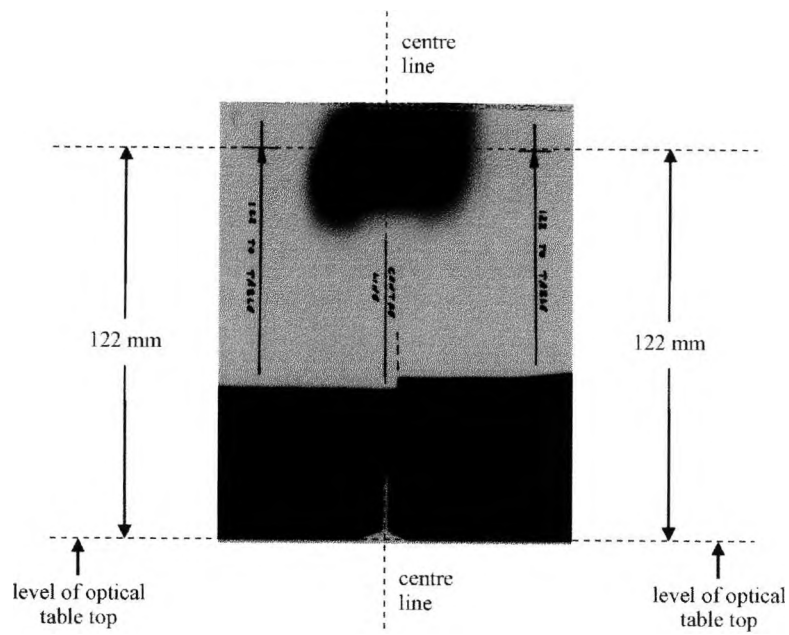


Figure 2-4. Aligning the tube using focal spot imaging. The bottom line of the image is at the level of the optical table top, 122 mm above which is the centre of the focal spot. The developed film was repositioned in the same location as at exposure time and a laser was set to target the centre of the focal spot image.

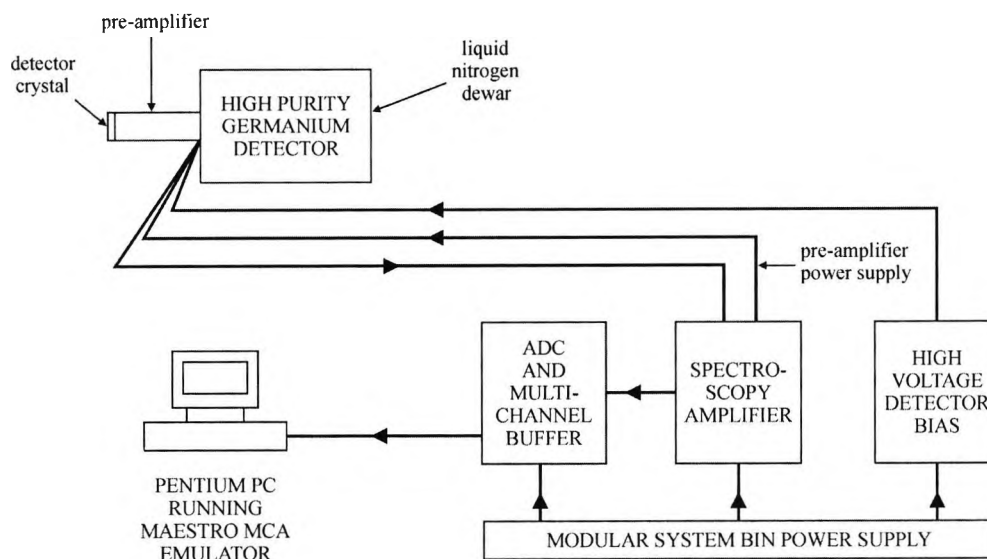


Figure 2-5. Schematic diagram of the multichannel analyser based spectroscopy system.

consists of header information (containing, for example, calibration information) and the measured data pairs of the energy channels and a count of the number of photons detected within the energy range of each channel. Once a measurement was completed, the spectrum files were converted into a Microsoft Excel file of data pairs. This conversion was achieved using a specially written executable file called AttenCHN, details of which can be found in appendix E, section E.1. The program listing provides details of the CHN file format.

2.2.1 Detection System Calibration

The multichannel buffer component of the MCA includes an analogue to digital converter which converts and stores collected data before the CHN file is created. This unit converts the detected spectrum from continuous data to discrete channels. Each channel contains a count of photons detected within a small energy range, centring on the photon energy value assigned to the channel. The MCA must therefore be calibrated so each channel is assigned a photon energy that matches the mean of this small range. Since the total number of channels is fixed, channel width is determined by the calibration (the energy range across all the channels).

Method

The detection system was assembled as shown in figure 2-5. A calibration source was chosen that emitted photons at two discrete energies spanning the range of interest for this project, being between 0 and 80 keV. An Americium-241 source (Amersham FV 227, 370 kBq) was used, being ideally suited for calibrating between 10 to 60 keV (Knoll, 1989). The source was positioned at a distance of 100 mm from the detector to enable a maximum photon flux within acceptable dead time limits (maximum of 10%). Since Americium-241 emits photons at known energies, the detected spectrum was used to assign energy values to matching channels, calibrating the system.

Results

Figure 2-6 shows an Americium-241 spectrum detected using this system. The low energy of 13.9 keV and the high energy of 59.54 keV were used for MCA calibration, optimising detection accuracy over the energy range used throughout the project.

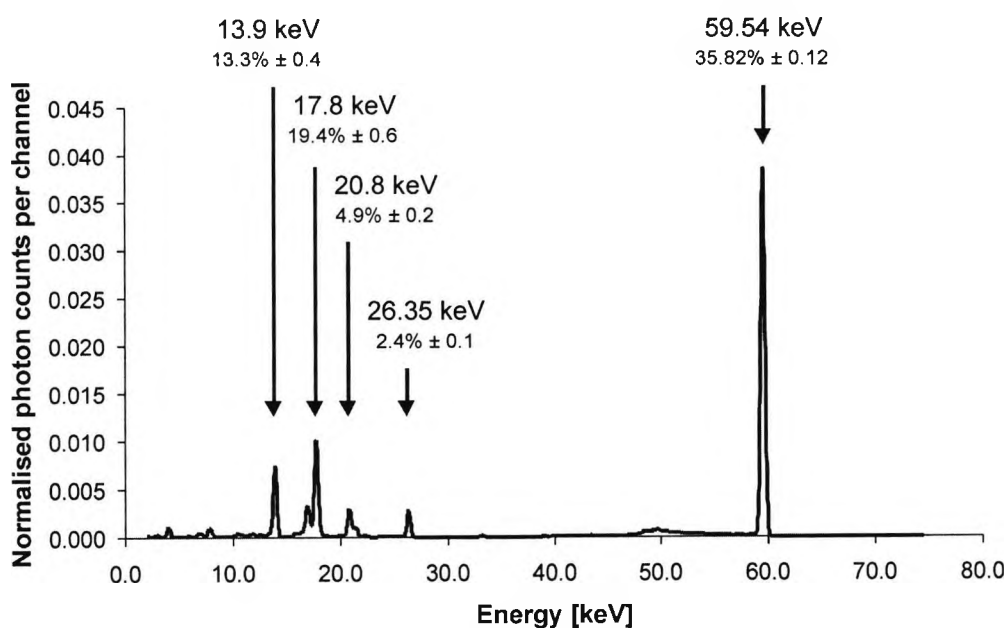


Figure 2-6. Americium-241 spectrum (normalised to unity) measured by the detection system for 10 000 seconds. The energy peaks at 13.9 keV and 59.54 keV were used for MCA energy calibration. The relative yield of each photon energy is also shown. (Data from Campbell and McGhee, quoted in Knoll, 1989.)

Conclusions

The detection system was initially calibrated using this method and checked for drift using the Americium-241 source at the start of each subsequent EDXRD experiment. Calibration was found to be stable throughout and required no further adjustment.

2.2.2 Detection System Energy Resolution

An important aspect of a detection system is its response to a true monoenergetic (delta function) radiation source. An ideal response would be to detect the original delta function at its single energy but system factors combine to degrade this response, spreading the delta function into a Gaussian peak. Detector energy resolution, here described in terms of full width at half maximum (FWHM) for a given energy, describes the ability of a detection system to distinguish between two radiations of similar energy.

Germanium detectors, such as the model used throughout this project, have good energy resolution for gamma/x-ray spectroscopy. Three factors of the germanium detection system contribute to the FWHM (W_T) of the peak:

1. Statistical variance in the number of charge carriers created. FWHM contribution, W_D , is given by:

$$W_D^2 = (2.35)^2 F \epsilon E \quad [2.1]$$

where F is the Fano factor, ϵ is the energy required to create an electron-hole pair, and E is the energy of the photon. The Fano factor (of a detector) corrects for the departure of observed charge carrier statistical variation from that expected from Poisson statistics.

2. Variations in charge collection efficiency due to incomplete charge collection. FWHM contribution, W_X , may be estimated experimentally.
3. Electronic noise from all detection system components following the detector. FWHM contribution, W_E , may be measured by replacing the detector with a precision pulse generator.

The total FWHM contribution, W_T , is given by:

$$W_T^2 = W_D^2 + W_X^2 + W_E^2 \quad [2.2]$$

Energy [keV]	FWHM [keV]
13.9	0.374
17.8	0.399
20.8	0.412
26.35	0.375
59.54	0.446

Table 2-1. FWHM measurements for each energy peak of Americium-241.

Method

The Americium-241 spectrum generated by the method described in section 2.2.1 was used for this energy resolution assessment. Each of the energy peaks was isolated and Gaussian peaks fitted, using SPSS PeakFit 4 (SPSS Inc.) software. The results generated by this fitting method include FWHM data.

Results

The FWHM values for each Americium-241 peak are given in table 2-1.

Conclusions

In general, detector resolution varies as a function of energy. However for this system the FWHM measurements over the energy range of interest do not change significantly.

2.2.3 Mapping Detector Effective Size

It is essential that the active area of the detector has an even response throughout, with no dead regions, so any small positioning errors between experiments have a minimal effect on the measurements. This section describes an experiment to verify this and to confirm the size of the active area as stated in the detector literature (25 mm diameter, 13 mm depth).

Method

The Americium-241 point source was collimated and positioned as shown in figure 2-7.

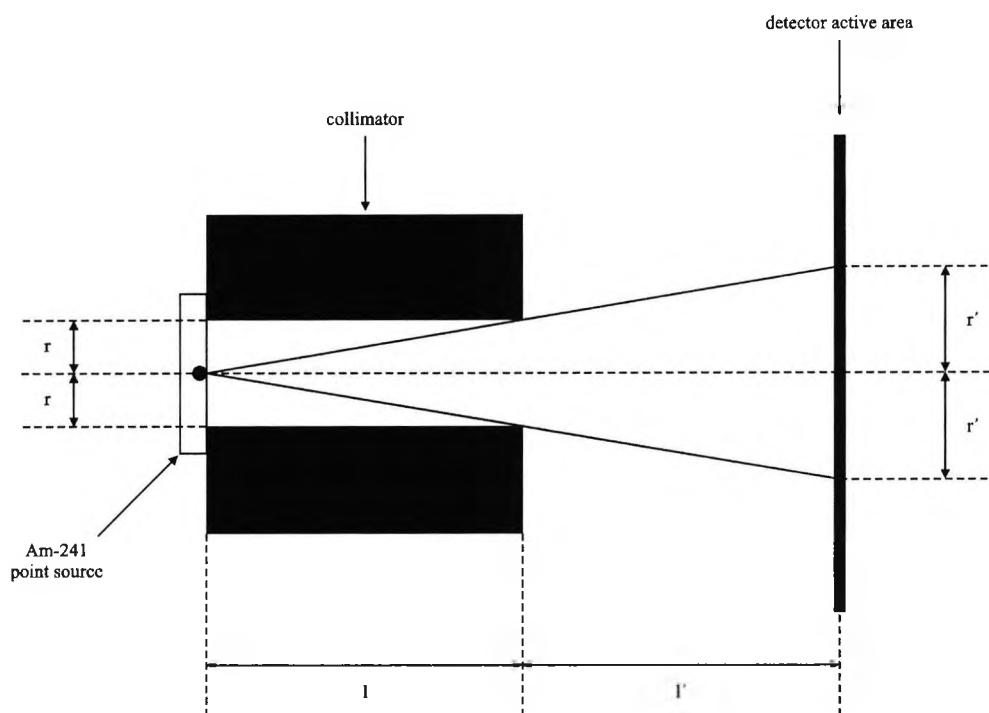


Figure 2-7. The experimental geometry used to map the active area of the detector.

The collimation diameter was 1 mm ($r = 0.5$ mm) and the channel length, l , was 29 mm. The collimator was positioned 29 mm from the detector surface ($l' = 29$ mm) so the radius of the incident radiation spot, r' , was 1 mm (diameter 2 mm).

This whole system was mounted on translators that allowed the radiation spot to be mapped across the whole of the active area of the detector. Starting at the centre of the detector surface, Americium-241 spectra were recorded (each for 500 seconds) in 2 mm steps, ± 14 mm horizontally and vertically from the centre. An area (of radiation spot centres) of 784 mm^2 was mapped.

Results

Figure 2-8 shows a plot of the mapped surface of the detector. The response drops away sharply when the radiation spot centre is greater than a 10 mm radius from the active area centre. Since the radiation spot has a diameter of 2 mm, this mapped area has an effective diameter of 22 mm. It was expected that the response would drop away at

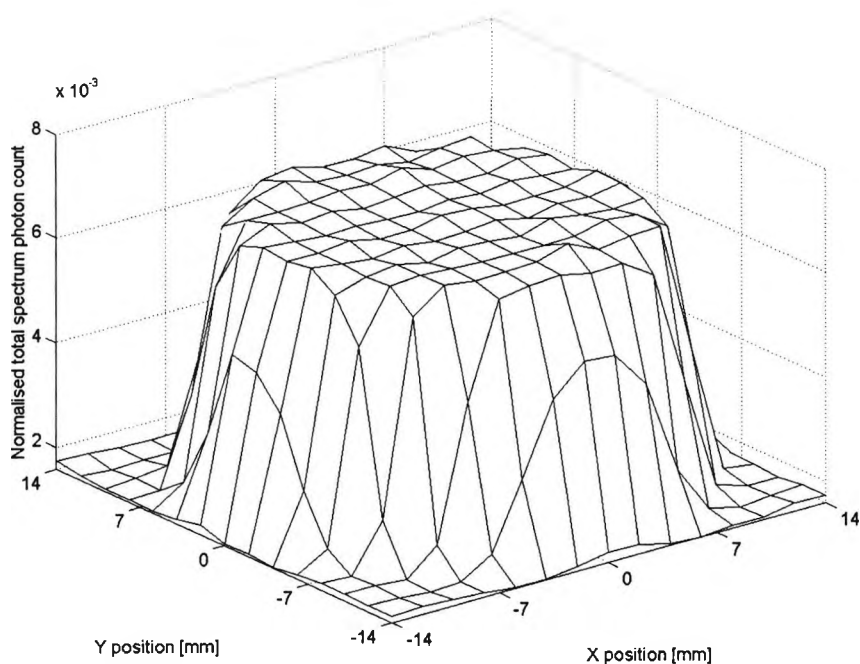


Figure 2-8. Map of the detector active area, generated using an Americium-241 point source. X position refers to horizontal mapping co-ordinates and Y position to vertical mapping co-ordinates.

positions of 12 mm radius (or greater) as this maps an area of 26 mm diameter, greater than the 25 mm area specified by the manufacturer.

Within the 22 mm diameter area, two standard deviations (approximately 95%) of the spectrum counts at each position are within 2% of the mean photon counts of all positions.

Conclusions

The active area of the detector as mapped by this experiment confirms that of the supplied detector data (diameter 25 mm). Maximum uniformity of detection may therefore be achieved providing experimental geometry is constrained within this area. This was easily managed for the EDXRD systems since the maximum slit area of the diffractometers used for this project was 10 mm (height) % 1 mm (width). To maximise consistency between experiments, this slit area was always aligned to the centre of the detector active area.

Chapter 3

EDXRD EXPERIMENTAL GEOMETRY AND BONE PHANTOM CONSTRUCTION

Bone and marrow mix phantoms with varying degrees of bone content were prepared for two main roles in this project. The first was for use in a pilot study to ensure the chosen parameters of the final EDXRD system provided the optimum data for bone density measurement (chapter four). The second use of the phantoms was to provide calibration data for the final EDXRD system, for absolute bone density measurement in the two component (excised bone specimens and marrow) experiments, described in chapter eight.

The dimensions of the bone + marrow phantoms were decided with two considerations in mind. The first was to optimise the sample size to provide sufficient bone material for EDXRD data gathering. This necessitated calculations to ascertain optimum experimental geometry for the EDXRD system (and therefore the scattering volume defined). The second consideration was to determine the maximum viable size of trabecular bone specimens with respect to the removal of bone marrow. Once bone specimen dimensions were determined, the phantoms were prepared with matching dimensions and pilot EDXRD measurements conducted to confirm efficient geometry.

The maximum size of the bone specimens, with respect to cleaning, was determined by a number of timed defatting experiments using trabecular bone cubes of different sizes. $15 \times 15 \times 15 \text{ mm}^3$ was found to be practicable. The cleaning method is described in chapter four.

This chapter comprises:

- Section 3.1 A consideration of EDXRD diffractometer geometry with respect to scattering volume and sample dimensions ($15 \times 15 \times 15 \text{ mm}^3$).
- Section 3.2 A description of the manufacture of the bone + marrow phantoms. Phantom surrounds and the bone + marrow mix are examined.

3.1 EDXRD DIFFRACTOMETER GEOMETRY

A schematic of a general EDXRD diffractometer is shown in figure 1-17 (chapter one, section 1.8.1). The geometry of such a system for bone density measurement has been previously modelled, discussed in chapter one, by the development of software that accounted for the influence of key physical factors. This model and experimental investigation (Farquharson, 1996) narrowed the optimal EDXRD geometry (for ribbon beam collimation) to within the ranges shown in table 3-1. This data provided the initial geometric parameters upon which the pilot experiments in this study were based (also table 3-1).

3.1.1 Diffractometer Scattering Volume

Trabecular bone cubes of $15 \times 15 \times 15 \text{ mm}^3$ were found to be practicable and so the phantoms were also made to be $15 \times 15 \times 15 \text{ mm}^3$. These dimensions were also based on calculations made to ensure that the diffractometer scattering volume for each geometric variation fitted within the sample.

Figure 3-1a shows the rhomboid shape of the plan view of the scattering volume. This is defined by the experimental scattering angle, 2θ , and the primary and secondary collimation channel width, d . The scattering volume height of 10 mm (into the page) produces a ribbon beam, the height of which fits within the sample dimension.

	Ribbon Beam Collimation Width [mm]	Ribbon Beam Collimation Height [mm]	Ribbon Beam Collimation Channel Length [mm]	Experimental Scattering Angle, 2θ [°]
Minimum ^(a)	0.5	20	200	5
Maximum ^(a)	1.0	20	300	6
Pilot study parameters ^(b)	0.50, 0.75, 1.00	10	300	4, 5, 6, 7

Table 3-1. Optimum EDXRD ribbon beam diffractometer geometry ranges for bone densitometry, (a) as ascertained by Farquharson (1996), and (b) as considered for this study. 10 mm collimation height was used for this study in order to keep the scattering volume within the volume of the $15 \times 15 \times 15 \text{ mm}^3$ cubes.

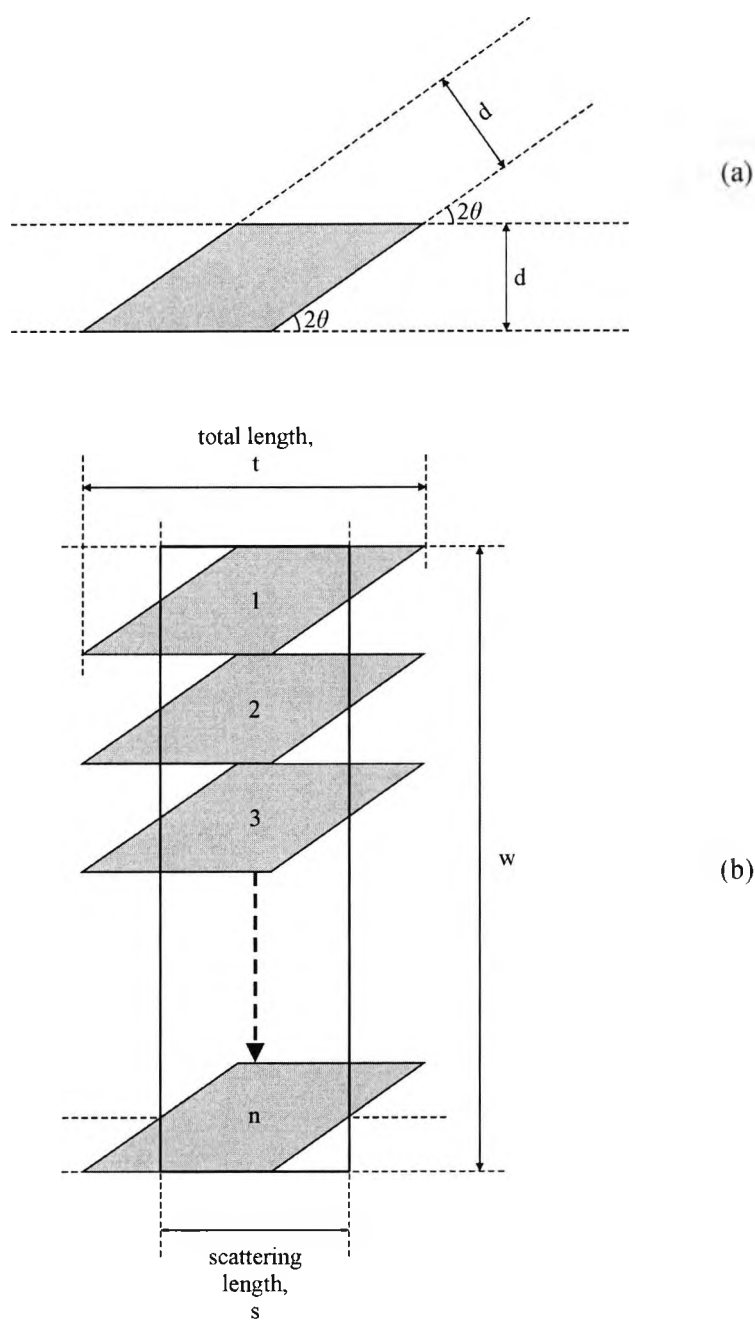


Figure 3-1. Plan views of the experimental scattering volume. The first diagram (a) shows how the collimation channels, with experimental angle 2θ and spacing d , form a rhomboid shape. The second diagram (b) shows how an approximate rectangle is formed over the total area scanned with width w and length s . In this case, the collimator spacing, d , is equal to the distance translated for each position. If d were less than the distance translated, there would be spaces between the scatter volumes. If d were more than the distance translated, the scatter volumes would overlap.

Collimation Width, d [mm]	Experimental Scatter Angle, 2θ [°]	Scatter Length, s [mm]	Total Length, t [mm]
0.50	4	7.17	14.32
	5	5.74	11.45
	6	4.78	9.54
	7	4.10	8.17
0.75	4	10.75	21.48
	5	8.61	17.18
	6	7.18	14.31
	7	6.15	12.26
1.00	4	14.34	28.64
	5	11.47	22.90
	6	9.57	19.08
	7	8.21	16.35

Table 3-2. Scattering volume lengths for various experimental geometries.

For these experiments, the scattering volume is translated across the sample (using a stepper motor) through a number of positions, n , so the majority of the sample consistency contributes to the final bone density result (figure 3-1b). For each collimator spacing, d , the sample is translated through $n = 10$ steps of 1 mm. Thus the width of the total area, w , is 10 mm for all measurements.

Providing the total length falls within the sample dimensions, the overall scattering area approximates to a rectangle of scattering length s and width w . The small scatter area triangles not included in the rectangle are the same as those within the rectangle where scattering does not occur. The triangular areas are close enough within the sample for the significance of this assumption to be small.

Scattering length, s , and total length, t , may be calculated from knowledge of collimation width, d , and experimental scattering angle, 2θ (formulae derivations in appendix A, section A.2):

$$s = \frac{d}{\sin(2\theta)} \quad [3.1]$$

$$t = \frac{d}{\sin(2\theta)}(1 + \cos(2\theta)) \quad [3.2]$$

Table 3-2 shows scattering lengths and total lengths for the experimental geometries of interest. All the scattering lengths fit within the $15 \times 15 \times 15 \text{ mm}^3$ samples but some total lengths are greater than 15 mm. Ideally the total length would fit within the sample length (15 mm in this case), so the whole scattering volume fits within the sample.

3.2 BONE PHANTOM CONSTRUCTION

With consideration to both cleaning and EDXRD experimental geometry, bone cube sample dimensions of $15 \times 15 \times 15 \text{ mm}^3$ were considered to be optimum for this study (some geometries having a little scattering volume overflow). The bone phantoms for pilot studies and calibration were therefore manufactured with the same dimensions.

Method

The phantoms were made with cleaned, ground bone mixed with marrow substitute, which provided a supporting medium for the bone powder. Each phantom was made with a different bone/marrow ratio.

Figure 3-2 shows the supporting structure used for the phantoms. They consisted of four

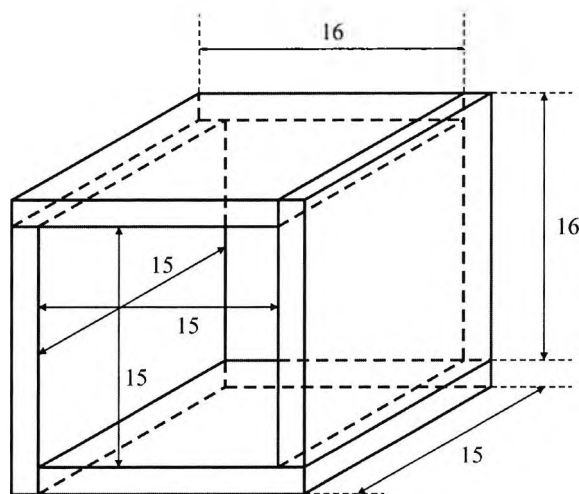


Figure 3-2. Perspex supporting structure for the phantoms.

sides made from 1 mm Perspex sheet with the front and back sides left open. To form the Perspex cube, four 15 mm × 16 mm rectangles of the Perspex were cut. They were assembled as shown, around a 15 mm × 15 mm form to ensure the internal dimensions of the phantom structure were accurate. Dichloromethane was used to soften the connecting surfaces to allow them to join.

The bone powder was prepared from pieces of trabecular bone taken from femoral heads, excised during hip replacement operations. The pieces were thoroughly cleaned (using the method described in chapter four) and then ground to powder using an IKA Labortechnik A10 grinder. The marrow substitute used was animal fat (lard).

The initial mix of bone and fat simulated an average bone/marrow ratio found in a healthy person. This is approximately 20% bone to 80% marrow (by volume) (Woodard and White, 1982) or 33% bone to 67% marrow (by mass) (ICRU, 1989) in healthy trabecular bone. The healthy bone and marrow content was calculated by using an average 'all-tissue density' (bone and marrow) of adult spongiosa (1.180 g/cm³ from ICRU, 1989), using the mass ratio:

$$\text{apparent density of trabecular bone} \approx \text{density of spongiosa} \times \frac{33}{100} \quad [3.3]$$

$$\text{apparent density of marrow} \approx \text{density of spongiosa} \times \frac{67}{100} \quad [3.4]$$

This yields an apparent density of trabecular bone of 0.389 g/cm³, and an apparent density of marrow of 0.791 g/cm³. These values were confirmed by taking the material density of trabecular bone (1.92 g/cm³) and bone marrow (1.004 g/cm³, the mean of red (1.03 g/cm³) and yellow (0.98 g/cm³) marrow) (ICRU, 1989) and using the volume ratio:

$$\text{apparent density of trabecular bone} \approx \text{material density of bone} \times \frac{20}{100} \quad [3.5]$$

$$\text{apparent density of marrow} \approx \text{material density of marrow} \times \frac{80}{100} \quad [3.6]$$

This results in an apparent density of trabecular bone of 0.384 g/cm³ and an apparent density of marrow of 0.804 g/cm³. Adult cortical bone density was used as an approximation for trabecular bone material density (chapter one, section 1.3 for definitions).

Bone Mass Loss from Healthy Norm [%]	Bone Mass [%]	Marrow Mass [%]	Apparent Density of Bone [g/cm^3]	Apparent Density of Marrow [g/cm^3]
0.0	33.00	67.00	0.389	0.791
0.5	32.84	67.17	0.387	0.793
1.0	32.67	67.33	0.386	0.794
2.0	32.34	67.66	0.382	0.798
5.0	31.35	68.65	0.370	0.810
10.0	29.70	70.30	0.350	0.830
15.0	28.05	71.95	0.331	0.849
20.0	26.40	73.60	0.312	0.868
25.0	24.75	75.25	0.292	0.888
30.0	23.10	76.90	0.273	0.907
35.0	21.45	78.55	0.253	0.927

Table 3-3. Quantity details of the phantoms produced.

The initial phantom mix was made by melting and weighing a precise mass of fat. The necessary mass of bone powder was added and mixed in to the fat. The mix was stirred until the fat was sufficiently solidified to support the bone powder.

Cling film was used to seal this phantom mix into the $15 \times 15 \times 15 \text{ mm}^3$ space within a Perspex cube. One end was sealed first, the phantom mix poured in and then the final end was sealed and the phantom labelled. With no Perspex in the path of the photon beam, attenuation contribution is minimised.

Subsequent phantoms represented progressive stages of bone loss, with a decreasing bone/marrow ratio. The mix was softened again and a precise amount of additional fat added to reduce the bone volume, in order to simulate 0.5% bone mass loss. Some of this mix was poured off to fabricate the second phantom. In this manner, the range of phantoms shown in table 3-3 was produced. The phantoms were made in 5% reduction steps, with additional bone loss concentrations of 0.5%, 1% and 2% made at the start of the range. These small difference bone phantoms were made in order to obtain an initial idea of the minimum limits of bone density detection modalities.

Each phantom was stored frozen for as much of its life as possible, in order to minimise any settling of the contents.

Conclusions

These bone + marrow phantoms were used for initial EDXRD and DEXA minimum limit studies (chapter four) and as a reference for final study experiments (chapter eight). They were used with the proviso that there may be a small degree of bone/marrow ratio inaccuracy, predominantly due to ingredient weighing error and the homogeneity of the phantom mix.

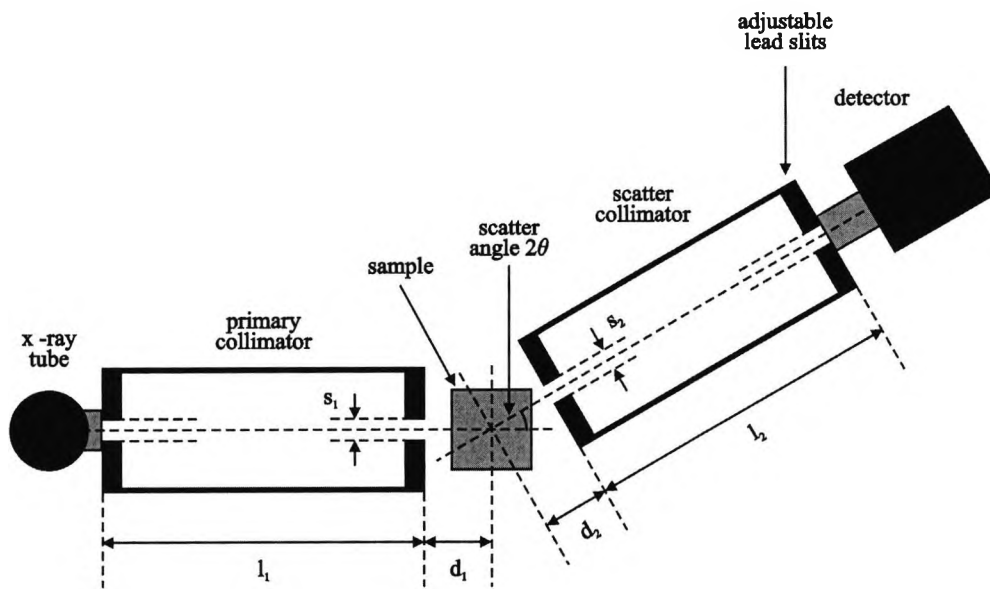


Figure 4-1. Parameters of the experimental EDXRD diffractometer (variable version). The collimators consisted of two sets of adjustable lead slits mounted on dural tubes. Variable parameters included the experimental scattering angle, 2θ , the collimation channel widths, s_1 and s_2 , and the distance of each collimator to the centre of the sample, d_1 and d_2 .

polyenergetic source of x-ray photons was generated using the x-ray tube characterised in chapter two. Primary lead slit collimators, mounted using a dural tube, were used to closely collimate the photons into a beam, which was aligned to be incident on the sample. Secondary lead slit collimators, mounted and aligned in the same way, were arranged at the experimental scatter angle 2θ using a rotator adjustment, so only photons scattered at the chosen angle were detected. 10 mm lead apertures were positioned on the primary and secondary collimators to form a 10 mm slit height. Collimator alignment along the incident photon beam path was set correctly with the aid of a diode laser, before setting the scattering angle. The detector was then positioned closely to the output end of the secondary collimator. A dural shield was used to reduce the level of unwanted photon scatter and electrical interference at the detector, optimising the detected photon signal.

In this way, the scattering volume was positioned within the sample, in this case one of the phantoms described in chapter three. The scattered photons resulting from this

geometry were detected using the high purity germanium detector (characterised in chapter two) and their energy distribution recorded using a multichannel analyser.

For these experiments, spectra were collected using the range of phantoms shown in table 3-3 (not the 35% density reduction phantom), with the following experimental geometry ranges:

1. Experimental scatter angle 2θ was set to 5° , 6° and 7° .
2. Primary and secondary collimation channel lengths l_1 and l_2 were fixed at 300 mm and the sample centre to channel distances d_1 and d_2 were 14.0 mm.
3. Primary and secondary collimation channel slit widths s_1 and s_2 were set to 0.50 mm, 0.75mm and 1.00 mm (using feeler gauges).
4. Primary and secondary collimation channel heights h_1 and h_2 (not shown in figure 4-1) were fixed at 10 mm (initial measurements using a 20 mm collimation height resulted in poorer spectral resolution).
5. The x-ray source settings were fixed at 70 kV_p, 8 mA.
6. The spectra were recorded with a collection time of 1000 seconds each.

The phantom was translated through the scatter volume in 1 mm steps, the width of the total area traversed being 10 mm (100 seconds collection time per position). Sets of EDXRD spectra were collected with the x-ray beam applied directly to the phantoms (unattenuated) and then repeated with attenuation in the primary beam to simulate cortical bone (1.5 mm of aluminium) and soft tissue (5 mm of Perspex). Unattenuated in this instance does not mean that no attenuation occurs. A degree of self attenuation takes place in each of the phantoms. The use of the terms 'attenuated' or 'unattenuated' for the purposes of this experiment refer to the inclusion or otherwise of the additional attenuating material.

Each experiment was repeated five times to enable errors in terms of repeatability to be calculated.

Results

Each EDXRD spectrum was analysed by first normalising the total spectrum counts to unity and then by selecting a momentum transfer region of interest that corresponded with the predominant scattered bone peak (figure 4-2). The spectra were normalised by

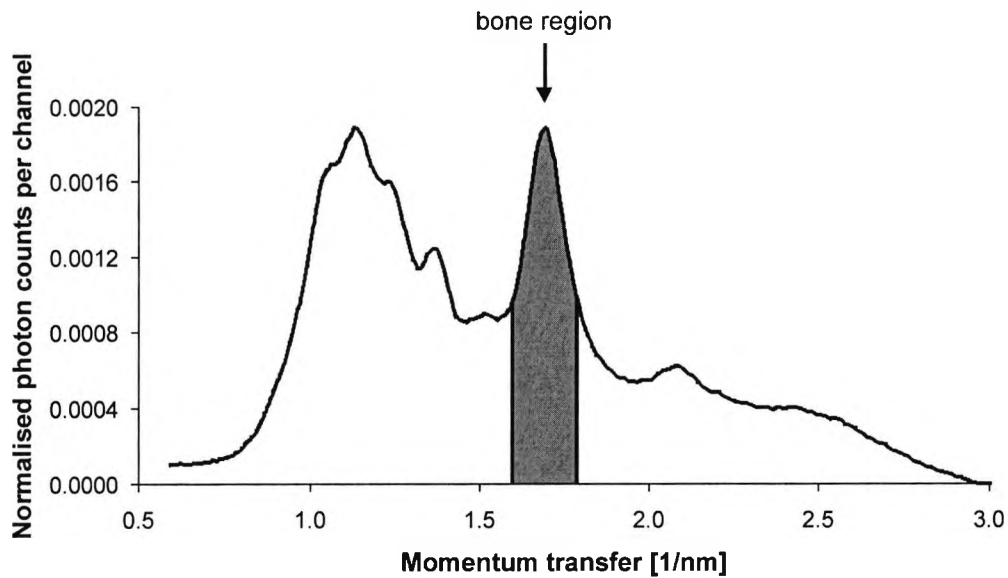


Figure 4-2. Illustration of a bone + marrow spectrum, normalised to unity, showing the region of interest chosen to match relative photon counts to the apparent bone density of the phantoms. The region is from the momentum transfer range between 1.5953 nm^{-1} to 1.7874 nm^{-1} , inclusive.

dividing the photon count of each channel by the total photon count of the spectrum. This normalisation allows the spectra to be compared directly, compensating for any fluctuation in photon flux over measurement time (although chapter two, section 2.1.1 showed this to be minimal). Region of interest was chosen using full width at half maximum (FWHM) of the main bone peak (normal bone/marrow ratio spectra), centring about the peak maximum. The region extended far enough to include as much of the peak as possible without impinging onto other peaks. It should be noted that there is a contribution to the photon counts in this region from scattering by the marrow component. By using momentum transfer, comparison between spectra recorded using different scattering angles was possible.

Total peak photon counts from the normalised spectra were plotted against phantom bone density reduction from the norm. Each point on a plot therefore represents the relationship between phantom bone density and measured bone peak from the detected spectra regions of interest. The results were regression fitted with linear trend lines.

Precision (or minimum detectable limits) of the system across the sample range were

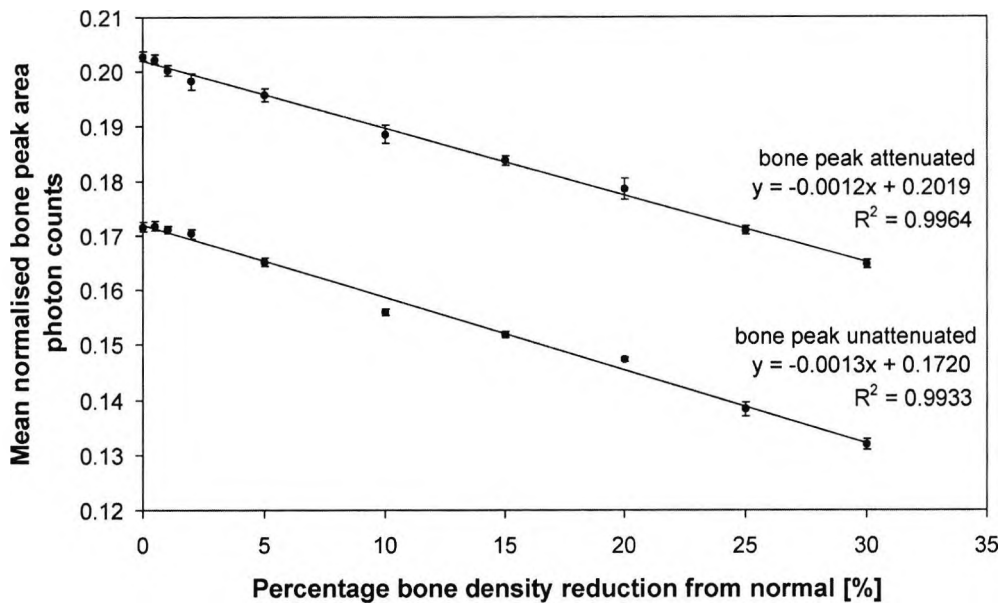


Figure 4-3. EDXRD normalised bone peak photon counts for the phantom set with and without additional attenuation (simulating cortical bone and soft tissue). The peak areas were taken from spectra generated using a 6° experimental scattering angle and a collimator slit width of 1 mm. The error bars shown are ± two standard deviations. The attenuated peak area counts are higher due to the effects of normalising the spectra. Since attenuation preferentially suppresses the lower energy photons of the spectrum, the normalised peak area increases (relatively) with the addition of attenuation.

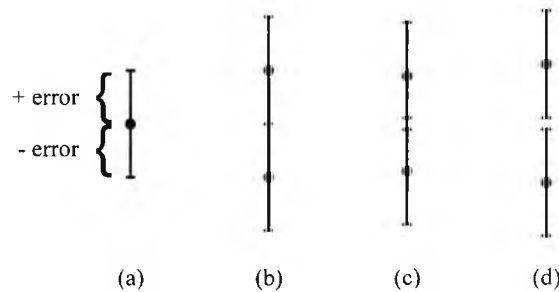


Figure 4-4. An illustration of the reasoning behind the calculation of precision. A plus and minus error for each data point was first calculated (a), in this instance from ± two standard deviations. The limit of precision, where two samples of differing densities may be distinguished, is 2 × the ± error (b). If the point separation is less than this (c), distinction cannot be guaranteed. A greater point separation (d) guarantees distinction.

calculated by first taking the spread of the repeat measurements of each phantom. These uncertainty estimates, marked on the plots (figure 4-3), were generated by taking \pm two standard deviations of the normalised peak region photon counts. This is reasonable since, if a normal distribution is assumed, approximately 95% of these measurements fall within \pm two standard deviations of the mean. The precision of the system (for this range of samples) was calculated by taking twice the mean plus two standard deviations of these errors. The reasoning for this calculation is illustrated by figure 4-4. A back calculation was performed in order to express the precision in terms of a minimum detectable bone density change.

The quality of the linear fit to the data is expressed in terms of the square of the Pearson product moment correlation coefficient (R^2), where:

$$R = \frac{n \left(\sum_{i=1}^n X_i Y_i \right) - \left(\sum_{i=1}^n X_i \right) \left(\sum_{i=1}^n Y_i \right)}{\sqrt{\left[n \left(\sum_{i=1}^n X_i^2 \right) - \left(\sum_{i=1}^n X_i \right)^2 \right] \left[n \left(\sum_{i=1}^n Y_i^2 \right) - \left(\sum_{i=1}^n Y_i \right)^2 \right]}} \quad [4.1]$$

or

$$R = \frac{\text{covariance}(X, Y)}{\sqrt{\text{variance}(X) \cdot \text{variance}(Y)}} \quad [4.2]$$

The R^2 value may be considered as the proportion of the variance in X attributable to the variance in Y.

It was found that, in terms of minimum detectable limits and best linear fit (R^2), the most effective EDXRD results (presented in figure 4-3) were obtained from spectra generated using a 6° experimental scattering angle (2θ) and collimator slit widths of 1 mm (s_1 and s_2). Other experimental parameters were 300 mm collimation channel lengths (l_1 and l_2), 10 mm collimation channel heights (h_1 and h_2) and x-ray source settings of 70 kV_p, 8 mA. The minimum detectable resolution was a bone density change of 1.9% (bone density error of $\pm 0.97\%$), with an R^2 value of 0.9933. The additional attenuation degraded the minimum resolution to 3.3% (bone density error of $\pm 1.67\%$), with an R^2 value of 0.9964.

At all scatter angles, 0.5 mm collimation slit widths (s_1 and s_2) resulted in a significant loss of photon flux and bone density change resolution when compared to the greater collimation widths. 0.75 mm collimation resulted in a comparable bone density change resolution to that of 1.0 mm.

Conclusions

These results were used to obtain a set of EDXRD experimental parameters to be used for the main EDXRD investigations (chapters seven and eight). They do provide an initial indication to the effectiveness of an EDXRD bone density measurement system but should not be considered conclusive. The experimental parameters were set as accurately as possible but, due to the high level of variability, may not be considered entirely accurate. For example the set of lead collimation slits may not have been aligned precisely, effectively reducing s_1 and s_2 .

In addition, only five repeated measurements were taken for each condition, which is not ideal for a good statistical result.

These and other concerns were addressed for the subsequent experiments.

It should be noted that reducing collimator slit widths increased peak resolution (by reducing angular blurring) at the expense of photon flux. Part of the objective of this pilot study was concerned with finding the best compromise between flux and resolution for good bone density measurement. The assessment of bone density is not necessarily improved with better peak resolution. An optimal combination of flux and peak resolution produces the most favourable results.

These results concur with the results of Farquharson (1996), who concluded that the optimum experimental scatter angle was between 5° and 6° using beam widths between 0.5 mm and 1.0 mm.

4.2

DEXA EXPERIMENTS

A Hologic QDR 4500 machine at University College Hospital, London, was used to record DEXA bone mineral density (BMD) measurements. This machine consists of a fixed patient table with a surrounding C arm upon which is mounted a fan beam x-ray source (below the table) and an array of detectors (above the table). DEXA data is recorded by scanning the arm across the stationary patient. Data is then analysed with a PC running QDR 4500A 9.10C software, which also drives the data collection routine.

Method

For these measurements, a soft tissue equivalent surround to the region of interest was required. Since the QDR 4500 was primarily designed for use with patients, the software interprets collected data as if this soft tissue was present. The same phantom set as used for the EDXRD experiments (section 4.1) was arranged on the patient table with a soft tissue equivalent (30 mm of Perspex), as shown in figure 4-5.

The QDR 4500 was set for lumbar spine measurement, since analysis software for this setting allowed for discrete bone density areas to be defined. In this manner, a single DEXA scan could be used to record data for a number of phantoms.

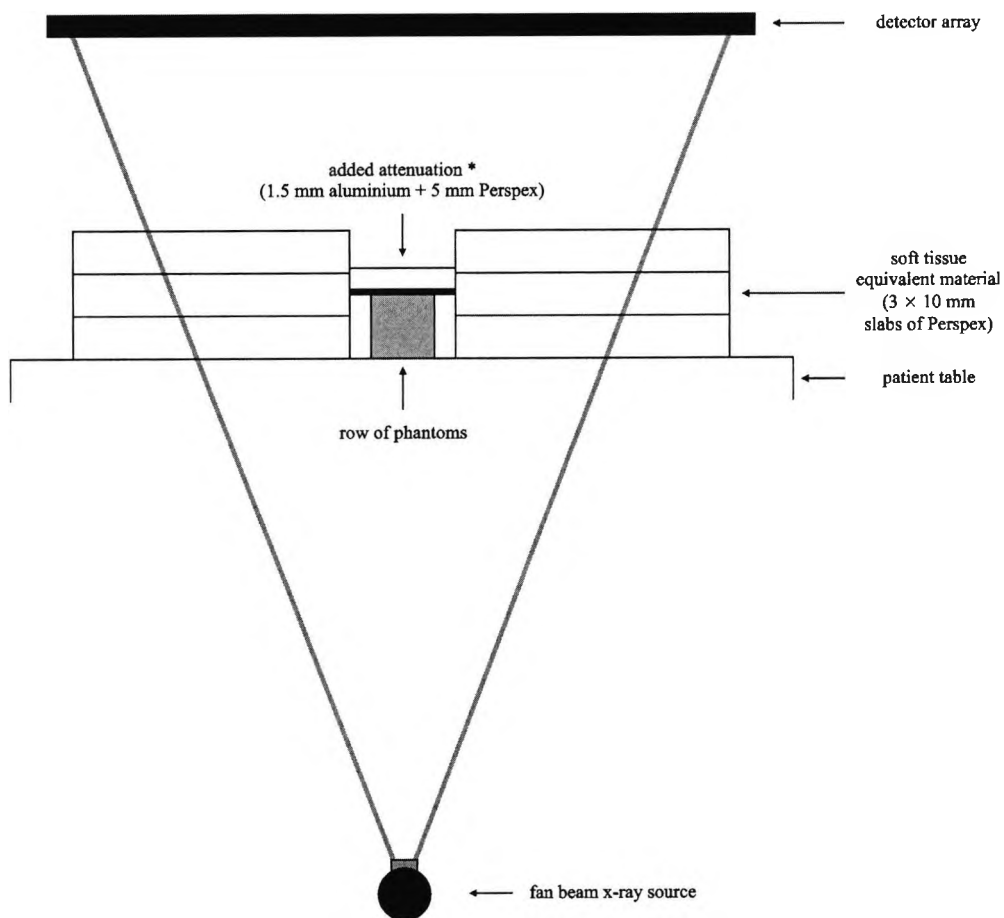


Figure 4-5. Phantom arrangement for the DEXA experiments. The x-ray fan beam and detector array, mounted together on a C arm, scan the phantoms. The added attenuation (marked *) was not present for the first set of DEXA results.

Sets of DEXA measurements were collected by scanning with the x-ray source applied directly to the phantoms (unattenuated) and then repeated with added attenuation to simulate cortical bone (1.5 mm of aluminium) and soft tissue (5 mm Perspex).

Each experiment was repeated five times to enable errors in terms of repeatability to be calculated.

Results

The DEXA scans were analysed by using a 'Subregion analysis' option from the Hologic software. The DEXA bone mineral density (BMD) result for each phantom was isolated and recorded. These BMD values (obtained as a BMD per unit area, in g/cm^2) were plotted against phantom bone density reduction from the norm. The results were regression fitted with linear trend lines (figure 4-6).

Precision (or minimum detectable limits) of the system across the sample range were calculated in the same manner as for the EDXRD experiments, the errors marked on the plots (figure 4-6) being generated by taking \pm two standard deviations of the BMD

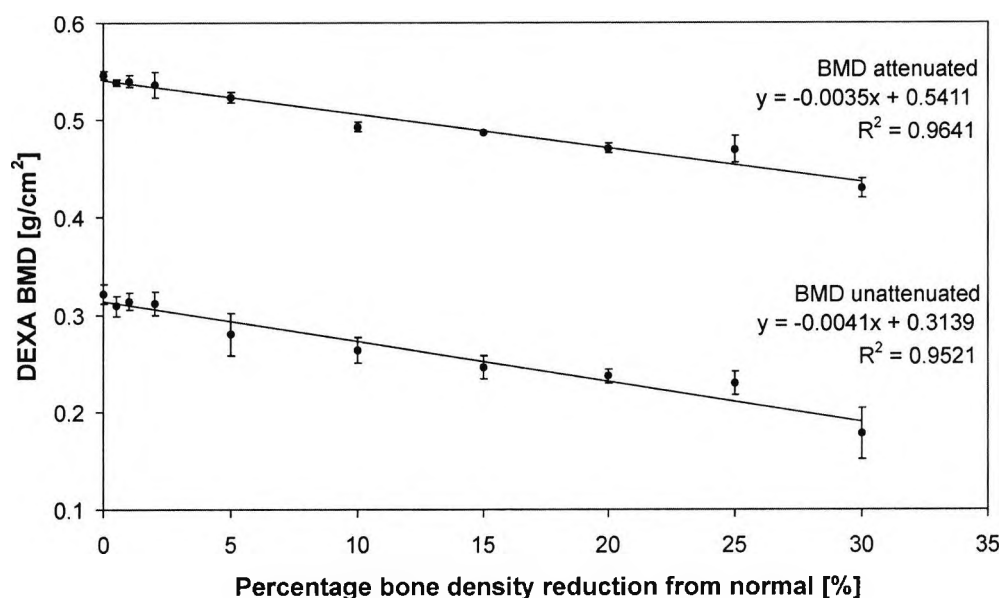


Figure 4-6. DEXA bone density measurement results for the phantom set with and without additional attenuation (simulating cortical bone and soft tissue). The errors shown are \pm two standard deviations. The attenuated densities are higher as the additional attenuation is included as part of the bone density measurement. Note that DEXA reports bone density as BMD area, with g/cm^2 units (table 1-1, chapter one).

results. Again the system precision (for this range of samples) was calculated by taking the mean plus two standard deviations of these errors. The quality of the linear fit to the data is expressed in terms of R^2 .

The DEXA results in terms of minimum detectable limits and best linear fit (R^2) are presented in figure 4-6. The minimum detectable resolution was a bone density change of 12.4% (bone density error of $\pm 6.19\%$), with an R^2 value of 0.9521. The additional attenuation improved the minimum resolution to 8.5% (bone density error of $\pm 4.27\%$), with an R^2 value of 0.9641, similar to the unattenuated result.

Conclusions

The QDR 4500 is optimised for use with patients and so these experimental results may not reflect the ability of the machine when used under these more usual conditions. This is indicated by the improvement of minimum detectable limits and the R^2 value when attenuation is added. This attenuation goes some way to simulate the effect of cortical bone and soft tissue surrounding the region of interest, as for the *in-vivo* condition. There is no reason to dispute the manufacturers stated precision for the QDR 4500, being 1% bone density change.

In addition, only five repeated measurements were taken for each condition, which may not be sufficient for a good statistical result.

These and other concerns were addressed for the subsequent experiments.

4.3 COMPARING EDXRD AND DEXA RESULTS

These initial results suggest that this EDXRD experiment provides a greater bone density measurement precision than that of DEXA. When using unattenuated phantoms, the precision of EDXRD is over six times better than that of DEXA. With the added attenuation, the precision of EDXRD demonstrates an improvement of approximately $2\frac{1}{2}$ times that of DEXA.

However, in addition to the points already noted in the EDXRD and DEXA conclusions, the dose ramifications deserve a mention. For both techniques, the majority of attenuated photons are transmitted, as opposed to scattered. In order to achieve parity of detected photon flux, the scattering method (EDXRD) must have a greater input photon flux than that of the transmission method (DEXA). In other words, DEXA is more photon efficient than EDXRD as a bone densitometry modality. As a consequence, the radiation

dose to the patient is many times greater for EDXRD (quantified in chapter nine) and would require significant reduction before this method could be considered for clinical use. Possible adaptations and analysis methods to reduce the dose are investigated as part of the main study.

4.3.1 EDXRD and DEXA Sensitivity

An indication of the sensitivity of each data set may be realised by comparing the gradient of each linear fit (i. e. the steeper the gradient, the more likely that different bone densities may be distinguished). To allow direct comparison, each trend plot was normalised to unity. Figure 4-7 presents normalised gradients for EDXRD and DEXA, unattenuated and attenuated. With attenuation, the EDXRD gradient was reduced to 88% of its unattenuated gradient whereas the DEXA gradient was reduced to 47% of its unattenuated gradient.

It can be stated that, with respect to these results for this range of bone densities, DEXA is affected by the applied attenuation more than four times as much as EDXRD.

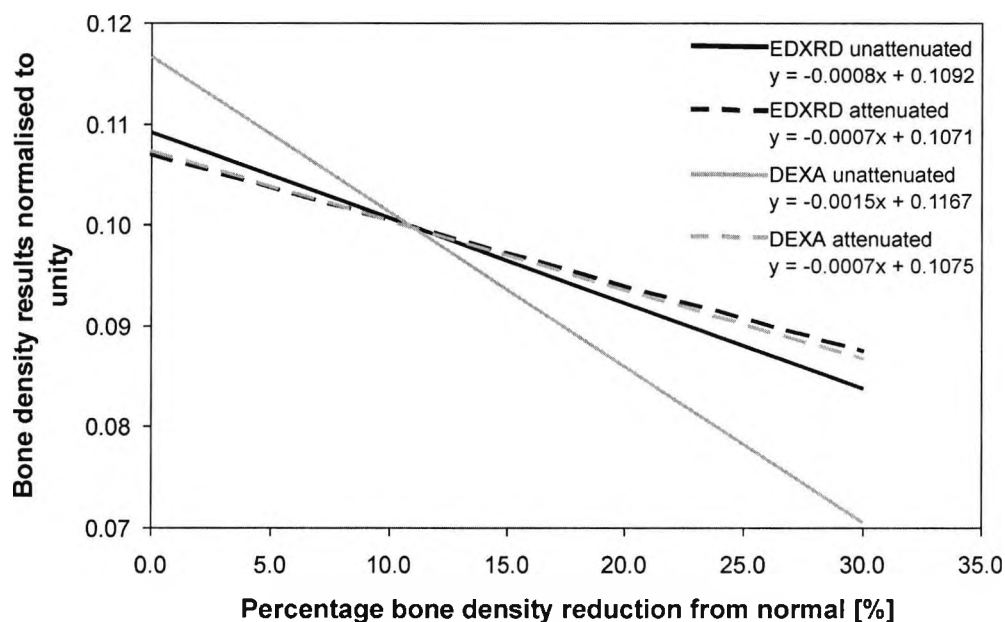


Figure 4-7. Sensitivity comparison of EDXRD and DEXA results by normalising to unity. By this method, the plot gradients may be directly compared. The DEXA gradients are affected more significantly than the EDXRD gradients.

Chapter 5

TRABECULAR BONE SAMPLE

PREPARATION AND DEMINERALISATION

This chapter discusses methods for the preparation and demineralisation of trabecular bone samples, used to provide a tool for the assessment of bone density measurement techniques (chapter seven). Knowledge of the quantity and uniformity of bone mineral mass removal is necessary for investigating system detection limits for the bone density measurement modality under investigation. This chapter covers sample cleaning, demineralisation control and uniformity:

- Section 5.1 The location (from within excised femoral heads) and removal technique of the trabecular bone study samples is discussed.
- Section 5.2 A technique is presented for cleaning marrow lipid from $15 \times 15 \times 15 \text{ mm}^3$ samples using an enzyme based temperature dependant detergent.
- Section 5.3 Plots are provided for guidance to the time of exposure to weak solutions of ethylenediaminetetra-acetic acid (EDTA) required for controlled bone mineral reduction, in order to replicate in-vivo bone mineral loss.
- Section 5.4 The uniformity of the demineralisation method is investigated using microdensitometry of radiographs.
- Section 5.5 A method is discussed that provides a means of calculating the bone density of a region of interest within the bone sample from knowledge of the whole cube density and microdensitometry data.
- Section 5.6 A technique is described for the introduction of a bone marrow substitute into the trabecular spaces of cleaned sample cubes.

5.1 STUDY SAMPLE SITE FROM WITHIN THE FEMORAL HEAD

The samples used in this study are $15 \times 15 \times 15 \text{ mm}^3$ cubes of trabecular bone cut from a precise position from within the femoral head. Femoral heads are routinely removed as

part of hip replacement operations and so may be harvested, although quantities are limited since many are retained in bone banks for use in surgical revisions. The trabecular regions of such femoral heads were used for these studies on density measurements and stress tests.

Whitehouse and Dyson (1974) state that the high variation in the trabeculae of the proximal femur must 'cast doubt on the results of any observations in which trabecular bone from the proximal femur has been studied without careful examination of the local structure of the samples to ensure they are homogeneous'. Their conclusions state that only the medial (M) group has an explained relationship with local stresses. Other systems are not satisfactorily understood (system nomenclature explained in chapter one, section 1.2.2). There is also high diversity between different femora, making standardisation of results from the samples less straightforward. Selecting and removing a trabecular region from within the femoral heads must be executed with care. Uncertainties are unavoidable and must be borne in mind when interpreting results from this study.

The aim of selecting a site of interest is to provide samples that are most suitable for use with both bone density loss and mechanical compression experiments. The samples should contain no cortical bone and consist of trabecular structure with as few variations between samples as possible. Selecting a sample of trabecular bone from the medial group of trabeculae, whilst avoiding (as far as possible) other trabeculae best fulfils these criteria. The medial group is the most satisfactorily described system with good evidence to suggest that it provides the singular function of transmitting compression forces to the femoral shaft. It therefore complies with requirements for the investigation of both bone density (strong presence of trabeculae) and compression (force specific structure). Additionally, it may be the only trabecular system available in a low density subject, if other systems have deteriorated (demonstrated by the Singh index, discussed in chapter one, section 1.5.1). The chosen sample site is shown in figure 5-1.

Method

Before cutting, each femoral head was radiographed in two projections to provide images for cube location. This procedure enables consistent orientation when cutting samples. The images were also useful for comparing and referencing the samples.

15 × 15 × 15 mm³ cubic samples of trabecular bone were cut from within femoral heads

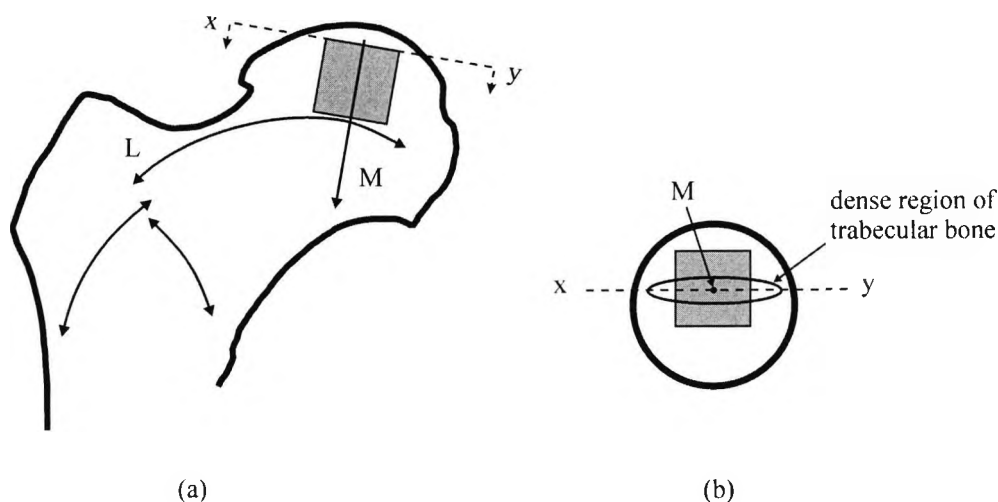


Figure 5-1. Diagram of the proximal femur showing sample site selection: (a) orientation from the antero-posterior view and (b) orientation shown from a superio-inferior view (section x-y). Note how the medial group 'column' passes through the centre of the sample cube in the x-y section view. Trabecular system nomenclature is explained in chapter one, section 1.2.2.

using an Isomet 1000 precision circular saw with a diamond encrusted blade. Additional chucks were designed and manufactured for this saw to secure the sample at various cutting stages. Drawings and details of chuck usage may be found in appendix B, section B.1.

Figure 5-1 shows cube location with respect to the trabeculae systems and cortical bone. The cubes were cut so the medial system 'column' centre passed through the axis of the cube, as closely as was possible. The top of each cube was cut as near to the cortical bone as was possible without inclusion. This provided a datum point for cube cutting and also kept the sample site away (as far as was possible) from other more intricate trabecular regions where the lateral group decussates with the medial group. The vertical faces of the cube were cut to have the same orientation as the sample radiographs.

5.2 CLEANING THE TRABECULAR BONE SAMPLES

Once cut, it is necessary to clean the bone marrow lipids from the samples. Thorough defatting is important, without damaging the trabeculae, since the samples must be completely free of marrow lipid for even bone demineralisation. Some methods that

have been used to clean bone samples include: washing marrow out with a jet of cold water (Whitehouse and Dyson, 1974); cycles of submerging in detergent and evaporation (Majumdar *et al.*, 1998); cycles of ethanol and water irrigation (Jiang *et al.*, 1998); immersion in ether and then in hydrogen peroxide (Crummy *et al.*, 1997); immersion in three parts 1,1,1-trichloroethane to one part methanol (Davis and Payne, 1992).

The sample size of $15 \times 15 \times 15 \text{ mm}^3$ was selected based on the adopted cleaning process. Larger cube sizes were harder to clean, greater penetration of cleaning solution being required. In addition, it was more difficult to avoid cortical bone when cutting. Smaller cube sizes would not offer a great enough volume or face surface area for useful bone density measurement studies. In addition, An and Bensen (2000) recommend a length to diameter ratio of between one and two for compression tests in order to avoid difficulties with buckling (higher ratio) and friction effects (lower ratio). Pilot studies showed that $15 \times 15 \times 15 \text{ mm}^3$ samples may be thoroughly cleaned and are therefore feasible.

Method

The defatting method chosen for this study involved a temperature controlled ultrasonic bath in conjunction with Alconox Terg-a-zyme, an enzyme based detergent. The temperature controlled environment (40°C for Terg-a-zyme) allowed the detergent to work at its greatest efficiency and the agitation generated by the ultrasound induced a more even and rapid distribution of the solution throughout the bone sample. The detergent was used in a 5% (by mass) solution.

A standard qualitative biochemical test to indicate the presence or absence of lipid was used to determine if the marrow was completely removed by the cleaning process. The bone sample was agitated in ethanol, again using the ultrasound bath to ensure complete penetration. The liquid was filtered off and poured into water. A cloudy appearance indicated the presence of lipid (it precipitates from the ethanol) whereas a clear liquid indicated no lipid present.

Pilot studies have shown that there is a large range of exposure times needed to completely clean a $15 \times 15 \times 15 \text{ mm}^3$ sample in the ultrasound bath, dependant on bone density and trabecular spacing. The minimum time for a thorough clean was of the order of 30 hours with a maximum of around 100 hours. This large time range means that each sample must be verified as clean using the ethanol test.

The cleaned bone samples were stored dry (any residual moisture might encourage fungal growth) and extremes of temperature and humidity were avoided (Davis and Payne, 1992).

The following summarises the method used to clean the $15 \times 15 \times 15 \text{ mm}^3$ samples.

1. The sample was cleaned in an ultrasound bath with a 5% Terg-a-zyme solution at 40°C (optimum temperature for enzyme action). When the ultrasound was not running, the sample was left to soak. If removed, the solution would have to re-penetrate the sample.
2. After 60 hours, the sample was rinsed in fresh water (in the ultrasound bath) for 10 hours to remove residual detergent, and then dried.
3. The sample was immersed in 10 ml of ethanol in a test tube (supported in the ultrasound bath) for 10 hours of ultrasound. The ethanol was filtered into a clean test tube and purified water was added. If the solution turned cloudy, lipid was present and the test was repeated. If the solution remained clear, the sample was clean. The ethanol also completes the cleaning and disinfection process.
4. If the sample was clean, it was dried and was ready for experimental use. If the sample was not clean, it was returned to the ultrasound bath for further cleaning.

5.3 SIMULATING BONE MINERAL DENSITY LOSS

In order to perform comparative measurements to test the detection limits of a bone density measurement modality, a controlled demineralisation technique was developed. It was necessary to be able to remove small, known amounts of bone mineral evenly throughout each of the trabecular bone sample cubes so the choice of mineral reduction agent was important to achieve this. However it is not possible to demineralise with complete uniformity.

Evenness of demineralisation is determined by a number of factors, including the trabecular structure and overall bone density. Minimisation of unevenness may be achieved by slowing the demineralisation, using, for example, dilute EDTA or formic acid rather than strong mineral acids such as nitric acid (Mawhinney *et al.*, 1984). The demineralisation is more evenly spread since the demineralising agent has more of a chance to propagate to the centre of the sample. However if the agent is too dilute, it takes an unacceptable amount of time to achieve the required mineral reduction and the agent may completely react before it reaches the centre of the sample.

Different types of mineral reduction agent, such as lactic acid, formic acid and EDTA, were considered for the technique, finally favouring the chelating agent EDTA ((HO₂CCH₂)₂N.CH₂.CH₂.N(CH₂CO₂H)₂). Although nominally 'acid', it does not act as a mineral or organic acid, rather it captures metallic ions, principally calcium. Therefore EDTA was chosen because the demineralisation specifically removes calcium with minimal change to the bone protein matrix. In a study of decalcification using EDTA, an absence of proteins was found in the EDTA after decalcification, indicating no degradation of the organic bone matrix had occurred (Shah *et al.*, 1995).

It should be noted that EDTA does not completely mimic osteoporosis, in which the bone protein matrix is also affected. However it was considered prudent that one factor only (i.e. bone mineral) should be reduced for bone density measurement evaluation in order to achieve more experimentally valid results. This enabled the effect of the acid to be more accurately assessed.

Kiviranta *et al.* (1980) experimented with EDTA of varying strengths on 0.5 mm bone slices to provide an indication of complete demineralisation times. It was found that the slice was completely decalcified with 15% (0.40 M) EDTA in 24 hours, with 8% (0.22 M) EDTA in three days and with 4% (0.11 M) EDTA in five days. Higher temperatures resulted in slightly increased rate (initial temperature 4°C) as did increases in acidity from neutral pH.

Method

Various concentrations of EDTA solution were used, with ultrasonic agitation for more uniform penetration, to generate a range of demineralisation plots as a function of time. A range of bone sample densities was used to develop the technique.

The following steps summarise the bone demineralising procedure used to generate demineralisation plots. For a chosen time interval of 20 minutes, steps one to three initialise the process and steps four to eight, repeated to 400 minutes, generate the plot data. Solution concentrations of EDTA used were 1%, 2% and 3.72% (0.1 mol/litre).

1. The sample was washed in 10 ml of purified water in a test tube to ensure no residues or loose particulates. The tube was supported in the ultrasound bath and, with ultrasonic agitation, the sample was placed into the purified water, ensuring complete immersion.

2. After washing for a sufficient time interval (five hours was found to be sufficient), the water was poured off. The sample was removed and dried with hot air.
3. The sample mass was measured and recorded as initial mass.
4. 10 ml of EDTA was poured into a test tube supported in the ultrasound bath. Dilute solutions of 1%, 2% or 3.72% were used.
5. With ultrasonic agitation, the sample was placed into the EDTA solution in the test tube, ensuring complete immersion.
6. After a time interval of 20 minutes, the EDTA was poured off and the sample immediately immersed in clean water (in the ultrasound bath) for 15 minutes, to stop the activity of the agent.
7. The sample was removed and dried with hot air, and the sample mass was measured and recorded.
8. Steps 4 to 7 were repeated until data from 400 minutes of EDTA immersion time were recorded.

Results

For each concentration of EDTA (1%, 2% and 3.72%), demineralisation was performed on three bone cube samples of average, high and low density. Figure 5-2 shows the means of these sample demineralisation curves as a percentage of original mass. Errors originate from the weighing error of the electronic balance (Sartorius PT310). The smallest mass that the balance could discriminate was 0.01 g. This was taken as the weighing error and propagated to the percentage demineralisation plots.

These plots provide a good indication to the demineralisation effect for a given EDTA concentration and may be used as a starting point to decide the exposure time necessary for a required amount of demineralisation.

Mawhinney *et al.* (1984) concluded that bone density reduction using nitric acid follows an approximate exponential path:

$$m_{(t)} = m_{(0)} e^{-\lambda t} \quad [5.1]$$

where $m_{(t)}$ is mass at time t , $m_{(0)}$ is the initial mass, and λ is a factor depending on the sample and demineralising agent.

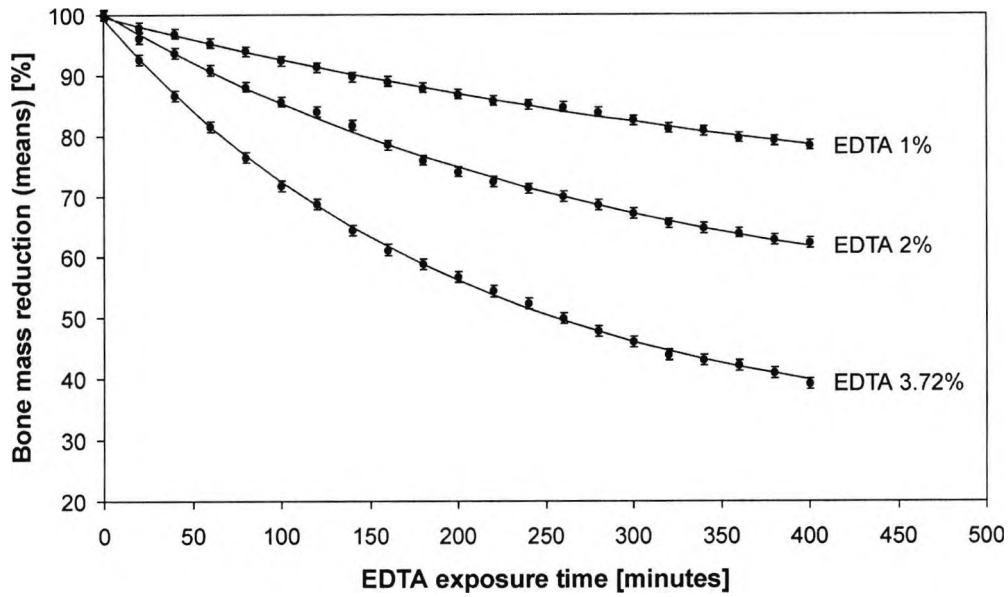


Figure 5-2. Percentage reduction of bone sample mass as a function of exposure time to EDTA. Each curve was generated from the mean demineralisation of three bone samples. Errors are derived from balance weighing accuracy.

Expressed as a percentage mass loss, equation 5.1 becomes:

$$m_{p(t)} = 100 \frac{m(t)}{m(0)} = 100e^{-\lambda t} \quad [5.2]$$

where $m_{p(t)}$ is the percentage of original mass at time t .

However the EDTA results (figure 5-2) show the curves do not tend towards zero mass but towards a constant mass greater than zero. This is expected as the EDTA is removing bone mineral only, leaving the protein base of the sample. Thus, equation 5.2 becomes:

$$m_{p(t)} = ae^{-\lambda t} + c \quad [5.3]$$

where a and c are constants, summing to 100 since $m_{p(t)}$ is expressed as a percentage.

The EDTA demineralisation data was fitted (non-linear regression), using equation 5.3, to produce the curves shown in figure 5-2. The parameters resulting from these fits are given in table 5-1.

EDTA Concentration [%]	a [%]	λ [minutes ⁻¹]	c [%]
1	37.0446	0.00209316	62.6042
2	52.4694	0.00328485	47.6381
3.72	69.1390	0.00490439	30.1270

Table 5-1. Parameters for the fitted EDTA demineralisation curves, using equation 5.3. These parameters may be used to estimate an EDTA exposure time for a required percentage of demineralisation, with a starting knowledge of EDTA concentration and sample density (equation 5.4).

When using this data to select exposure time (t) for bone cube demineralisation (by a given percentage of starting mass, m_p), equation 5.3 is rearranged:

$$t = -\ln\left(\frac{m_p - c}{a}\right) / \lambda \quad [5.4]$$

As a point of note, it is expected that the constants 'a' and 'c' should have approximately the same ratio for each EDTA concentration, since the ratio of mineral density to protein matrix density are approximately the same for each sample cube. This would become more apparent than with the results presented here if demineralisation was continued until the entire mineral component was removed. However, the requirement for this investigation was to develop curves for small amounts of demineralisation, so it was considered unnecessary to spend time demineralising to zero mineral levels.

5.4 DEMINERALISATION HOMOGENEITY ASSESSMENT USING MICRODENSITOMETRY

Ideally, demineralisation should be as even as possible throughout a sample for the investigation of bone density measurement techniques. These measurements could then be performed with the confidence that whatever internal volume of the sample is exposed to the measuring technique, approximately the same amount of mineral will have been removed. However demineralisation will not be even throughout the sample. Factors such as cube porosity, local density variations, proximity to external surfaces and acid concentration will affect how evenly mineral reduction occurs. It is therefore

important to evaluate the level of demineralisation within the region of interest used for densitometry assessment (which cannot be measured directly) as compared to the demineralisation of the whole cube (which can be measured by weighing). Bone densitometry assessment may then be performed using this region of interest.

Radiographic microdensitometry was used to assess the evenness of sample demineralisation. There are inherent errors associated with this method, which tend to be more problematic in clinical applications. They arise for reasons such as uneven x-ray intensity, beam hardening of the polyenergetic radiation, unevenness of the 'background' film density, uneven soft tissue thickness and attenuation coefficient, uneven scatter distribution, uneven film development and densitometer and operator error. Care to minimise these errors can yield useful results (Tothill, 1989). Most of these problems are minimised by the simultaneous exposure of a reference wedge alongside the samples to be measured, allowing film, exposure and processing inconsistencies to be largely removed from the results. Other measures to improve the technique include the use of a small film and exposure area (the intensity of an x-ray beam is much more uniform near the centre), small samples with similar radiographic properties (with no soft tissue) and a large focus film distance (FFD), which minimises image distortion and the heel effect (a smaller cone of radiation is used to cover a given area).

It should be noted that it was not proposed to develop microdensitometry as a clinical procedure for the measurement of bone density. As a clinical method, bone densitometry is no longer widely used (Alhava, 1991). Errors can arise for a variety of reasons, as previously discussed. The use of microdensitometry in this study was to assess demineralisation uniformity for the bone samples, which will be used as analytical standards by which to evaluate practical procedures.

Method

Radiographic images of the bone cube samples, both before and after demineralisation, were taken with aluminium stepwedges included in the primary beam. The stepwedges allow optical densities from the bone image to be normalised to equivalent thicknesses of aluminium. Density information from each of the bone radiograph images may then be compared directly (Matsumoto *et al.*, 1994). Each radiograph was acquired using

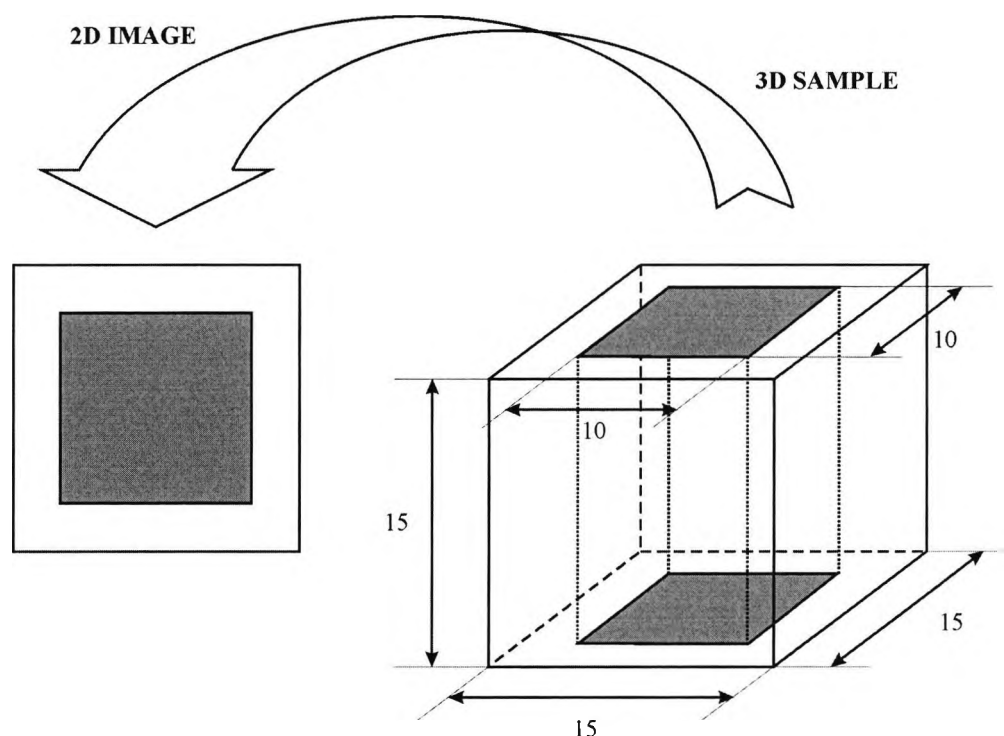


Figure 5-3. Region of interest of a bone sample cube. The region is chosen to ascertain a measure of the evenness of demineralisation. The density information from the three-dimensional sample is represented as a two-dimensional film image. The dimensions are given in millimetre units.

Kodak Min-R 2000 mammographic film with a Kodak Min-R 2 cassette (Min-R 2000 screen). Exposure factors were 40 kV_p, 80 mAs (fine focus) with an FFD of 140 cm. These exposure factors were chosen to keep the optical densities of the image within the linear region of the film's characteristic curve.

The information offered by the radiographs is a two-dimensional amalgam of the whole depth of the three-dimensional cube (similar in fashion to DEXA). For the purposes of these minimum bone density detection limit studies, a three-dimensional 10 × 10 × 15 mm³ region of interest was selected from within the cube. This translates to a two-dimensional 10 × 10 mm² optical density region of interest from within the cube image (figure 5-3).

A J L Automation Microdensitometer 3CS was used to scan the radiographic images of

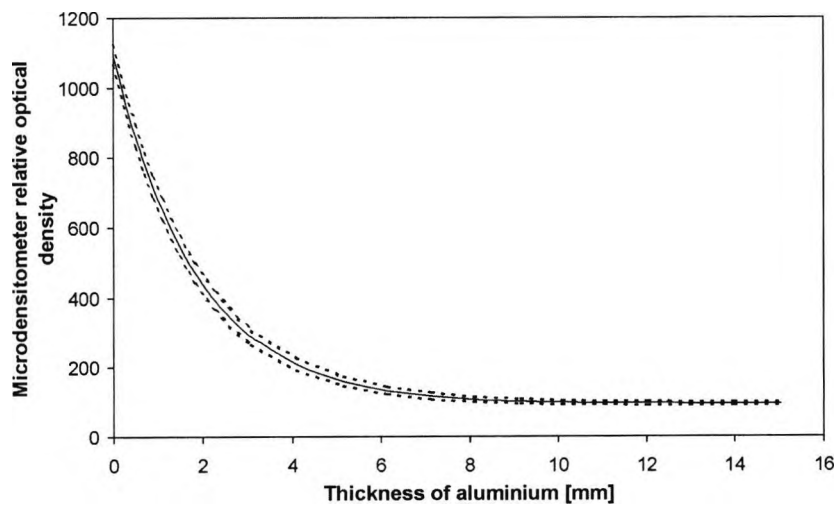
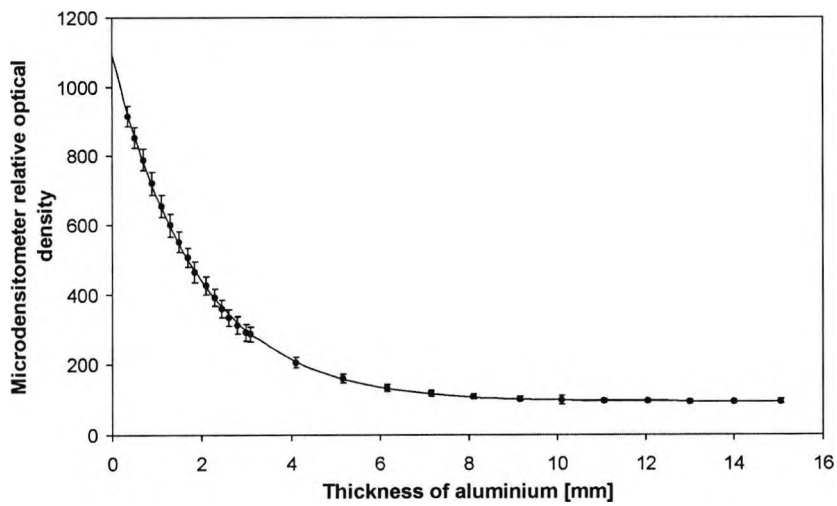


Figure 5-4. Example of a stepwedge optical density plot with fitted exponential function. Errors are \pm two standard deviations of the relative optical density data sets for each thickness of aluminium (wedge step). These errors are presented (a) as discrete points (for each step) with error bars and (b) with fitted error bands.

the bone cubes with their associated stepwedge images. The optical density pixel size was set to 0.1 mm^2 and each image was scanned as a series of relative optical densities with no pixel overlap, effectively digitising the radiographic image.

Results

Each step of the stepwedge represents a relative optical density which was converted to an equivalent thickness of aluminium. A mean relative optical density was calculated for each step using the measured pixels. An example plot of these mean relative optical densities with an exponential function (which does not tend towards zero) fitted (using a non-linear regression fit) is shown in figure 5-4. Errors presented are \pm two standard deviations of pixel relative optical density. Figure 5-4a shows the steps as discrete points with error bars and the exponential fit. The error spreads were then fitted in the same way, shown in figure 5-4b as error bands. This enabled any pixel value from the bone sample scans to be assigned an error.

The fitted stepwedge data was used to convert the relative optical densities of each bone image pixel into an equivalent thickness of aluminium, allowing the data from each image to be directly compared. Each resultant equivalent thickness of aluminium bone image matrix had an associated minimum and maximum pixel matrix generated using the error bands.

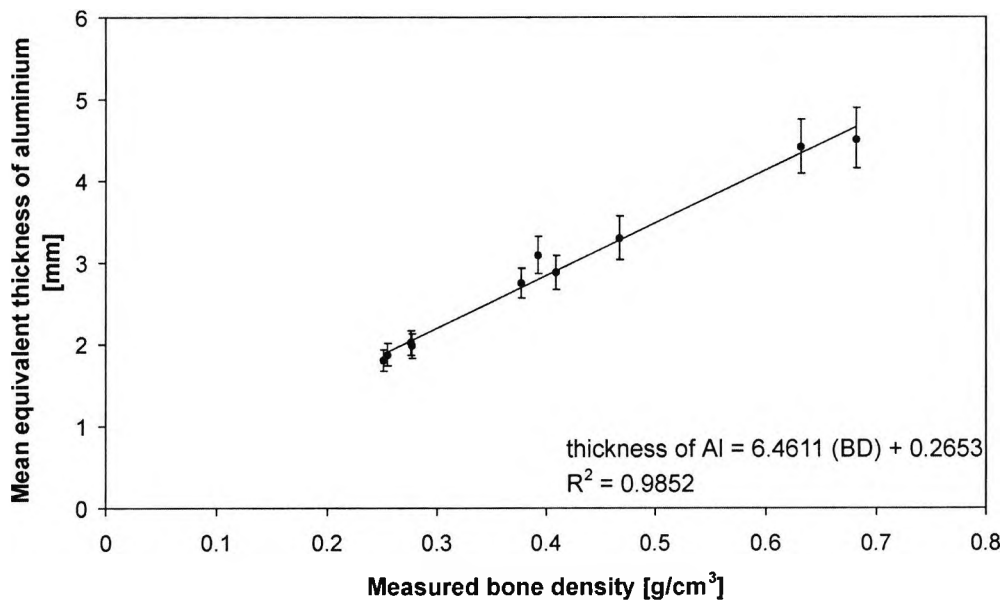


Figure 5-6. Calibration line for determining mean bone density (BD) from a knowledge of the mean equivalent thickness of aluminium (Al) from microdensitometry. Errors are derived from \pm two standard deviations of the relative optical density data sets for each thickness of aluminium. This calibration is valid for clean $15 \times 15 \times 15 \text{ mm}^3$ trabecular bone samples.

Demineralisation Status	Trabecular Bone Sample	Full Cube 15 × 15 × 15 mm ³		Region of Interest (ROI) 10 × 10 × 15 mm ³				BD Ratio Full Cube : ROI [%]	DEF [%]
		Measured BD [g/cm ³]	Post : Pre BD Ratio [%]	Calculated BD [g/cm ³]	Calculated BD Error + [g/cm ³]	Calculated BD Error - [g/cm ³]	Post : Pre BD Ratio [%]		
Pre-demin.	FHD1/1	0.410		0.416	0.032	0.032		98.5	
	FHD1/2	0.277		0.284	0.025	0.024		97.5	
	FHD1/3	0.277	n/a	0.284	0.024	0.024	n/a	97.5	n/a
	FHD2	0.681		0.669	0.057	0.054		101.8	
	FHD3	0.393		0.441	0.036	0.035		89.1	
Post-demin.	FHD1/1	0.378	92.2	0.404	0.030	0.029	97.0	93.5	95.0
	FHD1/2	0.251	90.5	0.261	0.021	0.021	91.7	96.3	98.7
	FHD1/3	0.255	92.2	0.268	0.022	0.021	94.3	95.3	97.8
	FHD2	0.631	92.7	0.673	0.053	0.051	100.5	93.9	92.2
	FHD3	0.213	54.3	0.119	0.017	0.016	27.0	179.2	201.2

Table 5-2. Comparison of measured densities of trabecular bone sample cubes with calculated region of interest (ROI) densities. ROI density errors are derived from the equivalent thickness of aluminium image errors. Bone density (BD) reductions of whole cubes are presented along with a calculated density reduction within the ROI area, expressed as a percentage of original mass. Ratios of the whole cube density against ROI density are also given. The final column is a demineralisation evenness factor (DEF) which provides an indication of demineralisation distribution (see text).

Two pixel matrix images are shown in figure 5-5, which represents a trabecular bone cube before and after demineralisation. The equivalent thickness of aluminium matrixes have been converted to greyscale.

In order to relate equivalent thickness of aluminium to measured density, bone sample densities were calculated from cube dimensions (using Vernier callipers) and mass (using a Sartorius PT310 electronic balance). Means of the total number of equivalent thickness of aluminium pixels for each cube image (approximately $15 \times 15 \text{ mm}^2$) were calculated and plotted against the respective measured cube densities (figure 5-6). A linear regression fit to these points provided the calibration line shown in the figure.

The calibration line was used to calculate density values for the region of interest of each cube. The mean equivalent thickness of aluminium for each region of interest was calculated and converted to an equivalent bone density. Examples of these conversions are shown in table 5-2, along with the ratios of the densities of the whole cubes compared to those of the region of interest.

MatLab M-file functions were written to perform stepwedge and sample cube data processing (appendix E, section E.2).

The ratios of whole cube to region of interest densities were used to provide an indication of the evenness of demineralisation throughout the cube. If for pre- and post-demineralisation the ratio between the density of the whole cube and the density of the region of interest remains the same, it may be stated that, on the gross level of the two areas, demineralisation is distributed evenly. The more the ratios differ pre- and post-demineralisation, the less even the bone density reduction. A further ratio of pre- and post-demineralisation ratios provides a relative demineralisation evenness factor (DEF) for these sample cubes and their regions of interest:

$$\text{DEF} = 100\% \times (\text{BD ratio}_{\text{pre-demin}} / \text{BD ratio}_{\text{post-demin}}) \quad [5.5]$$

Conclusions

As shown in table 5-2, samples FHD1/1, FHD1/2 and FHD1/3 were demineralised to 92.2%, 90.5% and 92.2% of their original densities, respectively, using 3.72% EDTA solution. These demineralisation levels are typical of those required for bone density measurement investigations. The calculated density reductions within the regions of interest were of a similar order (97.0%, 91.7% and 94.3%) and the DEFs of 95.0%,

98.7% and 97.8% indicate a relatively high level of control over demineralisation. Ideally the DEF would be 100%, for maximum control.

Sample FHD2 was demineralised to 92.7% of its original density. For this example, a higher acid concentration was used (100% formic acid) and a sample cube was chosen with a relatively uneven density. These conditions were chosen in order to simulate and investigate an uneven demineralisation situation. Region of interest demineralisation was calculated to be 100.5%. Within system errors, this indicates a zero or negligible bone density loss (table 5-2). The DEF of 92.2% indicates a reduction in demineralisation evenness from the previous examples.

Sample FHD3 was demineralised using 3.72% EDTA to 54.3% of its original density (using a relatively long exposure time), in order to investigate the effect of a large amount of demineralisation. The calculated density reduction within the region of interest was 27.0% of its original density. For low EDTA exposure (low demineralisation), region of interest demineralisation would generally be expected to be less since the EDTA has had less time to penetrate to the deeper trabeculae. For this long exposure time, the region of interest exhibits greater demineralisation compared to that of the whole cube, regional exposure variations becoming less significant with longer exposure time. The DEF is therefore poor, being 201.2%.

To summarise, 3.72% (0.1 mol/litre) EDTA solution has been shown to offer a relatively high degree of control over small levels of bone density reduction (of the order of 10%) from the chosen region of interest within a whole sample cube ($DEF \geq 95\%$). Results using a stronger acid solution and a sample with more uneven bone density distribution suggest less control ($DEF \approx 92\%$) while control is shown to be poor ($DEF \approx 200\%$) with higher levels of demineralisation (order of 50%).

5.5 BONE SAMPLE CUBE DENSITY CORRECTION

Since the EDXRD experiments were set to scan an approximate $10 \times 10 \times 15 \text{ mm}^3$ volume (figure 5-3) from within the $15 \times 15 \times 15 \text{ mm}^3$ cubes, calculation of the whole sample density by mass and volume measurement was not sufficient. A similar method to the radiographic microdensitometry technique was used to correct bone sample cube dry apparent densities, used for the densitometry assessments of this project.

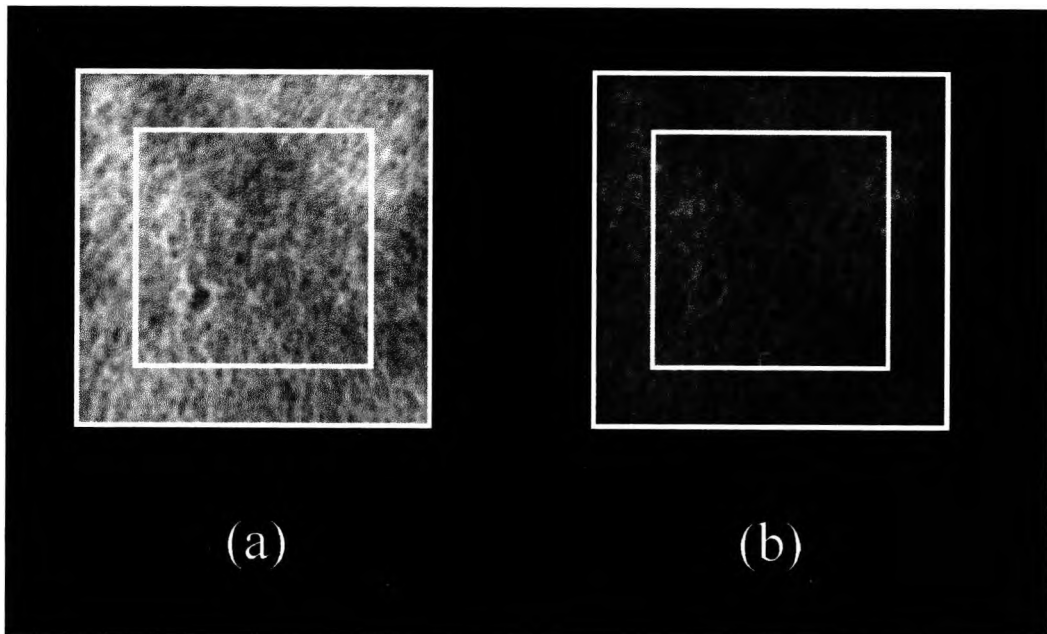


Figure 5-5. Digitised radiographs of a trabecular bone sample cube (a) before and (b) after demineralisation, using microdensitometry. The cube shown in image (b) has been demineralised to approximately 54% of its original density. The $10 \times 10 \text{ mm}^2$ region of interest is also shown for each sample. These images were created by converting microdensitometry data into PGM format image files (appendix E, section E.3).

Method

Each cube dry apparent density was calculated using measurements of the sample mass (using a Sartorius PT310 electronic balance) and dimensions (using Vernier callipers). The cubes were also radiographed in the same manner as for the microdensitometry (section 5.4), again with aluminium stepwedges included in the primary beam. Each radiograph was acquired using Kodak Min-R 2000 mammographic film with a Kodak Min-R 2 cassette (Min-R 2000 screen). Exposure factors were 40 kV_p, 80 mAs (fine focus) with an FFD of 140 cm. These exposure factors were chosen to keep the optical density of the image within the linear region of the characteristic curve of the film.

For this technique, the radiographs were scanned at a resolution of 1200 DPI (8-bit greyscale) using an Epson Expression 1640XL set for transmission scanning (positive film). The scanned images were saved in PGM file format for ease of processing (appendix E, section E.3). Each pixel was converted to an equivalent thickness of aluminium as with the microdensitometry (section 5.4).

Figure 5-5 illustrates the whole cube image with the region of interest that approximates the EDXRD scanned volume (even though this image was generated using the microdensitometry method rather than 1200 DPI scanning). The approximate bone density of the EDXRD region was calculated by comparing the array of equivalent thickness of aluminium values for each pixel of the whole cube ($15 \times 15 \times 15 \text{ mm}^3$, represented by the $15 \times 15 \text{ mm}^2$ image) with those for the EDXRD region ($10 \times 10 \times 15 \text{ mm}^3$, represented by the $10 \times 10 \text{ mm}^2$ image region). The ratio of the mean equivalent thickness of aluminium values for the whole cube image to that of the EDXRD scanned region was calculated. This ratio was used to correct the measured density of the whole cube to an approximation of the density of the EDXRD scanned region.

MatLab M-file functions were written to perform stepwedge and sample cube data processing (appendix E, section E.2).

Conclusions

In general, this correction is not large in comparison with the density of the whole cube. However it is important for the EDXRD analysis that it is performed. Since each cube is centred around the medial trabecular group, the correction may be significant for some samples. The required correction level is sample dependent.

5.6 INTRODUCTION OF MARROW SUBSTITUTE INTO SAMPLE TRABECULAR SPACES

EDXRD and DEXA bone density investigations of chapter seven use marrow free trabecular bone samples (a 'one component sample system') for both calibrated and comparative (pre- and post-demineralisation) measurements. The sample preparation and demineralisation techniques discussed previously are sufficient for these experiments but those of chapter eight required trabecular bone samples with marrow filled trabecular spaces (a 'two component sample system'). This was necessary since the investigations of this chapter concentrated on the measurement of various clinical site simulations, marrow being an integral component.

The trabecular bone cubes were initially cleaned of marrow (as previously described), necessary to determine dry apparent bone density using physically measured sample mass and dimensions. Once density was determined, the trabecular spaces were refilled with a marrow substitute to form the two component sample system condition.

Method

The marrow substitute introduced into the bone sample trabecular spaces was animal fat, as used for the phantom preparation described in chapter three (section 3.2). Hot air was used to gently heat a Pyrex beaker to slowly and completely melt marrow substitute fat contained within. Once there was sufficient liquid fat in the beaker, a trabecular bone cube was immersed and the beaker covered with filter paper, secured to prevent fat splashing. The beaker was quickly transferred to the sample table of a vacuum generator (Edwards E2M5 two stage high vacuum pump with EF4 Modulyo freeze dryer unit) and the vacuum cover applied. A vacuum was generated that caused the air in the trabecular spaces to be replaced completely with the liquid fat.

The beaker with sample and fat was left in the vacuum until there were no further bubbles emitted from the sample and the fat was partially solidified. (It was found by various trials that the most effective procedure to introduce fat into all the trabecular spaces was to leave the beaker in the vacuum for one pass only, i.e. no removal and re-heating.) The beaker was removed and left overnight so the fat completely solidified. The sample was then removed and sealed using cling film and tape. Care was taken to ensure the cube faces that were to be presented to the photon beams for EDXRD and DEXA measurement had only one layer of film with no tape or film folds.

Once the marrow introduction sequence was complete, the sample was labelled for identity and orientation and, when not being used, stored cold to prevent fat seepage.

For the experiments described in chapter eight, 10 samples with a wide density range were used. Samples from the higher end of this range were chosen to be tested for complete fat penetration since, intuitively, these would be the most likely to exhibit problems with the marrow replacement technique. The greater density suggests smaller trabecular spaces into which the fat must penetrate.

The selected sample cubes with marrow substitute (i.e. now two component) were scanned using a magnetic resonance imaging (MRI) scanner at University College, London. The MRI equipment used was a Bruker research spectrometer operating at seven tesla with a custom made radio frequency (RF) coil for the bone sample measurements. The MRI scanner was set for a high resolution three dimensional gradient echo scan with a resolution of $176 \times 176 \times 176$ micron voxel size. This MRI data was produced by M. Yiannakas.

Results

Figure 5-7 illustrates two trabecular bone sample cube slices generated using the MRI data. The first image (figure 5-7a) shows a cube slice with marrow successfully introduced into all the trabecular spaces using the method described. The second image (figure 5-7b) shows a cube slice with marrow introduced using an inferior method (short repeated cycles of vacuum and heat). Air space can be clearly identified where the fat has failed to penetrate.

Conclusions

This MRI imaging test showed that marrow was successfully introduced into all trabecular space for samples treated using this method.

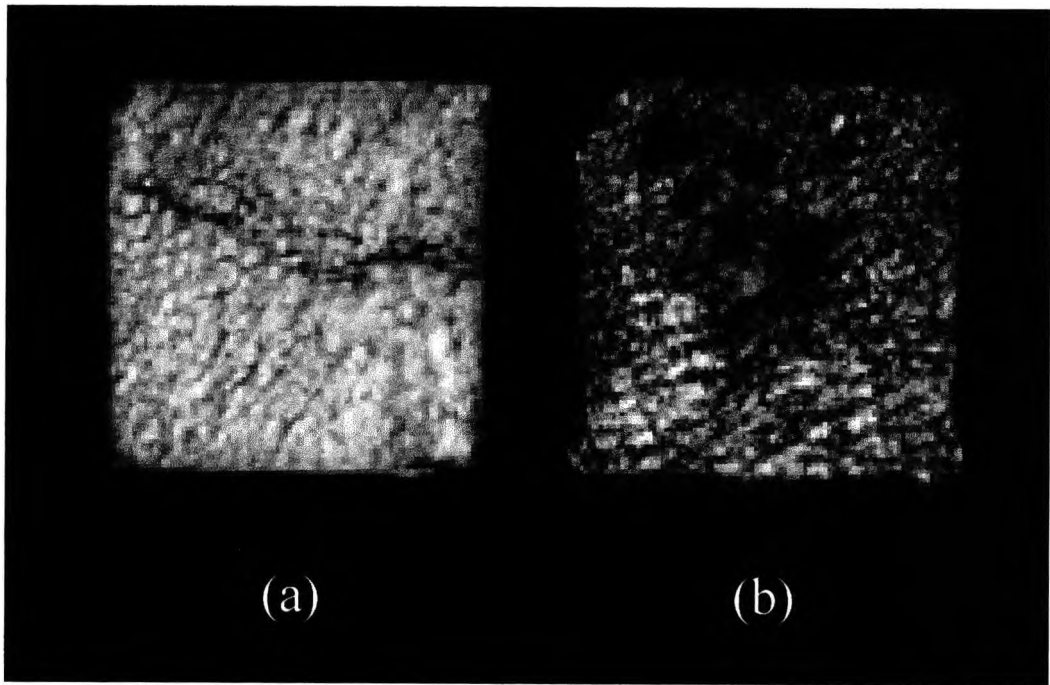


Figure 5-7. Images of two trabecular bone sample cube slices generated from data acquired using a Bruker MRI scanner at University College, London. These images contrast with those of figure 5-5 inasmuch as the light areas represent reintroduced marrow fat to the trabecular spaces. The dark areas show only where there is no fat. All the dark non-marrow regions of image (a) show trabecular bone patterns, indicating full space filling with fat. Much of the dark areas of image (b) show spaces where marrow has not penetrated. Note the thicker dark line dividing image (a). This is due to the presence of the denser bone material of an epiphyseal scar (chapter one, section 1.2.2). (MRI data courtesy of M. Yiannakas.)

Chapter 6

A FIXED PARAMETER DIFFRACTOMETER AND ATTENUATION CORRECTION

The key advantage that x-ray scattering techniques have over bone densitometry methods utilising non-tomographic x-ray transmission is that a volume within the material under investigation may be defined. Figure 1-1 (chapter one) shows how the detected information differs between these modalities. In the scattering example (figure 1-1b), the experimental geometry is defined such that only photons from a volume of trabecular bone are detected. The transmission example (figure 1-1a) detects photons attenuated by both trabecular and cortical bone.

However, by following the geometric path of both transmission and scattering techniques in the figure, it can be seen that for both methods, similar volumes of both trabecular and cortical bone attenuate the photon beam. This attenuation is the basis of the transmission technique and is therefore necessary, although the density of a trabecular region alone cannot be obtained. With the scattering technique, attenuation is detrimental to the final result. If a number of samples are considered, each having an equal bone density for the defined scattering volume, different spectra may be recorded depending on the attenuating effects of the rest of the sample. Figure 6-1 illustrates some conditions that may result in different scattered spectra for a defined scattering volume of the same density. In addition to these conditions (that increase the quantity of bone material in the photon beam path), further circumstances may change scattered spectra attenuation, such as variation in the nature, density and quantity of surrounding soft tissue. An illustration of the effect of such differing attenuating conditions, despite the scattering volume having equal density, is shown in figure 6-2. A single $15 \times 15 \times 15 \text{ mm}^3$ marrow free trabecular bone cube was used to generate these scattering spectra with increasing thicknesses of aluminium attenuation being introduced into the path of the primary beam.

Under specific experimental conditions, the influence of attenuation may not affect results significantly. The EDXRD experiments discussed in chapter four resulted in good minimum detectable limits, being 1.9% for bone and marrow mix phantoms with

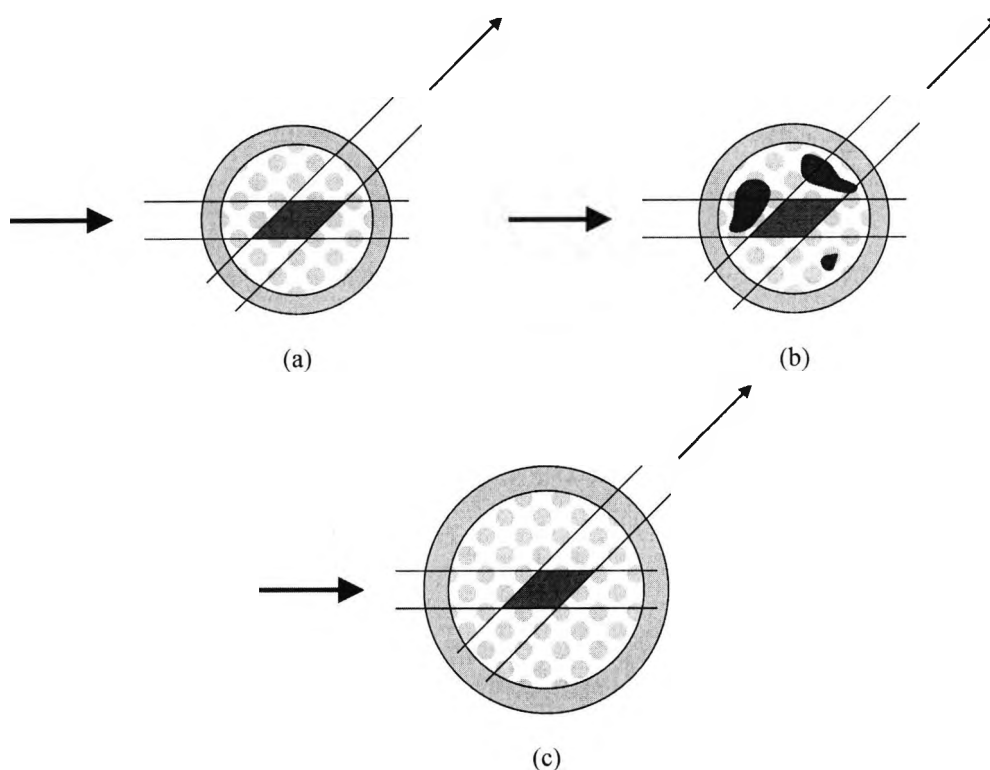


Figure 6-1. Examples of conditions that result in differing attenuation of scattered spectra from a defined scattering volume of equal density. Condition (b) differs from condition (a) since both the primary and secondary beams pass through denser bone volumes (dark grey) beyond the boundaries of the defined region. Condition (c) differs from condition (a) since the whole bone is larger, resulting in more trabecular and cortical bone in the paths of the primary and secondary beams. The arrows indicate the passage of the photons.

no additional attenuation and 2.3% for the same phantoms with additional attenuation simulating cortical bone and soft tissue. However, in order to achieve an absolute bone density measure for the scattering region, a separate calibration line for each attenuation condition would be required. These calibrations would only be valid for the known attenuation for which they were generated. In addition, further inaccuracies would be apparent due to inconsistent levels of the self attenuation of each phantom with differing bone densities. In a clinical situation, self attenuation by the scattering site and additional attenuation by the surrounding materials would be unknown. In order to generate a single calibration for absolute bone density measurement with unknown

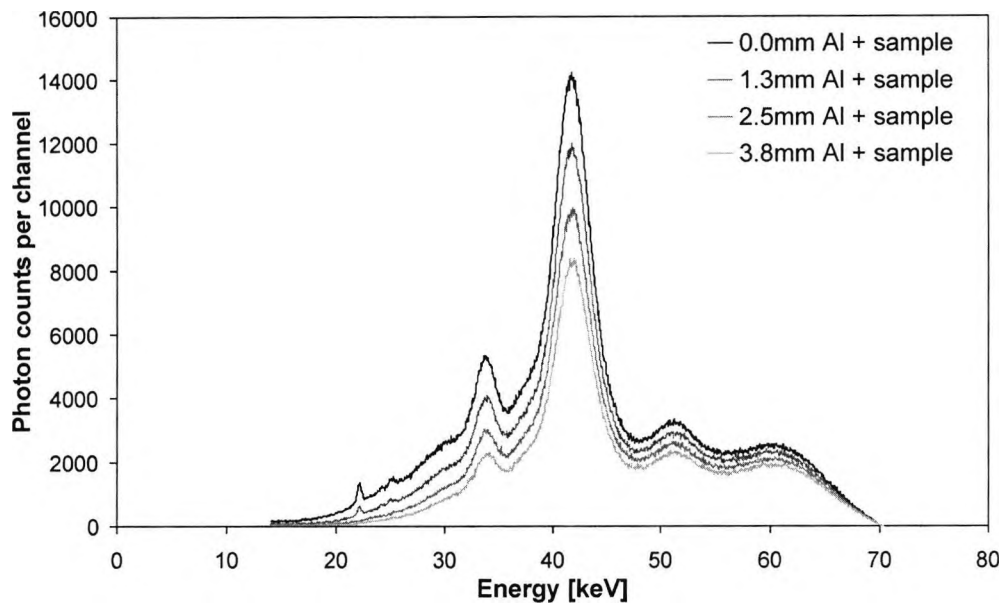


Figure 6-2. Spectra generated using a single marrow free trabecular bone cube. Increasing quantities of aluminium attenuation were introduced into the path of the primary photon beam, which resulted in decreasing photon counts for equal measurement mAs (tube current \times time).

attenuation, a correction technique must be employed. One method used with some success to overcome this problem was to employ a multivariate analysis technique (Farquharson *et al.*, 1997a).

The attenuation correction method used for the remainder of the EDXRD measurements in this project was adapted from that used with Compton scattering bone densitometry techniques (described in chapter one, section 1.5.4 and by Speller *et al.*, 1989, and Tothill, 1989). The method, illustrated by figure 6-3, relies on a transmission spectrum being measured, ideally at the same time as the scattered spectrum. This transmission spectrum provides information about the attenuation subjected to the scattered spectrum. The attenuation effects of the specimen are calculated by comparing the transmission spectrum with a reference spectrum measured with no specimen or additional attenuation in the path of the beam. An attenuation ratio, calculated for each energy channel of the spectrum, is then applied to each channel of the scattered spectrum to correct for the attenuation experienced.

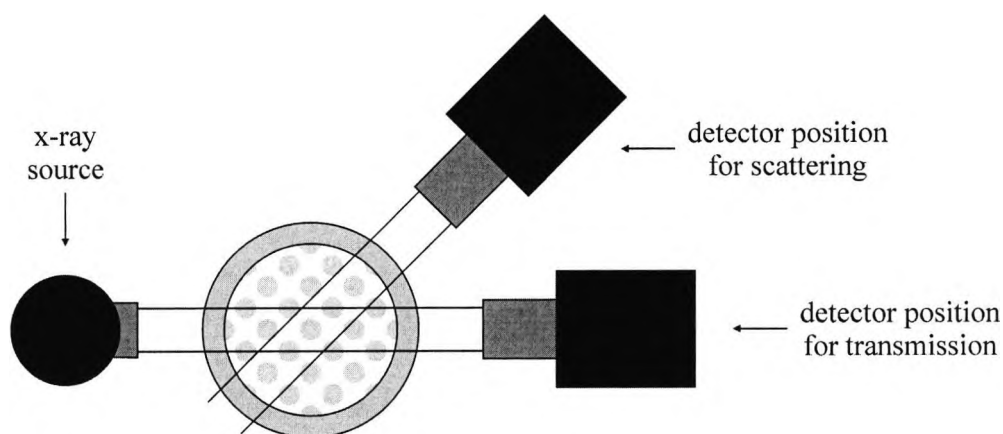


Figure 6-3. Schematic illustrating the geometry for the measurement of scattering and transmission spectra, collecting data to enable attenuation correction.

In addition to the 2θ scattering channel, a 0° collimation channel must be incorporated into the diffractometer to execute this method of correction.

This remainder of this chapter comprises:

- Section 6.1 A description of the fixed parameter EDXRD diffractometer, purpose designed and built for the main studies of this project.
- Section 6.2 An assessment of the attenuation correction technique used for the remainder of the EDXRD measurements of this project.

6.1 THE FIXED PARAMETER EDXRD ASSEMBLY

This EDXRD diffractometer was newly designed and built with most parameters, such as scattering angle and collimation channel width, fixed. Parameters were chosen from the results of chapter four and were fixed in order to minimise repeatability variation. This section describes the assembly, as used for this chapter's attenuation correction experiment and all subsequent EDXRD experiments.

Method

The diffractometer assembly, shown in figure 6-4, consisted of primary and secondary

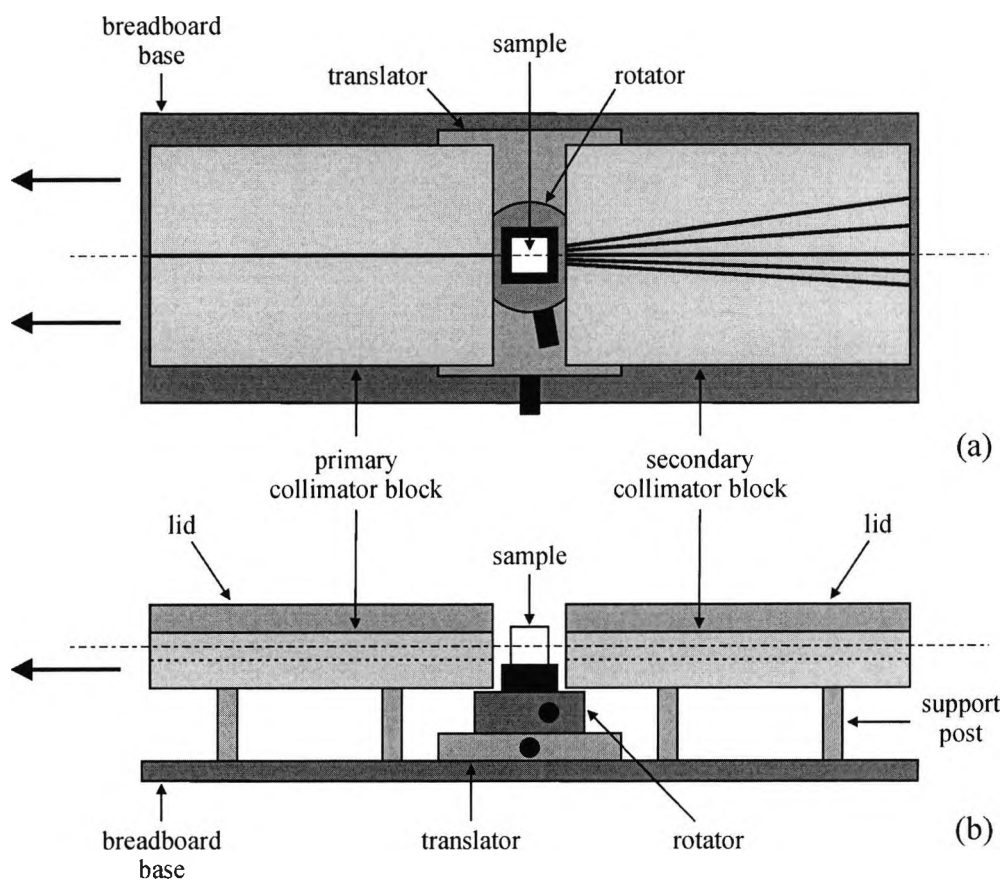


Figure 6-4. The fixed parameter EDXRD diffractometer assembly. The plan view (a) is pictured without lids to expose the collimation channels. Note the transmission channel in the secondary collimator block for attenuation correction measurements. The side elevation (b) shows the sample micro-translator (driven by a stepper motor) and micro-rotator (for fine adjustment). The three heavy arrows show the adjustment direction of the primary collimator block for sample space size adjustment, if required.

collimation blocks made from dural, mounted on a breadboard using steel support posts. In this way the whole assembly could be moved without disassembling the diffractometer and introducing errors on reassembly. In order to enclose the channels (to complete full collimation), plain dural lids were positioned above each block. A range of scattering angle channels were incorporated to increase the capability of the diffractometer, but the 6° scattering and 0° transmission channels were the only ones used for the remaining EDXRD experiments. Affixing lead shields blocked unwanted channels. The secondary block channels focused at a point 35 mm from the end of the

block. Technical drawings of both collimation blocks may be found in appendix B, section B.2.

Also mounted on the breadboard was the sample platform with a translator and rotator for initial sample positioning and translation during experimental measurement. The translator was driven using a stepper motor. The platform included guide locators to enable precise sample positioning.

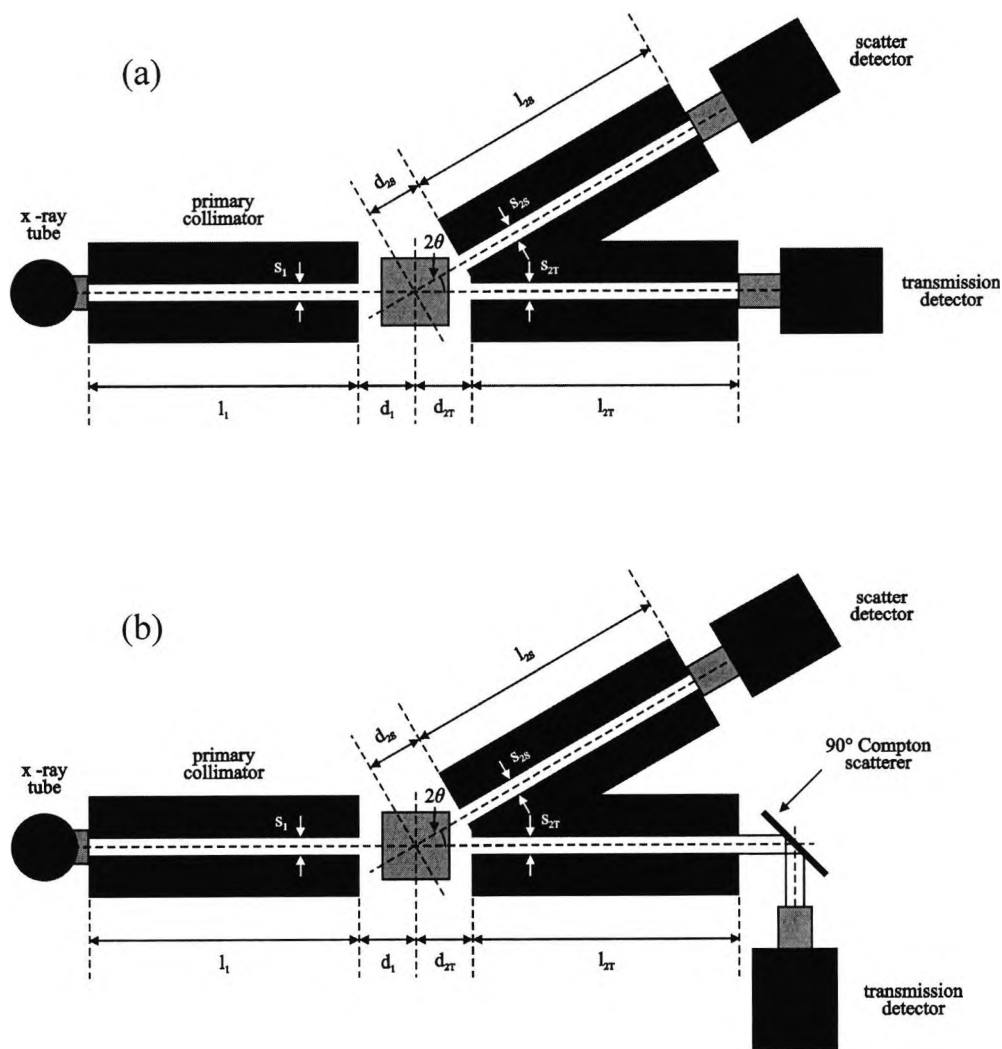


Figure 6-5. Parameters of the experimental EDXRD diffractometer (fixed version). The ideal configuration (a) would have the transmitted photons directly detected. However, due to saturation problems, the transmitted photons were detected after being 90° Compton scattered by 6 mm of Perspex positioned at 45° to the beam.

The whole assembly, aligned with the aid of a diode laser, was mounted on a laboratory optical table. A polyenergetic source of x-ray photons (the x-ray tube characterised in chapter two) was positioned at the primary collimation input (to the left of the figure) and a germanium detector (also characterised in chapter two) was positioned closely to the secondary collimation output (to the right of the figure). A dural shield, with additional lead shielding positioned at crucial points of the assembly, was used to reduce the level of unwanted photon scatter at the detector. The measured spectra were processed using a multichannel analyser.

A schematic of the EDXRD experiment (in two dimensions) shows the geometric parameters of the diffractometer (figure 6-5a), the values of which were used for the remainder of these experiments. The experimental scatter angle 2θ was 6° . The primary and secondary collimation channel lengths l_1 and l_{2T} were 300 mm and l_{2S} was 301.7 mm. The slit widths s_1 , s_{2T} and s_{2S} were 1.00 mm and slit heights h_1 , h_{2T} and h_{2S} were 10 mm. The sample centre to secondary channel distances d_1 and d_{2T} were 35.0 mm and d_{2S} was 35.2 mm. The secondary scattering channel length l_{2S} and distance d_{2S} were slightly longer due to the layout of the secondary block.

A problem was encountered that necessitated a variation to the technique described. With no sample or aluminium in place, the transmitted photon flux was too great for the detection system, which saturated and was unable to take measurements. This problem was overcome with the introduction of a Compton scattering medium at the output of the secondary collimation channel (figure 6-5b). 6 mm of Perspex was positioned at 45° to the transmission channel, allowing the detector to be positioned at 90° . The photon flux was reduced sufficiently for all transmission spectra to be recorded in this manner. Since all transmission spectra were recorded in this way, the attenuation per channel ratios were still valid. However, channel energy correction for Compton shift was required.

6.2 ASSESSING THE ATTENUATION CORRECTION TECHNIQUE

The attenuation correction method, described earlier in this chapter, uses ratios of a spectrum transmitted through the sample (and any additional attenuation) to a reference transmitted spectrum with no sample or additional attenuation in the photon beam path. The ratios, calculated for each energy channel, are then applied to the scattered spectrum photon counts to correct for attenuation effects.

This experiment was designed to evaluate the technique in order to ascertain its effectiveness.

Method

The fixed parameter EDXRD diffractometer was assembled according to the method described in section 6.1. X-ray source settings were set to 70 kV_p and 8 mA.

A single bone sample cube with a dry apparent density of 0.471 g/cm³ was located on the positioning device and left in place throughout the majority of this experiment. For both scattering and transmission spectra measurement, the sample was translated by 10 steps of 1 mm, the width of the total volume traversed being 10 mm. For the scattered spectra, the effect was to generate a spectrum from the sample EDXRD scattering volume (chapter three, section 3.1.1). A measurement of 200 seconds at each position was recorded, the final spectrum being an integral sum of photon counts from a total collection time of 2000 seconds.

EDXRD scattering spectra were collected with the sample alone in the first instance and then with increasing quantities of aluminium being positioned in the path of the primary beam. The thicknesses of aluminium added were 1.3 mm, 2.5 mm and 3.8 mm, respectively.

The transmission spectra were collected in the same way, again with the 0.471 g/cm³ sample in place, by positioning the detector at the 0° collimation output. The detector itself was positioned at 90° to this collimation channel, with 6 mm of Perspex at 45° as a Compton scattering medium (figure 6-5). Spectra were collected for the same attenuation conditions with a final transmission spectrum being recorded with no sample or aluminium in place. This spectrum forms the reference condition for no attenuation.

Results

The first data processing task necessitated correcting the energy scale of the transmitted spectra, which was shifted due to the Compton scattering method used to collect the data. Figure 6-6a shows an example of a transmitted spectrum as measured and after this correction. Equation 1.22 (chapter one) was rearranged to enable it to be used for this energy correction:

$$E_1 = \frac{E_2}{1 - \frac{E_2(1 - \cos\theta)}{511}} \quad [6.1]$$

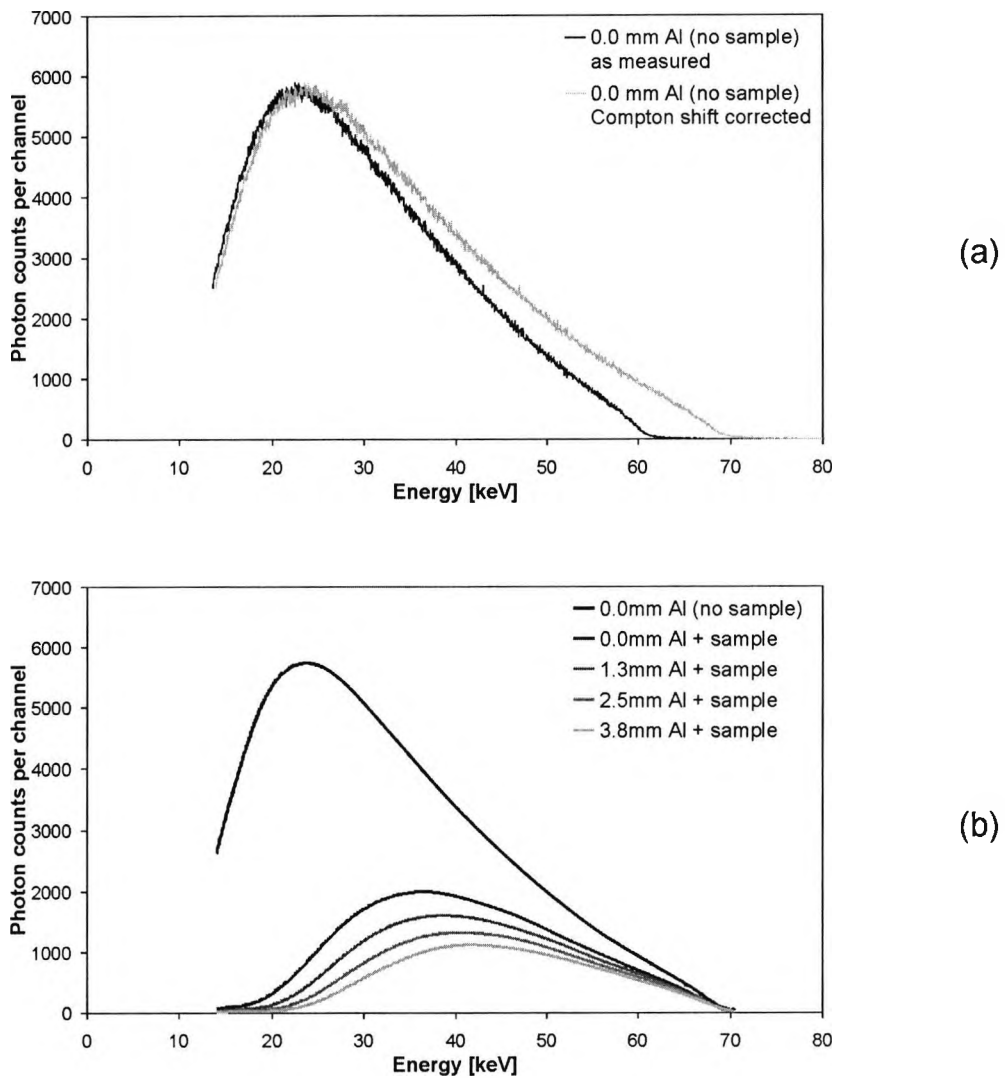


Figure 6-6. Transmitted spectra measured to correct for attenuation. Once measured, the Compton energy shift was corrected, one such example shown (a). The spectra were then fitted (using SPSS TableCurve, SPSS Inc.) and matched to the energy channel values of the scattered spectra (b). Note the progressive beam hardening.

where E_1 is the original energy before Compton shift (in keV), E_2 is the measured energy after Compton shift (also keV) and θ is the photon scattering angle. Since the photon scattering angle is set at 90° (twice the 45° Perspex angle), equation 6.1 becomes:

$$E_1 = \frac{E_2}{1 - E_2/511} \quad [6.2]$$

Equation 6.2 was used to correct the Compton shifted energy of each channel of the transmitted spectra.

After correcting for energy shift, the energy values of the transmitted spectra channels no longer matched those of the scattered spectra as calibrated (chapter two, section 2.2.1). In addition, despite a long collection time of 2000 seconds per spectrum (and therefore a relatively high mAs), the transmitted spectra were not sufficiently smooth to calculate attenuation ratios (figure 6-6a).

The second of these issues was addressed by fitting each transmitted spectrum with a function, using SPSS TableCurve 2D 5.0 (SPSS Inc.) software. TableCurve was allowed to select the function from its library that best fit the transmitted data, in terms of correlation coefficient R^2 .

The channel energy mismatch was addressed by preparing an M-file function for use with The MathWorks MatLab 6.1 software (appendix E, section E.2). The M-file function interpolated the image data (photon counts from the TableCurve fitted function) with respect to its arguments (channel energies) to form a new set of image data. In this

Attenuation Correction Procedure	Attenuation Condition				
	No Attenuation	Self Attenuation by the Sample	Sample Plus 1.3 mm Aluminium	Sample Plus 2.5 mm Aluminium	Sample Plus 3.8 mm Aluminium
Fully Correcting to the 'No Attenuation' Condition	•	• ←	• ←	• ←	• ←
Partially Correcting to the 'Self Attenuation' Condition		•	• ←	• ←	• ←

Table 6-1. Chart showing attenuation correction ratios calculated for this experiment. To correct for all attenuation (including by the sample material), the ratios (of each channel) of each transmitted spectrum to the transmitted spectrum with no attenuation were used. As part of the verification of this technique, the ratios of each transmitted spectrum to the transmitted spectrum with sample attenuation only were also generated.

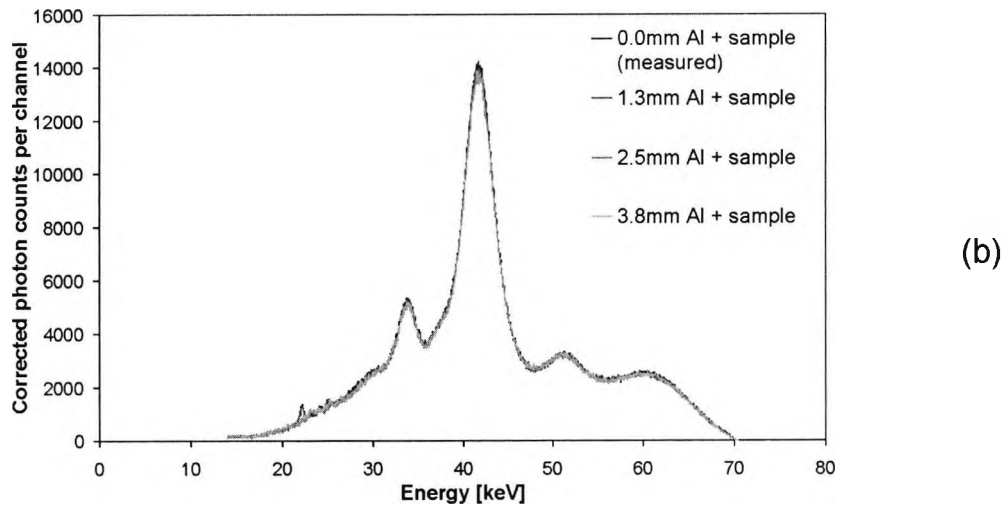
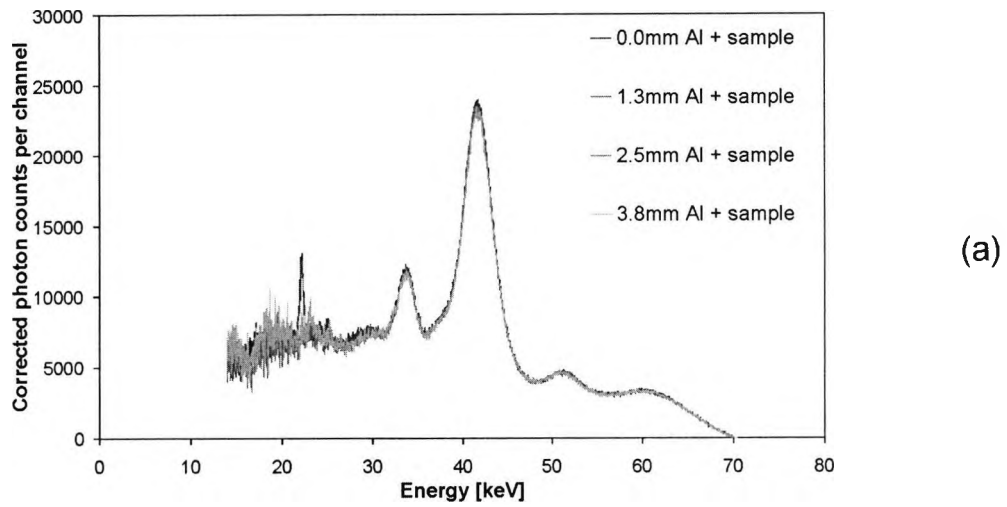


Figure 6-7. The EDXRD spectra as corrected for attenuation. The spectra were corrected for all attenuation, including that by the sample material (a) and for additional attenuation only (b). The latter correction allows direct comparison to a measured EDXRD spectrum.

way the fitted transmission spectra channel energy values were matched to those of the scattered spectra.

The attenuation correction ratios for each channel were calculated and applied to the corresponding measured EDXRD spectra (figure 6-2), as shown in table 6-1.

The most useful correction ratios were derived by calculating the ratio of each transmitted spectrum channel (for a given attenuation condition) with respect to the transmitted spectrum generated with no attenuating material in the beam path. These ratios corrected for all attenuation (including by the sample material) and was the method adopted throughout the remainder of this project (i.e. 'full correction').

Since a scattered spectrum could not be generated in the absence of sample material, these fully corrected spectra could not be compared with an EDXRD spectrum. As part of the verification of this technique, additional ratios were generated of each transmitted spectrum to the transmitted spectrum with sample attenuation only (table 6-1). This allowed the corrected scattered spectra to be compared to a measured EDXRD spectrum with no additional attenuation (i.e. 'partial correction').

The corrected EDXRD spectra from both sets of ratios ('fully corrected' for all attenuation (aluminium and sample) and 'partially corrected' for additional attenuation (aluminium) only) are presented in figure 6-7.

To evaluate the technique, first uncorrected attenuation effects were quantified. The total photon counts (between energies of 13.51 keV and 70.41 keV inclusive) of each uncorrected EDXRD spectrum with added attenuation were compared to that of the sample only (spectra shown in figure 6-2). It was found that 1.3 mm of aluminium reduced the count by 17.73 %, 2.5 mm reduced the count by 32.27 % and 3.8 mm by 42.90 %. The fully corrected spectra (figure 6-7a) were then compared in the same way, results shown in the third column of table 6-2. It was found that a significant improvement was obtained by using the correction technique.

For the spectra corrected for additional attenuation only, total photon count comparisons were made (between the same energies) to the measured EDXRD spectrum with no additional attenuation (figure 6-7b). The results are shown in the second column of table 6-2. Again a significant improvement is indicated but it should be noted that, since the correction ratios are significantly less, spectral noise is also less significant.

Conclusions

In terms of photon count area matching, the results shown in table 6-2 demonstrate that this technique provides a satisfactory method for attenuation correction under these conditions. For fully corrected spectra, total photon counts differ by less than 4%, as compared to the uncorrected spectra which, as expected, differ considerably.

Attenuation Condition	EDXRD Spectrum Total Photon Count Reduction [%]		
	Uncorrected Spectrum with Added Attn. c/w Measured Spectrum with No Added Attn.	Partially Corrected Spectrum with Added Attn. c/w Measured Spectrum with No Added Attn.	Fully Corrected Spectrum with Added Attn. c/w Fully Corrected Spectrum with No Added Attn.
Sample Plus 1.3 mm Aluminium	17.73	0.20	0.83
Sample Plus 2.5 mm Aluminium	32.27	1.97	3.79
Sample Plus 3.8 mm Aluminium	42.90	1.86	1.67

Table 6-2. Attenuation correction results expressed in terms of total spectrum photon count reduction. The first column shows the uncorrected reduction due to attenuation. The second column shows the improvement for partially corrected EDXRD spectra (to 'sample only' condition) as compared to a measured spectrum with no additional attenuation. The third column shows the improvement for fully corrected EDXRD spectra as compared to a fully corrected spectrum with no additional attenuation.

It should be noted that, due to lack of suitable equipment, the scattered and transmitted spectra were not measured simultaneously. The performance might be further improved if this were so, since, for example, both measurements would be subjected by the same degree to any photon flux variations. Simultaneous measurement would be essential in a clinical situation in order to minimise radiation dose to the patient.

There are some aspects of the technique that should be considered, especially if applying the method to clinical attenuation conditions (locations within a patient's body). An assumption was made concerning the photon path difference post scattering region, between the scattered 6° and transmitted 0° geometries. For these experiments, this difference was considered to be negligible, but it does affect these corrections to a certain degree. The path difference will become more significant for larger material volumes (figure 6-1c), increasing the likelihood of encountering regions with significant

density inconsistencies (figure 6-1b). The impact of this problem might be reduced by adopting the two source method employed by the Compton scattering densitometry techniques (chapter one, section 1.5.4), in which all photon pathways are considered when correcting for attenuation.

One other problem, most visible when correcting for all attenuation, is the amplification of scattering spectrum noise at the lower energies (figure 6-7a). This is due to the predominant attenuation of photons of lower comparative energy, resulting in a greater correction ratio. This is clearly illustrated by the transmission spectra of figure 6-6b. Fortunately the majority of photons coherently scattered by hydroxyapatite bone material appear at higher energies in the detected spectrum (the bone peaks in figure 6-7) and so the noise amplification problem is less significant. However the noise problem does impinge on the energy window occupied by the majority of photons scattered due to marrow material (not shown in the illustrations in this chapter but EDXRD marrow peaks may be seen in chapter one, figure 1-19). One method of analysing EDXRD bone + marrow spectra involves calculating the ratio between the bone and marrow photon count regions. The noise amplification may therefore introduce inaccuracies. This situation might be improved by fitting the EDXRD spectra before the ratio is taken, a method explored in chapter eight.

The attenuation correction technique is summarised as follows, MatLab M-files being listed in appendix E, section E.2:

1. Both scattered and transmitted experimental spectra were collected under the same attenuation conditions. An additional transmission spectrum reference (with no attenuation) was also measured. The transmitted spectra energies were corrected for Compton shift (using a MatLab M-file), a consequence of the spectrum collection method.
2. The spectra were fitted using TableCurve function fitting software to produce smooth transmission spectra. The results were collected together into one 'attenuation correction' file (MatLab M-file).
3. Transmitted spectra photon counts were interpolated to those corresponding to the channel energy values of the scattered EDXRD spectra (MatLab M-file). This was necessary since the Compton shift corrected channel energies no longer matched those of the EDXRD spectra.

4. The correction ratios for each channel were calculated and applied to the EDXRD spectra to correct for attenuation (MatLab M-file).

Part Two

STUDY

Chapter 7

EDXRD AND DEXA INVESTIGATION INTO ONE COMPONENT TRABECULAR BONE DENSITY MEASUREMENT

This and the following chapter describe the two major sets of EDXRD experiments, designed to test the method using techniques described in the previous chapters. DEXA experiments were performed for comparison.

Two bone sample conditions were investigated, one for each experiment set. The first featured EDXRD and DEXA bone density measurement using marrow free trabecular bone sample cubes, which enables demineralisation to be performed. This sample condition is referred to as a 'one component sample system'. This sample system does not resemble a clinical situation (i.e. the condition of bone within a living body) and so the methods described would only be employed in a laboratory environment. Investigations using samples such as prepared excised bone or archaeological specimens could be performed using these one component techniques.

The second sample condition featured density measurement using trabecular bone sample cubes with a marrow substitute reintroduced to the trabecular spaces. This sample condition bears closer resemblance to clinical situations and is referred to here as a 'two component sample system'. These experiments are described in chapter eight.

The review of bone in chapter one, section 1.1 reveals that dry, marrow free trabecular bone consists of more than one component. It could be considered to be a two component system, consisting of minerals and the protein matrix in which they are embedded. However, in order to retain sample structure for these measurements, the protein matrix and embedded minerals are not separated. In addition, at this stage it is not possible to separate the protein component from the mineral component of EDXRD bone spectra. The marrow free bone is therefore considered as one sample component.

This chapter comprises:

Section 7.1 A discussion of the EDXRD experiments using trabecular bone samples with no marrow (one component sample system). Absolute

(calibrated) and comparative (before and after demineralisation) results are presented.

Section 7.2 A discussion of the DEXA experiments using trabecular bone samples with no marrow (one component sample system). Absolute (calibrated) and comparative (before and after demineralisation) results are presented.

Section 7.3 A comparison of the EDXRD and DEXA results. Calibrated and comparative methods are considered.

7.1 EDXRD BONE DENSITY MEASUREMENTS USING A ONE COMPONENT SAMPLE SYSTEM

This first experiment set was designed to test the EDXRD diffractometer system capabilities with one component trabecular bone samples. An absolute density measurement method was adopted using samples with no marrow present in the trabecular spaces. The one component samples provided a more fundamental measurement and made it possible to take bone density measurements both before and after partial sample demineralisation. Thus a comparative method was also adopted to determine the limits of the method. Each set of measurements was repeated with additional attenuation to further test the method.

It was not possible to produce phantoms to calibrate the EDXRD diffractometer for one component sample system measurement. There is no medium to support the varying quantities of powdered bone necessary, unlike the two component bone + marrow calibration phantoms where marrow substitute was used to support the bone powder (chapter three, section 3.2). To partially overcome this problem, a reference set of 10 marrow free samples was measured for use as a calibration model. This situation is not ideal since there is less confidence in the physically measured bone density of the samples as there would be with specially prepared phantoms but this is the best method available.

Method

A set of 58 trabecular bone sample cubes ($15 \times 15 \times 15 \text{ mm}^3$) were cut from excised femoral heads and cleaned of marrow, as discussed in chapter five (sections 5.1 and 5.2).

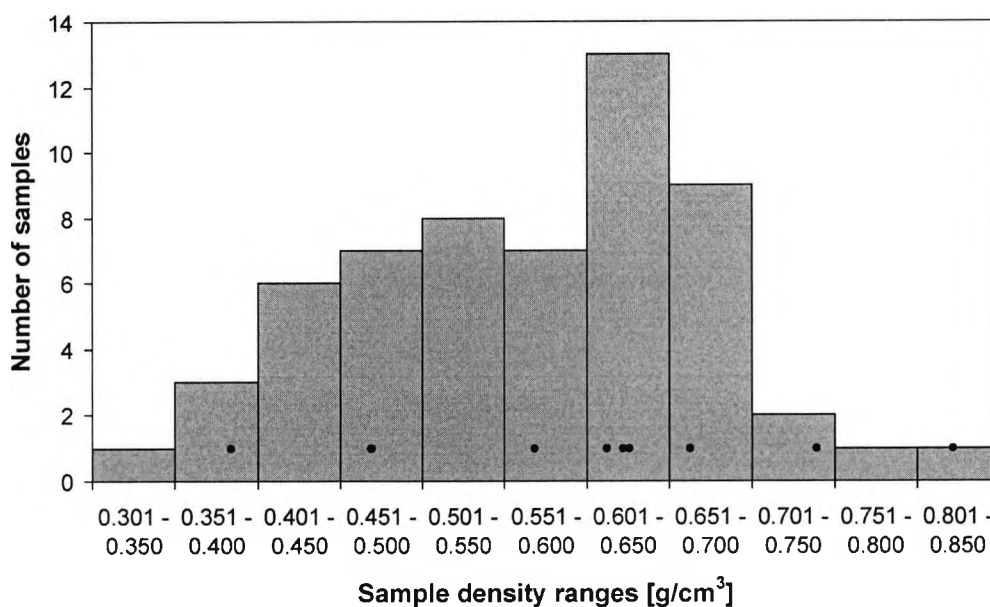


Figure 7-1. Histogram illustrating the density range and distribution of the 58 trabecular bone sample cube set. Each sample contributes a count to one of 11 density groups, each with a range of 0.050 g/cm^3 . The black points indicate densities of the 10 samples selected for the reference set (two samples share a density of 0.469 g/cm^3). The inequalities in the density distribution result from subtle volume differences since the reference set was chosen to have an even mass distribution.

They were sorted by dry mass order, from 1.10 to 2.70 g. Dry apparent densities of these samples ranged from 0.345 to 0.822 g/cm^3 , incorporating minor volume variations. It should be noted that the average apparent density of trabecular bone in a human body (being 0.389 g/cm^3 , calculated in chapter three, section 3.2), falls near the lower end of this range.

A reference set of 10 samples was selected from (approximately) evenly spaced mass intervals through the range. They were used throughout these final experiments and were not demineralised. The remaining 48 specimens formed a measurement set, which was used for these one component experiments and the compression investigation described in chapter ten. The spread of densities throughout the sample set is shown in figure 7-1, along with the densities of the reference set.

The fixed parameter EDXRD diffractometer was used in accordance with the method described in chapter six, section 6.1. The x-ray source was set to 70 kV_p and 8 mA throughout these experiments.

Each bone sample cube from both reference and measurement sets was located on the EDXRD positioning device and left in place for any repeat measurements performed. For both scattering and transmission spectra, the sample was translated by 10 steps of 1 mm, the width of the total volume traversed being 10 mm. In order to determine increasing system precision with total measurement time, spectra were recorded for a range of nine live time intervals, being 2, 5, 10, 20, 50, 100, 200, 500 and 1000 seconds. Each spectrum time consisted of equal data collection at each of the 10 sample positions, for example 20 seconds of data from each position for the 200 second spectra. An exception was made for the two and five second spectra as the system was unable to record for less than one second in a given position. These spectra were entirely generated from a central position.

Spectrum collection time was multiplied by the x-ray tube current in the final analysis, since this quantity (mAs) is related to photon flux (with a constant tube accelerating voltage, kV_p), and therefore radiation dose. This becomes more significant with the two component sample system, investigated with clinical situations in mind.

EDXRD scattering spectra were collected with the sample alone in the first instance and then with 2.5 mm of aluminium being positioned in the path of the primary beam. This was intended as an investigation into detrimental effects of additional attenuation to the method. For each of the reference set of 10 samples, 10 repeated spectra were measured to allow system precision to be determined. Calibration was also achieved using the reference set. One spectrum per sample was recorded for the measurement set.

Corresponding transmission spectra were collected in the same way, again with the sample in place, by positioning the detector at the 0° collimation output. Spectra were collected for the same attenuation conditions with a final transmission spectrum being recorded with no sample or aluminium in place. This spectrum forms the reference condition for no attenuation (chapter six, section 6.1 describes this and how detector saturation problems were overcome).

This collected set of data was sufficient for the first analysis (section 7.1.1), which investigated the effectiveness of ascertaining the bone densities of the measurement set from a calibration. A second analysis (section 7.1.2) was performed to determine the system capability of determining comparative bone density loss in the same samples. This necessitated further spectra collection after the measurement set samples were partially demineralised.

The measurement set samples were arranged in mass order and a demineralisation aim of between 1% and 10% assigned to the first 10 samples, then to the second 10, etc., until the whole set was assigned. This method spread the demineralisation range through the sample mass (subsequently density) range. The samples were demineralised as described in chapter five, section 5.3, using a 3.72% concentration of EDTA. Acid exposure time for the assigned demineralisation was estimated using formula 5.4 (from the curve shown in figure 5-2).

The actual degree of demineralisation was determined by comparing sample mass before and after this procedure was performed. Dry mass was measured by drying each sample in hot air until no further mass reduction occurred (measured to ± 0.005 grams using a Sartorius PT310 electronic balance). This procedure was necessary as it was found that the samples were increased in mass by up to 0.09 g by taking up water from air humidity. Pre- and post-demineralisation densities were calculated using these dry masses and cube dimensions measured using Vernier callipers.

Sample Set	Number of Experimental Conditions				
	Samples	Repeated Measurements	Spectra Recording Times	Attenuation Conditions	Total Spectra
Reference (for calibration and precision)	10	10	9	2	1800
Measurement pre-demineralisation	48	1	9	2	864
Measurement post-demineralisation	48	1	9	2	864
Total Spectra for All Variations					3528

Table 7-1. Summary of the number of experimental variations that each generated an EDXRD scattered spectrum. Corresponding transmission spectra were also measured for attenuation correction.

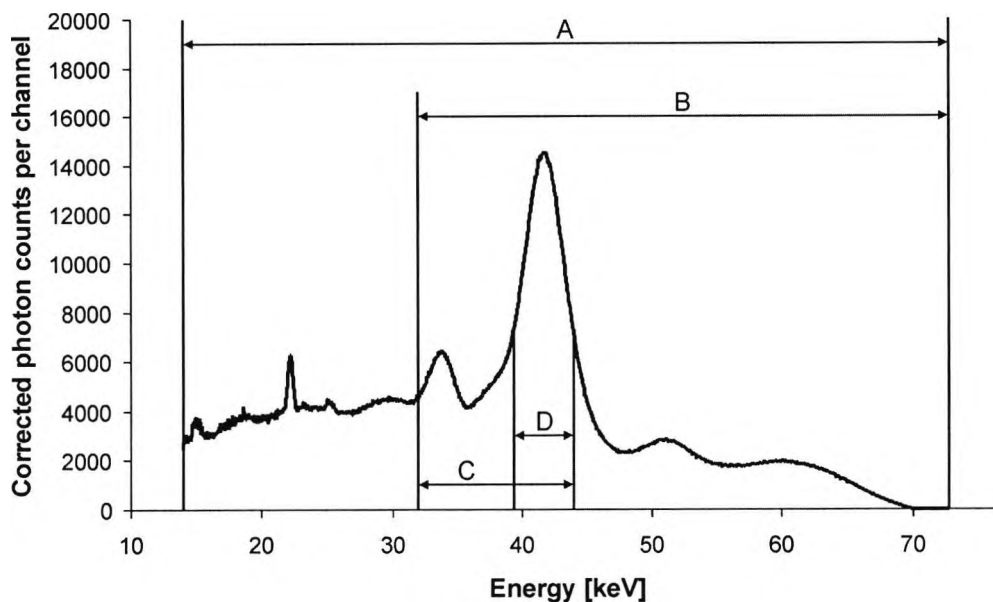


Figure 7-2. Example of a one component sample system EDXRD scattered spectrum, corrected for attenuation (each channel count is a mean of 10 measurements of 1000 seconds each). The marked regions are those chosen for examination to determine which offered the best for bone density information (with respect to variation between repeated spectra). The regions considered were the whole spectrum A (13.98 to 72.73 keV inclusive), the upper spectrum B (31.95 to 72.73 keV), the prominent bone peaks C (31.95 to 43.92 keV) and the main peak D (39.29 to 43.92 keV). The whole spectrum (A) was found to be most suitable.

A second set of post-demineralisation EDXRD scattered spectra and transmission spectra were recorded in the same way as described for the pre-demineralisation measurements.

The number of experimental variations is summarised in table 7-1.

It should be noted that one component sample system EDXRD analysis may suffer from an inability to normalise the spectra reliably. Two component spectra have distinct bone and marrow regions at different energy ranges (figure 1-19, chapter one). These spectra may be normalised (to unity or by using bone/marrow region ratios) to reduce the effects of photon flux variation between spectra, whilst still retaining bone density information. One component spectra are composed entirely of counts from photons scattered from bone material (figure 7-2). If these spectra are normalised, quantitative bone density

information would be lost. Since one component EDXRD spectra cannot be normalised, any results will be compromised to a certain degree by any photon flux variation.

7.1.1 Calibrated One Component EDXRD Analysis

This and the following section deal with the two analysis methods, being bone density calculation using a calibration model and comparative bone density loss calculation from demineralised samples. The first analysis deals with calibration.

Results

All the EDXRD spectra from the reference and pre-demineralisation measurement sets were corrected for attenuation using the method described in chapter six, section 6.2. The four stages of this method are summarised at the end of section 6.2.

The next task was to ascertain the most effective method of extracting bone density information from the corrected EDXRD spectra. Four energy regions from the 100 reference set spectra (10 repeats using 10 samples) measured for 1000 seconds with no additional attenuation (best case) were examined with respect to variations between repeats. Total corrected photon counts were taken from the regions illustrated in figure 7-2, being the whole spectrum, the upper spectrum, the prominent bone peaks and the main bone peak. For each of the samples, standard deviations were calculated for the regions using the 10 repeated EDXRD spectra. The best case (lowest standard deviation) for each sample was not consistent for the same region, so the mean standard deviation for each sample-region was calculated. The results, shown in table 7-2, suggest that

EDXRD Spectrum Range (see figure 7-2)	whole spectrum (A)	upper spectrum (B)	prominent bone peaks (C)	main bone peak (D)
Mean of Standard Deviations of Corrected Photon Counts [%]	0.411	0.534	0.512	0.561

Table 7-2. Variation between repeated measurements of attenuation corrected EDXRD scattered spectra photon count regions, expressed as standard deviations. The 10 sample reference set was used.

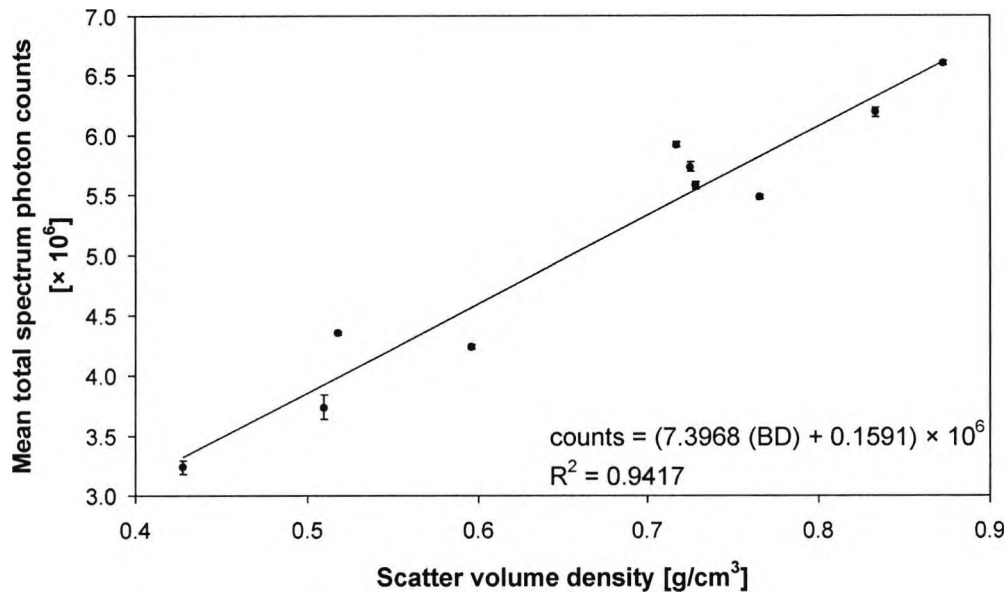


Figure 7-3. One component sample system calibration model. Each point represents the mean total spectrum photon count for a reference set sample (1000 seconds acquisition time, 8 mA tube current). Errors were derived from \pm two standard deviations. The linear regression fit may be rearranged (equation 7.1) to provide a calibration for the relationship between corrected EDXRD spectra photon counts and bone density (BD).

taking photon counts from the whole spectrum results in the least variation, so this value was adopted in the subsequent calculations.

A calibration model for all EDXRD spectra corrected for attenuation was generated using the 10 sample best case reference set measurements (no added attenuation, 1000 seconds acquisition time, 8 mA tube current). This calibration, shown in figure 7-3, was derived from a linear regression fit to the mean total spectrum photon counts of 10 repeated measurements for each sample. This fit was used to calculate all density measurements from one component trabecular bone EDXRD corrected total spectrum photon counts:

$$\text{apparent bone density} = \frac{\text{corrected photon counts} - 159111}{7396814} \quad [7.1]$$

for 10^3 seconds, no additional attenuation, standard x-ray tube conditions. The units of apparent bone density are in g/cm^3 .

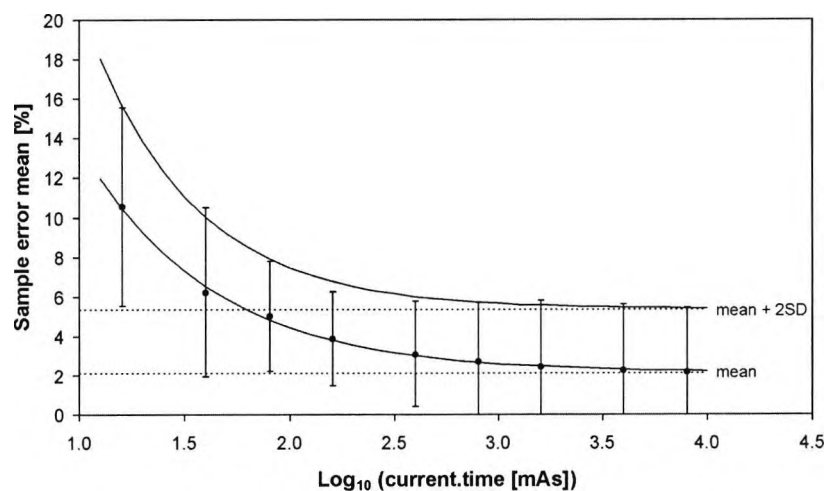
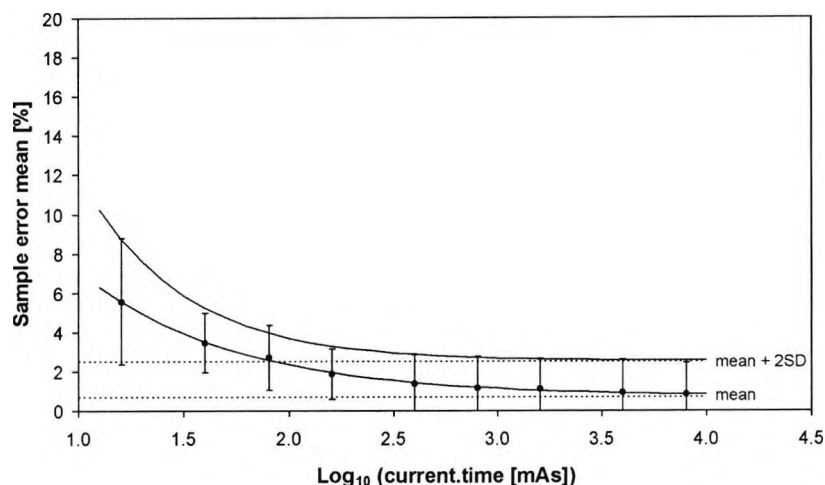


Figure 7-4. One component sample system errors as a function of \log_{10} (mAs). Plots are presented for the no added attenuation (a) and the 2.5 mm aluminium added attenuation (b) conditions. The points were calculated from the mean error of each reference sample set (10 samples). Errors were calculated from \pm two standard deviations of these errors. The exponential regression fits provide an indication of the ultimate minimum errors achievable if acquisition tube current \times time was sufficiently large.

The errors shown in figure 7-3 are derived from \pm two standard deviations of the 10 repeated spectra counts of each sample. As the figure demonstrates, this error was not found to be related to bone density so a generalised error for this sample condition (no added attenuation, 1000 seconds acquisition time, 8 mA tube current) was calculated by

Attenuation Condition	Error Fit	a [%]	b [(log mAs) ⁻¹]	c [%]
no added attenuation	mean + 2SD	78.103	2.104	2.538
	mean	25.494	1.382	0.728
2.5 mm aluminium	mean + 2SD	115.387	2.007	5.381
	mean	57.904	1.610	2.132

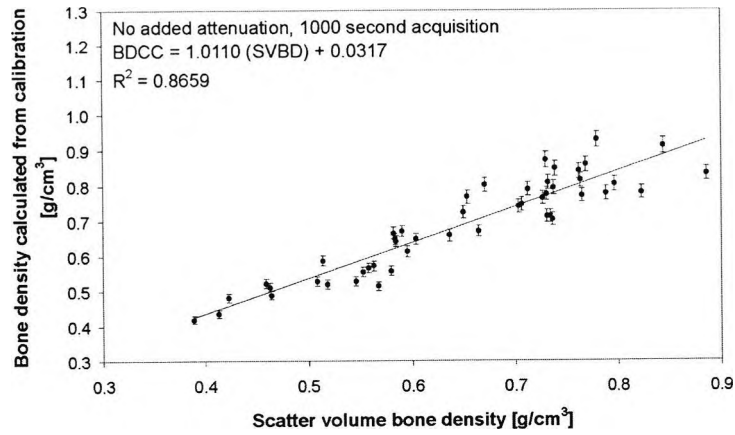
Table 7-3. Parameters for the one component sample system error fits, using equation 7.2.

taking the mean plus two standard deviations of the reference set errors. In the same way, a generalised error was calculated for each measurement condition using corresponding reference set measurements. The measurement conditions were two seconds to 1000 seconds acquisition time, 8 mA tube current, both for no added attenuation and added attenuation of 2.5 mm of aluminium).

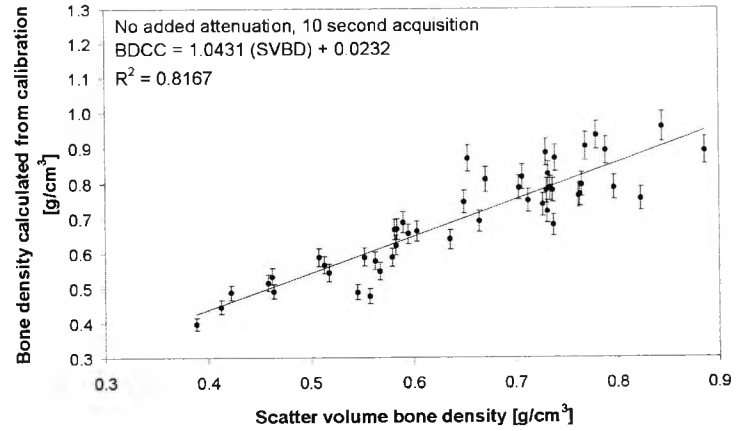
These generalised errors provide the method for calculating the precision (or minimum detectable limits) of the system across the sample range. Figure 7-4 shows plots of the generalised errors against tube current × time (mAs) after a back calculation was performed in order to express the precision in terms of a minimum detectable bone density change (as a percentage of density). A plot is provided for each attenuation condition.

An exponential function was fitted (using SPSS 8.0, SPSS Inc.) to each mean and mean plus two standard deviation trend:

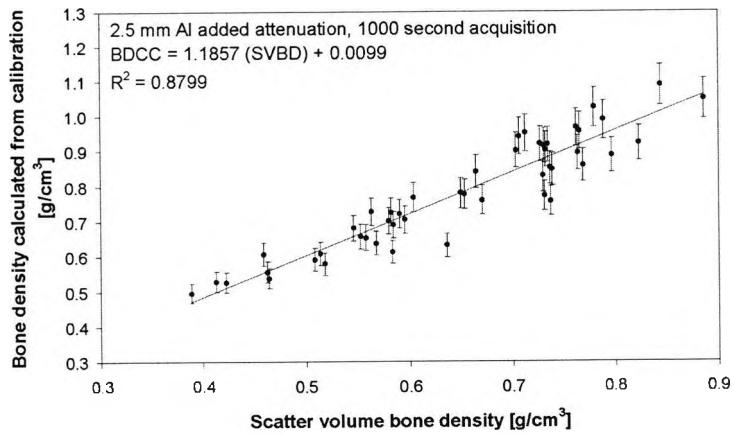
Figure 7-5 (following page). Examples of measured one component samples processed using the calibration formula (equation 7.1). Errors were derived from the generalised error calculations for each measurement condition using corresponding reference set measurements. The examples shown here are from the no added attenuation condition measured for 1000 seconds (a) and 10 seconds (b) and from the 2.5 mm added aluminium attenuation condition, again for 1000 seconds (c) and 10 seconds (d). The linear regression fits shown relate bone density calculated from the calibration (BDCC) to the scatter volume bone density (SVBD). Corresponding R² correlations are also shown.



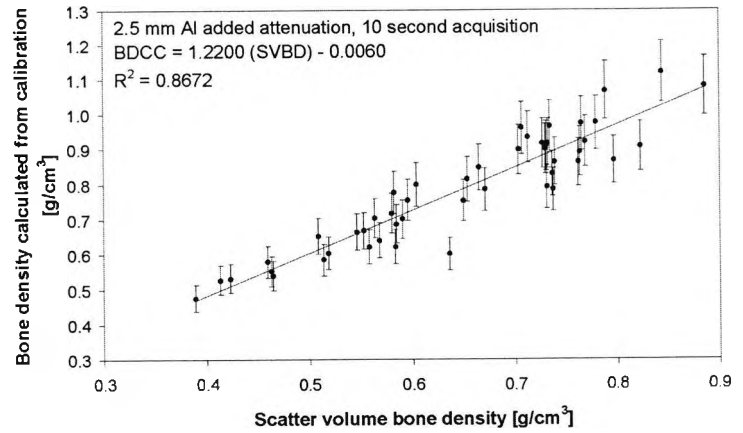
(a)



(b)



(c)



(d)

$$m_p = ae^{-b(\log \text{ mAs})} + c \quad [7.2]$$

where m_p is the sample error mean (or mean + two standard deviations) as a percentage, $\log \text{ mAs}$ is the \log_{10} of tube current \times time, and a , b and c are constants. The fitted constants are presented in table 7-3.

The bone density change minimum detectable resolution for a given mAs and attenuation condition is taken to be twice the generalised bone density error (see chapter four, section 4.1). Generalised errors are given in the first block of results in table 7-4.

The ultimate minimum errors achievable, if acquisition mAs was sufficiently large, may be estimated by taking the constant 'c' from each of the fits. These constants, illustrated by the dotted lines in figure 7-4, are the errors to which the exponential functions tend. For the condition with no additional attenuation, the mean error plus two standard deviations tend to 2.54%, giving a precision (minimum detectable bone density resolution) of 5.1%. For the added attenuation condition (2.5 mm of aluminium), the mean error plus two standard deviations tend to 5.38%, giving a precision of 10.8%.

An 'impressiveness factor' for precision (IF_p) for each acquisition mAs and attenuation condition (including the projected ultimate) was calculated:

$$IF_p = 1 - \left(2 \times \frac{\text{generalised bone density error}}{100} \right) \quad [7.3]$$

They are given in the first block of results in table 7-4, the intention being to be able to easily compare the effectiveness of each condition in terms of precision. The best case would yield an IF_p of 1.

The 48 sample measurement set total spectrum photon counts (corrected) were evaluated for each condition using the calibration formula (equation 7.1). Each of these sets of results were plotted against bone densities calculated using mass and volume measurements (chapter five, section 5.5). Errors were derived from the generalised error calculations for each measurement condition using corresponding reference set measurements. The plotted sets of results were regression fitted with a linear trend, resulting in a formula for each set:

$$\text{BDCC} = a (\text{SVBD}) + b \quad [7.4]$$

Attenuation Condition	Current × Time [mAs]	Log Current × Time [log mAs]	Sample Error % Mean	Sample Error % Mean +2SD	Precision IF _P	Linear ax+b Fit a	Linear ax+b Fit b	Accuracy IF _A	Linear ax+b Fit R ² (IF _C)	EDXRD IF
no added attenuation	16	1.20	5.56	8.78	0.8244	1.1044	0.0017	0.8939	0.8591	0.6331
	40	1.60	3.46	4.97	0.9005	1.0473	0.0231	0.9296	0.8225	0.6885
	80	1.90	2.70	4.34	0.9131	1.0431	0.0232	0.9337	0.8167	0.6963
	160	2.20	1.87	3.15	0.9371	1.0372	0.0245	0.9383	0.8639	0.7596
	400	2.60	1.38	2.84	0.9432	1.0251	0.0308	0.9441	0.8704	0.7751
	800	2.90	1.16	2.75	0.9451	1.0245	0.0300	0.9455	0.8688	0.7763
	1600	3.20	1.10	2.68	0.9465	1.0152	0.0330	0.9518	0.8698	0.7836
	4000	3.60	0.93	2.62	0.9477	1.0096	0.0334	0.9570	0.8674	0.7867
	8000	3.90	0.82	2.45	0.9510	1.0110	0.0317	0.9573	0.8659	0.7883
∞	∞	0.73	2.54	0.9492						
2.5 mm aluminium added attenuation	16	1.20	10.54	15.54	0.6891	1.3068	-0.0322	0.6610	0.7990	0.3640
	40	1.60	6.22	10.51	0.7897	1.1984	0.0123	0.7893	0.8637	0.5384
	80	1.90	5.02	7.81	0.8438	1.2200	-0.0060	0.7740	0.8672	0.5664
	160	2.20	3.87	6.27	0.8745	1.1822	0.0171	0.8007	0.8732	0.6114
	400	2.60	3.08	5.78	0.8844	1.1936	0.0117	0.7947	0.8712	0.6123
	800	2.90	2.69	5.70	0.8860	1.1918	0.0119	0.7963	0.8741	0.6167
	1600	3.20	2.45	5.83	0.8834	1.1939	0.0099	0.7962	0.8764	0.6164
	4000	3.60	2.27	5.63	0.8874	1.1865	0.0098	0.8037	0.8771	0.6256
	8000	3.90	2.18	5.45	0.8909	1.1857	0.0099	0.8044	0.8799	0.6306
∞	∞	2.13	5.38	0.8924						

Table 7-4. Results from the EDXRD one component sample system calibrated experiments. They are divided into three blocks, being error results from repeatability (leading to a precision impressiveness factor, IF_P), linear regression fit parameters (leading to an accuracy impressiveness factor, IF_A), and linear regression fit correlation results (leading to a correlation impressiveness factor, IF_C). Repeatability errors are derived from the mean of reference set errors (first column in the block) plus two standard deviations (SD) (second column). These errors are also projected for an infinite measurement time. The final column combines the results into an all-inclusive EDXRD IF.

where BDCC is the bone density calculated from spectra count calibration, SVBD is the scatter volume bone density calculated from mass and volume, and a and b are the linear fit parameters (gradient and intercept), given in the second block of results in table 7-4. Selected examples of these plots are shown in figure 7-5.

The a and b parameters of each fit were used to calculate an impressiveness factor for accuracy (IF_A):

$$IF_A = 1 - (|1 - a| + |b|) \quad [7.5]$$

They are given in the second block of results in table 7-4. The best case would yield an IF_A of 1.

Each linear regression fit has a corresponding Pearson correlation coefficient (R^2), given in the third block of results in table 7-4. This is also taken to be an impressiveness factor for correlation (IF_C), without further treatment. Again, the best case would yield an IF_C of 1.

An indication of overall one component EDXRD capability, with respect to precision, accuracy and correlation, may be obtained by combining the three impressiveness

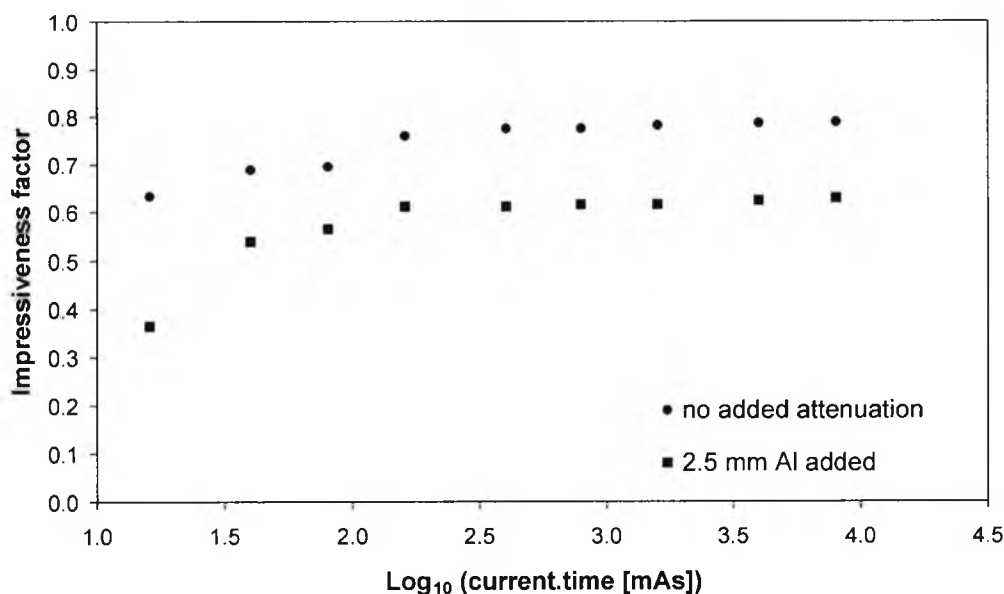


Figure 7-6. One component EDXRD impressiveness factors (IF). The IF, shown for both attenuation conditions, improves as acquisition mAs (and therefore photons detected) increases.

factors thus:

$$IF = IF_p \times IF_A \times IF_C \quad [7.6]$$

The final EDXRD IFs are given in the final results column in table 7-4. They are shown diagrammatically in figure 7-6.

In summary, the maximum precision (minimum detectable resolution) achieved was a bone density change of 4.9% (bone density error of $\pm 2.45\%$), with an R^2 value of 0.8659. These results, with an accuracy impressiveness factor (IF_A) of 0.9573, combine to an overall EDXRD IF of 0.7883. Precision was projected to a baseline of 5.1%, if acquisition mAs was sufficiently large. This suggests system limits have been reached with the 4.9% maximum.

The additional attenuation degraded precision to 10.9% (bone density error of $\pm 5.45\%$), with an R^2 value of 0.8044. These results, with an accuracy impressiveness factor (IF_A) of 0.8044, combine to an overall EDXRD IF of 0.6306. Precision was projected to a baseline of 10.8%.

Conclusions

General problems with the one component EDXRD system as a whole include the inability to apply normalisation (discussed in the method part of section 7.1) and the calibration model, which may suffer from being acquired using trabecular bone samples rather than phantoms with homogeneous bone densities. However the calibration R^2 correlation coefficient of 0.9417 is not unreasonable and is comparable to the correlation coefficients from the phantom based models described in chapter eight (for example, an R^2 of 0.9585 for the bone/marrow ratio model of section 8.1.1).

With reference to table 7-4, it can be seen that one component EDXRD precision, accuracy and correlation all tend to improve with increasing measurement tube current \times time, as expected. This would be at the cost of increased radiation dose if used in a two component sample system clinical environment. However, one component trabecular bone density measurement would usually be applied in laboratory environments as an investigative tool, so radiation dose is not an issue.

The performance of precision (IF_p) and accuracy (IF_A) is reduced with the addition of 2.5 mm of aluminium attenuation. The reduction in precision is likely to be predominantly due to the decrease in photon counts and therefore an increase in

statistical variation. This will also be a factor in the reduction of accuracy, along with the increased loss of low energy photons from the spectra (from the filtering effect of the additional attenuation). The attenuation correction procedure cannot accurately recover all attenuated photon counts, especially at these lower energies, and will therefore affect the match to the calibration. Correlation performance (IF_C) is marginally increased.

7.1.2 Demineralised One Component EDXRD Analysis

The work in this section tests the EDXRD one component system performance in a practical setting, comparing sample measurements made before and after partial demineralisation. In other words, it examines the system ability to distinguish levels of bone mineral loss. The method of demineralisation and data collection is discussed in the method part of section 7.1.

Results

The post-demineralisation sample EDXRD data was processed in the same way as for the pre- demineralisation data, using the calibration method described in section 7.1.1. This resulted in 48 pairs of EDXRD bone density results (pre- and post-demineralisation) for each measurement condition, with corresponding errors. The measurement conditions were two seconds to 1000 seconds acquisition time, 8 mA tube current, both for no added attenuation and added attenuation of 2.5 mm of aluminium.

Sample density reduction was calculated by taking the difference between pre- and post-demineralisation measured mass as a percentage of pre-demineralisation mass. It was reasonable to equate density reduction with mass reduction since sample volume did not change significantly for these small levels of demineralisation. EDXRD density reduction was calculated in the same way, using densities calculated from the calibration (equation 7.1).

EDXRD density reduction was plotted against measured density reduction for each measurement condition. The resultant best case condition (no added attenuation, 1000 second acquisition time, 8 mA tube current) scatter plot is shown in figure 7-7. In order to highlight the results, errors are not shown for this plot.

For confident discrimination between pre-and post demineralisation sample densities, errors must be considered. For each sample of each measurement condition, errors were

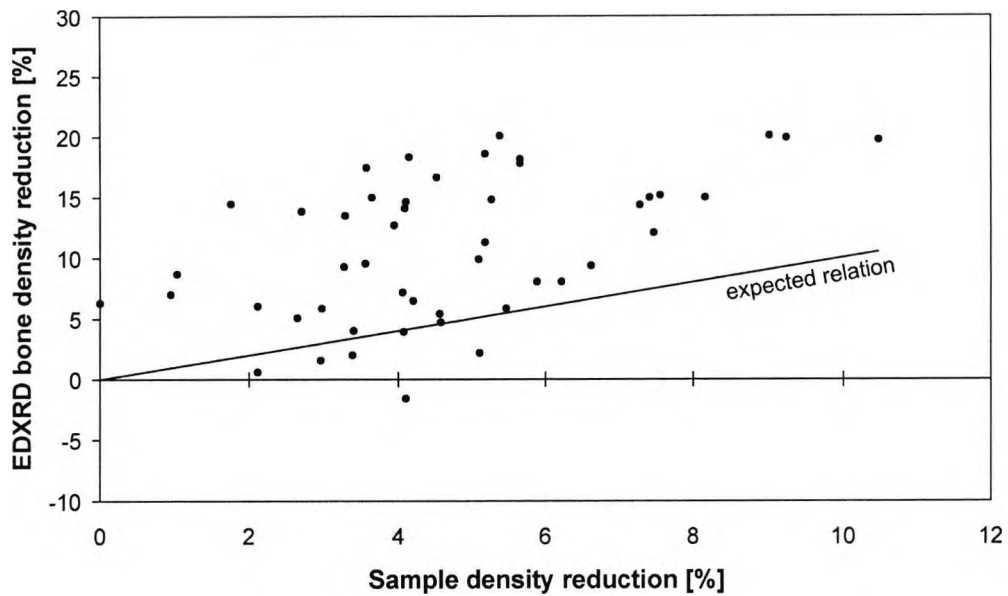


Figure 7-7. Example scatter plot of one component EDXRD bone density reduction measurements (no added attenuation, 1000 second acquisition time, 8 mA tube current). Errors are not shown for clarity (c/w figure 7-8a).

calculated by first taking the pre- and post- errors as a percentage of sample density. They were evaluated as bone density (BD) values in the following way:

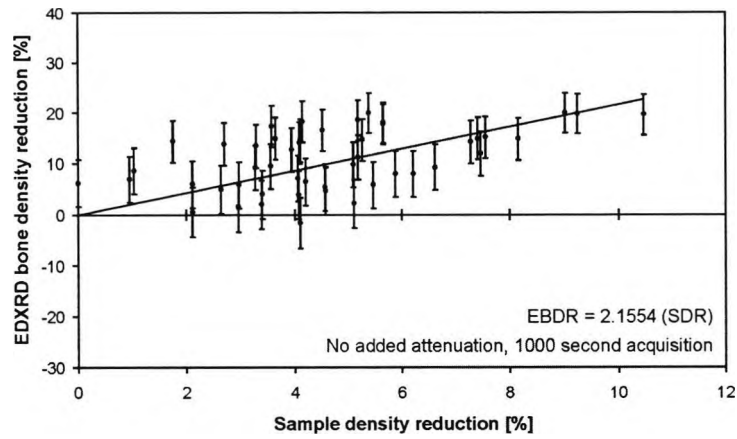
$$BD_{\text{maximum}} = BD \times (1 + BD_{\% \text{ error}})$$

$$BD_{\text{minimum}} = BD \times (1 - BD_{\% \text{ error}}) \quad [7.7]$$

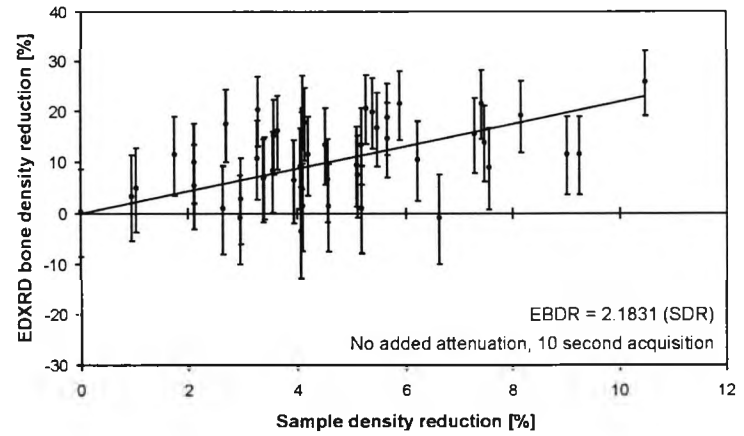
These bone density extremes were translated into pre- and post-demineralisation errors by calculating best and worst case EDXRD percentage density reduction (PDR):

$$PDR_{\text{best case}} = 100 \times \left(1 - \frac{BD_{\text{minimum, post-demin}}}{BD_{\text{maximum, pre-demin}}} \right)$$

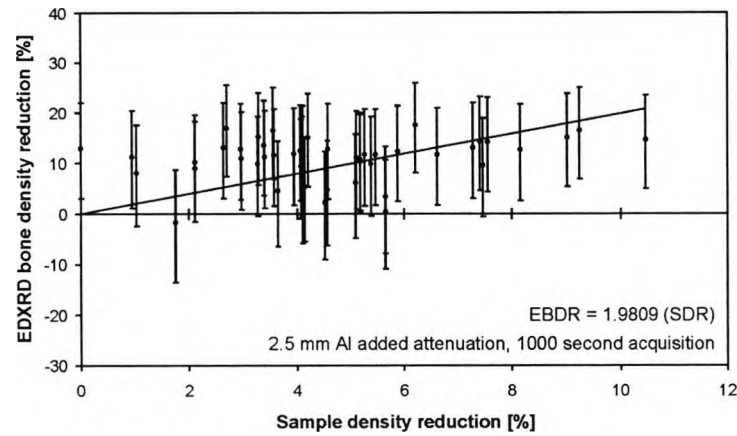
$$PDR_{\text{worst case}} = 100 \times \left(1 - \frac{BD_{\text{maximum, post-demin}}}{BD_{\text{minimum, pre-demin}}} \right) \quad [7.8]$$



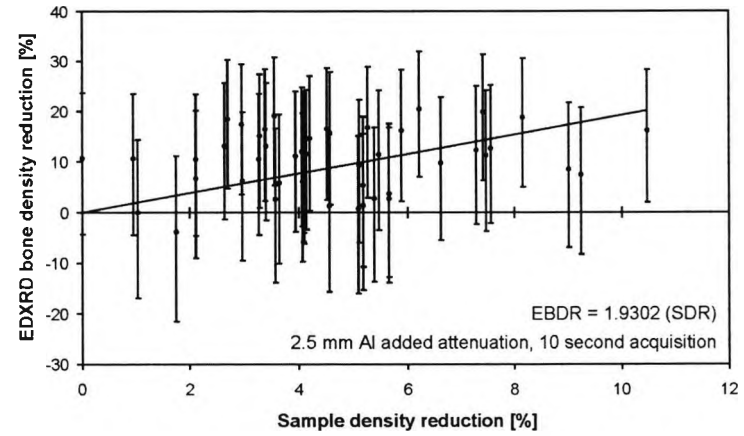
(a)



(b)



(c)



(d)

Attenuation Condition	Current × Time [mAs]	Log Current × Time [log mAs]	Density Reduction Detection Failure Maximum [%]	Density Reduction Detection Failure Mean [%]	Density Reduction Detection Failure Mean+2SD [%]
no added attenuation	16	1.20	9.2	4.2	8.6
	40	1.60	6.6	3.8	7.0
	80	1.90	6.6	3.4	6.8
	160	2.20	6.6	3.3	7.1
	400	2.60	5.1	3.6	5.7
	800	2.90	5.1	3.5	5.5
	1600	3.20	5.1	3.5	5.4
	4000	3.60	5.1	3.6	5.5
2.5 mm aluminium added attenuation	8000	3.90	5.1	3.7	5.6
	16	1.20	10.5	4.6	9.1
	40	1.60	10.5	4.6	9.3
	80	1.90	9.2	4.4	8.7
	160	2.20	5.7	3.9	6.8
	400	2.60	7.5	4.3	7.4
	800	2.90	7.5	4.2	7.5
	1600	3.20	7.5	4.0	7.3
4000	3.60	7.5	4.1	7.2	
8000	3.90	7.5	7.5	4.0	7.3

Table 7-5. Results from the EDXRD one component sample system demineralisation experiments. The maximum, mean and mean plus two standard deviations of measured density reduction that cannot be distinguished by the system are shown.

$PDR_{\text{best case}}$ and $PDR_{\text{worst case}}$ form the upper and lower error limits respectively for each EDXRD density reduction point in the scatter plot examples of figure 7-8. In order that discrimination between pre- and post demineralisation sample densities is confident, the

Figure 7-8 (previous page). Example scatter plots of one component EDXRD bone density reduction measurements, generated in the same manner as figure 7-7. The examples shown here are from the no added attenuation condition, measured for 1000 seconds (a, also figure 7-7) and 10 seconds (b), and from the 2.5 mm added aluminium attenuation condition, again for 1000 seconds (c) and 10 seconds (d). The calculation of errors is described in the text. The regression fitted linear trend lines relate EDXRD bone density reduction (EBDR) to measured sample density reduction (SDR).

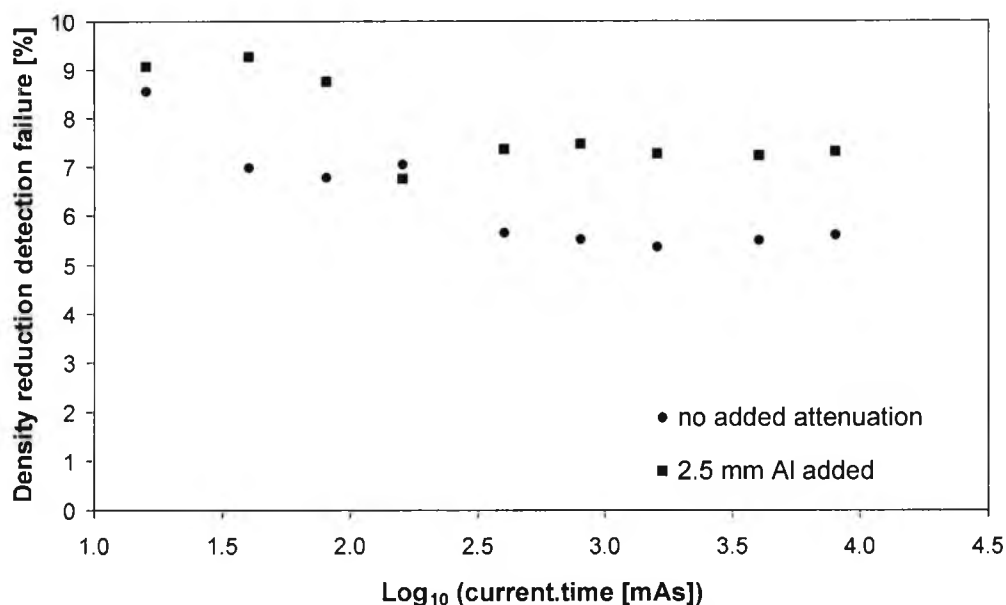


Figure 7-9. Density reduction detection failure points for each measurement condition. The failure points were calculated by taking the mean plus two standard deviations of all failure points.

lower error limit (or $PDR_{\text{worst case}}$) of a point must be greater than zero.

Regression fitted linear trends were fitted to the scatter plot data.

For each measurement condition, a detection failure point was determined, being the greatest measured sample density reduction that cannot be distinguished by EDXRD (i.e. $PDR_{\text{worst case}} \leq 0$). In order to reduce the effect of anomalies due to measurement inaccuracy, failure points were recalculated by taking the mean plus two standard deviations of all failures for each condition. These results are summarised in table 7-5 and presented in figure 7-9.

In summary, the best case (no added attenuation, 1000 second acquisition time, 8 mA tube current) failure point was found to be at a bone density reduction of 5.6%. The additional attenuation degraded the failure point to a bone density reduction of 7.3%.

Conclusions

The failure point of 5.6% for the condition with no added attenuation compares well with the maximum system precision of 4.9% found from the calibration results (section

7.1.1). The additional attenuation failure point of 7.3% is less than the maximum system precision of 10.9% (section 7.1.1).

The linear trends regression fitted to the scatter plot data would ideally show a relationship of unity between EDXRD bone density reduction and measured density reduction. The fact it is not highlights the limitations of the method. However the relationships are relatively consistent for each condition.

This test inevitably suffers from the extra error components introduced, namely from physically measured sample density reduction and the fact that two sets of EDXRD measurements are compared, each with their own errors. With this in mind, these results should not be considered conclusive. The original system limit results from section 7.1.1 are a more accurate reflection of the ability of this EDXRD method for these one component samples. However the results of these demineralisation experiments are of similar order to those of the first experiments and therefore do provide further confidence in the conclusions of section 7.1.1.

7.2 DEXA BONE DENSITY MEASUREMENTS USING A ONE COMPONENT SAMPLE SYSTEM

These DEXA experiments were performed using the same one component trabecular bone sample sets that were used for the EDXRD experiments. They were intended to provide a comparison for the EDXRD results. DEXA measurements were obtained using the 10 sample reference set and the 48 sample measurement set, again both before and after demineralisation. Each set of measurements was repeated with additional attenuation to further test the method.

Method

DEXA measurements were obtained using the same method as described in chapter four, section 4.2, with the following minor variations. The surrounding soft tissue equivalent was 2×10 mm Perspex slabs and the additional attenuation was, when used, was 3.0 mm of aluminium and 10.0 mm of Perspex (simulating cortical bone and soft tissue). This did not match the additional attenuation of the EDXRD experiments but was intended to approach a more clinical condition at which DEXA was designed to operate.

Figure 7-10 shows how additional attenuation was employed for all the DEXA

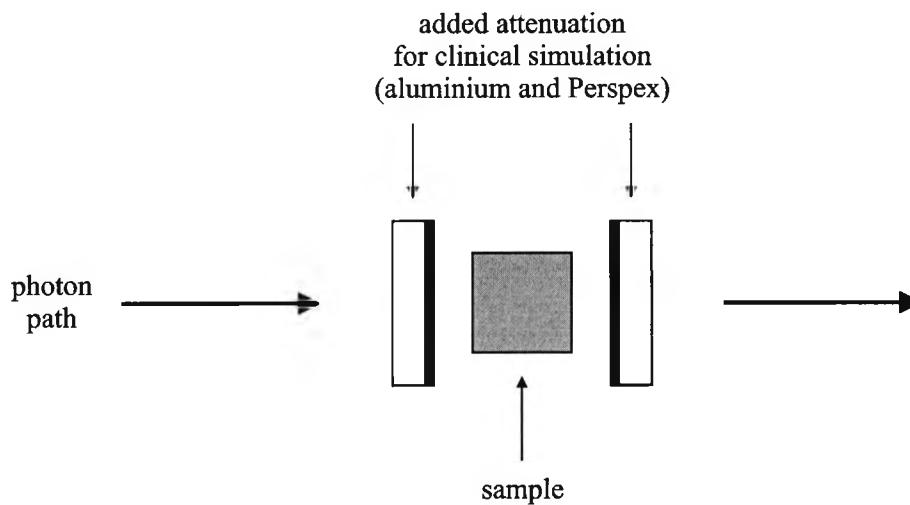


Figure 7-10. Configuration of trabecular bone sample and added attenuation (when used) for the DEXA experiments in this chapter. The aluminium and Perspex combination simulates cortical bone and soft tissue.

experiments described in this chapter. The attenuation was split into two sets of 1.5 mm of aluminium and 5.0 mm of Perspex, before and after the bone sample. Additional aluminium for legal filtration (required in the clinical environment) was not used since the DEXA machine has this in place at its photon source (c/w chapter eight).

The dual x-ray source was fixed at 100 and 140 kV_p and 2.5 mA by the DEXA machine throughout these experiments. Two scan settings were used, being fast array and high definition. High definition scans the order of four times as many lines as fast array.

Each bone sample cube from both reference and measurement sets was located on the patient table and left in place for any repeat measurements performed. Samples were orientated so the DEXA photon beam passed through the same cube faces as the EDXRD photon beam in the previous experiments.

DEXA scans were performed with the samples alone in the first instance and then with the additional attenuation being positioned in the path of the primary beam. For the reference set of 10 samples, 10 repeated scans were measured to allow system precision to be determined. One spectrum per sample was recorded for the measurement set, both before and after demineralisation.

The number of experimental variations is summarised in table 7-6.

Sample Set	Number of Experimental Conditions				
	Samples	Repeated Measurements	Scan Settings	Attenuation Conditions	Total Scans
Reference (for calibration and precision)	10	10	2	2	400
Measurement pre-demineralisation	48	1	2	2	192
Measurement post-demineralisation	48	1	2	2	192
Total Scans for All Variations					784

Table 7-6. Summary of the number of experimental variations used to generate DEXA scans. The two scan settings were fast array and high definition.

7.2.1 Calibrated One Component DEXA Analysis

This and the following section deal with the two analyses equivalent to those of EDXRD (section 7.1), being bone density assessment of pre-demineralised samples only and comparative bone density loss assessment using demineralised samples.

Results

As for EDXRD, the repeated measurements using the reference set provided a means to calculate expected error and therefore system precision. Four measurement conditions were investigated, being all combinations of fast array and high definition scanning and no added attenuation and additional attenuation in the DEXA beam path. Errors were derived from \pm two standard deviations of the 10 repeated DEXA bone mineral density results for each sample. A generalised error for each measurement condition was calculated by taking the mean plus two standard deviations of the reference set errors.

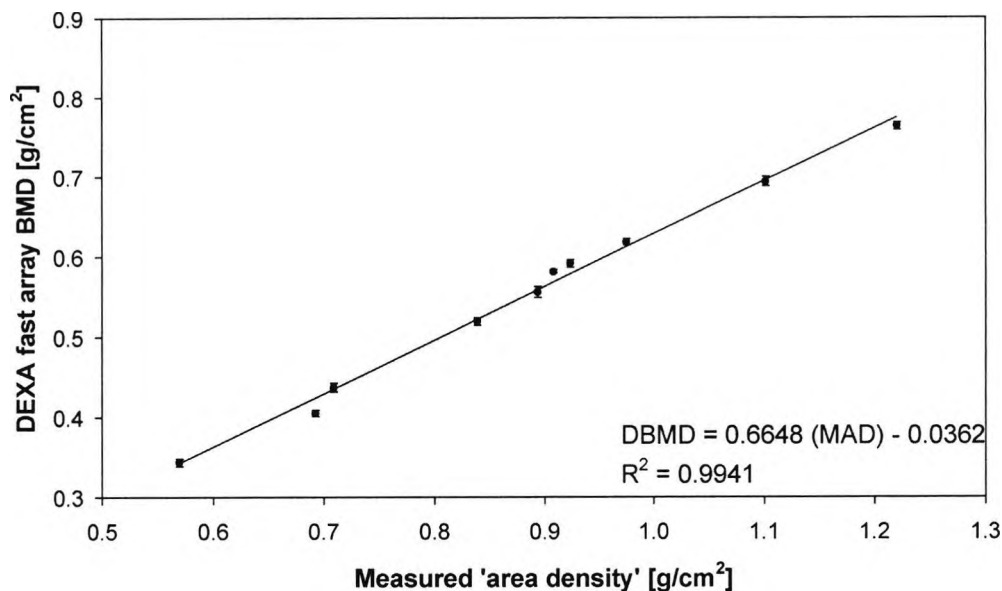


Figure 7-11. Example of DEXA reference set measurements. Each point represents the mean of 10 repeated DEXA scans using a reference set sample. This example was generated using the Hologic QDR 4500 fast array scan. Errors were derived from \pm two standard deviations. The linear regression fit shows the relationship between the DEXA bone mineral density (DBMD) values and sample measured 'area density' (MAD), converted to g/cm^2 since DEXA reports bone density with reference to area rather than volume.

Figure 7-11 presents an example of DEXA reference set measurements plotted against sample 'area density', calculated using physically measured mass and area. The discussion in chapter one (section 1.3) explains that DEXA reports bone density with reference to area rather than volume (as 'bone mineral density' (BMD) in g/cm^2). This is because DEXA is based on transmitted x-ray photon attenuation and therefore does not have the ability to determine measurement volume depth.

Bone density change minimum detectable resolution (or precision) for a given attenuation condition is taken to be twice the generalised bone density error. An impressiveness factor for precision (IF_p) for each DEXA scan setting and attenuation condition was calculated using equation 7.3. Generalised errors and IF_p s are given in the first block of results in table 7-7.

The 48 sample measurement set DEXA results were plotted against bone 'area densities' calculated using mass and area measurements directly from the samples. Errors were derived from the generalised error calculations for each measurement condition using

corresponding reference set measurements. The plotted sets of results were regression fitted with a linear trend, resulting in a formula for each set:

$$\text{DBMD} = a (\text{MAD}) + b \quad [7.9]$$

where DBMD is the DEXA BMD measurement, MAD is the measured area density calculated from mass and area, and a and b are the linear fit parameters (gradient and intercept), given in the second block of results in table 7-7. These DEXA plots are shown in figure 7-12. The DEXA BMD measurements shift up with added attenuation since the technique measures all bone material in the photon beam path. The added attenuation is therefore included in the DEXA measurement.

The a and b parameters of each fit were used with equation 7.5 to calculate an impressiveness factor for accuracy (IF_A). Fit parameters and IF_A s are given in the second block of results in table 7-7.

Each linear regression fit has a corresponding Pearson correlation coefficient (R^2), given in the third block of results in table 7-7. This is also taken to be an impressiveness factor for correlation (IF_C) without further treatment.

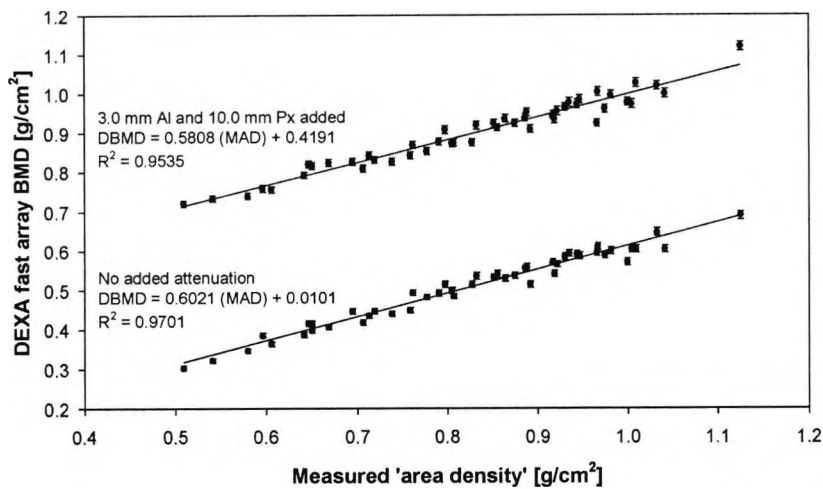
An indication of overall one component DEXA capability, with respect to precision, accuracy and correlation, was obtained by combining the three impressiveness factors (equation 7.6). They are given as DEXA IFs in the final results column in table 7-7.

In summary, the maximum precision (minimum detectable resolution) achieved was a bone density change of 3.0% for both fast array (bone density error of $\pm 1.51\%$) and high definition (bone density error of $\pm 1.49\%$). R^2 values were 0.9701 (fast array) and 0.9797 (high definition).

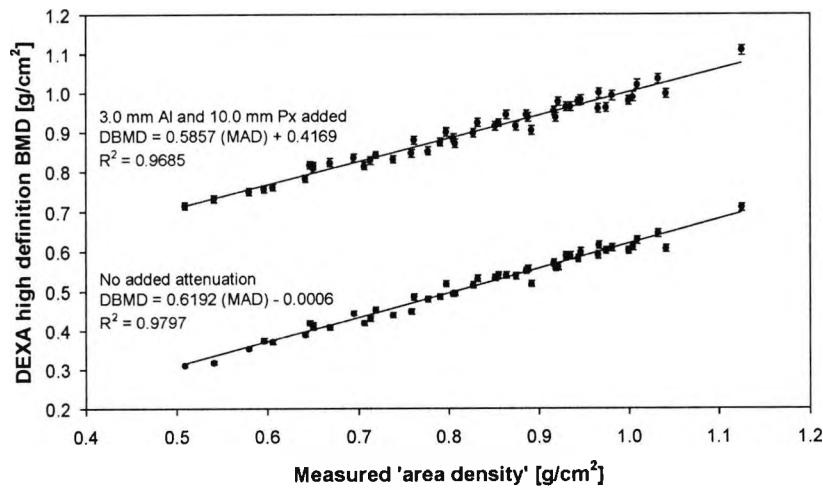
The additional attenuation simulating a clinical situation improved precision to 2.1% for fast array (bone density error of $\pm 1.06\%$) and 2.4% for high definition (bone density error of $\pm 1.18\%$). R^2 values were 0.9535 (fast array) and 0.9685 (high definition).

Conclusions

With reference to table 7-7, it is clear that precision (IF_P) is improved with the addition of attenuation for clinical simulation. The marginal deterioration of correlation (IF_C) has a small effect on the expected accuracy of any individually measured sample but, in general, this too is impressive.



(a)



(b)

Figure 7-12. DEXA measurement one component sample set results. Errors were derived from the generalised error calculations for each measurement condition using corresponding reference set measurements. The results were generated using the DEXA fast array (a) and high definition (b) scan settings. Each plot shows results from the no added attenuation and the 3.0 mm aluminium and 10.0 mm Perspex added attenuation conditions. Note how the DEXA BMD values shift up with increasing attenuation. The linear regression fits are shown relating DEXA bone mineral density (DBMD) to the measured 'area density' (MAD). Corresponding R² correlations are also shown.

Attenuation Condition	DEXA Scan Setting	Sample Error % Mean	Sample Error % Mean +2SD	Precision IF_P	Linear $ax+b$ Fit a	Linear $ax+b$ Fit b	Accuracy IF_A	Linear $ax+b$ Fit R^2 (IF_C)	DEXA IF
no added attenuation	fast array	0.90	1.51	0.9699	0.6021	0.0101	0.5920	0.9701	0.5570
	high definition	0.84	1.49	0.9703	0.6192	-0.0006	0.6186	0.9797	0.5880
3.0 mm aluminium and 10.0 mm Perspex	fast array	0.64	1.06	0.9789	0.5808	0.4191	0.1617	0.9535	0.1509
	high definition	0.67	1.18	0.9764	0.5857	0.4169	0.1688	0.9685	0.1596

Table 7-7. Results from the DEXA one component sample system calibrated experiments. They are divided into three blocks, being error results from repeatability (leading to a precision impressiveness factor, IF_P), linear regression fit parameters (leading to an accuracy impressiveness factor, IF_A), and linear regression fit correlation results (leading to a correlation impressiveness factor, IF_C). Repeatability errors are derived from the mean of reference set errors (first column in the block) plus two standard deviations (SD) (second column).

Accuracy (IF_A) results are not meaningful when taken in isolation (and therefore overall DEXA IF is also not meaningful). Since DEXA provides a measure of all bone material in the photon beam path, the poor IF_A s merely reflect the inability of DEXA to measure specific bone volume densities. However, although IF_A cannot be considered as an indication of DEXA accuracy, it may be compared to those of EDXRD in terms of specific volume density measurement (section 7.3).

7.2.2 Demineralised One Component DEXA Analysis

The work of this section tests the DEXA one component system performance in a practical setting, comparing sample measurements made before and after partial demineralisation. It examines the system ability to distinguish levels of bone mineral loss.

Results

The post-demineralisation sample DEXA data was processed in the same way as for the

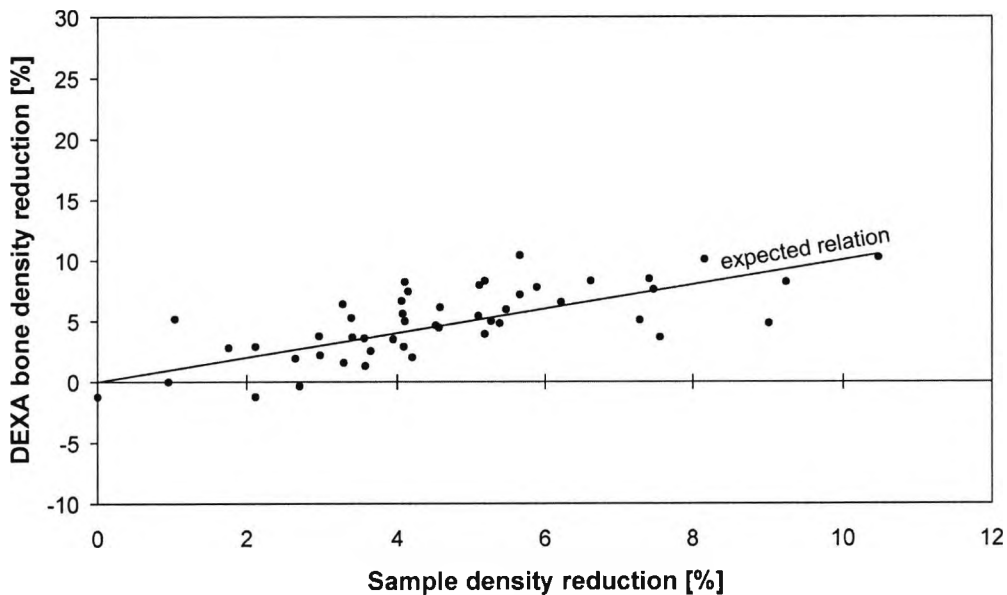


Figure 7-13. Example scatter plot of one component DEXA bone density reduction measurements (no added attenuation, high definition scan setting). Errors are not shown for clarity (c/w figure 7-14b). The scales are identical to those of EDXRD (figure 7-7) to allow comparison.

pre-demineralisation data, using the method described in section 7.2.1. This resulted in 48 pairs of DEXA bone density results (pre- and post-demineralisation) for each measurement condition, with corresponding errors. The measurement conditions were DEXA fast array and high definition scan settings, both for no added attenuation and added attenuation of 3.0 mm of aluminium and 10.0 mm of Perspex.

As for the EDXRD results, sample density reduction was calculated by taking the difference between pre- and post-demineralisation measured mass as a percentage of pre-demineralisation mass. DEXA density reduction was calculated in the same way.

DEXA density reduction was plotted against measured density reduction for each measurement condition. An example scatter plot is shown in figure 7-13, generated using the DEXA high definition scan setting with no added attenuation. Errors are not shown.

For each sample of each measurement condition, errors were calculated by first taking the pre- and post- errors as a percentage of sample density. They were evaluated as bone density (BD) values using equations 7.7. These bone density extremes were translated into pre- and post-demineralisation errors by calculating best and worst case DEXA percentage density reduction (PDR) (equations 7.8). The resultant $PDR_{\text{best case}}$ and $PDR_{\text{worst case}}$ form the upper and lower error limits respectively for each DEXA density reduction point in the scatter plots of figure 7-14.

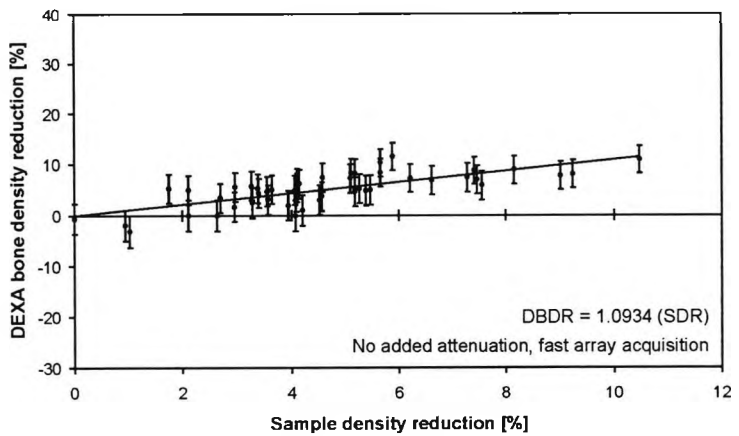
Regression fitted linear trends were fitted to the scatter plot data.

For each measurement condition, detection failure points were determined (the greatest measured sample density reduction that cannot be distinguished). Reliable failure points were calculated by taking the mean plus two standard deviations of all failures for each condition. These results are summarised in table 7-8.

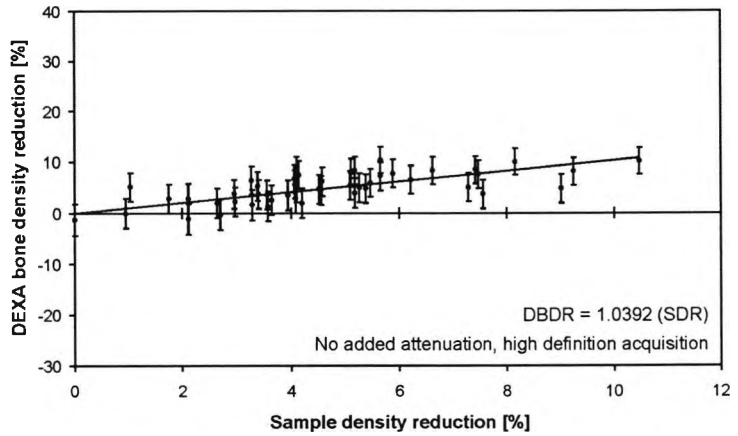
In summary, the best case (no added attenuation) failure points were a bone density reduction of 5.4% (fast array) and 5.1% (high definition). The additional attenuation degraded the failure points to bone density reductions of 8.5% (fast array) and 7.7% (high definition).

Conclusions

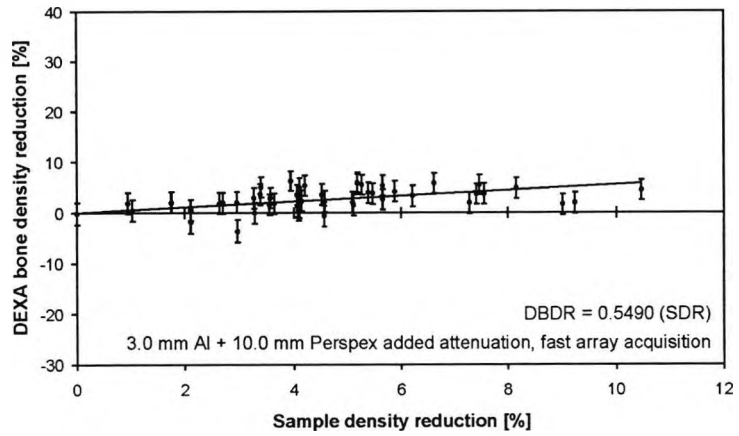
The failure points of 5.4% (fast array) and 5.1% (high definition) for the condition with no added attenuation compare reasonably well with the maximum system precision of



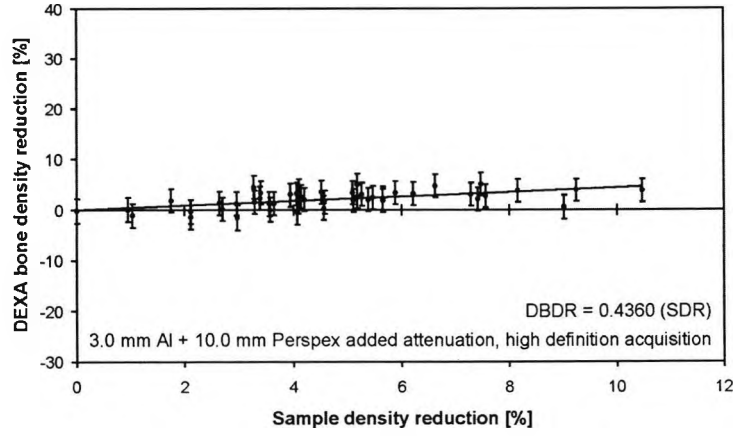
(a)



(b)



(c)



(d)

Attenuation Condition	DEXA Scan Setting	Density Reduction Detection Failure Maximum [%]	Density Reduction Detection Failure Mean [%]	Density Reduction Detection Failure Mean+2SD [%]
no added attenuation	fast array	4.2	2.5	5.4
	high definition	4.2	2.6	5.1
3.0 mm aluminium and 10.0 mm Perspex	fast array	9.2	3.7	8.5
	high definition	9.0	3.7	7.7

Table 7-8. Results from the DEXA one component sample system demineralisation experiments. The maximum, mean and mean plus two standard deviations of measured density reduction that cannot be distinguished by the system are shown.

3.0% for both fast array and high definition from the calibration results (section 7.2.1). The additional attenuation failure points of 8.5% (fast array) and 7.7% (high definition) compare less favourably with the maximum system precision of 2.1% for fast array and 2.4% for high definition (section 7.2.1).

The linear trends regression fitted to the scatter plot data for the conditions with no additional attenuation show a relationship between DEXA bone density reduction (DBDR) and measured sample density reduction (SDR) of near unity. This is

Figure 7-14 (previous page). Scatter plots of the one component DEXA bone density reduction measurements, generated in the same manner as figure 7-13. The examples shown here are from the no added attenuation condition, measured using fast array (a) and high definition (b, also figure 7-13), and from the 3.0 mm aluminium and 10.0 mm Perspex added attenuation condition, again using fast array (c) and high definition (d). The calculation of errors is described in the text. The regression fitted linear trend lines relate DEXA bone density reduction (DBDR) to measured sample density reduction (SDR). The scales are identical to those of EDXRD (figure 7-8) to allow comparison.

dramatically affected when attenuation is added, reducing the relationship of DBDR to SDR by approximately 50%.

These two sets of results indicate that in terms of detecting comparative trabecular bone density reduction, DEXA performs well when the reduced bone mass is not overwhelmed with surrounding attenuation. The additional attenuation effectively results in a drop in relative bone mass loss, leading to the reduction in DEXA capability.

Again, as with EDXRD, it should be borne in mind that the test suffers from the extra error components introduced from physically measured sample density reduction, and the fact that two sets of DEXA measurements are compared, each with their own errors.

7.3 COMPARISON OF EDXRD AND DEXA RESULTS

This study of EDXRD and DEXA measurement systems was conducted throughout using one component trabecular bone sample cubes and so the conclusions drawn from the results are with regard to this sample type. In addition, the results relate to these specific EDXRD and DEXA experiments and should not be taken as conclusive for all such measurement systems.

This study of DEXA and EDXRD methods involved two experiment types. The first aimed to achieve results concerning three areas of measurement system performance, namely precision (the spread of data obtained from experimental repetition), accuracy (the closeness of a result to the true value) and correlation (the interdependence between variables, which affects the expected accuracy of an individual measurement). These experiments necessitated measurement modality calibration of some description in order to attain absolute results.

The second experiment type investigated the ability of each measurement modality to distinguish between measurements of the same sample, before and after partial demineralisation. These experiments attained comparative results.

7.3.1 Comparison of Calibrated One Component Results

Impressiveness factors (IFs) for precision, accuracy and correlation were calculated for various measurement conditions for both EDXRD and DEXA. IFs calculated using data from the best case experimental conditions are summarised in table 7-9.

Attenuation Condition	Bone Density Measurement Modality	Best Case Condition Impressiveness Factors			
		Precision IF _P	Accuracy IF _A	(R ²) Correlation IF _C	Combined IF
no added attenuation	EDXRD	0.9510	0.9573	0.8659 _(a)	0.7883
	DEXA	0.9703	0.6186	0.9797	0.5880
2.5 mm Al	EDXRD	0.8909 _(b)	0.8044	0.8799	0.6306
3.0 mm Al and 10.0 mm Px	DEXA	0.9764 _(c)	0.1688	0.9685	0.1596

Table 7-9. Summary of best case condition impressiveness factors, presented here for comparison purposes. The (expected) best case measurement condition for EDXRD was 1000 seconds (8000 mAs) and for DEXA was high definition. In some cases, the best measurement condition did not yield a maximum IF. These cases are: (a) EDXRD IF_C (no attenuation) was a maximum of 0.8704 at 400 mAs; (b) EDXRD IF_P (added attenuation) was projected to a maximum of 0.8924 (≅ mAs); (c) DEXA IF_P (added attenuation) was 0.9789 for fast array.

In terms of precision, expressed in this chapter as an impressiveness factor for precision (IF_P, equation 7.3), DEXA is shown to outperform EDXRD under all measurement conditions. The best case EDXRD measurement condition for precision (no added attenuation, 1000 second acquisition time, 8 mA tube current) IF_P was surpassed by DEXA for every condition. Indeed, with the addition of attenuation, the EDXRD IF_P fell whereas the IF_P for DEXA increased. This increase in performance is likely due to the additional attenuation more closely approximating the clinical conditions under which DEXA is designed to operate.

DEXA also outperforms EDXRD in terms of correlation (IF_C (or R²), the impressiveness factor for correlation). DEXA IF_C, under conditions of both no added and added attenuation, yielded a performance best unsurpassed by EDXRD under any measurement condition. EDXRD IF_C improved with the addition of 2.5 mm of aluminium attenuation but did not approach the performance of DEXA.

The main strength of EDXRD is its ability to measure the density of selected volumes of bone. This is reflected by the impressiveness factor for accuracy (IF_A , equation 7.5). The best IF_A is, predictably, for the condition with no added attenuation, but is still reasonably high with the added aluminium. The inability to recover low energy photons in the EDXRD spectra using attenuation correction is likely to cause this IF_A drop. This problem might be partially overcome by adopting an analysis using higher energy EDXRD spectrum regions (figure 7-2), discussed as further work in chapter 11, section 11.3.2.

For a true representation of DEXA accuracy, total bone density should be calculated for each attenuation condition (i.e. the contribution of the added attenuation should be included). This is because DEXA was not designed to measure specific bone density volumes but all bone (or bone-equivalent) material in the photon beam path, and for this purpose no doubt performs well. With this caveat, the IF_A s of DEXA are not impressive (since IF_A expresses accuracy in terms of ability to measure specific volume density). With no added attenuation (where DEXA should perform at its best for IF_A accuracy), the best case IF_A is significantly lower than that of EDXRD. As expected, this drops dramatically with the addition of attenuation.

7.3.2 Comparison of Demineralised One Component Results

Results from the demineralisation experiments were calculated for various measurement conditions for both EDXRD and DEXA, being the bone density reduction failure point and the linear regression fit slope (for EDXRD or DEXA bone density reduction plotted against measured sample density reduction). The results, calculated using data from the best case experimental conditions, are summarised in table 7-10.

For both EDXRD and DEXA, the bone density reduction failure points are comparable for similar attenuation conditions. This failure point indicates the sample bone density reduction above which the measurement modality may confidently be expected to detect (comparative measurement). With no added attenuation, DEXA performance shows marginal improvement over EDXRD. The added attenuation conditions cannot be directly compared since the added attenuation for DEXA was greater than that of EDXRD. However, the failure points are roughly comparable.

The linear regression fitted slope would ideally demonstrate a relationship of unity. In other words, any sample bone density reduction would be reflected value for value by

Attenuation Condition	Bone Density Measurement Modality	Bone Density Reduction Failure Point [%]	Regression Fit Slope
no added attenuation	EDXRD	5.6	2.1554
	DEXA	5.1	1.0392
2.5 mm Al	EDXRD	7.3	1.9809
3.0 mm Al and 10.0 mm Px	DEXA	7.7	0.4360

Table 7-10. Summary of best case condition sample demineralisation results, presented here for comparison purposes. The best case measurement condition for EDXRD was 1000 seconds (8000 mAs) and for DEXA was high definition.

the measurement modality result. DEXA with no additional attenuation provided the fit closest to unity. Both EDXRD fits showed density reduction results of the order of twice that measured from the sample.

EDXRD is more impressive when considering the slope change with added attenuation. Again the results should not be directly compared (different quantity of added attenuation) but the DEXA slope does dramatically reduce (by the order of 50%) whereas the EDXRD slope only reduces by a small amount. This should not be taken as criticism of DEXA. Since the additional attenuation is included in the measured bone density, effectively the relative bone mass loss is reduced. However it does demonstrate the ability of EDXRD to measure specific bone volumes and shows the detrimental affect of additional attenuation to the DEXA technique.

Chapter 8

EDXRD AND DEXA INVESTIGATION INTO TWO COMPONENT TRABECULAR BONE DENSITY MEASUREMENT

This chapter describes the second of the two major sets of EDXRD experiments, which featured density measurements using trabecular bone sample cubes with a marrow substitute reintroduced into the trabecular spaces. This investigation is arguably the most important of the project since the sample condition bears the closest resemblance to clinical situations (i.e. the condition of bone within a living body) when compared with those of the previous chapter. This sample state is referred to as a 'two component sample system'. The methods described could be employed in a laboratory or clinical environment, the latter circumstance necessitating consideration of radiation dose.

The trabecular bone sample cubes were initially cleaned of marrow, necessary to determine dry apparent bone density using mass and dimensions. Once density was determined, the trabecular spaces were refilled with a marrow substitute to form the two component sample system.

As with the one component sample system work, described in chapter seven, corresponding DEXA experiments were performed for comparison.

Many of the techniques employed for the investigations in this chapter are identical or similar (with minor variations) to those of chapter seven. In order to prevent excessive repetition, the reader is on occasion referred to the relevant sections of the previously described work.

This chapter comprises:

Section 8.1 A discussion of the EDXRD experiments using trabecular bone samples with marrow substitute in the trabecular spaces (two component sample system). Absolute (calibrated) results are presented, including simulations of clinical sites. A peak fitting method to smooth the EDXRD spectra is introduced.

Section 8.2 A discussion of the DEXA experiments using trabecular bone samples

with marrow substitute in the trabecular spaces (two component sample system). Absolute (calibrated) results are presented, including simulations of clinical sites.

Section 8.3 A comparison of the EDXRD and DEXA results. Calibrated methods are considered.

8.1 EDXRD BONE DENSITY MEASUREMENTS USING A TWO COMPONENT SAMPLE SYSTEM

These two component sample system investigations were intended to investigate performance under clinical type conditions and as such a number of clinical sites were simulated, namely the calcaneus, radius and femoral neck. This was achieved with the addition of varying degrees of attenuation, aluminium simulating cortical bone and Perspex simulating soft tissue.

The two component sample system allows regions of recorded EDXRD spectra due to bone mineral and marrow to be isolated and calibrated to known densities, obtained using the bone + marrow calibration phantoms (chapter three). From suitable calibration models, further trabecular bone densities can be measured non-invasively and practically in isolation from the additional attenuation.

This method was an improvement over that described in chapter seven, where calibration was performed, by necessity, using trabecular bone samples. Calibration using bone + marrow phantoms was expected to be more reliable, since a homogeneous bone + marrow mix was used.

Calibrated results (absolute bone density) from two component trabecular bone sample measurements were compared to the directly measured bone densities of the samples.

Method

For these experiments, the measurement set of trabecular bone samples was reduced in number from that of the one component experiments. This was due to the high sample preparation and measurement time necessary for the experimental variations described in this chapter.

The 10 sample reference set from the previous chapter was used as the two component measurement sample set for these experiments. The 10 trabecular bone sample cubes ($15 \times 15 \times 15 \text{ mm}^3$), a subset of the original 58 samples, started this process free of marrow

(preparation discussed in chapter five, sections 5.1 and 5.2) with dry apparent densities ranging from 0.385 to 0.822 g/cm³. This density range, calculated from cube dimensions (measured using Vernier callipers) and mass (Sartorius PT310 electronic balance), is shown diagrammatically in figure 7-1 (chapter seven). It is worth repeating here that the average apparent density of trabecular bone in a human body (being 0.389 g/cm³, calculated in chapter three, section 3.2), falls near the lower end of this range.

Once the apparent density of each of the 10 samples was measured, marrow substitute (animal fat, as used for phantom preparation, chapter three, section 3.2) was introduced into the trabecular spaces. The method for this preparation is described in chapter five, section 5.6, and was performed for all 10 samples, which were carefully labelled (including for orientation) and, when not being used, stored cold to prevent fat seepage. MRI scans on dense examples showed that marrow substitute had penetrated all the trabecular spaces in the samples.

The fixed parameter EDXRD diffractometer was assembled according to the method described in chapter six, section 6.1. The x-ray source was set to 70 kV_p throughout these experiments. X-ray tube current was set to 8 mA for measurements with no additional attenuation but was increased under circumstances with additional attenuation to achieve a reasonable effective photon flux. Deviation from 8 mA tube current is indicated in the results when applicable.

Each bone sample cube from the 10 sample measurement set was located on the EDXRD positioning device and left in place for any repeat measurements performed. EDXRD scattered and transmitted spectra were recorded in the same way as for one component sample system spectra (chapter seven, section 7.1) with identical sample translation (total scanned volume width of 10 mm) and a slightly reduced number of spectra acquisition times (seven time intervals, being 10, 20, 50, 100, 200, 500 and 1000 seconds). Again, in the final analysis spectrum collection time was multiplied by the x-ray tube current, since current × time (mAs) is related to photon flux (with a constant tube accelerating voltage, kV_p), and therefore radiation dose.

EDXRD scattering spectra were collected with the sample alone in the first instance and then with varying degrees of additional attenuation, intended to simulate the three clinical sites (calcaneus, radius and femoral neck) plus the required legal filtration for clinical measurements (2.5 mm of aluminium). The arrangement of attenuation is shown in figure 8-1.

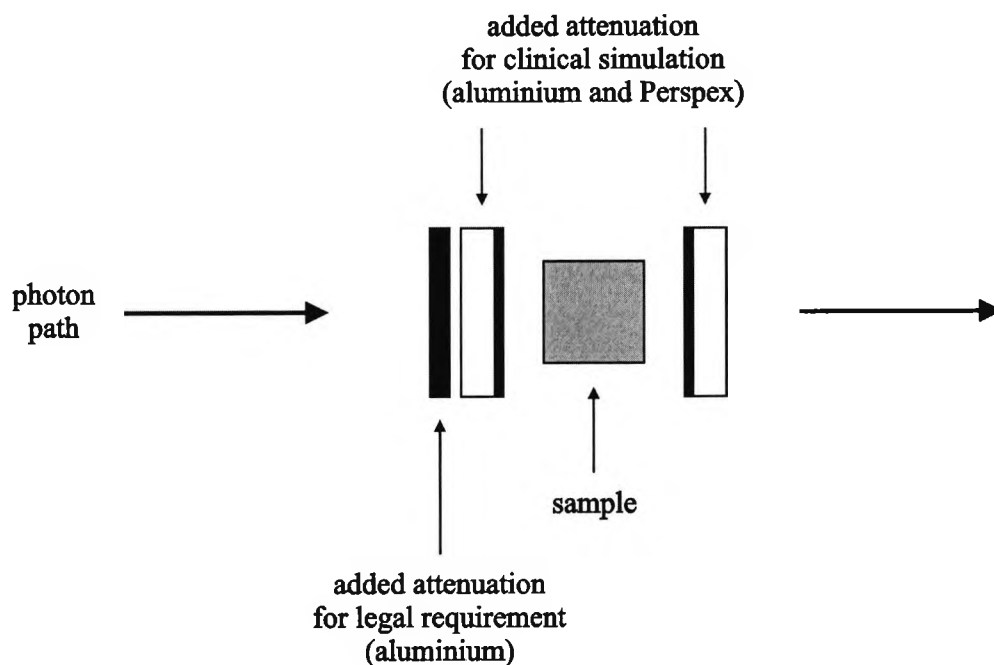


Figure 8-1. Configuration of trabecular bone sample and added attenuation (when used) for this and all subsequent experiments in this chapter. The aluminium and Perspex combination simulates cortical bone and soft tissue whilst additional aluminium is sometimes employed as a legally required filter for clinical situations (2.5 mm).

Clinical Site Simulation	Aluminium for Legal Filtration (*) [mm]	Aluminium for Cortex Simulation [mm]	Perspex for Soft Tissue Simulation [mm]
sample only	0	0	0
calcaneus	2.5	1.0	5.2
radius	2.5	3.0	10.0
femoral neck	2.5	6.5	50.0

Table 8-1. Quantities of aluminium and Perspex used for each clinical site simulation. The 2.5 mm legal filtration (*) was not added for any DEXA measurements since the aluminium equivalent filtration for each photon beam energy was already integral to the machine.

Quantities of added attenuation were taken for typical clinical sites, about which thickness variations of different degrees are found in different subjects. The quantities of attenuating material used here were taken from physical measurements made using radiographs of each site (data courtesy of M. Farquharson). The femoral neck simulation required some adjustment to the x-ray tube and detector positions (some Perspex was positioned directly after the tube and before the detector) in order to accommodate the attenuation without disrupting the diffractometer geometry. Table 8-1 gives the quantities of aluminium and Perspex used for each clinical site simulation.

For the measurement set of 10 samples (less for clinical site simulations due to time constraints on equipment availability), 10 repeated spectra were measured to allow

Sample Set	Number of Experimental Conditions				
	Samples	Repeated Measurements	Spectra Recording Times	Attenuation Conditions	Total Spectra
Phantoms (for calibration)	8	1	1	1	8
Measurement with repeats (for precision; NAA)	10	10	9	1	900
Measurement with repeats (for precision; AA)	3	10	9	3	810
Measurement without repeats (AA)	7	1	9	3	189
Total Spectra for All Variations					1907

Table 8-2. Summary of the number of experimental variations that each generated an EDXRD scattered spectrum. All measurements with no added attenuation (NAA) were repeated but those with added attenuation (AA) were not due to lack of equipment availability time. Corresponding transmission spectra were also measured for attenuation correction.

system precision to be determined. For two component EDXRD system calibration, spectra were also acquired using a subset of the phantoms described in chapter three (section 3.2), being eight phantoms of 0 to 35% apparent bone density reduction (5% steps). This provided an apparent bone density range from 0.253 to 0.389 g/cm³. EDXRD spectra were collected for a single acquisition time of 2000 seconds, 8 mA tube current, and with no additional attenuation.

Corresponding transmission spectra were collected in the same way as described in the previous chapter (section 7.1). A reference transmission spectrum was recorded with no sample or attenuation in place both for the general experimental layout and the adjusted tube and detector layout for the femoral neck simulation.

This calibration data set was used in the analysis to investigate the effectiveness of ascertaining the bone densities of the measurement set from a calibration (section 8.1.1). Data for comparative bone density loss measurements (using sample demineralisation) was not collected for the two component sample system due to time constraints.

The number of experimental variations is summarised in table 8-2.

8.1.1 Calibrated Two Component EDXRD Analysis

The analysis methods performed for the two component EDXRD measurements are all concerned with bone density calculation using calibration models. Three calibration models were generated, the first using spectrum data without normalisation (inviting comparison with the one component analysis of chapter seven), the second using spectrum data normalised using bone/marrow region ratios and the third using data normalised to unity.

EDXRD trabecular bone sample data was processed in two ways for use with the calibration models. This section deals with sample analysis calibrated using unfitted spectra generated using the samples with marrow substitute filling the trabecular spaces. The second sample analysis (section 8.1.2) features peak fitting to the same sample spectra in an attempt to improve measurements with low acquisition mAs (tube current × time). In all cases, the calibration bone + marrow phantom EDXRD spectra were fitted to produce a standard, 'best case' calibration model.

Table 8-3 summarises the analysis methods performed.

Clinical Site Simulation	Analysis with No Peak Fitting			Analysis with Peak Fitting		
	Spectrum Normalisation			Spectrum Normalisation		
	None	Region Ratio	Spectral Unity	None	Region Ratio	Spectral Unity
sample only	•	•	•	•	•	•
calcaneus	•	•	•			
radius	•	•	•			
femoral neck	•	•	•			

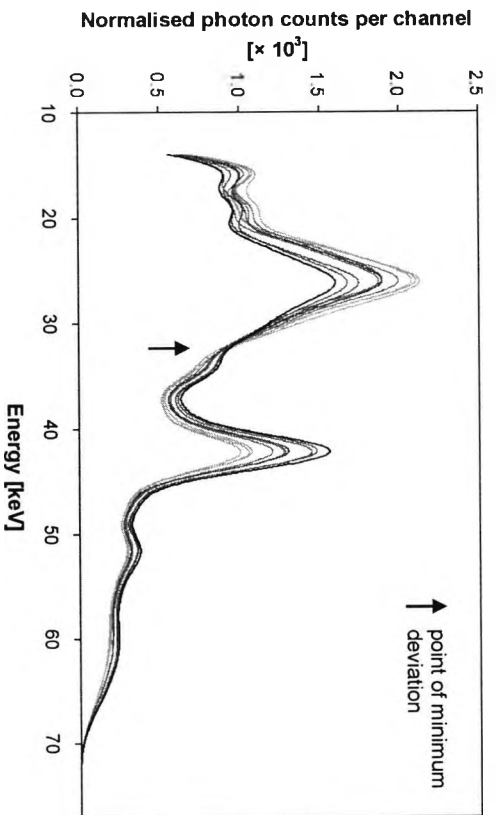
Table 8-3. Summary of the analysis methods performed using two component sample EDXRD spectra. Analysis using peak fitting was limited to sample only spectra for direct comparison to the results with no fitting.

Results

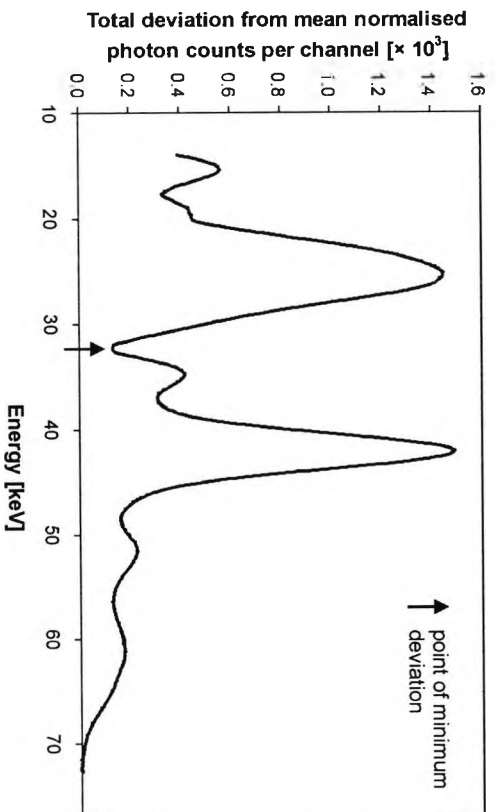
All the EDXRD spectra from the phantom calibration and measurement sets were corrected for attenuation using the method described in chapter six, section 6.2. The four stages of this method are summarised at the end of section 6.2.

For all three analysis methods (spectra not normalised, normalised using bone/marrow region ratios and normalised to unity), the attenuation corrected EDXRD spectra were divided into two energy regions. The lower energy region (A) was defined as that set of energy channels where photon counts were predominantly generated from scattering by the marrow component of the two component sample. The upper energy region (B) comprised of the energy channels where photon counts were predominantly generated from scattering by the bone component of the sample.

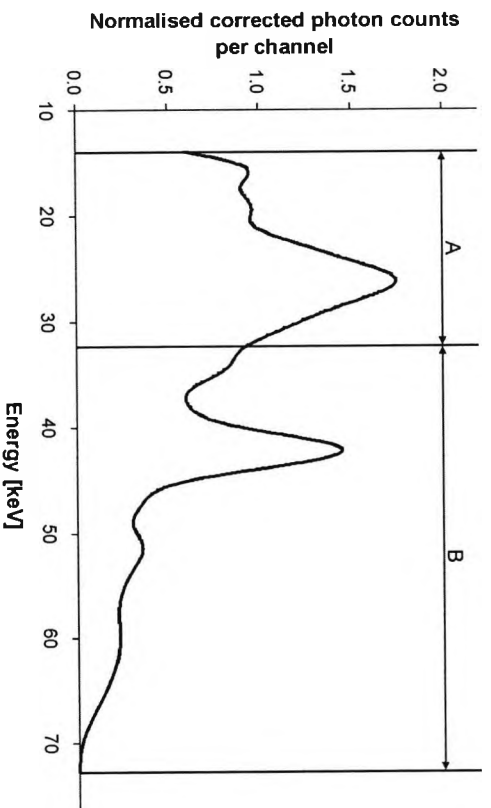
The plots shown in figure 8-2 illustrate the definition of the boundary energy separating the two spectral regions. Each of the 10 corrected sample spectra (measured with no additional attenuation) was fitted with peaks in order to smooth the data (see section 8.1.2 for a description of the peak fitting method) and then normalised to unity. Figure 8-2a shows these spectra (the light grey to black progression indicating increasing bone density) plotted together, a 'point of minimum deviation' being apparent. This is the energy at which the number of photons scattered by bone becomes greater than those



(a)



(b)



(c)

scattered by marrow (for increasing energy). The total deviation of each spectrum from the mean photon counts for each energy channel (of all the spectra) was calculated. The resultant plot against energy (figure 8-2b) shows a minimum deviation at the 32.31 keV energy channel. This energy of minimum deviation was taken as the boundary energy for the analysis regions, shown in figure 8-2c for an example spectrum. Each spectrum was similarly divided and total corrected photon counts produced for the marrow region, A (13.98 to 32.27 keV inclusive), and the bone region, B (32.31 to 72.73 keV).

This process was repeated using the spectra generated using the set of calibration phantoms, again with no added attenuation. The minimum deviation energy was found to be 31.99 keV, almost identical to that calculated using the trabecular bone samples. The analysis regions for the calibration phantoms were therefore defined using this energy, making the marrow region, A, 13.96 to 31.95 keV inclusive, and the bone region, B, 31.99 to 71.76 keV.

The total corrected photon counts for each spectrum region A and B were calculated for each of the calibration phantom spectra and the measurement set spectra obtained using the various attenuation conditions. Three analysis treatments were applied to these results, corresponding to the three analysis methods (spectra not normalised, normalised using bone/marrow region ratios and normalised to unity). For the unnormalised treatment, the total corrected photon counts from bone region B were related to measured bone density:

$$\text{apparent bone density} \propto \text{corrected counts from region B} \quad [8.1]$$

The second method related bone density to the ratio of photon counts from each region:

Figure 8-2 (previous page). EDXRD spectrum analysis area selection for the two component sample system. Normalised spectra measured using the 10 trabecular bone samples (plots light grey to black as bone density increases) and corrected for attenuation demonstrate a 'point of minimum deviation' (a). This is the energy at which the number of photons scattered by bone is greater than those scattered by marrow (for increasing energy). The mean photon counts for each energy channel was calculated and the total deviation of each spectrum from this mean plotted (b). The energy of minimum deviation was taken as the boundary energy for the analysis regions (c), being the marrow region, A (13.98 to 32.27 keV inclusive), and the bone region, B (32.31 to 72.73 keV).

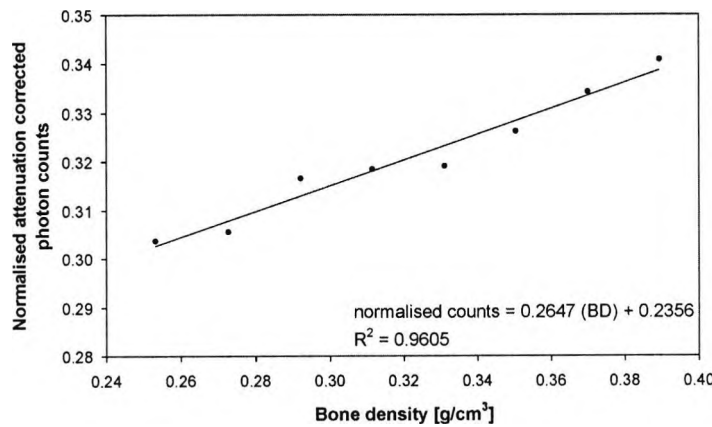
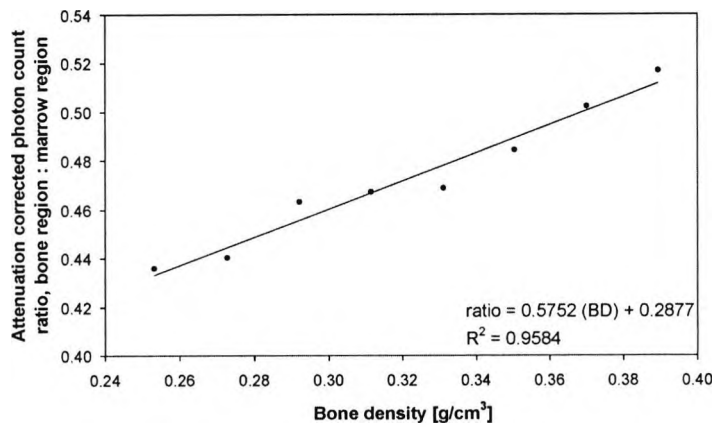
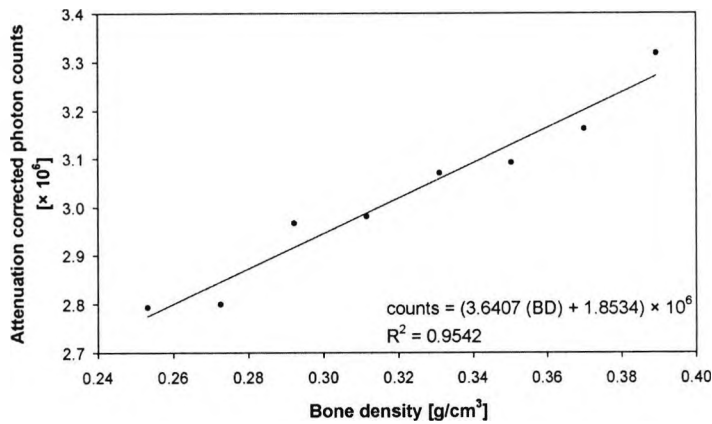


Figure 8-3. Two component sample system calibration models, generated using the bone + marrow phantom set. Each plot represents data extracted from the same attenuation corrected EDXRD spectra (8000 mAs acquisition) by one of three methods: (a) total bone region photon counts; (b) bone/marrow region photon count ratios; (c) normalised spectrum total bone region photon counts. No errors are shown since each point represents a single measurement. The linear regression fits may be rearranged (equations 8.4 to 8.6) to provide calibrations for the model relationships to bone density (BD).

$$\text{apparent bone density} \propto \frac{\text{corrected counts from region B}}{\text{corrected counts from region A}} \quad [8.2]$$

The third analysis method related the corrected photon counts from bone region B to bone density after dividing by the total spectrum corrected photon counts (equivalent to normalising the whole spectrum to unity before dividing into regions):

$$\text{apparent bone density} \propto \frac{\text{corrected counts from region B}}{\text{corrected counts from whole spectrum}} \quad [8.3]$$

Three calibration models for the EDXRD diffractometer were generated (one for each analysis method) using the results from the phantom set spectra (relationships 8.1, 8.2 and 8.3). The calibrations, shown in figure 8-3, were derived from linear regression fits to the results for each phantom. These fits were used to calculate density measurements from two component trabecular bone EDXRD corrected region photon counts, depending on the analysis method. For the unnormalised analysis method:

$$\text{apparent bone density} = \frac{\text{corrected counts from region B} - 1853441}{3640671} \quad [8.4]$$

For the ratio analysis method:

$$\text{apparent bone density} = \frac{\left(\frac{\text{corrected counts from region B}}{\text{corrected counts from region A}} \right) - 0.287691}{0.575155} \quad [8.5]$$

For the unity normalised analysis method:

$$\text{apparent bone density} = \frac{\left(\frac{\text{corrected counts from region B}}{\text{whole spectrum corrected counts}} \right) - 0.235627}{0.264662} \quad [8.6]$$

for 10^3 seconds, no additional attenuation, standard x-ray tube conditions. The units of apparent bone density are in g/cm^3 for all three relationships.

The 10 sample measurement set bone densities were evaluated for each attenuation condition using each of these three calibration formula (equations 8.4 to 8.6). Each of these sets of results were plotted against bone densities calculated using mass and volume measurements (chapter five, section 5.5). Selected examples of these plots for data with no additional attenuation are shown in figure 8-4. They show the three best

case (1000 second acquisition time, 8 mA tube current) results from each of the calibrations along with one example of a low acquisition time (10 seconds, 8mA) result using unity normalisation.

For comparison purposes, generalised errors were calculated using the full set of 10 errors from each plot. The same method as used in chapter seven (mean plus two standard deviations of the 10 measurement set errors) was applied for each calibration and acquisition mAs (all no added attenuation). They lead to the method for calculating the precision (or minimum detectable limits) of the system across the sample range. Figure 8-5 shows plots of the generalised errors against the \log_{10} of tube current \times time (mAs) after a back calculation was performed in order to express the precision in terms of a minimum detectable bone density change (as a percentage of density). A plot is provided for each calibration method.

An exponential function was fitted (using SPSS 8.0, SPSS Inc.) to each mean and mean plus two standard deviation trend:

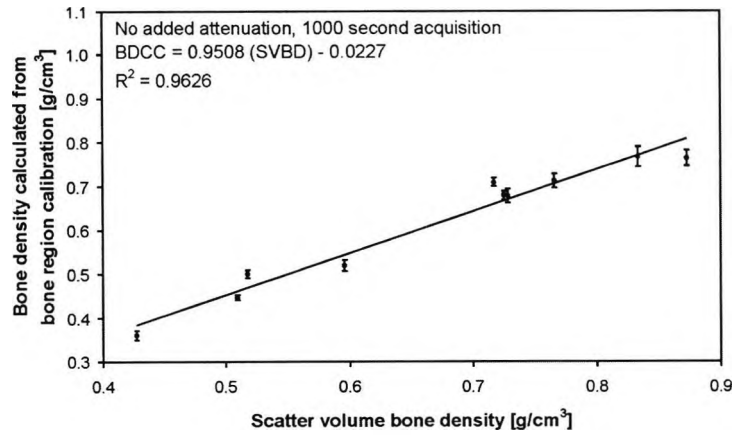
$$m_p = ae^{-b(\log \text{ mAs})} + c \quad [8.7]$$

where m_p is the sample error mean (or mean plus two standard deviations) as a percentage, $\log \text{ mAs}$ is the \log_{10} of tube current \times time, and a , b and c are constants. The fitted constants are presented in table 8-4.

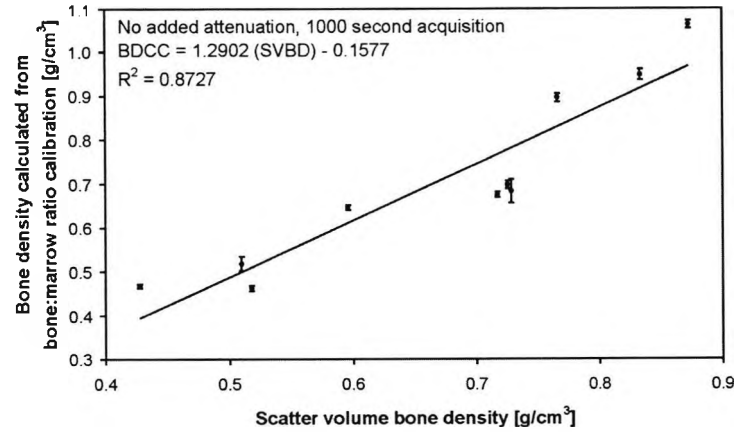
The bone density change minimum detectable resolution for a given mAs and attenuation condition is taken to be twice the generalised bone density error (see chapter four, section 4.1). Generalised errors are given in the first block of results in table 8-5.

The ultimate minimum errors achievable, all for the condition with no added attenuation, were estimated by taking the constant 'c' from each of the fits (acquisition mAs sufficiently large), illustrated by the dotted lines in figure 8-5. For the bone region

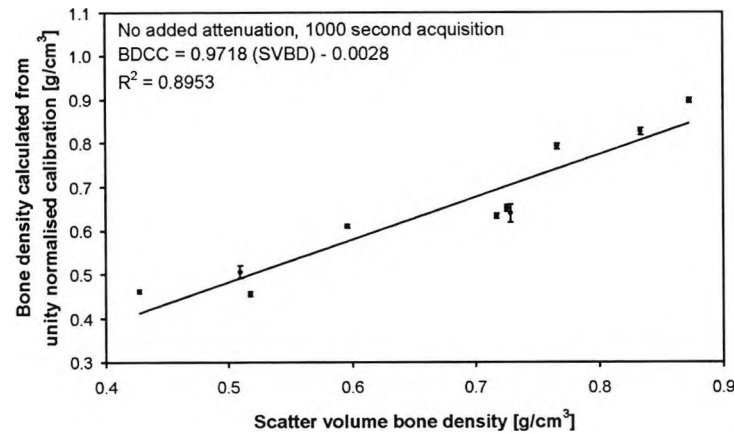
Figure 8-4 (following page). Examples of measured two component samples with no added attenuation, processed using the calibration formulae (equations 8.4 to 8.6). Each point represents the mean of 10 repeated measurements and errors are \pm two standard deviations. The examples shown here are all from the bone region counts with no added attenuation condition, measured with no normalisation for 1000 seconds (a), using the bone/marrow region ratios measured for 1000 seconds (b) and using unity normalisation measured for 1000 seconds (c) and 10 seconds (d). The linear regression fits shown relate bone density calculated from the calibration (BDCC) to the scatter volume bone density (SVBD). Corresponding R^2 correlations are also shown.



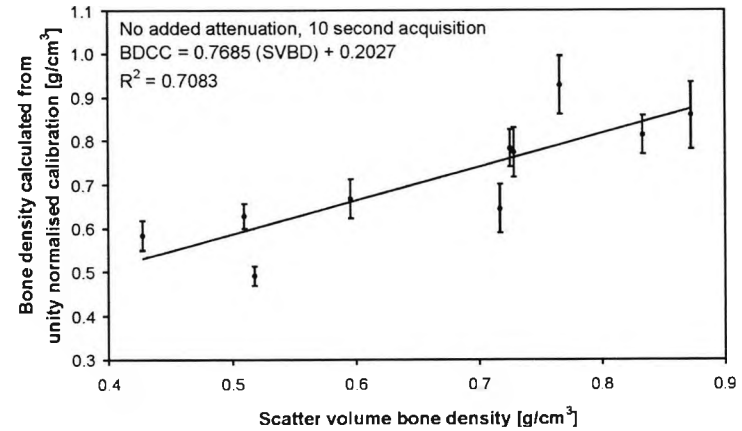
(a)



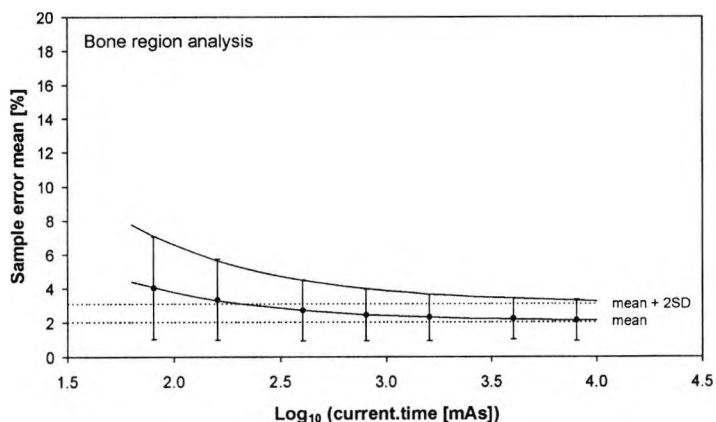
(b)



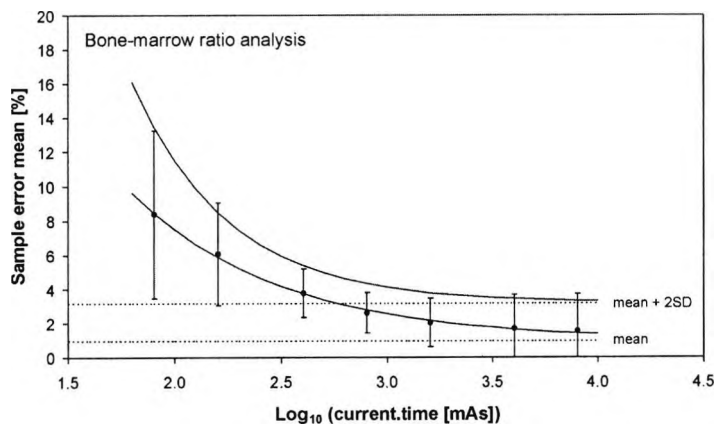
(c)



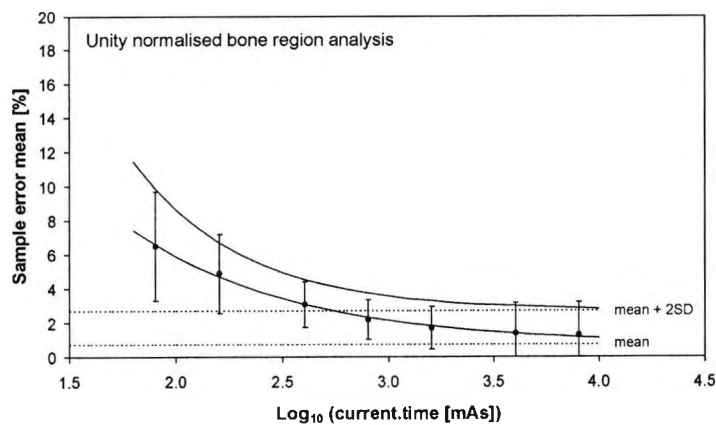
(d)



(a)



(b)



(c)

Figure 8-5. Two component sample system errors as a function of \log_{10} (mAs). Plots are presented for the no added attenuation condition for the three analysis methods: bone region photon counts (a), normalisation by bone/marrow ratio (b), and normalisation to unity (c). The points were calculated from the mean error of each measurement sample set (10 samples). Errors were calculated from \pm two standard deviations of these errors. The exponential regression fits provide an indication of the ultimate minimum errors achievable if acquisition tube current \times time was sufficiently large.

Analysis Method	Error Fit	a [%]	b [(log mAs) ⁻¹]	c [%]
bone region	mean + 2SD	69.495	1.500	3.083
	mean	39.775	1.566	2.032
bone/marrow ratio	mean + 2SD	698.531	2.218	3.213
	mean	112.234	1.424	0.983
unity normalised bone region	mean + 2SD	297.887	1.959	2.697
	mean	71.703	1.321	0.756

Table 8-4. Parameters for the two component sample system error fits, using equation 8.7.

analysis, the mean error plus two standard deviations tend to 3.08%, giving a precision (minimum detectable bone density resolution) of 6.2%. For the bone/marrow ratio analysis, the mean error plus two standard deviations tend to 3.21%, giving a precision of 6.4%. For the unity normalised bone region analysis, the mean error plus two standard deviations tend to 2.70%, giving a precision of 5.4%.

As for the one component results of chapter seven (section 7.1.1), an indication of the effectiveness of precision, accuracy and correlation for each analysis method was calculated as ‘impressiveness factors’ (IFs). The IFs were calculated using equations 7.3 and 7.5 (using fitted equation 7.4 parameters) and the Pearson correlation coefficient (R²). Equations 7.3 to 7.5 are repeated here for clarity as equations 8.8 to 8.10, with equation 8.11 for completeness.

Impressiveness factor for precision (IF_p):

$$IF_p = 1 - \left(2 \times \frac{\text{generalised bone density error}}{100} \right) \quad [8.8]$$

IF_ps are given in the first block of results in table 8-5.

The plotted measurement set results were regression fitted with a linear trend (selected examples in figure 8-4), resulting in a formula for each set:

$$BDCC = a (SVBD) + b \quad [8.9]$$

Analysis Method	Current × Time [mAs]	Log Current × Time [log mAs]	Sample Error % Mean	Sample Error % Mean +2SD	Precision IF _P	Linear ax+b Fit a	Linear ax+b Fit b	Accuracy IF _A	Linear ax+b Fit R ² (IF _C)	EDXRD IF
bone region	80	1.90	4.04	7.06	0.8588	0.8656	0.0785	0.7871	0.8375	0.5661
	160	2.20	3.34	5.71	0.8858	0.9119	0.0254	0.8865	0.9329	0.7326
	400	2.60	2.69	4.47	0.9107	0.9331	-0.0057	0.9274	0.9628	0.8132
	800	2.90	2.42	3.93	0.9214	0.9478	-0.0168	0.9310	0.9595	0.8231
	1600	3.20	2.29	3.63	0.9273	0.9506	-0.0198	0.9308	0.9607	0.8292
	4000	3.60	2.21	3.42	0.9317	0.9511	-0.0219	0.9292	0.9616	0.8325
	8000	3.90	2.11	3.31	0.9339	0.9508	-0.0227	0.9281	0.9626	0.8343
	∞	∞	2.03	3.08	0.9383					
bone/marrow ratio	80	1.90	8.36	13.28	0.7345	1.0691	0.0824	0.8485	0.6979	0.4349
	160	2.20	6.06	9.06	0.8189	1.1769	-0.0392	0.7839	0.8400	0.5392
	400	2.60	3.76	5.19	0.8962	1.2457	-0.1124	0.6419	0.8718	0.5015
	800	2.90	2.62	3.82	0.9236	1.2718	-0.1376	0.5906	0.8713	0.4753
	1600	3.20	2.04	3.45	0.9310	1.2854	-0.1507	0.5639	0.8711	0.4573
	4000	3.60	1.66	3.70	0.9261	1.2876	-0.1554	0.5570	0.8714	0.4495
	8000	3.90	1.55	3.74	0.9253	1.2902	-0.1577	0.5521	0.8727	0.4458
	∞	∞	0.98	3.21	0.9357					
unity normalised bone region	80	1.90	6.47	9.67	0.8065	0.7685	0.2027	0.5658	0.7083	0.3232
	160	2.20	4.86	7.18	0.8564	0.8698	0.0988	0.7710	0.8513	0.5621
	400	2.60	3.08	4.41	0.9118	0.9321	0.0362	0.8959	0.8893	0.7264
	800	2.90	2.16	3.31	0.9339	0.9543	0.0152	0.9391	0.8917	0.7820
	1600	3.20	1.69	2.91	0.9418	0.9663	0.0040	0.9623	0.8928	0.8092
	4000	3.60	1.38	3.14	0.9372	0.9695	-0.0007	0.9688	0.8940	0.8117
	8000	3.90	1.29	3.18	0.9364	0.9718	-0.0028	0.9690	0.8953	0.8124
	∞	∞	0.76	2.70	0.9461					

Table 8-5. Results from the EDXRD two component sample system calibrated experiments (no additional attenuation). They are divided into three blocks, being error results from repeatability (leading to a precision impressiveness factor, IF_P), linear regression fit parameters (leading to an accuracy impressiveness factor, IF_A), and linear regression fit correlation results (leading to a correlation impressiveness factor, IF_C). Repeatability errors are derived from the mean of measurement set errors (first column in the block) plus two standard deviations (SD) (second column). These errors are also projected for an infinite measurement time. The final column combines the results into an all-inclusive EDXRD IF.

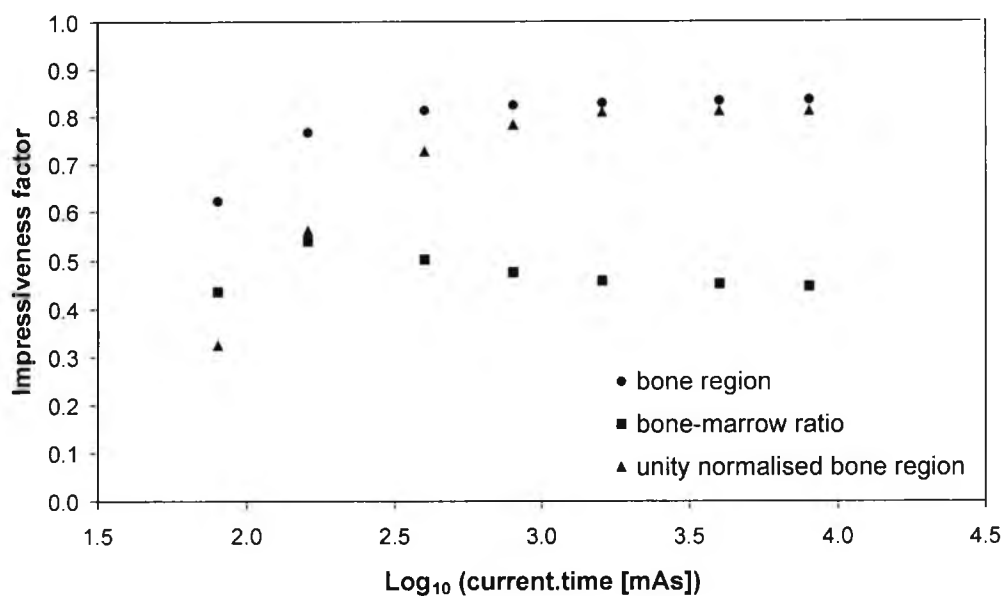


Figure 8-6. Two component EDXRD impressiveness factors (IF) for measurements with no additional attenuation. The IFs were calculated for all three analysis techniques (bone region photon counts, normalisation by bone/marrow ratio and normalisation to unity).

where BDCC is the bone density calculated from calibrated spectra region counts, SVBD is the scatter volume bone density calculated from mass and volume, and a and b are the linear fit parameters (gradient and intercept), given in the second block of results in table 8-5 and used to calculate the impressiveness factors for accuracy (IF_A):

$$IF_A = 1 - (|1 - a| + |b|) \quad [8.10]$$

IF_{AS} are given in the second block of results in table 8-5.

Impressiveness factor for correlation (IF_C):

$$IF_C = R^2 \quad [8.11]$$

IF_{CS} are given in the third block of results in table 8-5.

Overall two component EDXRD capability, with respect to precision, accuracy and correlation, is indicated by multiplying the three impressiveness factors:

$$IF = IF_p \times IF_A \times IF_C \quad [8.12]$$

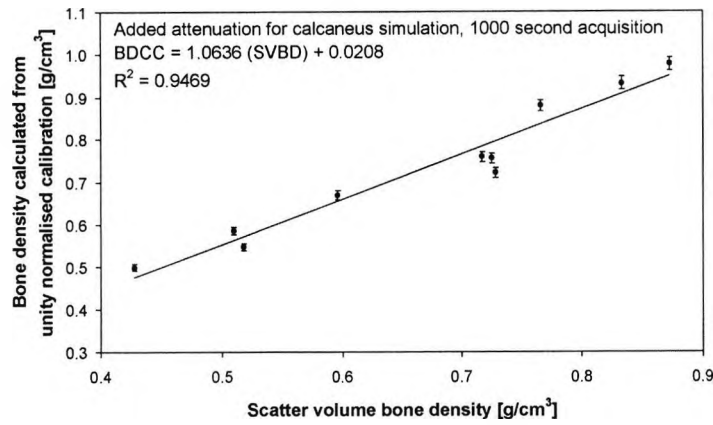
The overall EDXRD IFs are given in the final results column in table 8-5 and are shown diagrammatically in figure 8-6.

The two component EDXRD results for data collected with no additional attenuation are summarised, first for the bone region analysis. Maximum precision (minimum detectable resolution) was achieved at 8000 mAs acquisition, corresponding to a bone density change of 6.6% (bone density error of $\pm 3.31\%$), with an R^2 value of 0.9626. These results, with an accuracy impressiveness factor (IF_A) of 0.9281, combine to an overall EDXRD IF of 0.8343. Precision was projected to a baseline of 6.2%, if acquisition mAs was sufficiently large. A marginally improved accuracy IF_A was recorded at 800 mAs.

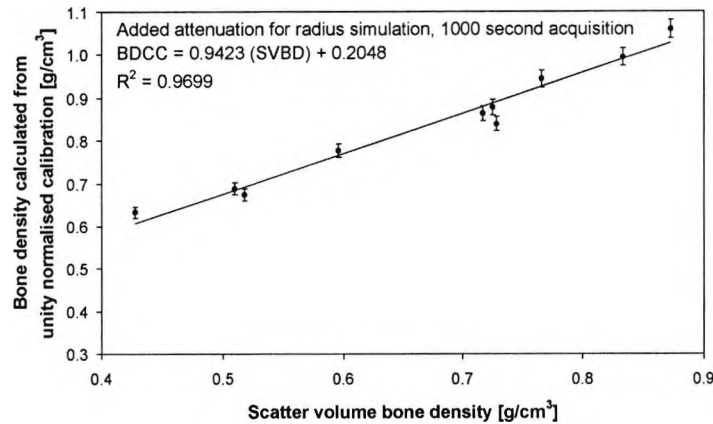
Performance was reduced in all three areas (precision, accuracy and correlation) when using bone/marrow ratio analysis. Precision at 8000 mAs acquisition was a bone density change of 7.5% (bone density error of $\pm 3.74\%$), with an R^2 value of 0.8727. The accuracy impressiveness factor (IF_A) was 0.5521. Overall EDXRD IF was 0.4458. Precision was projected to a baseline of 6.4%. A marginally improved precision IF_P was recorded at 1600 mAs with accuracy IF_A deteriorating (from a maximum at 80 mAs) with increasing acquisition time.

Bone region analysis precision and accuracy were improved by normalising to unity at the expense of correlation (and overall EDXRD IF). Precision at 8000 mAs acquisition was a bone density change of 6.4% (bone density error of $\pm 3.18\%$), with an R^2 value of 0.8953. The accuracy impressiveness factor (IF_A) was 0.9690. Overall EDXRD IF was 0.8124. Precision was projected to a baseline of 5.4%. Maximum precision was recorded at 1600 mAs, being 5.8%.

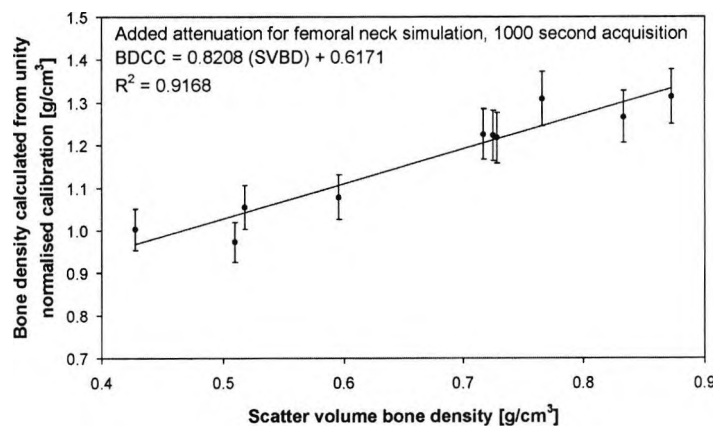
The results from the experiments with added attenuation to simulate the three clinical measurement sites were analysed in the same way as for those with no additional attenuation, except that repeated measurements for precision determination were only performed on three samples. This meant that errors for the plotted results (figure 8-7) were calculated as generalised errors (mean of repeated errors plus two standard deviations) and, strictly speaking, are not statistically valid (since only three sets of repeated measurements were used in the calculation). Therefore these results should not be directly compared with those from the measurements with no additional attenuation. However they may be compared with each other and with the DEXA results (section 8.2) obtained by the same means.



(a)



(b)



(c)

Figure 8-7. Examples of measured two component samples processed using the unity normalisation calibration formula (equation 8.6). Errors were derived from the generalised error calculations for each measurement condition using measurements from three samples of each set. The examples shown here, all spectra measured for 1000 seconds, are from the calcaneus simulation (a), the radius simulation (b), and from the femoral neck simulation (c). The linear regression fits shown relate bone density calculated from the calibration (BDCC) to the scatter volume bone density (SVBD). Corresponding R^2 correlations are also shown.

The selected results shown in figure 8-7 were all calculated using the unity normalised method of calibration, which the results from previous investigation suggest is the best in terms of precision and accuracy. All spectra used for these plots were acquired for 1000 seconds (16 000 mAs, since the tube current was increased).

Results tables for each attenuation condition follow (table 8-6a for the calcaneus simulation, table 8-6b for the radius simulation and table 8-6c for the femoral neck simulation). Errors were not fitted for ultimate precision estimation, again due to the limited number of repeated measurements, and so best case results were taken as those from the maximum acquisition mAs.

In terms of the stability of the results (i.e. the relationship of the improvement of results with increasing acquisition mAs), the analysis method using unity normalisation is most satisfactory for all attenuation conditions. The bone/marrow ratio method is the poorest in all cases.

In terms of best results, unity normalisation is most satisfactory for the calcaneus simulation attenuation condition. For precision and correlation, unity normalisation also provides the best result with radius simulation but is overtaken by bone region analysis with no normalisation in terms of accuracy. The most effective analysis method switches to bone region analysis with no normalisation for the femoral neck simulation, in terms of precision, accuracy and correlation. Barring a few marginal exceptions, the bone/marrow ratio method provides the poorest results in all cases.

The most effective two component EDXRD results are summarised, first for data collected with additional attenuation for calcaneus simulation. The unity normalised bone region analysis was found to be most satisfactory. Maximum precision (minimum detectable resolution) was achieved at 16 000 mAs acquisition, being a bone density change of 3.1% (bone density error of $\pm 1.54\%$), with an R^2 value of 0.9469. These results, with an accuracy impressiveness factor (IF_A) of 0.9156, combine to an overall EDXRD IF of 0.8403. A marginally improved best accuracy IF_A was recorded at 3200 mAs.

When using unity normalisation, the additional attenuation for radius simulation degraded precision to 4.1% (bone density error of $\pm 2.06\%$), with an R^2 value of 0.9699. These results, with an accuracy impressiveness factor (IF_A) of 0.7375, combine to an overall EDXRD IF of 0.6859. An improvement in the accuracy IF_A to 0.8584 was achieved when using the unnormalised bone region analysis method, leading to an overall IF of 0.7514. A best accuracy IF_A was recorded at 800 mAs, being 0.8758.

Analysis Method	Current × Time [mAs]	Log Current × Time [log mAs]	Sample Error % Mean	Sample Error % Mean +2SD	Precision IF _P	Linear ax+b Fit a	Linear ax+b Fit b	Accuracy IF _A	Linear ax+b Fit R ² (IF _C)	EDXRD IF
bone region	160	2.20	7.95	17.78	0.6444	0.9604	-0.0229	0.9375	0.8723	0.5270
	320	2.51	7.75	16.61	0.6678	0.9582	-0.0431	0.9151	0.9035	0.5521
	800	2.90	6.63	14.87	0.7027	0.9608	-0.0593	0.9015	0.9351	0.5923
	1600	3.20	6.21	15.20	0.6960	0.9520	-0.0554	0.8966	0.9301	0.5804
	3200	3.51	5.95	15.00	0.7001	0.9550	-0.0573	0.8977	0.9286	0.5836
	8000	3.90	5.80	14.51	0.7099	0.9629	-0.0631	0.8998	0.9307	0.5945
	16000	4.20	5.49	14.03	0.7194	0.9713	-0.0697	0.9016	0.9332	0.6053
bone/marrow ratio	160	2.20	13.49	26.92	0.4616	1.1772	0.0594	0.7634	0.8157	0.2875
	320	2.51	9.01	13.85	0.7230	1.3234	-0.0397	0.6369	0.8530	0.3928
	800	2.90	5.13	8.29	0.8342	1.3959	-0.1057	0.4984	0.9167	0.3811
	1600	3.20	3.71	5.63	0.8875	1.4841	-0.1628	0.3531	0.9111	0.2855
	3200	3.51	2.80	3.80	0.9240	1.4917	-0.1701	0.3382	0.9196	0.2874
	8000	3.90	1.75	2.69	0.9462	1.4992	-0.1763	0.3245	0.9257	0.2842
	16000	4.20	1.52	1.72	0.9657	1.5138	-0.1885	0.2977	0.9258	0.2661
unity normalised bone region	160	2.20	10.22	20.07	0.5986	0.8318	0.1952	0.6366	0.8313	0.3168
	320	2.51	6.97	10.44	0.7911	0.9296	0.1274	0.8022	0.8732	0.5542
	800	2.90	4.00	6.52	0.8696	0.9852	0.0775	0.9077	0.9318	0.7355
	1600	3.20	2.94	4.69	0.9062	1.0412	0.0402	0.9186	0.9319	0.7757
	3200	3.51	2.22	3.09	0.9382	1.0458	0.0355	0.9187	0.9408	0.8109
	8000	3.90	1.36	1.89	0.9622	1.0518	0.0307	0.9175	0.9466	0.8356
	16000	4.20	1.21	1.54	0.9692	1.0636	0.0208	0.9156	0.9469	0.8403

Table 8-6a. Results from the EDXRD two component sample system calibrated experiments with added attenuation for calcaneus simulation (see table 8-1). Repeatability errors are derived from the mean of three measurement set sample errors (first column in the block) plus two standard deviations (SD) (second column). The final column combines the results into an all-inclusive EDXRD IF. Since a limited sample set was used to determine repeatability, these results should only be used for equivalent comparisons.

Analysis Method	Current × Time [mAs]	Log Current × Time [log mAs]	Sample Error % Mean	Sample Error % Mean +2SD	Precision IF _P	Linear ax+b Fit a	Linear ax+b Fit b	Accuracy IF _A	Linear ax+b Fit R ² (IF _C)	EDXRD IF
bone region	160	2.20	4.10	6.68	0.8665	0.8092	0.0637	0.7455	0.9117	0.5889
	320	2.51	3.37	6.23	0.8753	0.8452	0.0283	0.8169	0.9446	0.6754
	800	2.90	3.26	6.97	0.8607	0.8999	-0.0241	0.8758	0.9519	0.7175
	1600	3.20	2.52	4.85	0.9030	0.9032	-0.0312	0.8720	0.9428	0.7424
	3200	3.51	2.45	3.81	0.9237	0.8784	-0.0175	0.8609	0.9314	0.7407
	8000	3.90	2.18	3.37	0.9327	0.8634	-0.0056	0.8578	0.9329	0.7464
	16000	4.20	2.31	3.22	0.9357	0.8716	-0.0132	0.8584	0.9356	0.7514
bone/marrow ratio	160	2.20	14.05	26.61	0.4678	1.1858	0.2424	0.5718	0.5277	0.1412
	320	2.51	13.29	20.98	0.5804	1.3447	0.1089	0.5464	0.8599	0.2727
	800	2.90	8.62	10.42	0.7917	1.3577	0.0727	0.5696	0.9418	0.4247
	1600	3.20	4.50	6.77	0.8646	1.4396	0.0153	0.5451	0.9535	0.4494
	3200	3.51	2.78	3.67	0.9266	1.4114	0.0308	0.5578	0.9472	0.4896
	8000	3.90	2.67	3.72	0.9255	1.4649	-0.0069	0.5282	0.9476	0.4632
	16000	4.20	2.37	2.77	0.9446	1.4737	-0.0109	0.5154	0.9521	0.4635
unity normalised bone region	160	2.20	10.16	19.27	0.6146	0.7306	0.3837	0.3469	0.5746	0.1225
	320	2.51	9.67	14.64	0.7072	0.8428	0.2933	0.5495	0.8692	0.3378
	800	2.90	6.46	7.92	0.8416	0.8666	0.2604	0.6062	0.9538	0.4866
	1600	3.20	3.35	4.60	0.9080	0.9236	0.2198	0.7038	0.9638	0.6159
	3200	3.51	2.07	2.36	0.9528	0.9059	0.2298	0.6761	0.9589	0.6177
	8000	3.90	1.99	2.40	0.9520	0.9368	0.2073	0.7295	0.9654	0.6705
	16000	4.20	1.77	2.06	0.9589	0.9423	0.2048	0.7375	0.9699	0.6859

Table 8-6b. Results from the EDXRD two component sample system calibrated experiments with added attenuation for radius simulation (see table 8-1). Repeatability errors are derived from the mean of three measurement set sample errors (first column in the block) plus two standard deviations (SD) (second column). The final column combines the results into an all-inclusive EDXRD IF. Since a limited sample set was used to determine repeatability, these results should only be used for equivalent comparisons.

Analysis Method	Current × Time [mAs]	Log Current × Time [log mAs]	Sample Error % Mean	Sample Error % Mean +2SD	Precision IF _P	Linear ax+b Fit a	Linear ax+b Fit b	Accuracy IF _A	Linear ax+b Fit R ² (IF _C)	EDXRD IF
bone region	160	2.20	12.92	20.64	0.5872	0.5455	0.0389	0.5066	0.7594	0.2259
	320	2.51	9.83	18.85	0.6231	0.5862	-0.0133	0.5729	0.8983	0.3207
	800	2.90	5.73	8.63	0.8274	0.6510	-0.0577	0.5933	0.9600	0.4712
	1600	3.20	4.95	8.46	0.8309	0.6463	-0.0580	0.5883	0.9418	0.4604
	3200	3.51	3.89	6.02	0.8796	0.6577	-0.0685	0.5892	0.9439	0.4892
	8000	3.90	2.47	4.47	0.9106	0.6657	-0.0762	0.5895	0.9435	0.5065
	16000	4.20	2.07	3.21	0.9357	0.6665	-0.0777	0.5888	0.9464	0.5214
bone/ marrow ratio	160	2.20	48.93	83.13	-0.6625	1.1852	0.9550	-0.1402	0.1588	-
	320	2.51	23.75	46.86	0.0628	1.3399	0.8566	-0.1965	0.3234	-
	800	2.90	20.65	43.30	0.1341	1.9242	0.4590	-0.3832	0.5933	-
	1600	3.20	16.99	29.00	0.4201	1.6910	0.4816	-0.1726	0.6971	-
	3200	3.51	17.83	38.99	0.2202	1.9102	0.2742	-0.1844	0.7511	-
	8000	3.90	9.22	19.17	0.6165	1.8325	0.3647	-0.1972	0.8596	-
	16000	4.20	5.44	8.31	0.8337	1.7905	0.3968	-0.1873	0.9171	-
unity normalised bone region	160	2.20	28.96	43.80	0.1240	0.5504	0.8526	-0.3022	0.1718	-
	320	2.51	14.72	27.06	0.4589	0.5705	0.8492	-0.2787	0.3290	-
	800	2.90	12.40	22.89	0.5422	0.8107	0.6843	0.1264	0.5985	0.0410
	1600	3.20	10.36	16.77	0.6645	0.7760	0.6538	0.1222	0.6990	0.0568
	3200	3.51	10.97	24.08	0.5184	0.8948	0.5445	0.3503	0.7242	0.1315
	8000	3.90	5.69	11.68	0.7664	0.8364	0.6038	0.2326	0.8567	0.1527
	16000	4.20	3.34	4.85	0.9030	0.8208	0.6171	0.2037	0.9168	0.1686

Table 8-6c. Results from the EDXRD two component sample system calibrated experiments with added attenuation for femoral neck simulation (see table 8-1). Repeatability errors are derived from the mean of three measurement set sample errors (first column in the block) plus two standard deviations (SD) (second column). The final column combines the results into an all-inclusive EDXRD IF. Note that if individual impressiveness factors (IF_P, IF_A, IF_C) are sufficiently poor to be negative, the combined IF is invalid. Since a limited sample set was used to determine repeatability, these results should only be used for equivalent comparisons.

Bone region analysis with no normalisation was also the most effective method for the femoral neck simulation. Maximum precision (minimum detectable resolution) was achieved at 16 000 mAs acquisition, being a bone density change of 6.4% (bone density error of $\pm 3.21\%$), with an R^2 value of 0.9464. These results, with an accuracy impressiveness factor (IF_A) of 0.5888, combine to an overall EDXRD IF of 0.5214. A marginally improved best accuracy IF_A and improved correlation IF_C (R^2) was recorded at 800 mAs. The unity normalisation analysis method is poorer for both precision and correlation and significantly poorer in terms of accuracy.

Conclusions

With reference to table 8-5, it can be seen that, with some marginal exceptions, two component EDXRD precision, accuracy and correlation results with no additional attenuation for unnormalised and unity normalised bone region analysis all tend to improve with increasing measurement mAs. This would be at the cost of increased radiation dose if used in a clinical environment.

For bone/marrow ratio analysis, precision and correlation generally improve with increasing acquisition mAs but accuracy deteriorates, indicating a problem with the calibration for this analysis method. As such, the EDXRD IFs remain fairly constant over the range of acquisition mAs (between 0.4349 and 0.5392).

Unnormalised and unity normalised bone region results are similar in performance, the final best case (8000 mAs) EDXRD IFs being 0.8343 and 0.8124 respectively. The unity normalised analysis is marginally better than the unnormalised bone region method in terms of precision and accuracy, with correlation being more impressive for the latter.

For all attenuation conditions, these results suggest that the bone/marrow ratio method of analysis is the poorest. It was initially thought that use of this ratio would increase the sensitivity of the effect of bone loss on calibrated results – as bone density is reduced, the volume of marrow increases, filling vacated space. Although peak ratios have been used successfully (Royle and Speller, 1995), for these results poor performance is likely to be due to the effect of the attenuation correction method.

Attenuation correction is most significant at the lower energies of the spectrum, amplifying repeatability errors. This problem coincides with the marrow region energies with little relative effect on the bone region photon counts. The problem is still present when unity normalising by dividing by the whole spectrum but is exacerbated when using the marrow region alone for normalising. The problem becomes more significant

with increasing attenuation since more correction is required and the effects of unrecoverable low energy photons (from the filtering effect of the additional attenuation) are more apparent. The attenuation correction procedure cannot accurately recover all attenuated photon counts, especially at these lower energies, and will therefore affect the match to the calibration.

The problem also begins to affect the unity normalisation method as attenuation levels increase, noticeable as the technique becomes less effective than bone region analysis with no normalisation. In other words, as attenuation increases, the low energy correction problems become more significant when normalising spectra to unity than repeatability variation without normalisation.

As stated in the results summary, in general the analysis method using unity normalisation is most satisfactory for all attenuation conditions in terms of results stability (the relationship of the improvement of results with increasing acquisition mAs). This is important, since best results achieved with shorter acquisition mAs cannot be predicted.

To summarise, for the results from samples with no added attenuation, unnormalised and unity normalised yield similar results at the higher acquisition mAs's. For clinical site simulation results, as attenuation increases, the most effective analysis method switches from the unity normalised bone region method to bone region analysis with no normalisation. The choice of analysis method should therefore be determined by the clinical measurement site (or expected attenuation in a laboratory environment) to be investigated. Ideally clinical measurement sites with low attenuation, such as the calcaneus, should be chosen for best results. This may also avoid having to switch analysis methods with increasing attenuation.

8.1.2 Calibrated Two Component EDXRD Analysis using Peak Fitting

This analysis section deals with measurements using peak fitted spectra to investigate any improvements achievable using the same collected data. The calibration spectra obtained using phantoms were smoothed using peak fitting for all the EDXRD analysis discussed in this chapter. Since these were obtained using high acquisition mAs's (8000 mAs), peak fitting will have made little difference. This method was expected to improve measured results collected with low acquisition mAs's.

The use of peak fitting over traditional smoothing methods is explained with reference to the top fitted spectrum of figure 8-8. The large spread of photon channel counts at the lower energies could not be satisfactorily smoothed by traditional means and so peak fitting was employed.

Results

The spectra obtained with no additional attenuation and corrected for self attenuation (section 8.1.1) were fitted with peaks using SPSS Peak Fit version 4 (SPSS Inc.) software, with identical starting parameters. This consisted of fixing Gaussian peaks at spectrum energies that corresponded with the interplanar spacings, d , for hydroxyapatite (the predominant mineral in bone material), tabulated by the JCPDS (1967). This table is reproduced in appendix C. The energies were calculated from the diffraction spacings using equation 8.15 generated by combining Bragg diffraction equation 1.32 (chapter one, section 1.7.1) with a diffraction order of one (equation 8.13) with equation A.7 (appendix A, section A.1) relating wavelength, λ , to energy, E (equation 8.14):

$$\lambda = 2d \sin \theta \quad [8.13]$$

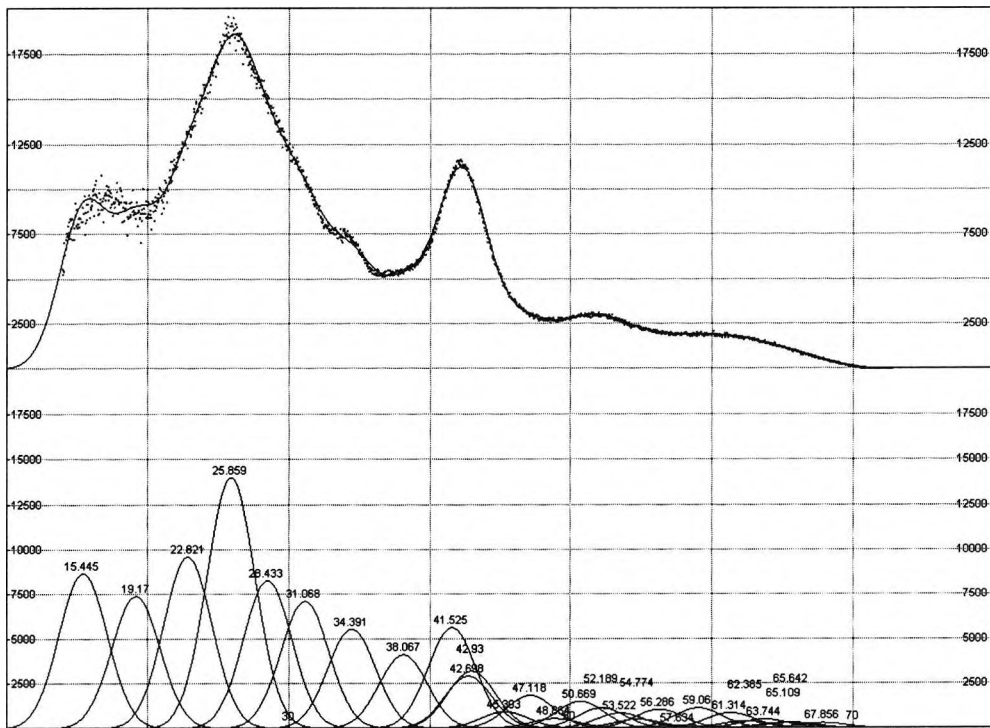
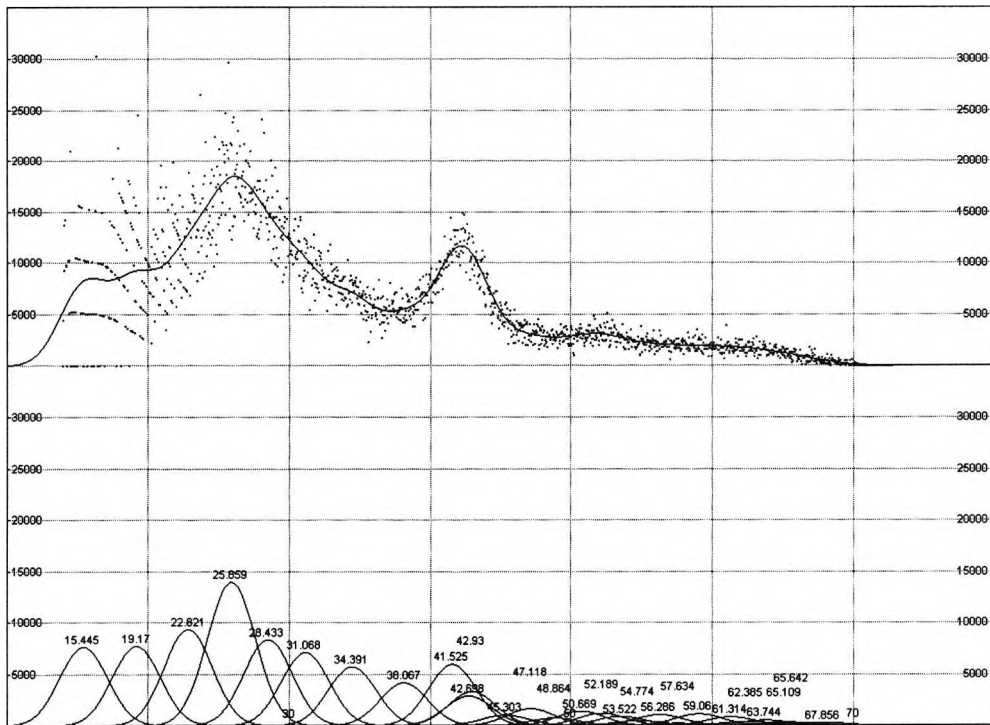
$$\lambda = \frac{hc}{E} = \frac{1.240 \times 10^{-6}}{E} \quad [8.14]$$

Therefore

$$E = \frac{1.240 \times 10^{-6}}{2d \sin \theta} \quad [8.15]$$

where θ is the Bragg scattering angle, h is Planck's constant and c is the speed of light. The units of energy are electronvolts (eV), since hc is calculated here with units of

Figure 8-8 (following page). Examples of peak fitted two component sample system spectra using the peak model. Both spectra were generated using the same bone + marrow sample (0.569 g/cm^3) and corrected for attenuation, the first with an acquisition time of 10 seconds (each channel count multiplied by 100) and the second, 1000 seconds (both 8 mA). The fitted Gaussian peaks are shown in the bottom half of each image with their corresponding centroid energy values (in keV). The individual points in the top half of each image represent the measured spectrum photon counts with the peak fitted spectrum (the sum of each peak contribution at each energy) shown as a continuous line. The vertical scale represents photon counts.



eV.m.

A total of 27 peaks were used for all bone + marrow spectrum fitting, including some additional peaks added to the marrow region energies of the spectrum. The poor definition of marrow region peaks did not allow calculation for definitive peak placing but those chosen were consistent for all spectra fitted.

A peak fit model was produced for all spectra, using the energy positioned peaks. A bone + marrow spectrum measured using the maximum acquisition mAs (8000) and a bone + marrow specimen from the middle part of the density range (apparent density 0.569 g/cm³) was fitted using the positioned peaks. Peak amplitudes were allowed to vary (within a 50% constraint), peak energies were locked and peak widths allowed to vary but fixed to be equal.

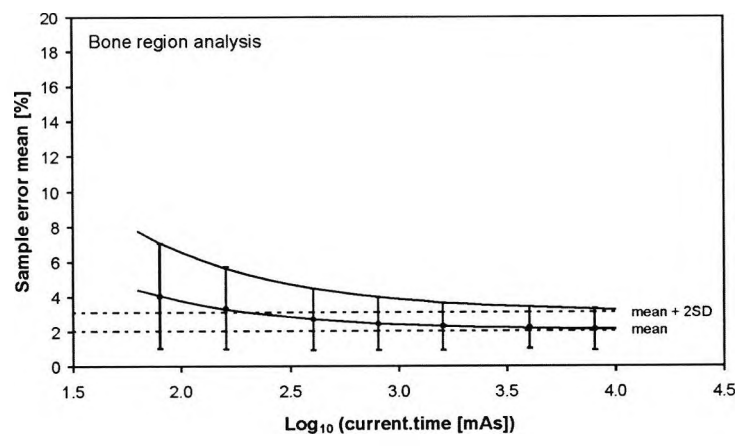
This peak fit model was used as the starting point for each fit for all attenuation corrected spectra at all acquisition mAs's. Each photon count channel for spectra recorded at less than 1000 seconds were multiplied by the time ratio (to 1000 seconds) so all spectra could be fitted using the same model. For all spectra fitting, the model peak amplitudes were allowed to vary (within a 50% constraint) and peak energies and widths were locked.

The resulting contributions of each peak for each spectrum energy channel were summed to provide a final set of smoothed spectra. Figure 8-8 illustrates how data collected using the same sample for significantly different acquisition times (the second spectrum was collected for 100 times longer period than the first) may yield similar spectra by using this peak fitting method.

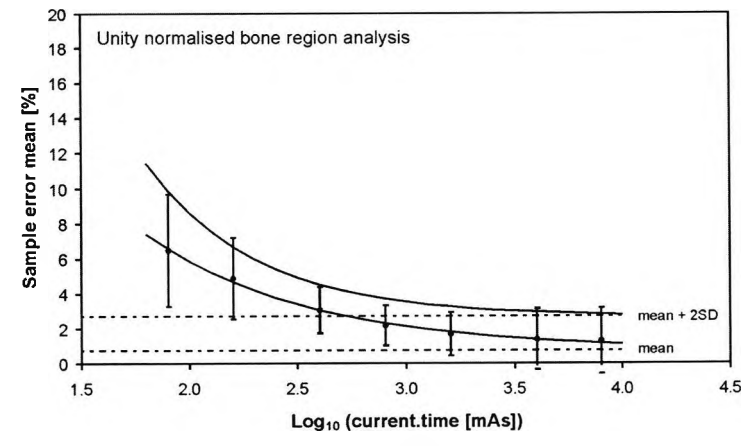
From this stage, analysis was completed in the same way as the corrected spectra with no additional attenuation in section 8.1.1.

The generalised errors were calculated and fitted with exponential functions (equation

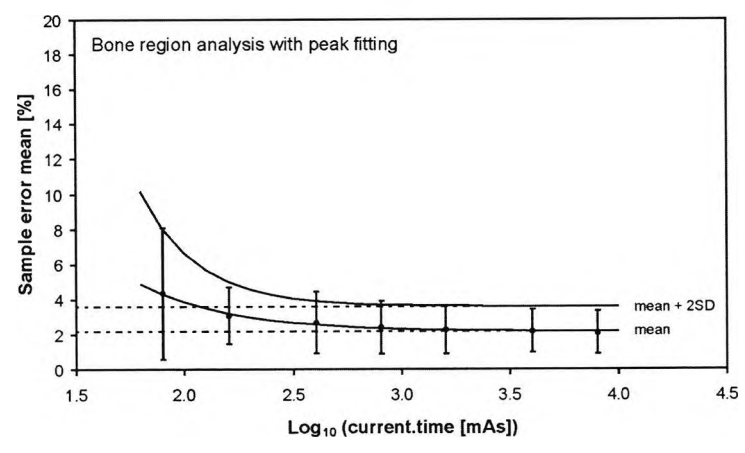
Figure 8-9 (following page). Peak fitted two component sample system errors as a function of log₁₀ (mAs). Plots are presented for the no added attenuation condition for both unfitted and peak fitted spectra (for the best two analysis methods), being unfitted bone region photon counts (a) and normalisation to unity (b) and peak fitted bone region photon counts (c) and normalisation to unity (d). The points were calculated from the mean error of each measurement sample set (10 samples). Errors were calculated from ± two standard deviations of these errors. The exponential regression fits provide an indication of the ultimate minimum errors achievable if acquisition tube current × time was sufficiently large.



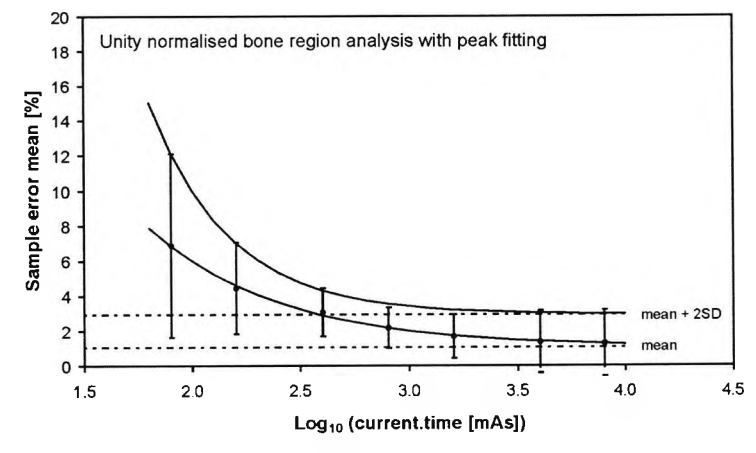
(a)



(b)



(c)



(d)

Analysis Method	Error Fit	a [%]	b [(log mAs) ⁻¹]	c [%]
bone region	mean + 2SD	6753.504	3.853	3.600
	mean	206.974	2.402	2.154
bone + marrow ratio	mean + 2SD	1574.636	2.593	3.381
	mean	169.613	1.656	1.268
unity normalised bone region	mean + 2SD	1622.232	2.719	2.936
	mean	129.038	1.632	1.050

Table 8-7. Parameters for the peak fitted two component sample system error fits, using equation 8.7.

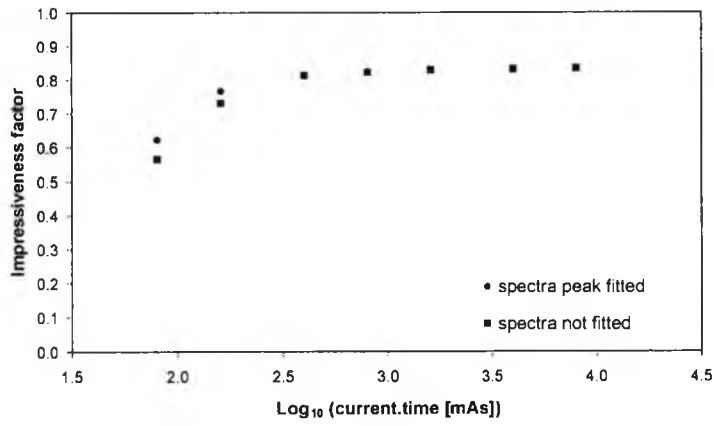
8.7) and are shown in figure 8-9 for the two most successful calibration methods (bone region and unity normalised bone region analysis). Exponential fit parameters for all calibration methods are presented in table 8-7. The equivalent plots from the unfitted data are also reproduced (from figure 8-5) to allow direct comparison. Note how the errors are reduced towards the baseline with less acquisition mAs with peak fitting when compared to the unfitted examples (figure 8-9). However the error baseline (parameter 'c' for mean plus 2SD in table 8-7, illustrated by the dotted lines in figure 8-9) is slightly raised for all calibration methods (c/w table 8-4).

For the bone region analysis, the mean error plus two standard deviations tend to 3.60% (3.08% unfitted), giving a precision (minimum detectable bone density resolution) of 7.2% (6.2% unfitted). For the bone/marrow ratio analysis, the mean error plus two standard deviations tend to 3.38% (3.21% unfitted), giving a precision of 6.8% (6.4% unfitted). For the unity normalised bone region analysis, the mean error plus two standard deviations tend to 2.94% (2.70% unfitted), giving a precision of 5.9 (5.4% unfitted).

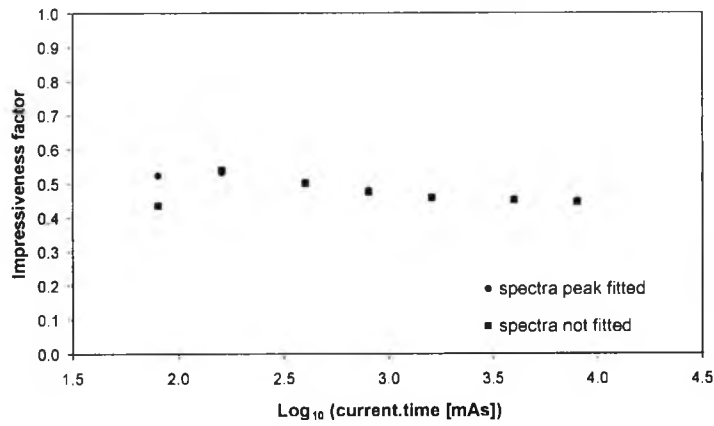
The remaining results for precision, accuracy and correlation were calculated (including impressiveness factors) and are presented in table 8-8 in the same manner as for the unfitted results. The final EDXRD IFs are given in the final results column in table 8-8 and are shown diagrammatically in figure 8-10 with corresponding IFs from the unfitted

Analysis Method	Current × Time [mAs]	Log Current × Time [log mAs]	Sample Error % Mean	Sample Error % Mean +2SD	Precision IF _P	Linear ax+b Fit a	Linear ax+b Fit b	Accuracy IF _A	Linear ax+b Fit R ² (IF _C)	EDXRD IF
bone region	80	1.90	4.33	8.07	0.8387	0.8664	0.0597	0.8067	0.9207	0.6229
	160	2.20	3.07	4.69	0.9061	0.9183	0.0181	0.9002	0.9401	0.7668
	400	2.60	2.67	4.41	0.9117	0.9320	-0.0042	0.9278	0.9632	0.8148
	800	2.90	2.38	3.89	0.9222	0.9464	-0.0151	0.9313	0.9599	0.8244
	1600	3.20	2.27	3.65	0.9271	0.9501	-0.0186	0.9315	0.9611	0.8300
	4000	3.60	2.19	3.41	0.9317	0.9508	-0.0208	0.9300	0.9619	0.8335
	8000	3.90	2.09	3.31	0.9339	0.9504	-0.0215	0.9289	0.9628	0.8352
	∞	∞	2.15	3.60	0.9280					
bone/ marrow ratio	80	1.90	8.57	14.63	0.7075	1.0985	0.0258	0.8757	0.8440	0.5229
	160	2.20	5.51	8.79	0.8242	1.1942	-0.0557	0.7501	0.8620	0.5329
	400	2.60	3.75	5.26	0.8948	1.2439	-0.1100	0.6461	0.8710	0.5036
	800	2.90	2.63	3.84	0.9231	1.2700	-0.1351	0.5949	0.8703	0.4779
	1600	3.20	2.05	3.49	0.9302	1.2838	-0.1484	0.5678	0.8699	0.4594
	4000	3.60	1.67	3.71	0.9258	1.2866	-0.1534	0.5600	0.8704	0.4512
	8000	3.90	1.56	3.74	0.9253	1.2891	-0.1558	0.5551	0.8718	0.4478
	∞	∞	1.27	3.38	0.9324					
unity normalised bone region	80	1.90	6.87	12.10	0.7579	0.8093	0.1494	0.6599	0.8474	0.4238
	160	2.20	4.43	7.04	0.8591	0.8864	0.0840	0.8024	0.8733	0.6020
	400	2.60	3.07	4.45	0.9109	0.9300	0.0385	0.8915	0.8883	0.7214
	800	2.90	2.17	3.31	0.9338	0.9520	0.0177	0.9343	0.8906	0.7770
	1600	3.20	1.69	2.94	0.9412	0.9642	0.0063	0.9579	0.8916	0.8039
	4000	3.60	1.38	3.15	0.9370	0.9678	0.0014	0.9664	0.8929	0.8085
	8000	3.90	1.29	3.18	0.9365	0.9701	-0.0007	0.9694	0.8944	0.8120
	∞	∞	1.05	2.94	0.9413					

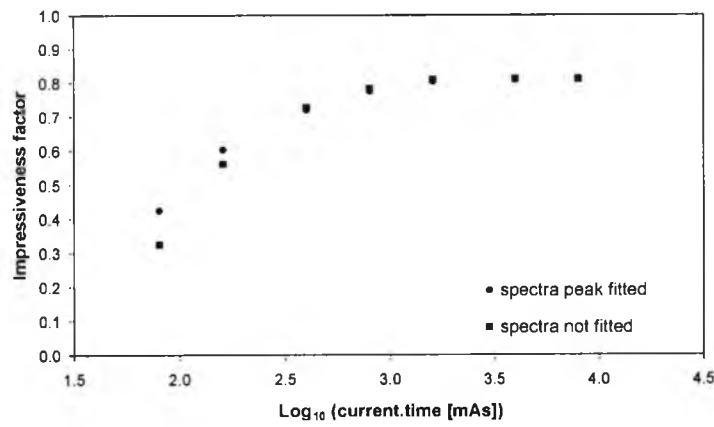
Table 8-8. Results from the EDXRD two component sample system calibrated experiments (no additional attenuation) with fitted peaks. They are divided into three blocks, being error results from repeatability (leading to a precision impressiveness factor, IF_P), linear regression fit parameters (leading to an accuracy impressiveness factor, IF_A), and linear regression fit correlation results (leading to a correlation impressiveness factor, IF_C). Repeatability errors are derived from the mean of measurement set errors (first column in the block) plus two standard deviations (SD) (second column). These errors are also projected for an infinite measurement time. The final column combines the results into an all-inclusive EDXRD IF.



(a)



(b)



(c)

Figure 8-10. Improvements in two component EDXRD impressiveness factors (IF) by using peak fitting, for measurements with no additional attenuation. The IFs were calculated for all three analysis techniques (bone region photon counts, normalisation by bone/marrow ratio and normalisation to unity). Note how the improvement is only effective for low spectra acquisition mAs.

results. Note how the improvement is apparent for low acquisition mAs with little change for higher mAs.

To summarise, the bone region analysis maximum precision (minimum detectable resolution) was achieved at 8000 mAs acquisition, being a bone density change of 6.6% (bone density error of $\pm 3.31\%$), identical to the unfitted result. The R^2 value is 0.9626 (near identical). These results, with an accuracy impressiveness factor (IF_A) of 0.9281 (again identical), combine to an overall EDXRD IF of 0.8343. Precision was projected to a baseline of 7.2%. A marginally improved accuracy IF_A was recorded at 1600 mAs.

Performance was reduced in all three areas (precision, accuracy and correlation) when using bone/marrow ratio analysis, in a similar fashion as unfitted. Again performance is generally poor when compared to the other analysis methods.

Bone region analysis precision and accuracy were improved by normalising to unity at the expense of correlation (and overall EDXRD IF). Precision at 8000 mAs acquisition was a bone density change of 6.4% (bone density error of $\pm 3.18\%$), identical to the unfitted result. The R^2 value was 0.8944 (marginally poorer than unfitted). The accuracy impressiveness factor (IF_A) was 0.9694 (near identical). Overall EDXRD IF was 0.8120 (near identical). Precision was projected to a baseline of 5.9%. Maximum precision was recorded at 1600 mAs.

The similarity with the unfitted results ends when considering the results at the lowest acquisition mAs. As demonstrated by figure 8-10, improvement in performance when using peak fitting (in terms of precision, accuracy and correlation) is most apparent at 80 and 160 mAs acquisition. Exceptions are precision at 80 mAs (all calibration methods) and accuracy at 1600 mAs (for bone/marrow ratio analysis, a generally poor method).

Conclusions

For higher acquisition mAs, peak fitted two component EDXRD results (no additional attenuation) are near identical and demonstrate similar patterns to the unfitted results. This is expected since the high photon counts associated with these acquisition mAs's provide good statistics for spectrum generation. In other words, the peak fitting does little to change the spectra. There is marginal reduction in the maximum precision performance obtained by fitting exponential curves to the errors but this is likely to be due only to the curve shape change at lower mAs levels. A greater number of spectra recording times would likely bring the error base in line with the unfitted results.

Peak fitting offers improvement at low acquisition mAs, notably at 80 and 160 mAs, clearly apparent in the IF plots of figure 8-10. Although the fitting does not improve performance to the maximum achievable at high acquisition mAs, the increase in performance might be important in clinical situations where dose considerations restrict longer patient exposure.

8.2 DEXA BONE DENSITY MEASUREMENTS USING A TWO COMPONENT SAMPLE SYSTEM

These DEXA experiments were performed using the same two component trabecular bone sample sets that were used for the EDXRD experiments. They were intended to provide a comparison for the EDXRD results. DEXA measurements were obtained using the 10 sample measurement set with three attenuation conditions to simulate the three clinical sites (calcaneus, radius and femoral neck). Measurements with no additional attenuation are not included.

Method

DEXA measurements were obtained using the same method as described for the one

Sample Set	Number of Experimental Conditions				Total Scans
	Samples	Repeated Measurements	Scan Settings	Attenuation Conditions	
Measurement with repeats (for precision)	3	10	2	3	180
Measurement without repeats	7	1	2	3	42
Total Scans for All Variations					222

Table 8-9. Summary of the number of experimental variations used to generate DEXA scans. Only scans for three samples were repeated to match the EDXRD data. The two scan settings were fast array and high definition.

component sample system in chapter seven (section 7.2). The additional aluminium and Perspex (simulating cortical bone and soft tissue) attenuation used for clinical site simulation is given in table 8-1, with the experimental configuration shown in figure 8-1. The added attenuation matches that of the EDXRD two component experiments. Again fast array and high definition DEXA scan settings were used.

The number of experimental variations is summarised in table 8-9.

8.2.1 Calibrated Two Component DEXA Analysis

This section discusses the DEXA results for the two component sample system with clinical site simulations equivalent to those of EDXRD (section 8.1).

Results

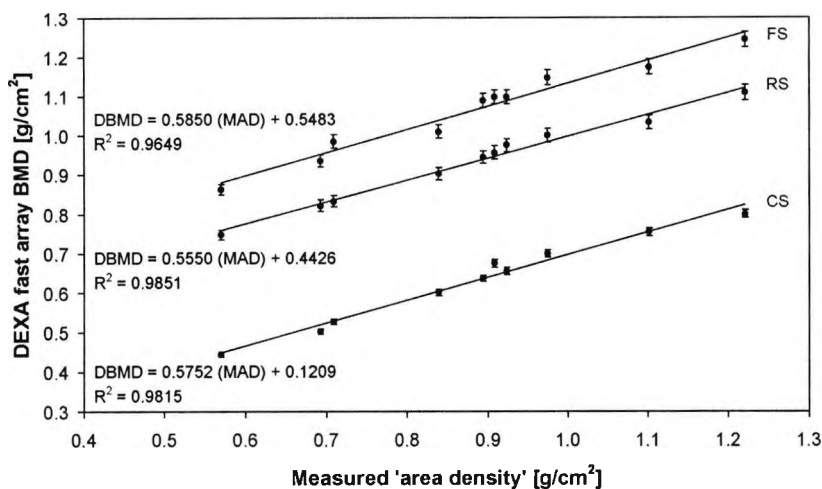
The same three samples as for EDXRD were used for repeat DEXA measurements to provide an indication of expected error and therefore system precision. With this limited set of repeats, errors for the plotted results (figure 8-11) were calculated as generalised errors (mean of repeated errors plus two standard deviations) and, as with EDXRD, are not statistically valid (since only three sets of repeated measurements were used in the calculation). These results should only be used for comparison with each other and the EDXRD results (section 8.1).

Six measurement conditions were investigated, being all combinations of fast array and high definition scanning with the three clinical site simulations. These results for the 10 sample measurement set are shown in figure 8-11. DEXA 'bone mineral density' (BMD, in g/cm^2) was plotted against sample 'area density', calculated using physically measured mass and area. As expected, the DEXA BMD plots shift up with added attenuation since the technique includes the added attenuation in the measurement.

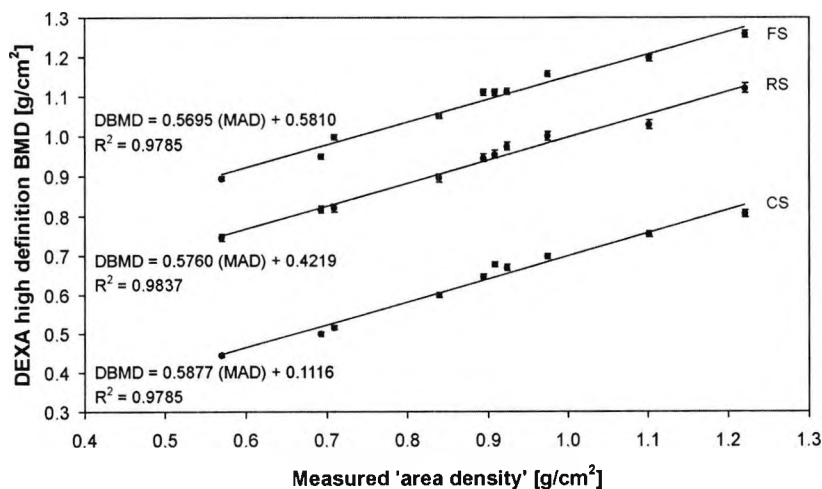
In the usual way, results for precision, accuracy and correlation were calculated (including impressiveness factors) and are presented in table 8-10.

In this summary, it must again be appreciated that the limited repeat measurements may not have provided sufficient data for statistical validity for general comparisons. However they may be compared with each other and the EDXRD results (section 8.1) obtained by the same means.

For the calcaneus simulation, the maximum precision (minimum detectable resolution)



(a)



(b)

Figure 8-11. DEXA measurement two component sample set results. Errors were derived from the generalised error calculations for each measurement condition using measurements of three samples from each set. The results were generated using the DEXA fast array (a) and high definition (b) scan settings. Each plot shows results from experiments with attenuation added for calcaneus simulation (CS), radius simulation (RS) and femoral neck simulation (FS). Note how the DEXA BMD values shift up with increasing attenuation. The linear regression fits are shown relating DEXA bone mineral density (DBMD) to the measured 'area density' (MAD). Corresponding R² correlations are also shown.

Attenuation Condition	DEXA Scan Setting	Sample Error % Mean	Sample Error % Mean +2SD	Precision IF _P	Linear ax+b Fit a	Linear ax+b Fit b	Accuracy IF _A	Linear ax+b Fit R ² (IF _C)	DEXA IF
calcaneus simulation	fast array	0.85	1.38	0.9725	0.5752	0.1209	0.4543	0.9815	0.4336
	high definition	0.71	1.09	0.9782	0.5877	0.1116	0.4761	0.9785	0.4557
radius simulation	fast array	0.94	1.73	0.9654	0.5550	0.4426	0.1124	0.9851	0.1069
	high definition	0.56	1.12	0.9776	0.5760	0.4219	0.1541	0.9837	0.1482
femoral neck simulation	fast array	1.09	1.63	0.9674	0.5850	0.5483	0.0367	0.9649	0.0343
	high definition	0.57	0.67	0.9866	0.5695	0.5810	-0.0115	0.9785	-

Table 8-10. Results from the DEXA two component sample system calibrated experiments with added attenuation for calcaneus, radius and femoral neck simulation (see table 8-1). Repeatability errors are derived from the mean of three measurement set sample errors plus two standard deviations (SD). Since a limited sample set was used to determine repeatability, these results should only be used for equivalent comparisons.

achieved was a bone density change of 2.2% (bone density error of $\pm 1.09\%$) when using high definition scanning. The R^2 values were similar, being 0.9815 (fast array) and 0.9785 (high definition).

The additional attenuation simulating the radius clinical situation yielded a similar best result, maximum precision being 2.2% (bone density error of $\pm 1.12\%$) for high definition. R^2 values were 0.9851 (fast array) and 0.9837 (high definition).

A marginal improvement in high definition maximum precision was apparent with the femoral neck simulation, being 1.3% (bone density error of $\pm 0.67\%$). R^2 values were 0.9649 (fast array) and 0.9785 (high definition).

Conclusions

Similar conclusions may be drawn from these two component sample system results as from the previous chapter for marrow free trabecular bone samples. Table 8-10 demonstrates a clear improvement in precision (IF_P) as attenuation simulating clinical sites increases. This might be expected, since the DEXA scan settings used were designed for axial region bone density measurement with relatively high surrounding tissue density. Correlation (IF_C) deteriorates marginally as attenuation increases but again is impressive.

As discussed in chapter seven (section 7.2.1), accuracy (IF_A) results are not meaningful – the poor IF_{AS} (and overall DEXA IFs) merely reflect the inability of DEXA to measure specific bone volume densities. These results should not be considered a criticism of the DEXA method but may be used as a comparative demonstration of EDXRD merits.

8.3 COMPARISON OF EDXRD AND DEXA RESULTS

This study of EDXRD and DEXA measurement systems was conducted throughout using two component trabecular bone sample cubes and so any conclusions are with regard to this specific sample type. As with the one component conclusions, the results relate to these specific EDXRD and DEXA experiments and should not necessarily be applied to all such measurement systems.

These two component sample system DEXA and EDXRD studies obtained results from three areas of measurement system performance, being precision, accuracy and correlation. For these comparisons, only the three clinical site simulations (calcaneus,

radius and femoral neck) are considered since DEXA was not performed without additional attenuation.

8.3.1 Comparison of Calibrated Two Component Results

Impressiveness factors (IFs) for precision, accuracy and correlation were calculated for various measurement conditions for both EDXRD and DEXA. IFs calculated using data from the best case experimental conditions are summarised in table 8-11 (table 8-12 details variations, generally minor, from the best performance patterns).

In terms of precision, expressed in this chapter as an impressiveness factor for precision (IF_P, equation 8.8), DEXA is shown to outperform EDXRD under all measurement conditions. This is consistent with the conclusion made for the one component sample experiments (chapter seven, section 7.3). The best DEXA precision performance was for the femoral neck simulation, likely due to the higher attenuation more closely approximating the clinical conditions under which these DEXA settings were designed

Attenuation Condition	Bone Density Measurement Modality	Best Case Condition Impressiveness Factors			
		Precision IF _P	Accuracy IF _A	(R ²) Correlation IF _C	Combined IF
calcaneus simulation	EDXRD _(UN)	0.9692	0.9156 _(a)	0.9469	0.8403
	DEXA	0.9782	0.4761	0.9785 _(b)	0.4557
radius simulation	EDXRD _(UN)	0.9357 _(c)	0.8584 _(d)	0.9356 _(e)	0.7514
	DEXA	0.9776	0.1541	0.9837 _(f)	0.1482
femoral neck simulation	EDXRD _(BR)	0.9357	0.5888 _(g)	0.9464 _(h)	0.5214
	DEXA	0.9866	- _(i)	0.9785	- _(j)

Table 8-11. Summary of best case condition impressiveness factors, presented here for comparison purposes. The (expected) best case measurement condition for EDXRD was 1000 seconds (16 000 mAs) and for DEXA was high definition. The best performing EDXRD analysis method changes from unity normalisation (UN) for low levels of added attenuation to bone region analysis (BR) for higher levels of added attenuation. In some cases, the best measurement condition did not yield a maximum IF. These cases, generally marginal, are detailed in table 8-12. Footnote (a) to (j) details are presented in table 8-12.

Attenuation Condition	Bone Density Measurement Modality	Impressiveness Factor Performance Deviation from Expected Best Case Condition
calcaneus simulation	EDXRD _(UN)	(a) IF _A was a maximum of 0.9187 at 3200 mAs.
	DEXA	(b) IF _C was 0.9815 for fast array.
radius simulation	EDXRD _(UN)	(c) IF _P improved to 0.9589 with unity normalisation.
	EDXRD _(UN)	(d) IF _A was a maximum of 0.8758 at 800 mAs.
	EDXRD _(UN)	(e) IF _C was a maximum of 0.9519 at 800 mAs.
	DEXA	(f) IF _A was 0.9851 for fast array.
femoral neck simulation	EDXRD _(BR)	(g) IF _A was a maximum of 0.5933 at 800 mAs.
	EDXRD _(BR)	(h) IF _C was a maximum of 0.9600 at 800 mAs.
	DEXA	(i) IF _A was negative (very poor) with high definition. There was only marginal improvement with fast array.
	DEXA	(j) Overall IF was not possible (because of i).

Table 8-12. Impressiveness factor performance deviation from expected best case condition. Generally they were marginal but are recorded here for completeness. The note letters may be cross referenced with those marked in table 8-11.

to operate. The results in table 8-11 show that DEXA has a fairly consistent precision performance whereas EDXRD deteriorates with increasing attenuation.

Also agreeing with the one component results, DEXA outperforms EDXRD in terms of correlation (IF_C, equation 8.11). This is clearly demonstrated by the results in table 8-11, which also show a fairly consistent correlation performance for both EDXRD and DEXA.

As expected, EDXRD surpasses DEXA in its ability to measure the density of selected volumes of bone. This is reflected by the impressiveness factor for accuracy (IF_A, equation 8.10). Once again, the best EDXRD IF_A is for the condition with least attenuation, the calcaneus simulation, deteriorating a little for the radius simulation and significantly with the femoral head attenuation. As for the one component sample

experiments, the inability to recover low energy photons in the EDXRD spectra using attenuation correction is likely to account for this IF_A drop.

It is worth repeating that although DEXA performs poorly in terms of accurately measuring the density of selected volumes of bone, DEXA was not designed to perform in this manner. It measures all bone in the photon beam path and, as such, the contribution of the added cortical bone simulation should be included in any calculation of the true accuracy of DEXA.

As a final comment on the performance of EDXRD as assessed in this project, it clearly does not perform to the same standard as DEXA in terms of precision and correlation. For the accurate determination of internal trabecular bone volume densities, an important consideration in the determination of osteoporosis, EDXRD shows some potential. These results suggest the most effective performance is likely to be in examining clinical sites with limited external attenuation, such as the calcaneus. Problems with data precision might also be improved with refinement of the experiment, discussed further in chapter eleven.

One final problem with EDXRD as a potential clinical application is the high dose experienced for highest performance. This is investigated in the following chapter.

Chapter 9

DOSE CONSIDERATIONS

The bone density measurement experiments described in chapter seven would only be performed in a laboratory environment since a one component sample system was employed. With this scenario, radiation dose would not need to be considered since a patient is not involved in the procedure. However if the two component sample system methods described in chapter eight were used in a clinical environment, radiation dose becomes an important factor. Benefits from performing a radiological procedure must outweigh risks to the patient (chapter one, section 1.6), including comparison between densitometry methods with respect to both effectiveness of the technique and the radiation dose required to achieve the results.

Radiation dose received from EDXRD measurements was estimated for the three clinical site measurements simulated in the experiments of chapter eight, being the radius, calcaneus and femoral head. These estimates were calculated to complement the measurement scan tube current \times time (mAs) variable, providing a 'dose cost' for each result. Finally these dose costs were compared to dose estimates in published literature for DEXA and other bone densitometry methods.

Definitions of the various dose expressions are provided in chapter one, section 1.6.1.

This chapter comprises:

Section 9.1 A description of the EDXRD effective radiation dose estimation experiments. The results are compared with estimates from other studies investigating the effective doses of other densitometry modalities, notably DEXA.

9.1 EDXRD DOSE ESTIMATION EXPERIMENT

The starting point for effective dose estimation is the measurement of absorbed dose. This was achieved by using thermoluminescent dosimetry (TLD), a discussion of which is provided in chapter one, section 1.6.2. Lithium fluoride TLD-100 chips with dimensions of approximately $3 \times 3 \times 1 \text{ mm}^3$ were used.

Method

For this experiment, 41 TLDs were required. 36 were used for the three clinical site simulations, within which were three dose site positions (four TLDs for each site). The dose sites measured for each simulation were the skin entrance, cortical surface and trabecular core. A further five TLDs were used for background radiation controls.

45 TLDs were calibrated (four more were calibrated but not used) by first annealing them to release any residual trapped electrons (using a Harshaw QS 3500 TLD reader). Five were placed well away from the x-ray source to provide background readings. The remaining TLDs were exposed to a known integrated dose using an x-ray tube, calibrated using a similarly exposed standard ionisation chamber.

A 15 cc ionisation chamber with Keithley 35050A dosimeter was exposed 12 times (72.3 kV_p (measured using a potential divider), 100 mA, 0.8 seconds, six exposures before the TLDs and six after). The absorbed dose in mGy was recorded for each and the mean calculated. The annealed TLDs were exposed six times with the same x-ray tube settings. Both the chamber and TLDs were positioned in the primary beam on five wax tissue equivalent slabs for these exposures, in order to introduce dose from tissue scattering (being more akin to the clinical situation).

A time-temperature profile (TTP) for each TLD was acquired using the Harshaw QS 3500 TLD reader. The TTP is a measurement of charge (in nanocoulombs) from photomultiplication related to TLD luminescence (as the TLDs are heated in the reader). Nitrogen gas was used to exclude oxygen during this procedure, since oxygen would add light by luminescence. Integrated charge for each TLD was recorded from the 'read' portion of the TTP (which also includes 'pre-heat', 'anneal' and 'cool' portions). A calibration factor for each TLD was calculated by relating charge to dose:

$$\text{calibration factor} = \frac{\text{reading} - \text{background mean}}{\text{absorbed dose}} \quad [9.1]$$

where the reading and background mean (from the TLDs) are in nC and the absorbed dose (from the ionisation chamber) is in mGy.

The fixed parameter EDXRD diffractometer was assembled as described in chapter six, section 6.1. The x-ray source was set to 70 kV_p and 8 mA throughout these experiments.

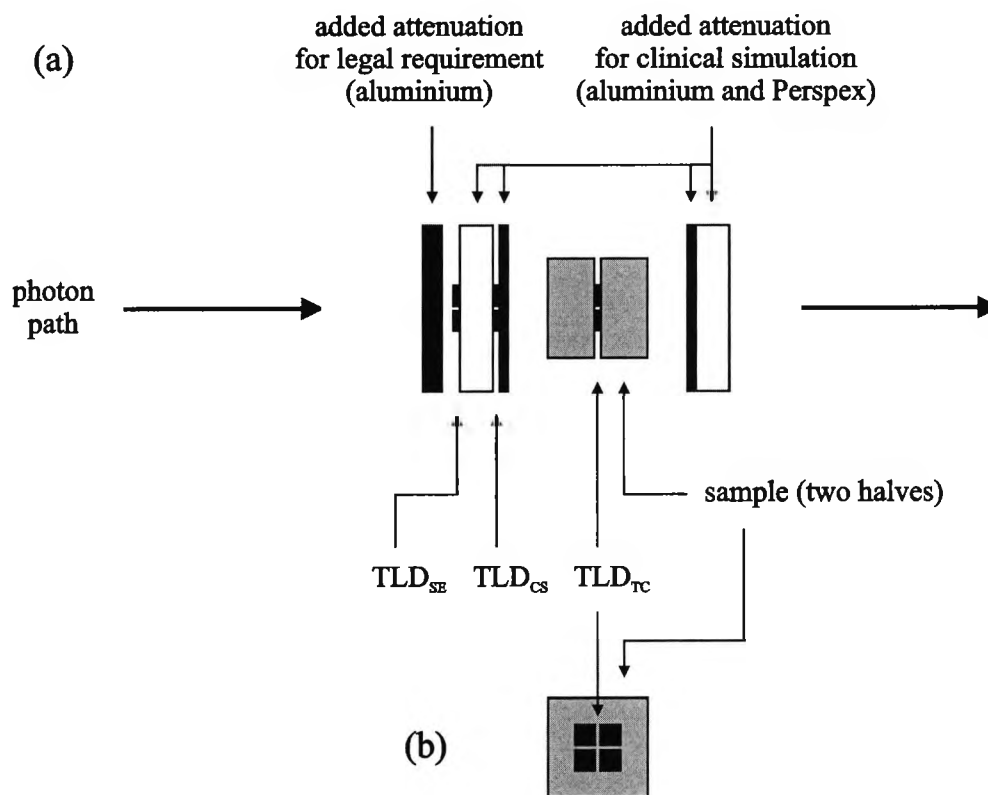


Figure 9-1. Positioning of the TLD devices at various points within a clinical site simulation. TLD location for skin entrance dose (TLD_{SE}), cortical surface dose (TLD_{CS}) and trabecular core dose (TLD_{TC}) is shown with aluminium and Perspex for the clinical simulation. The attenuation for legal filtration was fixed at 2.5 mm of aluminium throughout.

Sets of four TLDs were positioned at the three measurement sites shown in figure 9-1. These were intended to measure absorbed doses for estimation of skin entrance dose (TLD_{SE}), cortical surface dose (TLD_{CS}) and trabecular core dose (TLD_{TC}).

A single bone sample cube was used for all measurements of this experiment, with an apparent density chosen to fall within the middle of the sample range of the set of 10 cubes used for the experiments of chapter eight. This compromise was considered to yield sufficiently accurate results for these dose estimations. The cube was cut in half with the effect of losing approximately 1 mm from its depth. This was ideal since the trabecular core TLDs spaced the two halves by approximately this amount. Marrow substitute was introduced into the two halves (chapter five, section 5.6) and sealed using cling film and tape. It was particularly important to ensure these seals did not leak since

fat contamination of the TLDs would interfere with dose readings and cause permanent damage. Quantities of aluminium and Perspex for each clinical simulation are given in table 8-1 (chapter eight, section 8.1).

Five TLDs were placed well away from the x-ray source to provide background readings.

EDXRD exposures were made in the same manner as the measurements described in chapter eight. The sample was scanned in 10 positions of 1 mm steps for 60 seconds at each position. The x-ray tube current of 8 mA therefore resulted in 4800 mAs for each scan.

Integrated charges from the 'read' portions of the TTPs for each TLD were obtained using the TLD reader in the same manner as described above. They were converted into absorbed dose using equation 9.2 with the calibration factors previously obtained for each TLD.

$$\text{absorbed dose} = \frac{\text{reading} - \text{background mean}}{\text{calibration factor}} \quad [9.2]$$

Results

The first column in table 9-1 shows the absorbed dose results from these experiments. Each result was obtained from a mean of absorbed dose from the four TLDs at each location. Skin entrance dose, near identical for each clinical simulation, is presented as a mean from three experimental measurements. An absorbed dose rate (mGy / second at 8 mA) and absorbed dose rate per mA (mGy / mAs) for each dose is also presented for application to doses measured at exposures other than 600 seconds at 8 mA. This is useful since the EDXRD measurements in chapter eight (section 8.1) with clinical site simulation were obtained using a tube current of 16 mA.

The absorbed doses were then weighted for radiation type (equivalent dose) and tissue type (effective dose) according to the recommendations of the International Commission on Radiological Protection (ICRP, 1991) and the National Council on Radiation Protection and Measurements (NCRP, 1993). Discussion and formulae for these conversions may be found in the introduction (chapter one, section 1.6.1).

Equivalent doses are not shown since the weighting factor for x-rays is $w_R = 1$. The equivalent doses are simply the absorbed dose values expressed in Sieverts.

Clinical Simulation	Dose Measurement Site	Absorbed Dose			Effective Dose			
		Dose (for 4800 mAs) [mGy]	Dose Rate (for 8 mA) [mGy/s]	Dose Rate per mA [mGy/mAs]	Tissue Weighting Factor	Dose (for 4800 mAs) [mSv]	Dose Rate (for 8 mA) [μ Sv/s]	Dose Rate per mA [μ Sv/mAs]
radius	skin entrance	94.79	0.158	0.020	0.01	0.95	1.58	0.197
	cortical surface	75.28	0.125	0.016	0.01	0.75	1.25	0.157
	trabecular core	28.40	0.047	0.006	0.05	1.42	2.37	0.296
	total	-	-	-		3.12	5.20	0.650
calcaneus	skin entrance	94.79	0.158	0.020	0.01	0.95	1.58	0.197
	cortical surface	82.81	0.138	0.017	0.01	0.83	1.38	0.173
	trabecular core	38.27	0.064	0.008	0.05	1.91	3.19	0.399
	total	-	-	-		3.69	6.15	0.769
femoral head	skin entrance	94.79	0.158	0.020	0.01	0.95	1.58	0.197
	cortical surface	38.43	0.064	0.008	0.01	0.38	0.64	0.080
	trabecular core	11.56	0.019	0.002	0.05	0.58	0.96	0.120
	total	-	-	-		-	-	-

Table 9-1. Results from the EDXRD two component sample system dose estimation experiments. The first block of results shows the absorbed doses (in mGy), measured using TLDs for 600 seconds at 8 mA. An absorbed dose rate (mGy / second at 8 mA) and absorbed dose rate per mA (mGy / mAs) for each dose is also presented for application to doses measured at exposures other than 600 seconds at 8 mA. Equivalent doses are not shown since these are simply the absorbed dose values expressed in Sieverts. Effective doses are presented (along with dose rates) after conversion from equivalent doses using the relevant tissue weighting factors (w_T). Note that the skin entrance dose is calculated as a mean of three results and is the same for each clinical simulation. All results were obtained using an x-ray tube potential of 70 kV_p.

Clinical Simulation	Dose Measurement Site	Effective Dose (for each measurement time [seconds], 16 mA current) [μSv]						
		10 seconds (160 mAs)	20 seconds (320 mAs)	50 seconds (800 mAs)	100 seconds (1600 mAs)	200 seconds (3200 mAs)	500 seconds (8000 mAs)	1000 seconds (16 000 mAs)
radius	skin entrance	32	63	158	316	632	1580	3160
	cortical surface	25	50	125	251	502	1255	2509
	trabecular core	47	95	237	473	947	2366	4733
	total	104	208	520	1040	2080	5201	10401
calcaneus	skin entrance	32	63	158	316	632	1580	3160
	cortical surface	28	55	138	276	552	1380	2760
	trabecular core	64	128	319	638	1276	3189	6379
	total	123	246	615	1230	2460	6149	12299
femoral head	skin entrance	32	63	158	316	632	1580	3160
	cortical surface	13	26	64	128	256	641	1281
	trabecular core	19	39	96	193	385	964	1927
	total	-	-	-	-	-	-	-

Table 9-2. Effective dose estimates for each clinical simulation, dose measurement site and tube current × scanning time (mAs). Values for total effective dose may be estimated by summing the doses for each dose measurement site (appendicular sites only). Values are calculated for a tube current of 16 mA (at 70 kV_p) in order to match the clinical site simulation measurements of chapter eight (section 1.1.8).

Effective doses are presented (along with dose rates) after conversion from equivalent doses using the relevant tissue weighting factors (w_T) shown in table 9-1. They provide a proportional estimation of the probability of cancer or genetic effects occurring as a result of the radiation received by the designated tissue. Effective dose estimates for each clinical simulation, dose measurement site and tube current × scanning time were calculated from the effective dose rate per mA values from table 9-1 and are presented in table 9-2. A tube current of 16 mA (at 70 kV_p) was chosen to match the clinical site simulation measurements of chapter eight (section 1.1.8).

Measurement Modality	Equipment	Examination	Kusama <i>et al.</i> (1995)	Huda and Morin (1996)
			Effective Dose [μSv]	Effective Dose Equivalent [μSv]
DEXA	QDR-1000	whole body	4.2	
	QDR-1000	vertebra	1.3	
	DPX	whole body	-	
	DPX	vertebra	5.8	
	XR-26	whole body	0.08	
	XR-26	vertebra	3.7	
	-	PA scan		
QCT	-	vertebra	110	300
	-	SPR + 3 CT slices		
radiograph	-	AP or lateral		100

Table 9-3. Effective dose and effective dose equivalent estimates from studies by Kusama *et al.* (1995) and Huda and Morin (1996). Estimates are provided for DEXA, QCT and the production of a radiograph. For the Kusama *et al.* dose for DPX whole body, the result was below detection level. For the Huda and Morin QCT dose value, a 'scout' planar scan projection radiograph (SPR) was taken prior to the tomographic examination. Some examination equipment is not known (-).

Values for the total effective dose from a given radiological examination of an appendicular site may be estimated by summing the doses from each of the three measurement sites. They are given in table 9-2 for the radius and calcaneus simulations. They were not calculated for the femoral head simulation since additional complications arise from dose to adjacent organs due to photon scattering.

Conclusions

Effective dose estimates (table 9-2) may be considered as 'dose costs' for each of the rows in tables 8-6a, 8-6b and 8-6c (for the three clinical site simulations) of chapter eight, section 8.1. Clearly the dose cost increases with increased acquisition mAs and must be balanced against any increase in the precision, accuracy and correlation of the EDXRD results obtained.

Effective dose estimates may be used to compare risks from radiological examinations and are used here to compare the EDXRD dose risks from the measurements of this study with those of DEXA and other bone densitometry methods. Each densitometry method obtains a result by very different means and by measuring different sites in the body. It is however reasonable to compare estimated doses since the result of each modality is a measure of bone density, regardless of the method used to obtain it.

Effective dose estimates were taken from a study by Kusama *et al.* (1995) and effective dose equivalent estimates from Huda and Morin (1996). Effective dose equivalent is an older definition used to estimate risk from exposure to radiation. It was superseded by the effective dose, which is similar with different weighting factors. Relative dose values are comparable regardless of the method used and, in general, results from effective dose and effective dose equivalent calculations do not differ greatly (Huda and Morin, 1996). As such, the magnitudes of the results from each study may be compared.

By comparing the total effective dose estimates from tables 9-2 and 9-3, it can be seen that the EDXRD measurement method as it stands is costly in terms of radiation effects. Considering doses from quantitative computed tomography (QCT), an effective but dose costly densitometry method, EDXRD scanning time would have to be restricted to a range of approximately 10 to 30 seconds (at 16 mA, 70 kV_p) to be comparable (radius or calcaneus simulation). Similarly for radiographic methods, an EDXRD limit of 10 seconds would need to be imposed.

If a general effective dose of around 4 μ Sv is taken as a typical DEXA value, the dose limitations of EDXRD become very apparent. A mean of the lowest EDXRD tube current \times scanning time (160 mAs from 10 seconds at 16 mA, 70 kV_p) total effective doses for the radius and calcaneus (resulting in poor performance) is 114 μ Sv, a factor of around 29 times that of the general DEXA dose. The results of chapter eight, section 8.1.2 suggest that maximum EDXRD effectiveness in terms of precision might be approached by peak fitting bone region analysed spectra recorded for a minimum of

800 mAs (100 seconds at 8 mA, 70 kV_p). A mean of the radius and calcaneus total effective doses for an 800 mAs scan (50 seconds at 16 mA, 70 kV_p) is 568 μSv, a factor of around 142 times that of DEXA. (Peak fitting was not attempted with clinical simulations but the unattenuated results do suggest 800 mAs at 70 kV_p might be acceptable – figure 8-9c.) Tables 8-6a and 8-6b show the unfitted clinical simulation results are not improved significantly above 8000 mAs of EDXRD scanning (500 seconds at 16 mA, 70 kV_p). A mean of the radius and calcaneus total effective doses for an 8000 mAs (again 500 seconds at 16 mA, 70 kV_p) is 5675 μSv, 1419 times that of DEXA. In each of these cases, EDXRD has a lower precision and correlation than DEXA but is significantly better in terms of accuracy.

For EDXRD to compete with DEXA for clinical applications in terms of precision, the dose cost would need to be significantly reduced. Providing the peak fitting method offers similar improvements to the clinical situations, effective dose would still need to be reduced by approximately 142 times to be comparable to DEXA (still with lower precision, which would require improvement).

In addition to peak fitting, effective at lower mAs's (chapter eight, section 8.1.2), further methods to reduce EDXRD dose are suggested as further work in chapter 11, section 11.3.4. One such method involves the measurement of 12 EDXRD 6° scattered spectra simultaneously. Decreasing the 800 mAs scan (50 seconds at 16 mA, 70 kV_p) by this factor potentially reduces the EDXRD dose cost of 142 times that of DEXA to approximately 12 times. A further extension of this method collects 36 spectra at 5°, 6° and 7°. Although the effectiveness of the 5° and 7° spectra is likely to be reduced (chapter four, section 4.1), there is a potential dose cost saving of the order of something less than 36 times, bringing the EDXRD dose cost to the order of four times that of DEXA. If this dose cost is achievable and acceptable, EDXRD still has some potential in the clinical environment. If it is not acceptable, EDXRD would still have great potential in the laboratory environment, for example measuring bone densities of archaeological specimens with a far greater accuracy than DEXA can achieve (Farquharson *et al.*, 1997b).

Chapter 10

AN INVESTIGATION INTO BONE SAMPLE STRENGTH

This piece of work is intended to illustrate that trabecular bone strength, the internal resistance of a material to deformation, is not determined solely by density. Trabecular architecture, discussed in chapter one, section 1.2, is thought to play an important role in bone strength (trabecular systems coinciding with force direction) and therefore in determining risk of fracture (Maquet, 1985).

Compression testing is commonly used to determine the mechanical properties of both cortical and trabecular bone (Bensen, 2000). Trabecular bone may exhibit high variability in compression properties. One such investigation of bone cubes in three orientations (taken from various locations) demonstrating distinct anisotropic behaviour (Ciarelli *et al.*, 1991).

This study was not intended to be exhaustive research into this field. There is a large canon of literature on this topic to which the reader is directed, a broad selection of which is presented in the book by An and Draughn (2000). This work forms a coda designed to complement the bone mineral density (BMD) work already presented, in order to illustrate that bone strength is a function of both bone density and structure, not BMD alone.

This chapter comprises:

Section 10.1 A description of the trabecular bone compression experiments. The $15 \times 15 \times 15 \text{ mm}^3$ sample cubes were used with no marrow in the trabecular spaces.

10.1 TRABECULAR BONE SAMPLE COMPRESSION

The sets of 10 and 48 bone sample cubes ($15 \times 15 \times 15 \text{ mm}^3$) as used in the one component densitometry experiments of chapter seven were utilised for these compression tests.

Trabecular samples in isolation will not exhibit the same mechanical properties as whole bones but since the bone cubes were prepared with the same dimensions and were cut from approximately the same location within the femoral heads (chapter five, section 5.1), they are suitable for comparative experiments. In undertaking experiments of this kind, it is important to use samples of uniform size to enable direct comparison (An and Bensen, 2000). In addition, an uneven specimen surface results in a triaxial stress field, leading to an incorrect estimation of specimen stiffness. It was therefore important that during sample preparation the end surfaces were cut to be as parallel as possible (An and Bensen, 2000).

Ideally the cubes would have been subjected to these tests as two component specimens, with marrow substitute in the trabecular spaces. This approach would closer represent an *in-vivo* condition. Again the isolated nature of the cubes made this approach impossible since the marrow would not have been physically restrained at the cube surfaces.

Compression was performed using the one component samples dry since this condition was considered to offer the greatest level of control for these comparative tests. Such investigations have been performed employing both wet and dry methods (An and Bensen, 2000).

The tests were performed at room temperature.

Method

A Lloyd Instruments M30K Tensile Test Machine with Lloyd Instruments Data Analysis Package Dapmat 2.2 software was used to apply compressive forces to the bone samples (by two parallel lead screw drives) and record the resultant data. A 2000 newton force transducer (load cell) was used throughout, which contained the gauges used to measure the force being applied.

The M30K was calibrated using known weights with an extensometer. A guide template was made and used to enable central positioning of each cube on the load platen.

A number of bone cubes with apparent densities spanning the sample range were compressed to failure in order to ascertain a general load limit before the samples exhibited plastic behaviour (figure 1-5 in chapter one, section 1.2.3, illustrates the energy regions apparent when loading bone sample cubes). This limit was necessary in order to prevent sample damage, since at this point in the project they were still required

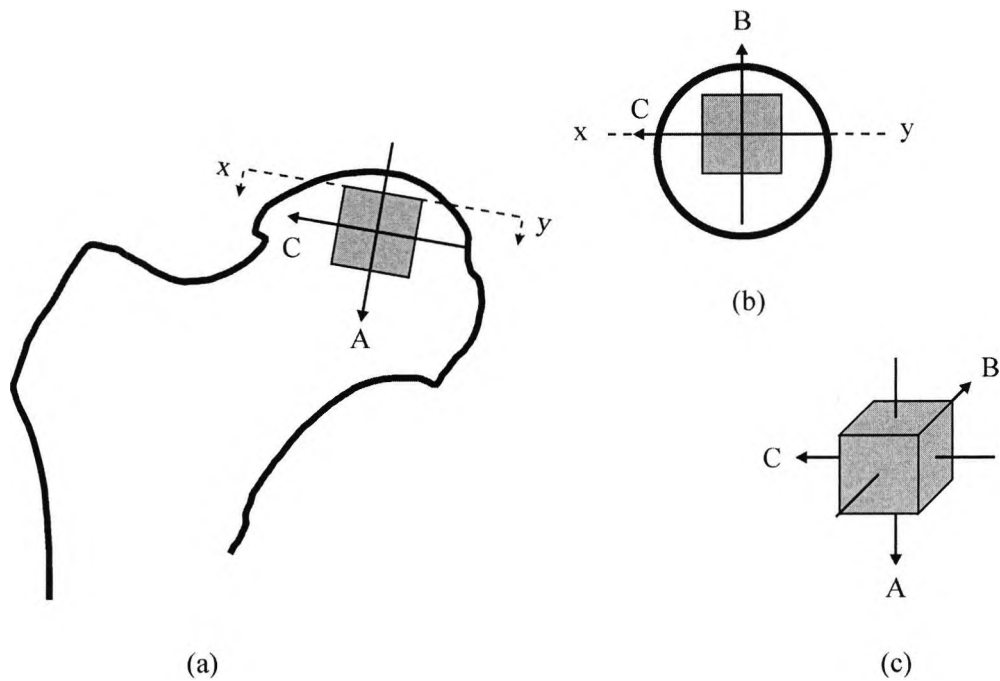


Figure 10-1. Diagrams showing how bone sample cube orientation relates to the original location within the femoral head (c/w figures 1-3 and 1-4, chapter one, section 1.2.2, and figure 5-1, chapter five, section 5.1). The illustrations show orientation from the antero-posterior view (a), from a superio-inferior view (b, section x-y), and how these orientations relate to the sample cube (c). The compression forces are shown as 'A', 'B' and 'C'. Note how compression force 'A' is parallel and forces 'B' and 'C' are perpendicular to the medial trabecular group, shown in the above referenced figures.

for post demineralisation densitometry experiments. A safe load limit was found to be 600 N, so the test machine was limited to this force. It was also set to apply a maximum displacement of 1 mm and to compress at a speed of 0.1 mm/minute.

Each of the bone cube samples was compressed within the limits described for each of the three possible orientations 'A', 'B' and 'C', illustrated by figure 10-1. The figure shows how the orientation of the bone sample cube relates to the original location within the femoral head (chapter one, section 1.2.2, and chapter five, section 5.1). The direction of compression force 'A' is parallel and forces 'B' and 'C' are perpendicular to the medial trabecular group, shown as 'M' in figures 1-3, 1-4 and 5-1. Force direction 'A' therefore simulates natural body forces incident on this trabecular region.

Load-displacement data was collected for each compression. Data was not recorded during the period when the force was removed since trabecular bone is known to exhibit some properties of inefficiency in the storage and release of energy, potentially resulting in a load-displacement hysteresis loop (An *et al.*, 2000a).

Compression measurements were collected once for each orientation for the set of 48 samples and 10 times for the set of 10 samples, in order to provide for a calculation of precision. The sample cubes were left in place in the test apparatus for the 10 compressions as this is the recommended best practice for repeated measurements (Keller and Liebschner, 2000).

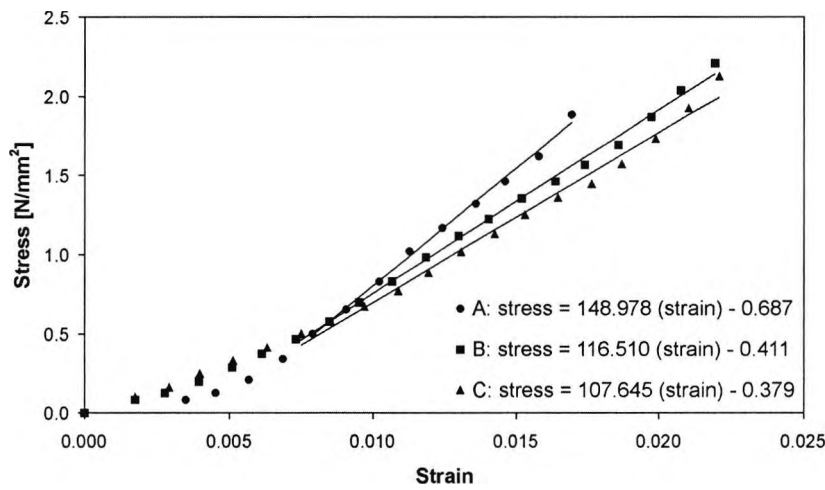
Sample dimensions measured using Vernier callipers were recorded between the midlines of each parallel pair of surfaces for each sample, prior to compression testing.

Results

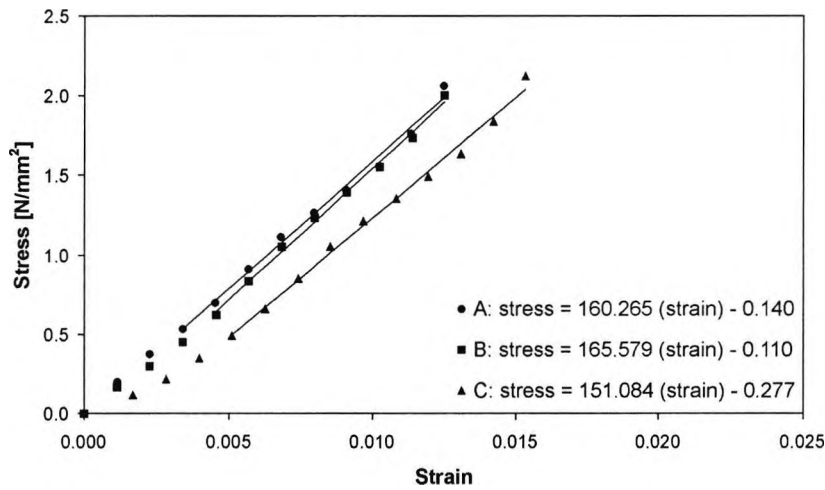
The Lloyd Instruments equipment recorded load-displacement data as a series of points (with fixed displacement steps) from zero load and displacement up to the pre-set limit of 600 N. From observation of the load-displacement data points and their linear elastic regions, it was thought reasonable to define a pre-load region of 0 to 100 N for all data sets. Therefore data points from 100 to 600 N inclusive were taken to be the elastic region for each compression data set. These points were fitted with a linear function using least squares regression.

It should be noted that the effect of microfractures was occasionally observed within a data set. This manifested as small deviations within the linear elastic region caused by single trabecular failure. The effect on the linear fit was minimal and considered to be acceptable within the scope of these experiments.

Load-displacement data was converted to stress-strain data using equations 1.1 and 1.2 (chapter one, section 1.2.3), stress calculated by dividing applied force by the area over which it acted and strain by dividing the original sample height by the change in this dimension. Example stress-strain plots for two trabecular bone sample cubes are shown in figure 10-2. Data sets for all three cube orientations are given with linear fits to the elastic regions. The gradient of these fits provides the Young's (elastic) modulus for the sample for the given orientation. A comparison of the three linear gradient sets between the two samples plots (a) and (b) shows that for some trabecular bone cubes orientation has more of an effect on the elastic modulus than for others.



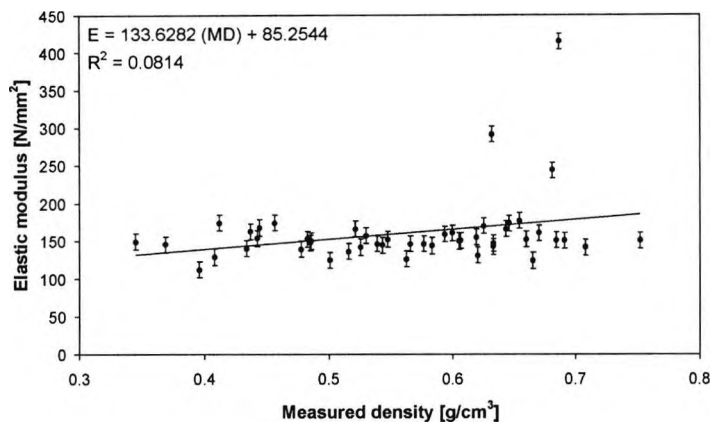
(a)



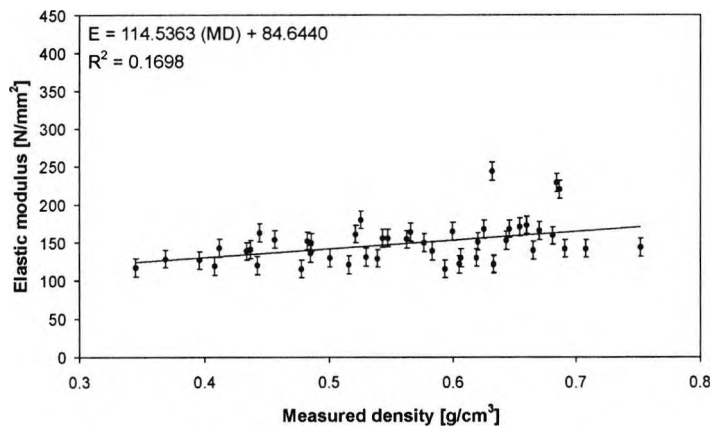
(b)

Figure 10-2. Stress-strain plot examples for two trabecular bone sample cubes, the first (a) having an apparent density of 0.345 g/cm³ and the second (b) of 0.670 g/cm³. Each sample was compressed in all three orientations, 'A', 'B' and 'C'. Note how for the sample in plot (a), orientation has more of an effect on the elastic modulus (the line gradient) than for the sample in plot (b).

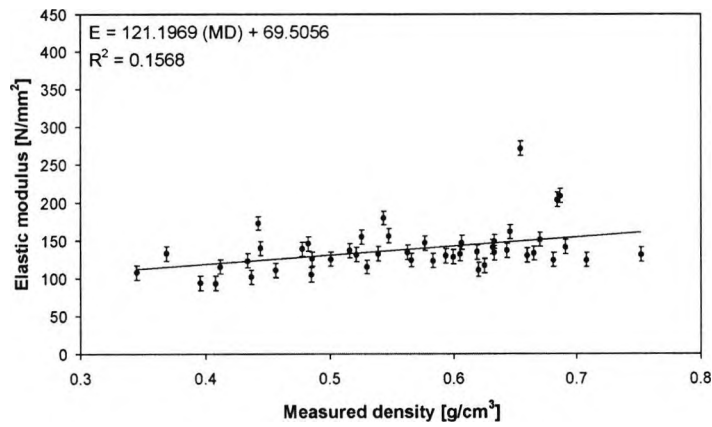
The elastic moduli of each sample was plotted against the measured bone sample density, one plot for each of the three orientations (figure 10-3). Errors were calculated using the elastic moduli from the 10 sample set compressions repeated 10 times. The variation in elastic modulus for each sample of this set did not demonstrate an obvious pattern with respect to apparent density, so a generic error for all samples was calculated by taking the mean plus two standard deviations of these errors.



(a)



(b)



(c)

Figure 10-3. Plots of Young's (elastic) moduli (E) against the measured density (MD) of the 48 bone sample cubes. Each plot (a, b and c) presents the Young's moduli from sample compression in each orientation ('A', 'B' and 'C' respectively). Errors were derived from 10 sample compressions repeated 10 times.

Conclusions

It is clear from observing the linear region gradients of the two example stress-strain plots in figure 10-2 that trabecular bone cube orientation has differing influence on the elastic modulus for different samples. This was expected, as it is known that trabecular strength and fracture risk is determined by a combination of bone density and architecture. Research has shown variations approaching a factor of 10 in stiffness measurements (the ability of a material to resist being deformed when a force is applied) on different orientations with the same anatomical location (Linde and Hvid, 2000). By using the same cube with different orientations, it forms its own control, the density being unchanged but effectively applying the same force to different trabecular structure.

The plots of elastic modulus against measured density (figure 10-3) illustrate the effect of bone architecture on strength for the sample cubes used in this project. It is clear that for each orientation there is a general trend for elastic modulus to increase with bone density, as shown by the equations of the linear fits to these data. However the important results for this study are the low R^2 Pearson correlation coefficients of each plot, being 0.0814, 0.1698 and 0.1568 for orientations 'A', 'B' and 'C' respectively. When considered in conjunction with the trend for elastic modulus to increase with bone density, it may be concluded that density is important to bone strength but is not the only factor involved.

Finally, it is interesting to note that the correlation for orientation 'A' is approximately half that of those for orientations 'B' and 'C'. Orientation 'A' was chosen so the applied force was parallel to the direction of the portion of the medial trabecular system within the sample cubes, responsible for transmitting stress through the femoral head (Whitehouse and Dyson, 1974). Orientations 'B' and 'C' result in the applied force being perpendicular to the medial trabecular group. The approximate factor two correlation difference for orientation 'A' suggests that when force is applied in a direction where trabecular architecture should be most influential, a greater significance to bone strength with respect to structure is observed.

Part Three

CONCLUSIONS

Chapter 11

DISCUSSION AND FURTHER WORK

This chapter provides a summary of conclusions from the work of this project. They are grouped into sections relating to each chapter of work from the project preparations of part one and the main study of part two. Suggestions are then offered for work required to further progress this project. The report is then concluded with a final discussion.

This chapter comprises:

- Section 11.1 A summary of conclusions from the chapters of part one of this report (two to six), the preparatory work.
- Section 11.2 A summary of conclusions from the chapters of part two of this report (seven to 10), the main study.
- Section 11.3 A discussion of further work pertinent to the continuation of this study.
- Section 11.4 Final conclusions for the project, discussing the state of the EDXRD system at this stage.

11.1 A SUMMARY OF CONCLUSIONS FROM THE PREPARATORY WORK

Extensive preparation was performed, taking the form of experimentation and calculation, along with reference to existing literature (the bulk of which is discussed in the introductory chapter). This preparatory work, discussed in part one of this report, was necessary to provide a thorough foundation from which to launch the main study.

11.1.1 Photon Source and Detection Components of the EDXRD System (Chapter Two)

This chapter investigated elements of the x-ray tube (output stability, mapping and experimental alignment) and the photon detection system (calibration, energy resolution and mapping the effective size of the detector).

Stability of the x-ray tube output at three distinct kV_p settings was found to be good, 30 and 70 keV being within 99% of the initial output and 120 keV being within 98%, with

potential improvement following a tube warm up cycle. From the results of x-ray tube output mapping, maximum photon flux was found to be at the centre of the tube aperture, which was subsequently aligned for each experiment for maximum efficiency. Alignment was achieved using a laser indicating photon beam path, set using focal spot imaging.

The detection system was energy calibrated at the start of each experiment using an americium-241 source. Calibration was found to be stable throughout this project. An investigation into detection system energy resolution indicated that the full width at half maximum (FWHM) of americium peaks did not change significantly over the energy range of the measurement system. The effective size of the detector was mapped and found to conform to the diameter quoted in the manufacturer's data (25 mm). Maximum uniformity of detection was achieved by constraining experimental geometry to within this area. To maximise consistency between experiments, diffractometer collimation was always aligned to the centre of the detector active area.

These x-ray tube output and detection system investigations were necessary to ensure the equipment was suitable for this project and that maximum efficiency was achieved when constructing the EDXRD experiments.

11.1.2 EDXRD Experimental Geometry and Bone Phantom Construction (Chapter Three)

The EDXRD diffractometer scattering volume lengths for various collimator widths and experimental scattering angles were calculated (table 3-2, chapter three, section 3.1.1). These calculations were used to select diffractometer geometries that could be aligned to fit or substantially fit within $15 \times 15 \times 15 \text{ mm}^3$ phantom and bone sample volumes.

Bone phantoms with volumes of $15 \times 15 \times 15 \text{ mm}^3$ were constructed with bone and marrow substitute mixes of varying proportions to simulate clinical bone mineral density conditions. The phantom volume was chosen to suit expected diffractometer geometry selection, bone sample cleaning practicalities and compression testing requirements (chapter five, section 5.2, and chapter 10, section 10.1). The phantoms were used for initial EDXRD and DEXA minimum limit studies (chapter four) and as a reference for final study experiments (chapter eight). They were used with the proviso that there may be a small degree of bone/marrow ratio inaccuracy, predominantly due to ingredient weighing error and the homogeneity of the phantom mix.

11.1.3 Initial Bone Density Measurements using Phantoms (Chapter Four)

The phantoms that were manufactured as described in chapter three were used for initial EDXRD and DEXA minimum limit studies using a variable angle and collimation width diffractometer. These experiments were performed in order to ascertain optimum geometry for a fixed angle and collimation width diffractometer manufactured for the main study experiments of part two. Results from these experiments indicated an optimum experimental scatter angle of 6° and a collimation width of 1.0 mm, concurring with the results of Farquharson (1996).

In addition, an initial indication to the effectiveness of an EDXRD bone density measurement system was provided, being a minimum detectable limit of 1.9% of bone density change with no additional attenuation and 3.3% with the addition of 1.5 mm of aluminium and 5 mm of Perspex.

It was noted that the reduction of collimator slit width increased peak resolution (by reducing angular blurring) at the expense of photon flux. However the assessment of bone density is not necessarily improved with better peak resolution since this method of measurement is optimised with a compromise between flux and resolution.

The DEXA experiments, performed using the same phantoms and attenuation with a Hologic QDR 4500 scanner, resulted in a minimum detectable limit of 12.4% of bone density change with no additional attenuation and 8.5% with the additional attenuation. However it was noted that this machine is optimised for use with patients and so these experimental results may not reflect the ability of the machine when used under these more usual conditions. This is indicated by the improvement of performance when attenuation is added, partially simulating the effect of cortical bone and soft tissue. There is no reason to dispute the manufacturers stated precision for the QDR 4500, being 1% total bone density change.

The EDXRD and DEXA results were compared, suggesting that when using unattenuated phantoms the precision of EDXRD is over six times better than that of DEXA. With the addition of appropriate attenuation, the precision of EDXRD demonstrated an improvement of approximately $2\frac{1}{2}$ times over that of DEXA. The high dose cost of EDXRD when compared with that of DEXA was acknowledged. This factor would require significant reduction before EDXRD could be considered for clinical use.

Finally, the sensitivities of each modality to bone density change were considered by comparing the gradients of linear fits to the unattenuated and attenuated results. It was found that, with respect to these results for this range of bone densities, DEXA was more than four times as sensitive to the applied attenuation than the EDXRD equivalent.

11.1.4 Trabecular Bone Sample Preparation and Demineralisation (Chapter Five)

This chapter first discussed the selection of the $15 \times 15 \times 15 \text{ mm}^3$ trabecular bone sample site within the femoral head. The site was chosen, as shown in figure 5-1 (chapter five, section 5.1), to fulfil the requirements of bone density loss and compression experiments. Samples were cut from as precise a location as possible from the medial trabecular system region, with regard to variability between samples. Radiographs were used to aid site selection.

A successful technique for removal of marrow lipid from the cut bone samples was presented.

Guidance plots were provided that offer a good indication of the time of exposure to weak EDTA solutions required for accurate density reduction by demineralisation, in order to simulate bone mineral density loss. These plots are dependant on the sample geometry (external surface area) and size (EDTA penetration depth), $15 \times 15 \times 15 \text{ mm}^3$ in this instance.

The homogeneity of demineralisation was assessed using microdensitometry, comparing demineralisation of the whole cube with that of a $10 \times 10 \times 15 \text{ mm}^3$ region of interest (approximately corresponding to the scattering volume traversed with EDXRD scanning). 3.72% (0.1 mol/litre) EDTA solution was shown to offer a relatively high degree of control over small levels of bone density reduction (of the order of up to 10%, the levels required for these bone density measurement investigations) from the chosen region of interest within a whole sample cube.

A calibration line for use with microdensitometry data was presented that was used to correct for bone density variations between the density of a whole $15 \times 15 \times 15 \text{ mm}^3$ sample and a $10 \times 10 \times 15 \text{ mm}^3$ region of interest. It was used to calculate the mineral density of the region of interest from a measured bone density of the whole cube and the microdensitometry data, via an equivalent thickness of aluminium. This calculation was necessary to obtain a bone density value for the bone volume measured using EDXRD.

Finally a technique was described to introduce a marrow substitute into bone sample trabecular spaces. The method utilised an Edwards E2M5 two stage high vacuum pump. Full lipid penetration into all trabecular space was confirmed by scanning the samples using magnetic resonance imaging.

11.1.5 A Fixed Parameter Diffractometer and Attenuation Correction (Chapter Six)

The EDXRD diffractometer used for the main body of bone density work was described in this chapter. Parameters such as experimental scattering angle and collimation width were chosen from the results of chapter four and were fixed in order to minimise repeatability variation. Moving parts were restricted to the sample transport mechanism. The whole assembly was mounted on a breadboard, allowing the diffractometer to be moved without disassembly (and therefore avoiding the introduction of errors by inconsistent reassembly).

The attenuation correction technique applied to scattered spectra for this and all subsequently collected EDXRD data was assessed, both in terms of fully correcting the spectra (as if no attenuation had occurred) and partial correction (correcting for attenuation by added materials but retaining attenuation effects by the bone sample). The latter assessment was performed to allow comparison of spectra attenuated by the sample and additional material with spectra collected using a bone sample alone. This comparison was not possible with full correction, where comparisons could only be made with other corrected spectra.

The method relied on the generation of attenuation correction ratios for each photon channel by recording transmitted spectra with and without the attenuating material in place. The ratios were then applied to each channel of the scattered spectra.

This correction was considered to be satisfactory as a technique to enhance the effectiveness of EDXRD. In terms of photon count area matching, total photon counts differed by less than 4% for fully corrected spectra. Further improvement might be achieved by detecting scattered and transmitted spectra simultaneously. The uncorrected spectra, as expected, differed considerably.

The significantly greater correction required at lower photon energies (most apparent for the full correction ratios) was recognised as a problem. A potential improvement by fitting the EDXRD spectra before applying the ratio was suggested. The main study

chapters seven and eight also explored EDXRD analysis techniques excluding the lower energy portions of the spectra.

Without attenuation correction, EDXRD could only be effective if knowledge of the attenuation by the scattering and additional materials were known, possible under some laboratory conditions but requiring additional investigation in the clinical environment, probably involving further exposure to radiation.

11.2 A SUMMARY OF CONCLUSIONS FROM THE MAIN STUDY

This work, discussed in part two of this report, formed the main research into EDXRD and DEXA as methods of measuring bone mineral density. Included in this part were chapters on dose considerations and bone sample strength.

11.2.1 EDXRD and DEXA Investigation into One Component Trabecular Bone Density Measurement (Chapter Seven)

Chapters seven and eight concentrated on extensive experimentation into one component (bone only as the material of interest) and two component (bone and marrow) sample systems respectively. Chapter seven formed the first of these studies into the EDXRD and DEXA techniques.

Calibrated (Absolute) Analysis

The first part of this chapter investigated an EDXRD method with calibration to generate absolute bone density results. These EDXRD bone densities were then compared with the physically measured sample bone densities.

The calibration model used for the analysis of this set of results was generated using trabecular bone samples rather than phantoms, which would have provided homogeneous bone densities. This was noted as a potential source of unavoidable error, due to the one component nature of the experiments.

EDXRD precision, accuracy and correlation all tended to improve with increasing measurement tube current \times time (mAs). In a clinical environment, this would be at the cost of increased radiation dose but one component trabecular bone density

measurement would usually be applied in laboratory environments as an investigative tool, radiation dose therefore not an issue.

The concept of 'impressiveness factors' was introduced, being measures of performance in terms of precision (the spread of data obtained from experimental repetition), accuracy (the closeness of a result to the true value) and correlation (the interdependence between variables, which affects the expected accuracy of an individual measurement). Each such factor, designated as IF_P , IF_A and IF_C respectively, all have a maximum value of 1 (the calculation of each being described in the relevant chapter sections). The intention was to provide performance figures that could be easily compared between experiments and bone density measurement modalities.

The performance of precision (IF_P) and accuracy (IF_A) was reduced with the addition of aluminium attenuation. It was concluded that the reduction in precision was likely to be predominantly due to the decrease in photon counts and therefore an increase in statistical variation, also a factor in the reduction of accuracy. The increased loss of low energy photons from the spectra (from the filtering effect of the additional attenuation) was also thought likely to contribute to decreasing IF_P and IF_A . This was because the attenuation correction procedure cannot accurately recover all attenuated photon counts, especially at lower energies, and therefore affects the match to the calibration model.

The inability to normalise one component EDXRD spectra was also noted as a problem, potentially resulting in a greater degree of inconsistency between repeated measurements (due to x-ray tube photon flux variation) than the two component equivalent. However, chapter two demonstrated good stability of the output of the x-ray tube used throughout the EDXRD experiments.

One component DEXA analysis (calibrated by the DEXA scan processing) with the addition of attenuation resulted in an improvement in precision (IF_P). It was noted that accuracy (IF_A) results could not meaningfully be compared to those of EDXRD, since the measurement volumes were not equivalent (DEXA provides a measure of all bone material in the photon beam path). Poor IF_A results merely reflect the inability of DEXA to measure specific bone volume densities. This was considered to demonstrate a strength of the EDXRD method.

The calibrated EDXRD and DEXA results were subsequently compared. In terms of precision, DEXA was shown to outperform EDXRD under all measurement conditions (varying attenuation and acquisition mAs). The best case EDXRD measurement condition for precision was surpassed by DEXA under every condition. Indeed, with the

addition of attenuation, the EDXRD IF_P fell whereas the IF_P for DEXA increased. This increase in performance was thought to be due to the additional attenuation more closely approximating the clinical conditions under which DEXA is designed to operate.

DEXA also outperformed EDXRD in terms of correlation. DEXA IF_C , without and with additional attenuation, yielded a best performance unsurpassed by EDXRD under any measurement condition. EDXRD IF_C improved with the addition of 2.5 mm of aluminium attenuation but did not approach the performance of DEXA.

The main strength of EDXRD was found to be its ability to measure the density of selected volumes of bone. This was reflected by the IF_A results, the best being for the condition with no added attenuation, but still reasonably high with additional aluminium.

It was noted that this study of EDXRD and DEXA measurement systems was conducted using one component trabecular bone sample cubes and so conclusions drawn from the results are with regard to this sample type. The results related to these specific EDXRD and DEXA experiments and should not be taken as conclusive for all such measurement systems.

The most impressive result for EDXRD at 70 kV_p was with no added attenuation at 8000 mAs. Precision IF_P was 0.9510 ($\pm 2.45\%$), accuracy IF_A was 0.9573 and correlation IF_C was 0.8659.

The most impressive result for DEXA with no added attenuation was using high definition scanning. Precision IF_P was 0.9703 ($\pm 1.49\%$) and correlation IF_C was 0.9797.

The most impressive result for DEXA with added attenuation was using high definition scanning. Precision IF_P was 0.9764 ($\pm 1.18\%$) and correlation IF_C was 0.9797.

All DEXA results were similar in terms of IF_P and IF_C .

Demineralised (Comparative) Analysis

The second one component experiment type investigated the ability of each measurement modality to distinguish between measurements of the same sample, before and after partial demineralisation. These experiments provided comparative results, as opposed to the absolute results from the calibrated analysis.

Results from these experiments were calculated under various measurement conditions for both EDXRD and DEXA. Measures of success were taken to be the bone density

reduction failure point (the sample bone density reduction above which the measurement modality may confidently be expected to detect, indicative of a minimum detectable change) and the linear regression fit slope (for EDXRD or DEXA bone density reduction plotted against measured sample density reduction).

For both EDXRD and DEXA, the bone density reduction failure points were comparable for similar attenuation conditions. With no added attenuation, DEXA performance showed marginal improvement over EDXRD. The added attenuation conditions could not be directly compared since the attenuation for DEXA was greater than that of EDXRD. However, the failure points were roughly comparable.

The linear regression fitted slopes would ideally have demonstrated a relationship of unity. In other words, any sample bone density reduction would be reflected value for value by the measurement modality result. The fact it was not highlighted the limitations of this comparative method.

This test inevitably suffered from the extra error components introduced, namely from physically measured sample density reduction and the fact that two sets of EDXRD or DEXA measurements are compared, each with their own errors. With this in mind, these results were not considered to be conclusive. The original calibrated system limit results more accurately reflected the ability of each method for the one component samples. However the results of the demineralisation experiments were of similar order to those of the calibration experiments and therefore were considered to provide further confidence in the earlier conclusions.

DEXA with no additional attenuation provided the fit closest to unity. Both EDXRD fits showed density reduction results of the order of twice that measured from the sample.

EDRXD was more impressive when the slope change with added attenuation was considered. The results could not be directly compared due to the different quantities of added attenuation but the DEXA slope did dramatically reduce (by the order of 50%) whereas the EDXRD slope only reduced by a small amount. This result was not taken as a criticism of DEXA. Since the additional attenuation is included in the measured bone density, effectively the relative bone mass loss is reduced. However it did demonstrate the ability of EDXRD to measure specific bone volumes and showed the detrimental affect of additional attenuation to the DEXA technique in terms of specific bone volume density measurement.

**11.2.2 EDXRD and DEXA Investigation into Two Component
Trabecular Bone Density Measurement
(Chapter Eight)**

This chapter complemented chapter seven, largely a repetition of experiments from the former, using a two component sample system as the scattering medium for EDXRD and material for the DEXA measurements.

Calibrated (Absolute) Analysis

This chapter investigated an EDXRD method with calibration to generate absolute bone density results. These EDXRD bone densities were then compared with the physically measured sample bone densities. This first part repeated the analysis methods of chapter seven.

Three calibration models were used for the analysis of this set of results, bone/marrow ratio, unnormalised and unity normalised bone region models. They were generated using the phantoms described in chapter three.

EDXRD precision, accuracy and correlation results with no additional attenuation for unnormalised and unity normalised bone region analysis all tended to improve with increasing measurement mAs. This would be at the cost of increased radiation dose if used in a clinical environment.

For bone/marrow ratio analysis, precision and correlation generally improved with increasing acquisition mAs but accuracy deteriorated, indicating a problem with the calibration for this analysis method. For all attenuation conditions it was concluded that the bone/marrow ratio method of analysis was the poorest. It was initially thought that use of this ratio would increase the sensitivity of the effect of bone loss on calibrated results – as bone density is reduced, the volume of marrow increases, filling vacated space. For these results, poor performance is likely to be due to the effect of the attenuation correction method, correction being most significant at the lower energies of the spectrum, amplifying repeatability errors. The conclusions of chapter eight, section 8.1.1 discusses this further, also with respect to the detriment on unity normalisation with higher added attenuation.

For the EDXRD results from samples with no added attenuation, unnormalised and unity normalised yielded similar results at the higher acquisition mAs's. For clinical site simulation results, as attenuation increased, the most effective analysis method switched

from the unity normalised bone region method to bone region analysis with no normalisation. It was therefore concluded that the choice of analysis method should be determined by the clinical measurement site (or expected attenuation in a laboratory environment) to be investigated. Ideally clinical measurement sites with low attenuation, such as the calcaneus, should be chosen for best results. This may also avoid having to switch analysis methods with increased attenuation.

Two component DEXA analysis (calibrated by the DEXA scan processing) demonstrated some improvement in precision (IF_p) as attenuation simulating clinical sites was increased. This was expected, since the DEXA scan settings used were designed for axial region bone density measurement with relatively high surrounding tissue density. Again, poor IF_A results reflected the inability of DEXA to measure specific bone volume densities and was considered to demonstrate a strength of the EDXRD method (not a criticism of the DEXA method).

For EDXRD and DEXA comparison, only the three clinical site simulations (calcaneus, radius and femoral neck) were considered since DEXA was not performed without additional attenuation.

In terms of precision (IF_p), DEXA was shown to outperform EDXRD under all measurement conditions (consistent with the observations made from the one component sample experiments). The best DEXA precision performance was for the femoral neck simulation, likely due to the higher attenuation more closely approximating the clinical conditions under which these DEXA settings were designed to operate. The results indicated that DEXA has a fairly consistent precision performance whereas EDXRD deteriorated with increasing attenuation.

DEXA outperformed EDXRD in terms of correlation (IF_c), also agreeing with the one component results. A fairly consistent correlation performance for both EDXRD and DEXA was demonstrated.

EDXRD surpassed DEXA in its ability to measure the density of selected volumes of bone, reflected by the impressiveness factor for accuracy (IF_A). Again, the best EDXRD IF_A was for the condition with least attenuation (the calcaneus simulation), deteriorating a little for the radius and significantly with the femoral head simulations. As with the one component sample experiments, the inability to recover low energy photons in the EDXRD spectra using attenuation correction is likely to account for this IF_A drop.

It was noted that if EDXRD were considered for potential clinical application, the high dose experienced for best performance would need to be addressed. This was investigated in chapter nine.

It was also noted that this study of EDXRD and DEXA measurement systems was conducted using two component trabecular bone sample cubes and so conclusions drawn from the results are with regard to this sample type. The results related to these specific EDXRD and DEXA experiments and should not be taken as conclusive for all such measurement systems.

The most impressive result for unnormalised EDXRD at 70 kV_p with no added attenuation was at 8000 mAs. Precision IF_P was 0.9339 ($\pm 3.31\%$), accuracy IF_A was 0.9281 and correlation IF_C was 0.9626.

The most impressive result for unity normalised EDXRD at 70 kV_p with no added attenuation was also at 8000 mAs. Precision IF_P was 0.9364 ($\pm 3.18\%$), accuracy IF_A was 0.9690 and correlation IF_C was 0.8953.

Unnormalised and unity normalised EDXRD results with no added attenuation were similar in terms of these three performance indicators.

The most impressive result for EDXRD at 70 kV_p with added attenuation for calcaneus simulation was at 16 000 mAs using unity normalisation. Precision IF_P was 0.9692 ($\pm 1.54\%$), accuracy IF_A was 0.9156 and correlation IF_C was 0.9469.

Unity normalisation yielded the best results under these conditions.

The most impressive result for unnormalised EDXRD at 70 kV_p with added attenuation for radius simulation was at 16 000 mAs. Precision IF_P was 0.9357 ($\pm 3.22\%$), accuracy IF_A was 0.8584 and correlation IF_C was 0.9356.

The most impressive result for unity normalised EDXRD at 70 kV_p with added attenuation for radius simulation was at 16 000 mAs. Precision IF_P was 0.9589 ($\pm 2.06\%$), accuracy IF_A was 0.7375 and correlation IF_C was 0.9699.

Unnormalised and unity normalisation yielded similar results under these conditions.

The most impressive result for EDXRD at 70 kV_p with added attenuation for femoral head simulation was at 16 000 mAs with no normalisation. Precision IF_P was 0.9357 ($\pm 3.21\%$), accuracy IF_A was 0.5888 and correlation IF_C was 0.9464.

No normalisation yielded the best results under these conditions.

The most impressive result for DEXA with added attenuation for calcaneus simulation was using high definition. Precision IF_P was 0.9782 ($\pm 1.09\%$) and correlation IF_C was 0.9785.

The most impressive result for DEXA with added attenuation for radius simulation was using high definition. Precision IF_P was 0.9776 ($\pm 1.12\%$) and correlation IF_C was 0.9837.

The most impressive result for DEXA with added attenuation for femoral head simulation was using high definition. Precision IF_P was 0.9866 ($\pm 0.67\%$) and correlation IF_C was 0.9785.

In general, DEXA performance was similar for all these conditions.

Calibrated (Absolute) Analysis using Peak Fitting

When peak fitting was applied to the spectra used for calibrated two component EDXRD analysis, improvement was observed at low acquisition photon flux, notably at 80 and 160 mAs (apparent in the plots of figure 8-10, chapter eight). For high acquisition mAs, peak fitted two component EDXRD results (no additional attenuation) were near identical and demonstrate similar patterns to the unfitted results. This was thought to be due to the high photon counts associated with these acquisition mAs's providing good statistics for spectrum generation.

Although the fitting did not improve performance to the maximum achievable at high acquisition photon flux, the increase in performance for low flux might be important in clinical situations where dose considerations restrict longer patient exposure. It may also become significant when using multiple spectra collection (section 11.3.4) at lower acquisition times.

11.2.3 Dose Considerations (Chapter Nine)

Experiments were conducted in order to estimate EDXRD dose costs for each of the three clinical site simulations. They were then compared with existing dose estimates for other bone density measurement modalities, notably for DEXA. The EDXRD dose cost increased with increasing acquisition mAs (photon flux) so it was necessary to balance this against increase in the precision, accuracy and correlation of the results obtained.

It was noted that each densitometry method obtained results by very different means and by measuring different sites in the body, but it was considered reasonable to compare estimated doses since the result of each modality is a measure of bone density, regardless of the method used to obtain it.

It was found that the EDXRD measurement method as it stood was costly in terms of radiation effects. Considering doses from quantitative computed tomography (QCT), an effective but high dose densitometry method, the EDXRD scanning time (at 16 mA) would have to be restricted to a range of approximately 10 to 30 seconds to be comparable. Similarly, when comparing to radiographic methods, an EDXRD limit of 50 seconds would need to be imposed.

When compared to DEXA, the dose limitations of EDXRD became very apparent. The lowest EDXRD scan time (10 seconds at 16 mA) doses for the radius and calcaneus (which provided poor performance) resulted in approximately 29 times that of a general effective dose for DEXA. For reasonable EDXRD performance (in terms of precision, a 50 second minimum acquisition time), this factor increased to approximately 142 times. For an EDXRD scan of 500 seconds, the dose increase was approximately 1419 times that of DEXA. In each of these cases, EDXRD had a lower precision and correlation than DEXA but was significantly better in terms of bone volume measurement accuracy. Suggestions for the reduction of EDXRD radiation dose are provided in section 11.3.4.

11.2.4 An Investigation into Bone Sample Strength (Chapter Ten)

Experiments were conducted using the bone sample cubes of this study in order to illustrate that both density and structure influence bone strength. The one component trabecular bone sample cubes were compressed within their elastic limits in all three orientations. Linear regions of each resulting stress-strain curve were regression fitted, each gradient taken to be the elastic moduli.

For many of the sample cubes, the elastic moduli of each orientation differed significantly, indicating different trabecular strength characteristics for the same density of bone. This conclusion was quantified when the elastic moduli were plotted against physically measured densities. Although there was a general trend for elastic modulus to increase with bone density, the correlation coefficients for each plot (figure 10-3, chapter 10) were low, indicating that density is important to bone strength but is not the

only factor involved. Trabecular architecture was shown to have an important significance.

Thus it was shown that, for the samples investigated, trabecular strength (and therefore fracture risk) is determined by a combination of bone density and architecture.

It was also noted that the correlation of elastic moduli versus bone density in the direction of the medial trabecular system was significantly lower than for the other two orientations, again suggesting the importance of trabecular structure to bone strength.

11.3 FURTHER WORK

This section presents ideas for the refinement and further progression of this project. Improvements are suggested for some of the techniques discussed in the chapters of this report, along with possible future directions for study.

11.3.1 Demineralisation Homogeneity Test Improvement

As part of the investigation into bone density measurement using one component (trabecular bone with no marrow) sample cubes, the densities were measured under various conditions using EDXRD and DEXA. The samples were subsequently demineralised using EDTA by varying degrees and the density measurements repeated. In this way, a minimum detectable bone density reduction was calculated for each measurement modality and experimental condition. As part of the conclusion for this work, it was noted that there were a number of sources of error that could be detrimental to the results. Reduction of these errors could therefore improve this investigation.

One problem associated with the demineralisation of the bone sample was an assessment of the homogeneity of bone removal throughout the cube volume. This was achieved as described in chapter five, section 5.4, using optical microdensitometry with radiographs of each sample. There are a number of inherent errors associated with this method (discussed in the aforementioned chapter) and, as such, microdensitometry is no longer widely used as a method of bone density measurement. Obvious error sources for the homogeneity assessment are the two stages of radiography and microdensitometry and the two-dimensional nature of the final result (this three- to two-dimension problem is illustrated by figure 5-3, chapter five).

The two stage and two-dimensional problems, along with the inherent microdensitometry errors might be overcome by the use of a microtomographic system

to image the bone samples. Such a system is in use at Surrey University and pilot scans have been performed using the bone samples of this project.

It is envisaged that homogeneity assessment could be performed using this three-dimensional third generation microtomographic apparatus. The bone cubes would be scanned both before and after demineralisation, data recorded as a cube of $1024 \times 1024 \times 1024$ $15 \mu\text{m}$ voxels. The first stage of analysis would involve the application of a binary threshold to the three-dimensional data, such that each voxel is defined as either bone or void. For each bone voxel, the distance to the central voxel would be calculated and also the distance to the nearest void voxel. A plot is generated of the mean distance from a bone voxel to a void voxel, against distance from the centre (before and after demineralisation). For a uniformly demineralised sample, the distance from bone to void would be independent of radial distance. Non-uniform demineralisation would manifest as a gradient.

Figure 11-1 presents bone cube slice images reconstructed from microtomographic data, both before and after demineralisation. On inspection, demineralisation is apparent throughout the whole slice.

11.3.2 One Component EDXRD Photon Flux Variation Correction

As a solution to the inability to normalise one component EDXRD bone spectra (chapter seven, section 7.1), a second detector to collect transmission spectra simultaneously is suggested. Mean photon counts for each channel over each repeated spectrum for the same sample conditions would be calculated. A ratio between each channel count for a single spectrum and its corresponding mean would provide a means of correcting for photon flux variation.

This method could be realised by using the transmission spectra collected for attenuation correction but would only be useful in situations where repeat measurements were made. The technique would therefore not be practical in clinical two component situations but might be employed in laboratory based one component experiments. However, it was established that flux variation for the equipment used was minimal (chapter two, section 2.1.1).

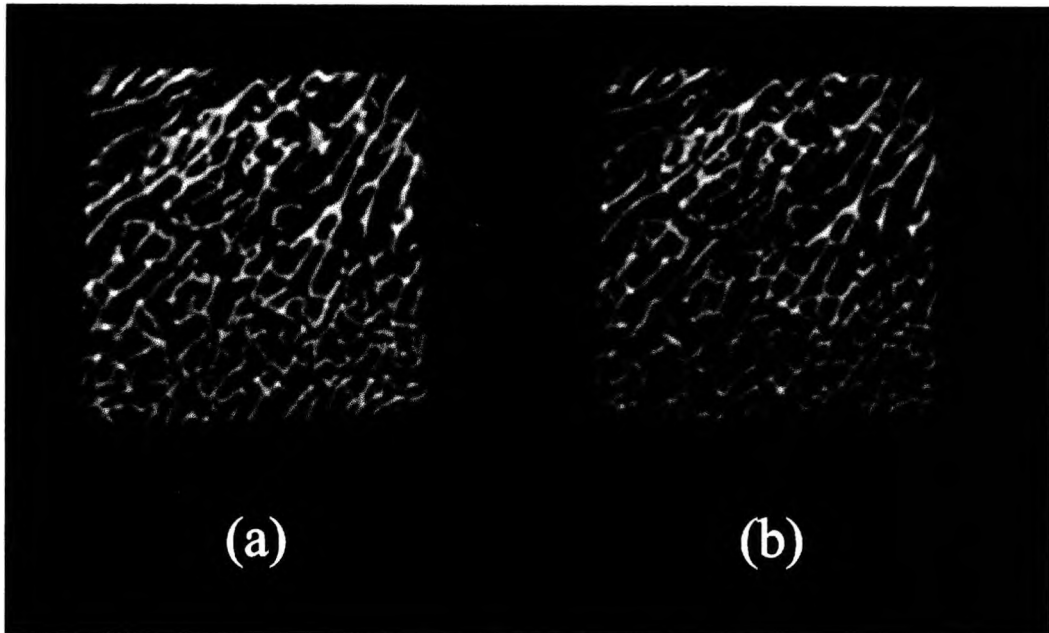


Figure 11-1. Images of a bone cube slice, reconstructed from data collected using microtomographic apparatus. The slice is shown before demineralisation (a) and after approximately 10% demineralisation using 3.72% EDTA solution (b). It is useful to compare these images with figure 5-5 (chapter five, section 5.4), two-dimensional radiographic images of a three-dimensional bone cube (see also figure 5-3, chapter five, section 5.4). (Images courtesy of Russell Luggar and Paul Jennesson, Surrey University.)

11.3.3 Two Component EDXRD Demineralisation Experiments

The most obvious omission from this body of work is a set of demineralisation measurements for the two component sample system (bone + marrow samples). These experiments were curtailed due to the unexpectedly high preparation and processing times for the samples (along with the necessarily reduced sample set for the calibrated investigation). Two component demineralisation would entail initial sample preparation (to the point of known density marrow free trabecular bone sample cubes), marrow replacement, densitometry measurements, marrow cleaning, demineralisation, then further marrow replacement and densitometry measurements.

Although omitted from this project, the importance of the two component method to a potential clinical application suggests this work would be useful.

11.3.4 EDXRD Analysis Improvement

In order to extract bone density information from measured EDXRD spectra, the main study results were analysed using various energy regions. The regions chosen are illustrated by figure 7-2, chapter seven (one component sample system) and figure 8-2, chapter eight (two component sample system).

With reference to figure 7-2, region A (the whole spectrum, post attenuation correction) was chosen to provide the photon count information for bone density calculation. The reasoning for this choice was that by comparing repeated spectra collected using the same bone samples, region A offered the least variation. Subsequent thought, with the hindsight of completed results, suggested that a region that excluded much of the low energy portion of the spectra (such as region B) would have yielded results more suited to the calibration (for the conversion of spectrum counts to a bone density value). Indeed the results from the two component sample system highlighted the problems of using counts from the low energy portion of EDXRD spectra. This was due to the greater attenuation, and therefore the necessarily larger correction at these low energies.

The choice of the boundary energy point above which photon counts would be used is dependent on the range of sample densities used for the calibration curve and subsequent spectrum measurements. Clearly an optimum boundary energy would be influenced by this range since attenuation affects would change depending on the sample densities. It is suggested that, for re-analysis of this one component data or for subsequent experiments, software is prepared that would test calibration against spectrum region

boundary selection. A regression method that tested a range of boundaries for a given sample range would provide a better calibration and final result for the data.

This approach would be beneficial to all subsequent EDXRD spectral analysis, both one and two component sample systems. The two component analysis methods of chapter eight demonstrated clear deterioration as use of low energy photon counts (in this instance from the marrow region) became more significant. The bone/marrow ratio analysis method was shown to be the least satisfactory for all experimental conditions and, as attenuation became more significant (for example, femoral head simulation), the unity normalisation method suffered. An analysis method that avoided use of photon counts from the low energy portion of the spectrum would clearly be more effective.

Further improvement to the analysis might be achieved by considering the (smaller) contribution of the marrow counts to the bone region, and *vice versa*. These contributions are illustrated by figure 1-18c (chapter one, section 1.8.2). Note that the marrow spectrum tail extends to the maximum energy (momentum transfer). If the bone and marrow spectra were separated prior to analysis, an improvement in the results might be observed. It should be possible to develop software to estimate marrow spectrum contribution to each channel of the bone region based on marrow peak counts/count distribution (and bone spectrum contribution to the marrow region). This would not be an inconsiderable task, especially when considering the additional complications caused by the larger spectrum fluctuations at lower energies as a result of the attenuation correction technique.

An alternative to these methods might be the use of multivariate analysis software. This approach has been used to process EDXRD bone scattered spectra with some success (Farquharson *et al.*, 1997a).

Additional considerations for future analysis methods might also include the use of peak fitting (or some other method of spectral smoothing) before attenuation correction was applied. This could be beneficial in reducing the quantity of low energy noise that was amplified by the attenuation correction method. The analysis of chapter eight, section 8.1.2, employed peak fitting once attenuation correction had been performed.

One final thought on the reduction of attenuation correction problems is that it is unnecessary to correct for the attenuation contribution from the 2.5 mm aluminium legal filtration. This was accounted for in the corrections of this study but since it is in place and constant for all measurements, this correction, with the associated problems, is not required. If all spectra, for both the calibration curve and sample measurements, were

corrected by considering the unattenuated source to be at the point after the legal filtration, much of the low energy problems would not be apparent. This method is unlikely to significantly improve the results in terms of errors from correction (both types of correction are to a fixed single 'unattenuated' spectrum) but there may be some improvement due to less 'unrecoverable' photon energy and minor correction error improvement. This method may also negate the need for the Compton shift stage of transmission spectrum measurement (direct transmission detection may be possible), which would also reduce error.

11.3.5 EDXRD Dose Reduction

The primary aim of this study was to ascertain the clinical viability of an EDXRD system to measure bone mineral density and provide a diagnosis tool for the early detection of osteoporosis. Although it has been shown that, within certain boundaries, this is possible (see the final conclusions of section 11.4), the major setback is the high radiation dose necessary to achieve useful results. Radiation dose estimates, discussed in chapter nine, relate to the use of a single EDXRD scattering channel in the experiments (figure 11-2a).

For EDXRD to be viable for clinical applications in comparison to DEXA, the dose cost would need to be significantly reduced. The results of chapter eight, section 8.1.2, suggest that maximum EDXRD effectiveness in terms of precision might be approached by peak fitting bone region analysed spectra recorded for a minimum of 50 seconds. This results in an effective dose of approximately 142 times that of DEXA (still resulting in lower precision than that of DEXA).

EDXRD dose reduction from this point might be achieved by measuring 12 EDXRD 6° scattered spectra simultaneously (figure 11-2b). Decreasing the 50 second scan time by this factor potentially reduces the EDXRD dose cost of 142 times that of DEXA to approximately 12 times. A further extension of this method collects 36 spectra at 5°, 6° and 7° (figure 11-2c). Although the effectiveness of the 5° and 7° spectra is likely to be reduced (chapter four, section 4.1), there is a potential dose cost saving of the order of something less than 36 times, bringing the EDXRD dose cost to the order of four times that of DEXA. If this dose cost is achievable and acceptable, EDXRD still has some potential in the clinical environment. If it is not acceptable, EDXRD would still have great potential in the laboratory environment, for example measuring bone densities of archaeological specimens with a far greater accuracy than DEXA can achieve.

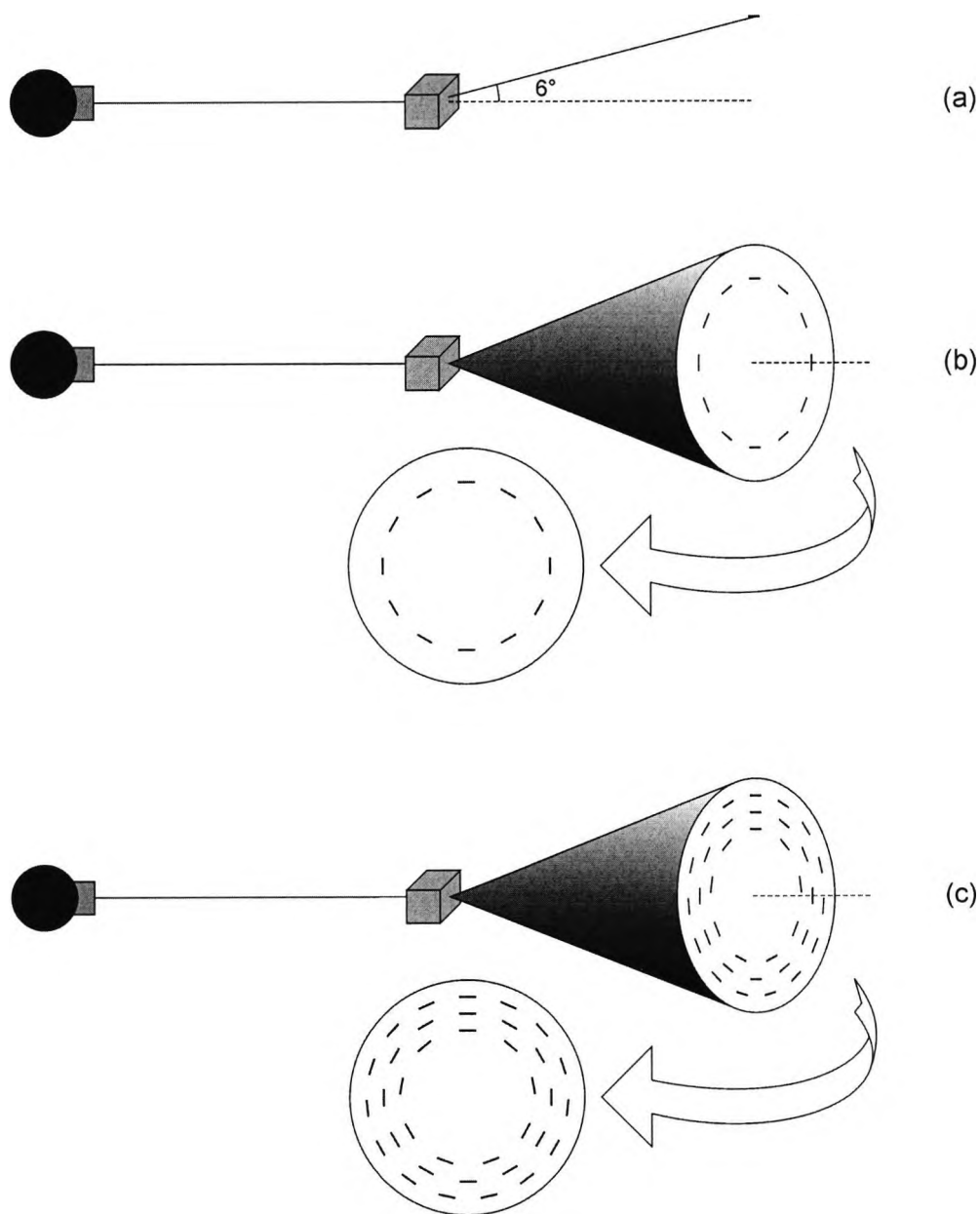


Figure 11-2. Illustration of a possible method of decreasing patient dose by measuring multiple spectra simultaneously. The first diagram (a) represents how EDXRD spectra were measured throughout this project, one spectrum only at 6°. The second diagram (b) shows how a secondary EDXRD collimator might be configured to measure 12 spectra at 6° simultaneously, reducing measurement time (and therefore radiation dose) by a factor of 12. The third diagram (c) presents a possible configuration for measuring 36 spectra simultaneously, 9 at 5°, 12 at 6° and 15 at 7°.

There are potential problems with the realisation of such a secondary collimator. Clearly the channels could not converge at the apex of the cone and would therefore require design adaptation and a consideration of factors such as angular blurring. In addition, the germanium detector used throughout this study would be unsuitable. One possible solution could be the adoption of detectors such as those manufactured using cadmium zinc telluride (CZT), which are available in small units since they operate at room temperature. They do not require bulky cooling apparatus. However, the resolution of CZT detectors is poor compared to that of the germanium detector, having an order of 10 times greater FWHM at the energies of this study (Knoll, 1989). The effectiveness of this detector type for this application would therefore require investigation. An alternative detection system might involve a specially made detector with regional detection capabilities.

11.3.6 Compression Tests

The compression tests described in chapter 10 were, by necessity, conducted using the isolated $15 \times 15 \times 15 \text{ mm}^3$ trabecular bone cubes of this study. This allowed sufficient experimental control to allow comparison between samples but was removed from the reality of *in vivo* bone strength, in this case of the femoral head. The isolated nature of the trabecular samples also did not allow for the inclusion of marrow in the trabecular spaces, since it could not be contained during compression.

The experiments described for this study were performed on dry bone sample cubes. Although this is perfectly valid, many such compression studies are performed using samples kept wet using a saline solution (An and Bensen, 2000). Repeating the compression studies using samples in this condition might therefore provide some further insight into the strength characteristics of trabecular bone.

11.4 FINAL CONCLUSIONS FOR THE PROJECT

This results of study have highlighted the differences between the EDXRD and DEXA methods of measuring bone mineral density. They results indicate strengths and weaknesses for each modality, suggesting that different applications rather than direct comparisons would be best suited for each.

EDXRD is clearly suited to the measurement of absolute density values of specific bone volumes from within a surround of additional bone and soft tissue. This study has shown

EDXRD to be capable of obtaining such values with some accuracy. The best performance of EDXRD was found to be from sites resulting in relatively low photon attenuation. This is demonstrated not only by the results of the main study (both one and two component samples) but by the initial measurements using phantoms (chapter four). Whereas precision deteriorated as attenuation increased and was always surpassed by DEXA when using complete bone samples (chapters seven and eight), the precision for the lower density phantom experiments was most effective. EDXRD minimum detectable limits of 1.9% with the phantom only (compared to 12.4% for DEXA) and 3.3% with additional attenuation (8.5% for DEXA) were obtained.

In a laboratory environment (for example, experiments measuring bone density values of bone volumes within archaeological specimens), EDXRD results could be further improved by increasing acquisition mAs, problematic in a clinical environment due to the high dose levels. A scheme to reduce dose is suggested in section 11.3.4.

EDXRD is essentially a compromise, offering density measurement of a bone volume with unknown surrounding attenuation but with reduced performance in terms of precision and correlation (with higher overall site densities).

The EDXRD system as it stands would also suffer in a repeat scan situation due to the difficulty with precise repositioning. This problem might be overcome by the development of a multiple source-detector scanning system, similar to the DEXA arrangement.

These studies have shown that DEXA is a very reliable method of monitoring bone mineral density. In terms of precision and correlation, EDXRD was generally outperformed by DEXA for all bone sample experiments. This indicates the strength of DEXA is in obtaining relative bone density values that can be compared to known models or with subsequent measurements, specifically in a clinical environment. The manufacturer of the Hologic QDR 4500 DEXA scanner used throughout this study quotes femoral neck scanning precision approaching 1%.

For a true investigation into the accuracy of DEXA, total bone density would need to be calculated for each attenuation condition (i.e. the contribution of the added attenuation should be included). This is because DEXA is not designed to measure specific bone density volumes but all bone in the photon beam path, and for this purpose performs well. DEXA is therefore unsuitable for measuring the density of specific bone volumes.

DEXA is very much suited to clinical measurements with respect to its comparatively very low radiation dose. Also the multiple source-detector scanning system negates repositioning problems for subsequent examinations.

EDXRD clearly suffers in comparison to DEXA in terms of radiation dose. For both techniques, the majority of attenuated photons are transmitted, as opposed to scattered. In order to achieve parity of detected photon flux, the scattering method (EDXRD) must have a greater input photon flux than that of the transmission method (DEXA). This results in DEXA being far more photon efficient than EDXRD as a bone densitometry modality. As a consequence, the radiation dose to the patient is many times greater for EDXRD and would require significant reduction before this method could be considered for clinical use.

As a final comment on the performance of EDXRD as assessed by this project, it clearly does not perform to the same standard as DEXA in terms of precision and correlation. However, for the accurate determination of internal trabecular bone volume absolute densities, an important consideration in the initial determination of osteoporosis, EDXRD shows some potential. These results suggest the most effective performance is likely to be in examining clinical sites with limited external attenuation, such as the calcaneus, or in the laboratory based assessment of isolated samples.

In summary, DEXA is a fast, low dose method, its good repeatability making it ideal for monitoring the progress of osteoporosis. EDXRD, as at the conclusion of this work, is a slow, high dose method, but has great potential for absolute bone density measurement.

APPENDICES

Appendix A

FORMULAE DERIVATIONS

This appendix provides derivations of formulae employed in the main text.

A.1 MOMENTUM TRANSFER

It is useful to be able to convert the energy axis of EDXRD spectra into a scale that is independent of the scattering angle. In this way, spectra measured using different scattering angles may be compared directly. An EDXRD spectrum with an energy scale (for example, keV units) may be converted into a spectrum with a momentum transfer scale (for example, nm^{-1} units).

Momentum transfer is defined as the momentum transferred to a coherently scattered photon such that it is deflected through an angle θ , represented diagrammatically in figure A-1. Momentum is transferred to a photon with initial momentum ρ_i , deflecting it through an angle of θ to its final momentum ρ_f . Momentum transfer ($\Delta\rho$) may therefore be written:

$$\Delta\rho = 2|\rho_i| \sin\left(\frac{\theta}{2}\right) \quad [\text{A.1}]$$

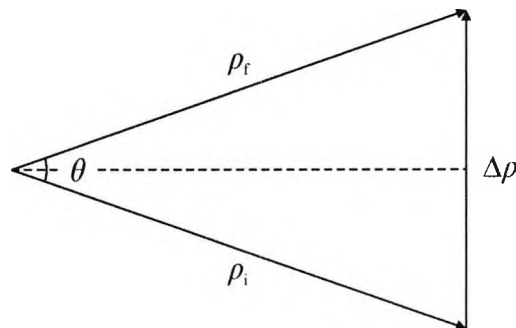


Figure A-1. A diagrammatic representation of momentum transfer. The initial momentum (ρ_i) of a photon is deflected through an angle θ to the final momentum (ρ_f) when momentum $\Delta\rho$ is transferred to the photon.

The initial and final momentum magnitudes are equal and related to photon wavelength, λ , and Planck's constant, h , being $6.626\ 076 \times 10^{-34}$ J s or $4.135\ 639 \times 10^{-15}$ eV s (seven significant figures).

$$|\rho_i| = |\rho_f| = \frac{h}{\lambda} \quad [\text{A.2}]$$

Therefore:

$$\Delta\rho = \frac{2h}{\lambda} \sin\left(\frac{\theta}{2}\right) = 2h x \quad [\text{A.3}]$$

Momentum transfer may be defined in terms of different unity systems, one such resulting in the convention of taking x as being the momentum transfer (essentially $2h = 1$):

$$x = \frac{1}{\lambda} \sin\left(\frac{\theta}{2}\right) \quad [\text{A.4}]$$

This definition of momentum transfer, expressed in units of $(\text{length})^{-1}$, is used throughout this project.

(Momentum transfer may be defined as q , the definition depending on the unity system in use, for example $q = 4\pi x$ (in units of $(\text{length})^{-1}$), or $q = 2h x$ (in units of h). The most usual system uses $h = 1$ and $c = 1$, where h is Planck's constant and c is the speed of light.)

It is useful to express x in terms of the energy of a photon, E . E is related to photon frequency, ν , by:

$$E = h\nu \quad [\text{A.5}]$$

Photon wavelength is related to frequency by:

$$\lambda = c/\nu \quad [\text{A.6}]$$

where c is the speed of light ($2.997\ 924\ 58 \times 10^8$ m/s). By combining equations A.5 and A.6, photon wavelength may be expressed in terms of energy:

$$\lambda = \frac{hc}{E} = \frac{1.240 \times 10^{-6}}{E} \quad [\text{A.7}]$$

providing the units of energy are electronvolts (eV), since hc is calculated here with units of eV m.

Substituting into equation A.4, momentum transfer, x , becomes:

$$x = \frac{E}{1.240 \times 10^{-6}} \sin\left(\frac{\theta}{2}\right) \quad [\text{A.8}]$$

Providing the units of energy are in eV, the units of momentum transfer are m^{-1} .

The EDXRD spectra acquired throughout this study have energy scales in keV units. Equation A.8 therefore becomes:

$$x = \frac{E}{1.240} \sin\left(\frac{\theta}{2}\right) \quad [\text{A.9}]$$

Providing the units of energy are in keV, the units of momentum transfer are nm^{-1} .

Equation A.9 is used throughout this study to perform any energy to momentum transfer conversion. The deflection angle θ is equivalent to the experimental scattering angle (expressed as 2θ throughout this study since it is twice the Bragg scattering angle, expressed as θ).

A.2 SCATTERING VOLUME FORMULAE

Some useful scattering volume formulae may be derived, with reference to figures A-2 and A-3, including the scattering length, the total length and the area of the plan view. Scattering length, s , is defined as the length of a line parallel to the primary photon beam passing through the plan of the scatter volume at $d/2$. Total length, t , is defined as the length of a line parallel to the primary photon beam that extends between the extremes of the plan area. Figure A-2 clarifies these definitions of scattering length and total length.

With reference to figure A-3, the width of the photon beam, d , is set by the collimator channel width (s_1 and s_2 (or s_{2T} and s_{2S}) in chapters four and six, assumed to be equal for these formulae) and 2θ , the experimental scattering angle. The height of the volume (perpendicular to the page so not shown) is set by the height of the diffractometer slits. The scattering volume, v_{scatt} , may be calculated by multiplying the area of the plan view, a_{scatt} (shaded grey in the figures) by the volume height.

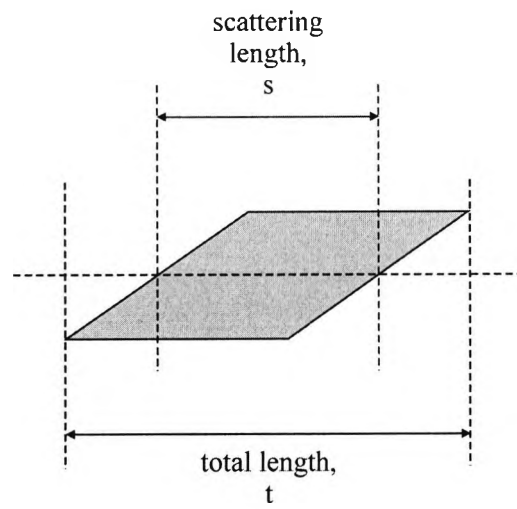


Figure A-2. Plan view of the scattering volume showing the scattering length and the total length.

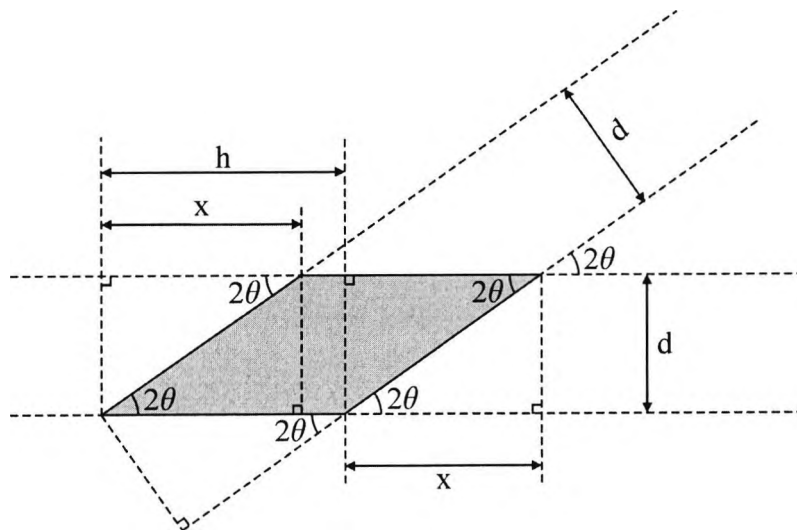


Figure A-3. Plan view of the scattering volume showing dimensions used for formulae calculations.

Considering similar triangles (figure A-3), it can be seen that the scattering length, s , is equal to the hypotenuse, h , of the triangles. It is simply calculated using:

$$s = \frac{d}{\sin(2\theta)} \quad [\text{A.10}]$$

Total length, t , may also be calculated using similar triangles (figure A-3):

$$\begin{aligned} t &= h + x \\ &= h + h \cdot \cos(2\theta) \end{aligned}$$

Since h is equivalent to the scattering length, s , equation A.10 may be substituted to derive total length, t :

$$t = \frac{d}{\sin(2\theta)} (1 + \cos(2\theta)) \quad [\text{A.11}]$$

An expression for the scattering area, a , may be derived by considering its three discrete sections (figure A-3):

$$\begin{aligned} a &= \frac{d \cdot h \cdot \cos(2\theta)}{2} + d(h - x) + \frac{d \cdot h \cdot \cos(2\theta)}{2} \\ &= d(h \cdot \cos(2\theta) + h - x) \end{aligned}$$

Since

$$h = \frac{d}{\sin(2\theta)} \quad \text{and} \quad x = h \cdot \cos(2\theta),$$

$$a = d \left(\left(\frac{d}{\sin(2\theta)} \cos(2\theta) \right) + \frac{d}{\sin(2\theta)} - \left(\frac{d}{\sin(2\theta)} \cos(2\theta) \right) \right)$$

Therefore, scattering area, a , is:

$$a = \frac{d^2}{\sin(2\theta)} \quad [\text{A.12}]$$

Appendix B

TECHNICAL DRAWINGS

This appendix presents technical drawings of equipment manufactured for use during this project. All dimensions given are in millimetres.

B.1 BONE CUTTING CHUCKS

The dimensions of the trabecular bone sample cubes used for this project were $15 \times 15 \times 15 \text{ mm}^3$. They were cut from within femoral heads using an Isomet 1000 precision circular saw with a diamond encrusted cutting blade (chapter five). In order to cut these samples accurately and squarely, additional chucks for the saw were required to secure the samples.

The first face of a cube was cut, with reference to a radiograph of the sample, using the general bone chuck supplied with the saw (block only). The second face was cut perpendicular to the first, again using the supplied chuck. The third face was cut, perpendicular to the first and second, using the first of the additional chucks (figure B-1). This resulted in a solid right angle being formed (half of the cube faces). The second additional chuck (figure B-2) was then used to hold this solid angle for the fourth face to be cut, followed by the fifth and sixth (final) faces in the same manner.

B.2 FIXED PARAMETER EDXRD DIFFRACTOMETER BLOCKS

The fixed parameter EDXRD diffractometer was designed for use with the final experiments (chapters six, seven and eight) in order to minimise repeatability discrepancies between experiment sets. It consisted of two dural blocks mounted on a breadboard using steel posts. These blocks were machined with channels to form the primary and secondary EDXRD collimation (figures B-3 and B-4). Unwanted channels were blocked using lead shields, fixed using the M4 tapped holes.

The EDXRD diffractometer assembly is discussed in chapter six.

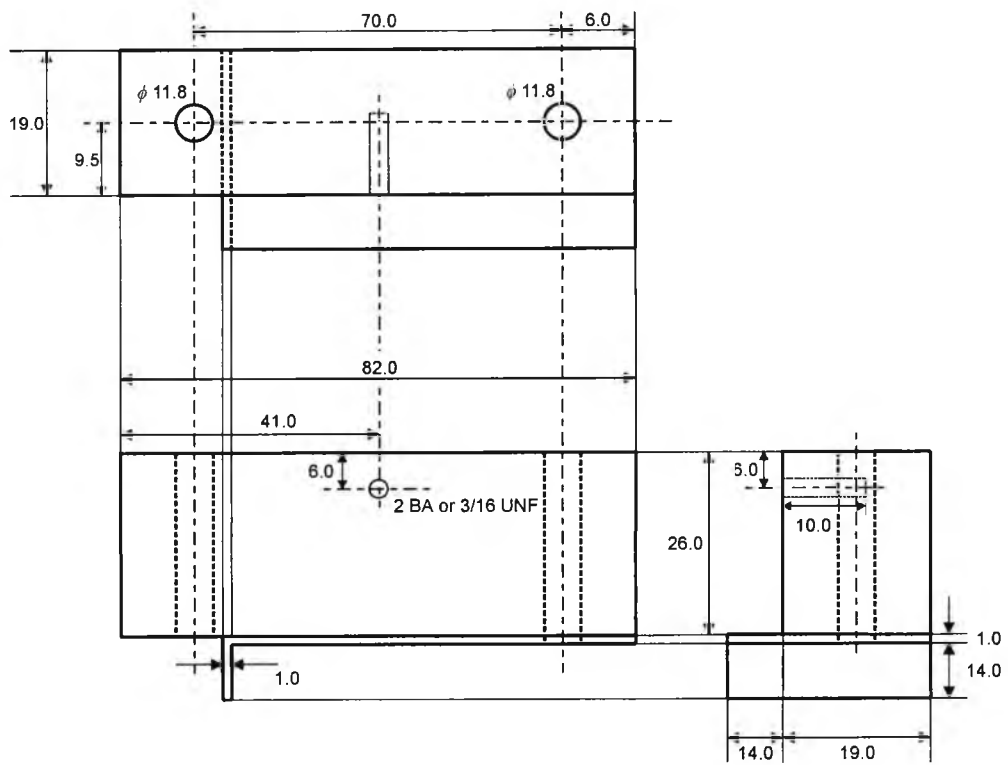


Figure B-1. Drawing of the first of two additional bone cutting chucks. The sample is held in place by a U-shaped clamp that is screwed into position through the two 11.8 mm diameter holes.

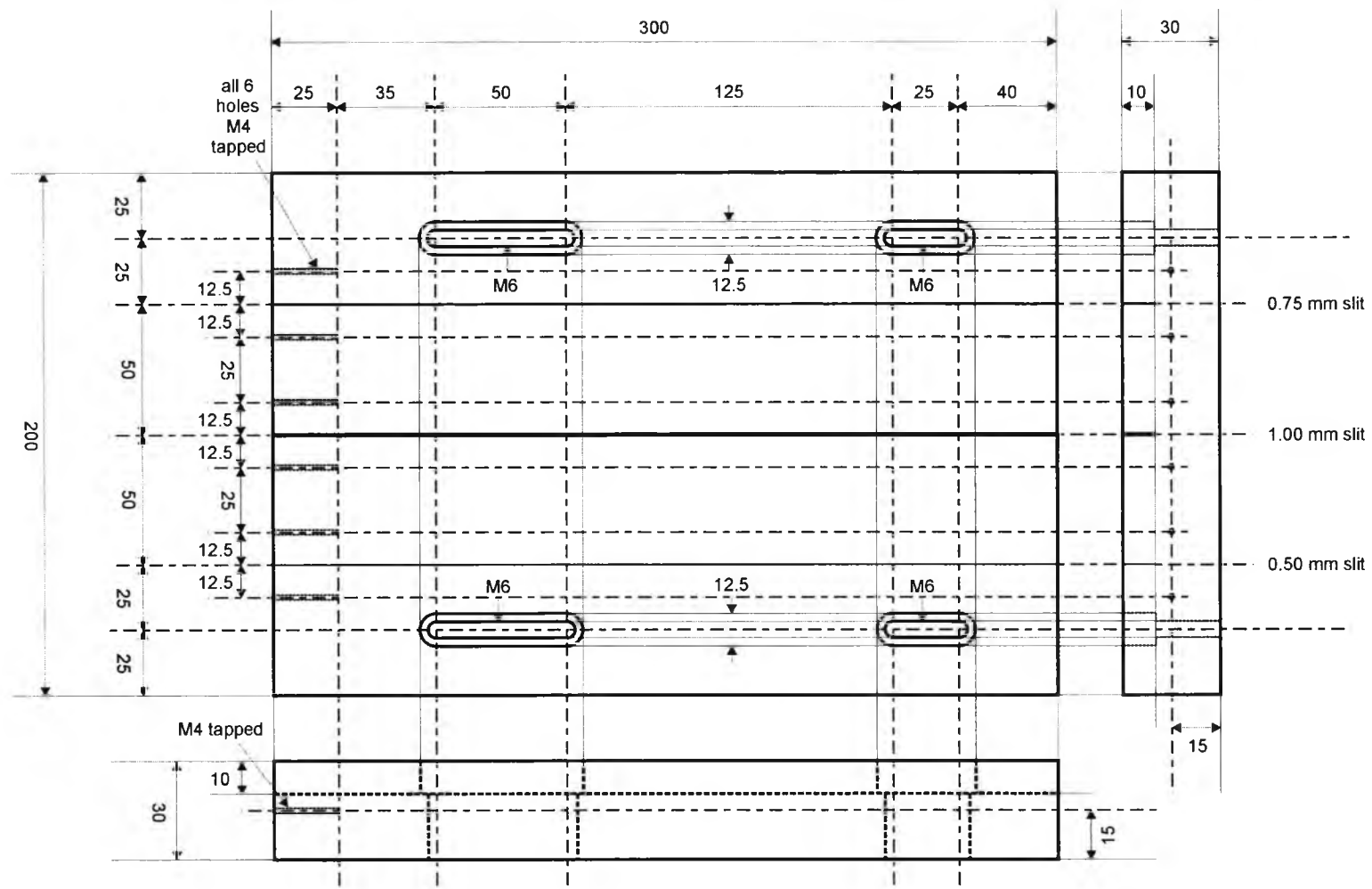


Figure B-3. Drawing of the primary block of the fixed parameter EDXRD diffractometer.

Appendix C

POWDER DIFFRACTION FILE DATA

This appendix provides the powder diffraction file data used in this project.

C.1 HYDROXYAPATITE

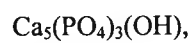
Table C-1 shows the interplanar spacings (d) from the powder diffraction file data for hydroxyapatite (calcium hydroxide orthophosphate), as compiled by the JCPDS (1967).

d [Å]	d [nm]	Proportion of strongest reflection [%]	d [Å]	d [nm]	Proportion of strongest reflection [%]
8.17	0.817	12	2.040	0.2040	2
5.26	0.526	6	2.000	0.2000	6
4.72	0.472	4	1.943	0.1943	30
4.07	0.407	10	1.890	0.1890	16
3.88	0.388	10	1.871	0.1871	6
3.51	0.351	2	1.841	0.1841	40
3.44	0.344	40	1.806	0.1806	20
3.17	0.317	12	1.780	0.1780	12
3.08	0.308	18	1.754	0.1754	16
2.814	0.2814	100	1.722	0.1722	20
2.778	0.2778	60	1.684	0.1684	4
2.720	0.2720	60	1.644	0.1644	10
2.631	0.2631	25	1.611	0.1611	8
2.528	0.2528	6	1.587	0.1587	4
2.296	0.2296	8	1.542	0.1542	6
2.262	0.2262	20	1.530	0.1530	6
2.228	0.2228	2	1.503	0.1503	10
2.148	0.2148	10	1.474	0.1474	12
2.134	0.2134	4	1.465	0.1465	4
2.065	0.2065	8	PLUS ADDITIONAL LINES		

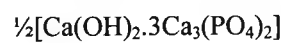
Table C-1. Hydroxyapatite interplanar spacings, d, from the JCPDS table 9-432 (JCPDS, 1967), presented in angstroms (Å) and nanometres (nm). The three strongest reflections are shown in bold (2.814 Å, 2.778 Å and 2.720 Å) along with the reflection at the largest interplanar spacing (8.17 Å).

This data was used to fit peaks to the EDXRD bone + marrow scattering spectra, discussed in chapter eight.

The chemical formula for hydroxyapatite may be expressed as:



or as:



Appendix D

RADIATION DOSIMETRY WEIGHTING FACTORS

This appendix provides weighting factors for radiation dosimetry as adopted by the International Commission on Radiological Protection (ICRP, 1991) and the National Council on Radiation Protection and Measurements (NCRP, 1993). Their use in this project is discussed in chapter nine.

D.1 RADIATION WEIGHTING FACTORS

Table D-1 shows the radiation weighting factors adopted by the ICRP (1991) and the NCRP (1993) by radiation and energy. They are used to calculate an equivalent dose from measured absorbed dose (chapter one, section 1.6.1).

Radiation type and energy	w_R
X-rays, γ -rays, electrons, positrons and muons	1
Neutrons to 10 keV	5
Neutrons, 10-100 keV	10
Neutrons, > 100 keV to 2 MeV	20
Neutrons, > 2-20 MeV	10
Neutrons, > 20 MeV	5
Protons, other than recoils, > 2 MeV	2 _(a)
α particles, fission fragments and relativistic heavy ions	20

Table D-1. Radiation weighting factors for equivalent dose (H_T) calculation (ICRP, 1991, and NCRP, 1993, table after Alpen, 1998). ICRP (1991) recommends a value of 5 for high energy protons (a).

D.2 TISSUE WEIGHTING FACTORS

Table D-2 shows the tissue weighting factors (NCRP, 1993) for calculation of effective dose from measured absorbed dose and subsequently calculated equivalent dose (chapter one, section 1.6.1).

$w_T = 0.01$	$w_T = 0.05$	$w_T = 0.12$	$w_T = 0.20$
Bone surface	Bladder	Bone marrow	Gonads
Skin	Breast	Colon	
	Liver	Lung	
	Oesophagus	Stomach	
	Thyroid		
	Remainder _(a)		

Table D-2. Tissue weighting factors for effective dose (*E*) calculation (NCRP, 1993, table after Alpen, 1998). 'Remainder' represents all other tissues not specifically listed (a).

Appendix E

SOFTWARE

This appendix presents software developed for the analysis of data generated by a number of experiments during this project.

E.1 CONVERTING MAESTRO CHN FILES: ATTENCHN

This program was written in C, for compilation and linking with the Borland C++ Builder 5 compiler (version 5.0), in order to convert PerkinElmer/EG&G Ortec Maestro CHN spectroscopy files into text files that may be used with analysis software such as The MathWorks MatLab or Microsoft Excel. It compiles to an EXE executable file and runs under Microsoft DOS.

```

/*****
*
* NAME
*
*   AttenCHN.c : File conversion from Maestro CHN to a usable format
*
*****/
*
* DETAILS
*
*   Version   1.0           Date   9.iv.'02           Author   Allan Allday
*
*   This program is based on 'readchn' from the PerkinElmer/EG&G Ortec
*   Maestro 32 manual (revision C, p. 194-195) and 'Acchn' by Captain
*   Andrew Bagshaw (version: apb 20/10/99).
*
*   Compiled and linked with Borland C++ Builder 5, version 5.0.
*
*****/
*
* DESCRIPTION
*
*   PerkinElmer/EG&G Ortec manufacture a range of gamma ray detector and
*   electronic analysis systems (multichannel analysers) for spectroscopy
*   applications. They may be controlled using a PC running the
*   PerkinElmer/EG&G Ortec software called Maestro. Maestro generates
*   spectrum files which by default are stored in an 'Integer CHN' format
*   with a '.chn' file extension.
*
*   AttenCHN was written to extract data from the CHN files and save it
*   in a format that is easy to use with other analysis packages. There
*   are a number of options that may be set in AttenCHN to adjust the
*   format of these output files.
*
*   AttenCHN is for anybody to use who may find it helpful.
*
*   AttenCHN is a program written in C.
*
*****/

```

```
*
* When the executable file AttenCHN.exe is run (from a DOS window),
* the program first checks the input style. If the name of a
* processing file (extension ATT) is included in the input line, for
* example 'C:\DIRECTORY> AttenCHN Process', processing is performed in
* accordance with the ATT file without AttenCHN menus. If the input
* line is just 'C:\DIRECTORY> AttenCHN', the menu system is used. The
* following description is mainly concerned with the menu system. The
* direct method simply runs internally option 2 then option 1 from the
* main menu.
*
* On running AttenCHN, the directory is searched for the default
* processing file (AttenCHN.att), which contains the last run
* processing options (information about the requirements for the output
* file(s)). If found, current processing details are displayed. Also
* the directory is searched for CHN files, the names of which are
* displayed if found. If the default ATT file is not present but
* another ATT file is found, the user is asked whether to use an
* alternative processing file or build a new one.
*
* The format of the ATT file is as follows:
*
* Line 1:  Indicator 1: File Handling
*          bit 0 = output all .chn file data to one file
*          bits 1-7 spare
*
*          Indicator 2: Headers in Output File
*          bit 0 = include header in o/p file
*          bit 1 = include .chn file names in output file
*          bits 2-7 spare
*
*          Indicator 3: Channel details in Output File
*          bit 0 = include channel numbers in o/p file
*          bit 1 = include channel energies in o/p file
*          bit 2 = bypass calibrated energies
*          bits 3-7 spare
*
*          Indicator 4: Spare Indicators
*          bits 0-7 spare
*
*          Example:  x'01'  x'02'  x'03'  x'00'
*
* Line 2:  Number of tabs to be added between data columns (only used
*          if indicator 1, bit 0 is on - output all CHN data to one
*          file).
*
*          Example:  1
*
* Line 3:  Lowest channel number and highest channel number required.
*          This information is necessary to ascertain the channel
*          counts that need to be copied to the output file.
*
*          Example:  60      1859
*
* Line 4:  Lowest channel energy and highest channel energy.
*          The energies are in keV and must be the energy values of
*          the lowest and highest channel numbers. This information
*          must be included in the processing file, even if channel
*          energies have not been requested in line 1. If the
*          calibrated energies from the CHN file are to be used
*          (indicator 3, bit 2 off), these values are set to a
*          default 0 and 1 respectively.
*
*          Example:  2.13    72.73
*
* Line 5:  Name of output file (only used if indicator 1, bit 0 is on -
*          output all CHN data to one file) and extension of output
*          file(s).
*
*          Example:  maestro  dat
*
* Line 6:  Number of Maestro CHN files to be processed. This must
*          match the number of file names provided in the list
*          starting at line 7.
```

Example: 3

Line 7: First of a list of Maestro CHN file names to be processed. The files must have a '.chn' extension and must be present in the directory or folder that AttenCHN is run from. The number of file names must match the number given in line 6.

Example: Spctrm01

An example of a processing file is shown below:

```

1      2      3      0
1
60     1859
0.000000  1.000000
maestro   dat
3
Spctrm01
Spctrm02
Spctrm03

```

When AttenCHN is run, the main menu is displayed, allowing the user to navigate through the various options available (as described in the INSTRUCTIONS FOR USE section below). If option 4 is selected (Update individual options or CHN file selection), a sub-menu is displayed. This allows the user to change processing settings individually, without having to set up the options again. The main menu also allows the user to save the current settings under a new processing file name (the .att extension is appended automatically), load a previously created processing file, create an entirely new processing set-up or process the CHN according to the current settings (ultimately this will be the user's action).

When the 'process data' option is selected, data is extracted from the specified Maestro CHN files and copied to an output file(s) in the format selected. This results in the creation of a new output data file(s) in the directory from which AttenCHN was run. The original CHN files remain in this directory unaltered.

The format of the CHN file is as follows. Note hexadecimal data of more than one byte is stored as little-endian (least significant byte has a lower address). There are 8736 bytes in the file in total.

```

BYTES 0000 - 0031 (32): FILE HEADER
Bytes 0000 - 0001 (2): File type (short/hex). A CHN file is
indicated by these bytes being set to
'255' & '255'.
Bytes 0002 - 0003 (2): MCA number (short/hex).
Bytes 0004 - 0005 (2): Segment number (short/hex).
Bytes 0006 - 0007 (2): Start time (char). Second.
Bytes 0008 - 0011 (4): Real time (long/hex). 20 mS ticks.
Bytes 0012 - 0015 (4): Live time (long/hex). 20 mS ticks.
Bytes 0016 - 0023 (8): Start date (char).
0016 - 0017 (2): Start date (char). Day.
0018 - 0020 (3): Start date (char). Month.
0021 - 0023 (3): Start date (char). Year. First two bytes
only.
Bytes 0024 - 0025 (2): Start time (char). Hour.
Bytes 0026 - 0027 (2): Start time (char). Minute.
Bytes 0028 - 0029 (2): Channel offset (short/hex). Data channel
start.
Bytes 0030 - 0031 (2): Number of data channels (short/hex).
BYTES 0032 - 8223 (8192): FILE DATA CHANNELS
Bytes 0032 - 0035 (4): Data channel 0 (long/hex).
Bytes 8220 - 8223 (4): Data channel 2047 (long/hex).
BYTES 8224 - 8735 (512): FILE TRAILER
Bytes 8224 - 8225 (2): Trailer type (short/hex).
Bytes 8226 - 8227 (2): Dummy type (short/hex).
Bytes 8228 - 8231 (4): Energy 1 (long/hex). Energy of first
channel.

```

```

*   Bytes 8232 - 8235   (4):   Energy 2 (long/hex). Energy slope
*                       (increment per channel).
*   Bytes 8236 - 8239   (4):   Energy 3 (long/hex). Dummy energy.
*   Bytes 8240 - 8243   (4):   FWHM 1 (long/hex). FWHM of first channel.
*   Bytes 8244 - 8247   (4):   FWHM 2 (long/hex). FWHM slope (increment
*                               per channel).
*   Bytes 8248 - 8251   (4):   FWHM 3 (long/hex). Dummy FWHM.
*   Bytes 8252 - 8255   (4):   Energy units (char). E.g. keV.
*   Byte  8480 - variable :   MCA name.
*   8480             (1):   MCA name (byte/hex). Number of characters
*                               in MCA name.
*   8481 - variable   :   MCA name (char). Number of characters
*                               matches byte 8480.

```

AMENDMENTS

INSTRUCTIONS FOR USE

AttenCHN is an executable file to be run in a DOS environment. Ensure a copy of 'AttenCHN.exe' resides in the directory with the Maestro CHN files to be converted. Windows users should then open a DOS window (from Start menu -> Programs -> MS-DOS Prompt). Change the directory to the one in use (C:\>CD\DIRECTORY). Then run the AttenCHN program (C:\DIRECTORY>AttenCHN).

1) First time use of AttenCHN (i.e. no processing files in directory)

Providing there are CHN files present in the directory, AttenCHN displays the CHN file names. There follows a series of prompts to build a default ATT processing set-up file:

Output all data to one file (y/n)?:

If yes ('y'), all data from the CHN files will be output in separate columns to the same file. A name for this file is then required (a file extension should not be entered at this stage).

If no ('n'), a separate file will be made corresponding to each CHN file. The file name will be the same as the CHN file name.

Output file extension (e.g.xls):

A three-character file extension is required (such as 'dat' or 'xls').

Lowest channel number:
Highest channel number:

This allows for the selection of the range of channel data to be extracted from the CHN file(s) (e.g. '60' to '1859'). Clearly these channel numbers must be within the total range of CHN file channels (e.g. '0' to '2047').

Include channels in o/p file (y/n)?:

If yes ('y'), the output file will include a column with the channel numbers corresponding to the channel data.

Include energies in o/p file (y/n)?:

If yes ('y'), the output file will include a column with the energy values (in keV) corresponding to the channel data.

Bypass calibrated energies (y/n)?:

If no ('n'), the Maestro calibration energies are used. If these energies are not to be used (for example, the calibration may be incorrect), these energies may be overridden by entering yes ('y'). If yes ('y'),

```
*
*   Lowest energy (keV):
*   Highest energy (keV):
*
* This allows for the selection of the range of channel energies to be
* entered, bypassing the Maestro calibrated energies (e.g. '0' to
* '80.10').
*
*   Include header in output file (y/n)?:
*
* AttenCHN generates useful information about the processing which is
* output as a separate '..._info.dat' file. If yes ('y'), this
* information is included as a header in the output data file as well.
* If all CHN data is output to one file, much of this header
* information will refer to the first CHN file only.
*
*   Include CHN file names in o/p file (y/n)?:
*
* If yes ('y'), the CHN file name is added as a column heading above
* the corresponding column of data. This option should certainly be
* used if the CHN file data is output to one file, in order to identify
* each column of data.
*
*   Include all CHN files (y/n)?:
*
* If yes ('y'), all the CHN files in the directory will be processed.
* If no ('n'), each CHN file name is offered for selection. Enter 'y'
* to include the CHN file or 'n' to exclude it.
*
* Now the processing parameters are all set up. They are displayed and
* the default processing file 'AttenCHN.att' is created. This file is
* updated whenever a processing parameter is changed.
*
* Providing 'AttenCHN.att' is in the directory being used, it is not
* necessary to build the parameters again. If AttenCHN is run with
* 'AttenCHN.att' in place, the parameters from this default processing
* file are loaded and displayed straight away. If the default ATT file
* is not present but other ATT files are found in the directory, the
* user is asked whether to use an alternative processing file or build
* a new one. The menu displayed is:
*
*   Options are: (0) Exit with no action
*                (1) Load alternative data set-up
*                (2) Create new data set-up
*
* If 'Load alternative data set-up' (1) is selected, the list of
* available ATT files is displayed. The required processing file name
* should be entered. The '.att' file extension is not required.
*
* If 'Create new data set-up' (2) is selected, the new processing file
* name is prompted for, followed by the processing file procedure
* previously described. On completion, the new ATT file is created
* along with an identical default 'AttenCHN.att' file.
*
* 2) Standard use of AttenCHN (i.e. 'AttenCHN.att' file in directory)
*
* This section describes the menu options available in AttenCHN, once a
* default processing file exists.
*
* Run AttenCHN in a DOS window in the directory of choice. Providing
* there are CHN files present in the directory, AttenCHN displays the
* default processing settings (providing 'AttenCHN.att' has been
* created) and CHN file names, followed by the main menu:
*
*   Options are: (0) Exit with no action
*                (1) Process data as above
*                (2) Load alternative data set-up
*                (3) Create new data set-up
*                (4) Update individual options or CHN file selection
*                (5) Save current data set-up
*
* If 'Process data as above' (1) is selected, providing the data set-up
```

```
* is correct and the CHN files are present, an output file(s) is
* created containing the extracted data and other requested information
* from the CHN file(s). In addition, an information file(s)
* ('..._info.dat') is created with further extracted information, such
* as CHN creation data and time, real, live and dead times and
* information about the CHN (input) and created file (output) channels.
*
* If 'Load alternative data set-up' (2) is selected, the list of
* available ATT files is displayed. The required processing file name
* should be entered. The '.att' file extension is not required.
*
* If 'Create new data set-up' (3) is selected, the new processing file
* name is prompted for (the '.att' file extension is not required),
* followed by the processing file procedure previously described. On
* completion, the new ATT file is created along with an identical
* default 'AttenCHN.att' file.
*
* If 'Save current data set-up' (5) is selected, a name for the current
* data set-up is prompted for (the '.att' file extension is not
* required). If 'AttenCHN' is entered as the name, the default
* processing file will be overwritten. A new ATT file containing the
* current data set-up is created which may be used by loading with
* option 2 or running with AttenCHN directly, as detailed below in
* section 3.
*
* If 'Update individual options or CHN file selection' (4) is selected,
* any item of the current data set-up may be adjusted without creating
* a whole new set-up using option 3. After the current data set-up, a
* sub-menu is displayed:
*
*   Options are: (0) Return to main menu
*                (1) Update output file options
*                (2) Update output file extension
*                (3) Update channel numbers
*                (4) Update channels to output option
*                (5) Update energies to output option
*                (6) Update header to output option
*                (7) Update CHN names to output option
*                (8) Update selected CHN file list
*
* 'Update output file options' (1) allows the 'output data to one file'
* option to be changed. If the response is yes ('y'), a file name is
* required. The option for tabs (empty columns) between data columns
* may then be set.
*
* 'Update output file extension' (2) allows the output file extension
* to be changed (e.g. 'dat' or 'xls').
*
* 'Update channel numbers' (3) allows the range of channel numbers in
* the output file to be changed.
*
* 'Update channels to output option' (4) allows the option to include
* channel numbers in the output file to be changed.
*
* 'Update energies to output option' (5) allows the option to include
* energy values in the output file to be changed. If yes ('y'), the
* Maestro calibrated energies may then be bypassed (for example, if the
* calibration is incorrect) and set to other values (corresponding to
* the lowest and highest channel numbers).
*
* 'Update header to output option' (6) allows the option for the header
* information (also provided in the '..._info.dat' file(s)) to be
* included in the output file to be changed.
*
* 'Update CHN names to output option' (7) allows the option for CHN
* file names to be added at the top of each data column to be changed.
* Useful if all CHN file data is output to one file.
*
* 'Update selected CHN file list' (8) allows the selection of CHN files
* to be processed to be altered. All CHN files in the directory may be
* selected or each CHN file may be included or excluded (with 'y' or
* 'n').
```

```

* 3) Direct use of AttenCHN (i.e. specify processing file in input) *
*
* This method allows AttenCHN to be used quickly without the need to *
* use the menu system. An ATT file must have been prepared with the CHN *
* files also present in the directory. Providing the processing set-up *
* is correct (ATT file), AttenCHN is run by entering *
* C:\DIRECTORY>AttenCHN [ATT_file_name]. The '.att' file extension is *
* not required. The ATT data set-up is loaded and processing is *
* performed with output file(s) and output information files being *
* produced. *
*
*****/
/*****
* Initial definitions. *
*****/

/* Function libraries. */

#include <stdio.h> /* input and output functions */
#include <math.h> /* mathematical functions */
#include <string.h> /* character string functions */
#include <stdlib.h> /* utility functions */
#include <dir.h> /* directory and path functions */
#include <ctype.h> /* character class tests */

/* Definitions. */

#define BITN 0 /* x'00' = binary '0000 0000' */
#define BIT0 1 /* x'01' = binary '0000 0001' */
#define BIT1 2 /* x'02' = binary '0000 0010' */
#define BIT2 4 /* x'04' = binary '0000 0100' */
#define BIT3 8 /* x'08' = binary '0000 1000' */
#define BIT4 16 /* x'10' = binary '0001 0000' */
#define BIT5 32 /* x'20' = binary '0010 0000' */
#define BIT6 64 /* x'40' = binary '0100 0000' */
#define BIT7 128 /* x'80' = binary '1000 0000' */
#define BITR 15 /* x'0F' = binary '0000 1111' */
#define BITL 240 /* x'F0' = binary '1111 0000' */
#define BITA 255 /* x'FF' = binary '1111 1111' */

#define CHN -1 /* CHN file type flag */

#define DETOFFSET 8480 /* offset bytes for detector name in CHN file */

#define MAXCHF 100 /* maximum number of CHN files to process */
#define MAXCHN 2048 /* maximum number of channels in a CHN file */
#define MAXCHR 256 /* maximum number of characters in file name */

/* Functions. */

void processread(void); /* read ATT file */
void processdisphhead(void); /* display ATT file header */
void processdisplist(void); /* display ATT file selected CHN files */
void processinput(void); /* input parameters for new ATT file */
void processcreate(void); /* create a new ATT file */

void chndisplist(void); /* display directory CHN files */
void attdisplist(void); /* display directory ATT files */

void fileread(void); /* open and read from CHN data file */
void filewrite(void); /* write to output file */
void filewriteone(void); /* write all data to one output file */
void filereport(FILE *); /* write report information to file */

/* Variables: File names. */

char f_name_process[256]; /* processing file name */
char f_name[256]; /* file name */
char f_name_save[256]; /* save file name over processing */

```

Software

```

char      f_ext[4];           /* file extension                */
char      f_name_in[256];    /* Maestro CHN file name        */
char      f_name_out[256];   /* output file name              */
char      f_name_report[256]; /* output report file name      */

/* Variables: Data from processing file.
int      p_ind1;             /* indicators - file handling    */
/* bit 0: output all .chn data to one file
/* bits 1-7 spare
int      p_ind2;             /* indicators - headers in output file
/* bit 0: header to o/p file
/* bit 1: .chn file names to output file
/* bits 2-7 spare
int      p_ind3;             /* indicators - channel details in output file
/* bit 0: channel numbers to o/p file
/* bit 1: energy to o/p file
/* bit 2: bypass calibrated energies
/* bits 3-7 spare
int      p_ind4;             /* spare indicators
/* bits 0-7 spare
int      p_tabs;             /* tabs between columns (one file o/p only)
int      p_low_chan;         /* lowest channel number in .chn file
int      p_high_chan;        /* highest channel number in .chn file
float    p_low_energy;       /* lowest channel energy in .chn file
float    p_high_energy;      /* highest channel energy in .chn file
char      p_output_file[256]; /* output file name
char      p_output_type[3];  /* output file type (e.g. .xls)

int      p_number_files;     /* number of .chn files to process
int      p_number_chans;     /* number of channels to transfer to output

char      p_name_array[100][256];
/* list of ATT files

double   p_energy_step;     /* energy increment for one channel (bypass)

/* Variables: Data from Maestro CHN files.

short     d_file_type[100];  /* file type (CHN)
short     d_mca_num[100];    /* MCA number (1-4 are valid)
short     d_segment[100];    /* segment number
char      d_acq_time_sec[100][2]; /* start time seconds
long      d_realtime[100];   /* real time (20 ms ticks)
long      d_livetime[100];   /* live time (20 ms ticks)
char      d_acq_date_day[100][2]; /* start date day
char      d_acq_date_month[100][3]; /* start date month
char      d_acq_date_year[100][3]; /* start date year
char      d_acq_time_hour[100][2]; /* start time hour
char      d_acq_time_min[100][2]; /* start time minute
unsigned short d_chan_offset[100]; /* first channel number
short     d_num_chans[100];  /* number of data channels

long      d_chan_data[100][2048]; /* MCA channel data to transfer to
/* output file

short     d_trltyp[100];     /* trailer record type
short     d_dummy1[100];     /* dummy (no information)
float     d_eng1[100];       /* energy zero (at start point)
float     d_eng2[100];       /* energy slope
float     d_eng3[100];       /* blank
float     d_FW1[100];        /* FWHM zero (at start point)
float     d_FW2[100];        /* FWHM slope
float     d_FW3[100];        /* blank
char      d_units[100][4];   /* energy units

int       d_detname_length[100]; /* detector name length (1 byte)
char      d_detname[100][256]; /* detector name

/* Variables: Calculated data.

```

```

double   c_realtime[100]; /* calculated real time in seconds */
double   c_livetime[100]; /* calculated live time in seconds */
double   c_deadtime[100]; /* calculated average dead time percentage */

short    c_high_chan_in[100]; /* calculated highest input channel */
float    c_high_eng_in[100]; /* calculated highest input channel energy */

float    c_low_eng_out[100]; /* calculated lowest output channel energy */
float    c_high_eng_out[100]; /* calculated highest output channel energy */

double   c_energy; /* energy value (incremented with channels) */
double   c_energy_step; /* energy increment for one channel (calib) */

/* Variables: General processing. */

struct   ffbk ffbk; /* file search */

int      done; /* file search */

int      option1; /* processing option: 0 = take no action
                  /* 1 = default display ATT
                  /* 2 = alternative ATT file
                  /* 3 = make new ATT file

int      option2; /* processing option: 0 = take no action
                  /* 1 = continue processing
                  /* 2 = start again

int      ind1; /* indicators - general work
               /* bit 0: request default 'AttenCHN.att'
               /* processing file
               /* bit 1: requested processing file does not
               /* exist
               /* bit 2: no ATT files exist
               /* bit 3: ATT file supplied in input
               /* bit 4: save ATT file
               /* bits 5-7 spare

int      ind2; /* indicators - general work
               /* bit 0: indicate a CHN file successfully
               /* found
               /* bits 1-7 spare

int      ind3; /* indicators - general work
               /* bit 0: indicate use updated CHN list (OFF
               /* use directory list)
               /* bit 1: use all CHN files from directory
               /* bits 2-3 spare
               /* bit 4: restrict reporting (multiple CHNs)
               /* bit 5: file report
               /* bits 6-7 spare

int      ind4; /* indicators - general work
               /* bit 0: save output file
               /* bits 1-7 spare

int      output_ind1; /* indicators - processing file options
                     /* bit 0: data to one file
                     /* bit 1: output file extension
                     /* bit 2: channel numbers
                     /* bit 3: channels to output
                     /* bit 4: energies to output
                     /* bit 5: header to output file
                     /* bit 6: CHN file names to output
                     /* bit 7: tabs between numbers

int      output_ind2; /* indicators - processing file options
                     /* bit 0: list of ATT files
                     /* bits 1-7 spare

int      f_error1[100]; /* indicators - CHN file errors
                       /* bit 0: file opening error
                       /* bit 1: channel count mismatch
                       /* bits 2-7 spare

```

```

int     count;           /* working count           */
short   s;              /* working short integer   */
int     i;              /* working integer         */
long    l;              /* working long integer    */
float   f;              /* working float           */
char    str[256];       /* working character string */

char    answer;         /* yes or no condition     */

int     count_files;    /* count of Maestro CHN files to process */
int     count_chans;    /* count of energy channels, Maestro CHN file */
int     num_chans_out;  /* number of channels in CHN files to output */
int     length;        /* length of character string */

/* File streams. */

FILE    *processingread; /* read processing file pointer */
FILE    *processingnew;  /* new processing file pointer */
FILE    *input;         /* Maestro CHN input file pointer */
FILE    *output;        /* requested output file pointer */
FILE    *outputreport;  /* output report file pointer */

/*****
* Main function.
*****/

int main(int argc, char *argv[])
{
beginning:

/* Initial variable values. */

option1 = 0;
option2 = 0;

ind1 = 0;
ind2 = 0;
ind3 = 0;
ind4 = 0;

output_ind1 = 0;
output_ind2 = 0;

num_chans_out = 0;

strcpy(p_output_file, "noname");
strcpy(p_output_type, "out");

p_tabs = 0;

p_low_chan = 0;
p_high_chan = 1;

p_low_energy = 0;
p_high_energy = 1;

/* Title. */

printf("\n\n\t\t\tATTENCHN");

start:

do /* loop until option 1 is selected */
/* (process CHN files) */
{
printf("\n");
}

/* Test for input style. If name of processing file is entered on */

```

```
/* instigating AttenCHN, set option1 = 0. */
{
    if(argc == 2)
    {
        strcpy(f_name_process,argv[1]);

        ind1 = ind1 | BIT3;          /* indicate ATT file supplied */
        option1 = 2;
    }
    else
    {

/* Check for any ATT files. */

        ind1 = ind1 & (BITA - BIT2); /* clear ATT not found indicator */
        done = findfirst("*.att",&fblk,0);

        if(done)
        {
            ind1 = ind1 | BIT2;      /* indicate NO ATT files found */
        }

/* Set up processing file name to open. */

        ind1 = ind1 | BIT0;          /* request default processing file */
        processread( );

        if((ind1 & BIT1) == 0)      /* if processing file found */
        {
            processdisphead( );
        }
        printf("\n");

        if((ind3 & BIT0) != 0)      /* if updated CHN list available */
        {
            processdisplist( );
        }
        else
        {
            chndisplist( );
        }

        if((ind1 & BIT1) == 0)      /* if processing file found */
        {
            processcreate( );
        }

        if (count_files == 0)
        {
            printf(" *** NO CHN FILES TO PROCESS ***\n");
            goto end;
        }
        else if((ind1 & BIT2) != 0) /* if NO ATT files found */
        {
            option1 = 3;
        }
        else
        {
            option1 = 0;            /* initialise option1 */

            printf("\nOptions are: (0) Exit with no action");

            if((ind1 & BIT1) == 0) /* if processing file found (default */

```

```

                                /* in this case)          */
{
    printf("\n          (1) Process data as above");
    printf("\n          (2) Load alternative data set-up");
    printf("\n          (3) Create new data set-up");
    printf("\n          (4) Update individual options or CHN");
    printf("\n file selection");
    printf("\n          (5) Save current data set-up");

    printf("\n\nEnter option: ");
    scanf("%d",&option1);
    while (i = getchar( ), i != 10);
                                /* clear any remaining input from */
                                /* stdin to line feed ('10')      */
}
else
{
    printf("\n          (1) Load alternative data set-up");
    printf("\n          (2) Create new data set-up");

    printf("\n\nEnter option: ");
    scanf("%d",&option1);
    while (i = getchar( ), i != 10);
                                /* clear any remaining input from */
                                /* stdin to line feed ('10')      */

    if(option1 == 1)            /* if option 1 chosen          */
    {
        option1 = 2;
    }
    else if(option1 == 2)      /* if option 2 chosen          */
    {
        option1 = 3;
    }
    else if(option1 == 3)      /* if option 3 chosen          */
    {
        option1 = 0;
    }
    else if(option1 == 4)      /* if option 4 chosen          */
    {
        option1 = 0;
    }
    else if(option1 == 5)      /* if option 5 chosen          */
    {
        option1 = 0;
    }
}
}

switch(option1)
{
    case 1:                    /* process displayed data      */

        processcreate( );

        break;

    case 2:                    /* load alternative data set up */

        printf("\n\n");
        attdisplist( );

        if((ind1 & BIT2) != 0) /* if NO ATT processing files found */
        {
            printf(" *** NO PROCESSING FILES AVAILABLE ***\n");

            goto end;
        }
        else
        {
            printf("\n\nEnter processing data filename: ");
            scanf("%s",&f_name_process);
        }
}

```

```
        break;

    case 3:                /* process new data set up          */
        if((ind1 & BIT2) == 0) /* if ATA processing files are found */
        {
            printf("\n\n");
            attdisplist( );

            printf("\n\nEnter new processing data filename: ");
            scanf("%s",&f_name_process);
        }

        break;

    case 4:                /* update options or CHN list      */
        break;

    case 5:                /* save current data set up        */
        printf("\n\n");
        attdisplist( );    /* display current ATT files      */
        ind1 = ind1 | BIT0; /* request default processing file */
        processread( );

        printf("\n\nEnter new processing data filename: ");
        scanf("%s",&f_name_process);
        strcat(f_name_process, ".att");

        break;

    default:              /* none of the above              */
        goto end;
}

switch(option1)
{
    case 1:                /* process displayed data          */
        break;

    case 2:                /* load alternative data set up    */
        if((ind1 & BIT0) == 0) /* if NOT default processing file */
        {
            strcat(f_name_process, ".att");
        }

        processread( );

        if((ind1 & BIT1) != 0) /* if processing file NOT found   */
        {
            goto end;
        }

        strcpy(f_name_process, "AttenCHN");
        strcat(f_name_process, ".att");

        processcreate( );
}
```

```

ind1 = ind1 | BIT0;          /* request default processing file */

processread( );

if((ind1 & BIT1) != 0)      /* if processing file not found */
{
    printf("\n\tProcessing file '%s' ",f_name_process);
    printf("does not exist.\n");

    goto start;
}

if((ind1 & BIT3) == 0)      /* if ATT file NOT supplied */
{
    if (count_files == 0)   /* no CHN files selected */
    {
        processdisphead( );
        printf("\n");
        processdisplist( );

        printf(" *** NO CHN FILES SELECTED ***\n");

        goto end;
    }
}
else
{
    option1 = 1;           /* ATT file supplied so process */
}

break;

case 4:                    /* update options */

do                          /* loop until option 0 is selected */
{                            /* (return to main menu) */
    option2 = 0;           /* initialise option2 */

    printf("\n");
    processdisphead( );

    printf("\nOptions are: (0) Return to main menu");
    printf("\n                (1) Update output file options");
    printf("\n                (2) Update output file extension");
    printf("\n                (3) Update channel numbers");
    printf("\n                (4) Update channels to output option");
    printf("\n                (5) Update energies to output option");
    printf("\n                (6) Update header to output option");
    printf("\n                (7) Update CHN names to output option");
    printf("\n                (8) Update selected CHN file list");

    printf("\n\nEnter option: ");
    scanf("%d",&option2);
    while (i = getchar( ), i != 10);
        /* clear any remaining input from */
        /* stdin to line feed ('10') */

    switch(option2)
    {
        case 1:           /* output file options */

            output_ind1 = output_ind1 | (BIT0 + BIT7);
            printf("\n\nUpdating processing file o/p options-->\n");
            processinput( );
            processcreate( );

            break;

        case 2:           /* output file extension */

            output_ind1 = output_ind1 | BIT1;

```

```
printf("\n\nUpdating o/p file extension-->\n");
processinput( );
processcreate( );

break;

case 3:          /* channel numbers          */

output_ind1 = output_ind1 | BIT2;
printf("\n\nUpdating processing file o/p option-->\n");
processinput( );
processcreate( );

break;

case 4:          /* channels to output        */

output_ind1 = output_ind1 | BIT3;
printf("\n\nUpdating processing file o/p option-->\n");
processinput( );
processcreate( );

break;

case 5:          /* energies to output          */

output_ind1 = output_ind1 | BIT4;
printf("\n\nUpdating processing file o/p options-->\n");
processinput( );
processcreate( );

break;

case 6:          /* header to output          */

output_ind1 = output_ind1 | BIT5;
printf("\n\nUpdating processing file o/p option-->\n");
processinput( );
processcreate( );

break;

case 7:          /* CHN names to output          */

output_ind1 = output_ind1 | BIT6;
printf("\n\nUpdating processing file o/p option-->\n");
processinput( );
processcreate( );

break;

case 8:          /* CHN file selection          */

printf("\n\n");
chndisplist( );

output_ind2 = output_ind2 | BIT0;
printf("\n\nUpdating selected CHN file list -->\n");
processinput( );
processcreate( );

break;

default:        /* return to main menu          */

option2 = 0;

ind1 = ind1 | BIT0;          /* request default processing file */
processread( );
if((ind1 & BIT1) != 0)      /* if processing file not found    */
```

```

    {
        printf("\n\n\tProcessing file '%s' ",f_name_process);
        printf("does not exist.\n");
    }
    goto end;
}

if (count_files == 0)
{
    processdishead( );

    printf("\n *** NO CHN FILES SELECTED ***\n");

    goto end;
}

}
while(option2 != 0);          /* DO WHILE updating options      */

break;

case 3:                      /* process new data set up      */

if((ind1 & BIT2) != 0)       /* if NO ATT processing files found */
{
    printf("\n\nBuilding processing parameters -->");
}
else
{
    printf("\n\nCreating '%s' processing file -->",f_name_process);
    strcpy(f_name_save,f_name_process);
}

printf("\n");

output_ind1 = output_ind1 | BITA;
output_ind2 = output_ind2 | BIT0;

processinput( );

ind1 = ind1 | BIT0;         /* request default processing file */

processcreate( );

if((ind1 & BIT2) == 0)       /* if ATT processing files found */
{
    strcpy(f_name_process,f_name_save);
    strcat(f_name_process, ".att");
}

case 5:                      /* save current processing set up */

/* Check that processing file does not already exist. */

if((ind1 & BIT2) != 0)       /* if NO ATT processing files found */
{
    ind1 = ind1 & (BITA - BIT2);
    /* clear ATT not found indicator */
}
else
{
    done = findfirst(f_name_process,&ffblk,0);

    if (!done)
    {
        length = strlen(ffblk.ff_name) - 4;
        strncpy(f_name,ffblk.ff_name,length);
        strcpy(f_name + length, "\0");

        printf("\n\nProcessing file '%s' already exists.",f_name);
    }
}

```

```

printf(" Overwrite (y/n)?: ");
scanf(" %c",&answer);
answer = toupper(answer);

if(answer == 'Y')
{
    ind1 = ind1 | BIT4;
                                /* request save ATT file      */
}
}
else
{
    ind1 = ind1 | BIT4; /* request save ATT file      */
}

if((ind1 & BIT4) != 0) /* if ATT file to be saved      */
{
    processcreate( );

    ind1 = ind1 & (BITA - BIT4);
                                /* clear save ATT file indicator */
}

ind1 = ind1 | BIT0; /* request default processing file */

processread( );

if((ind1 & BIT1) != 0) /* if processing file not found */
{
    printf("\n\n\tProcessing file '%s' ",f_name_process);
    printf("does not exist.\n");

    goto end;
}

if (count_files == 0)
{
    processdisphhead( );

    printf("\n *** NO CHN FILES SELECTED ***\n");

    goto end;
}
}

break;
}
}
while(option1 != 1); /* DO WHILE NOT processing data */

/* ----- */

/* Read in data from processing file. */

if((ind1 & BIT3) == 0) /* if ATT file NOT supplied */
{
    printf("\n");
}

ind1 = ind1 | BIT0; /* request default processing file */

processread( );

if((ind1 & BIT1) != 0) /* if processing file not found */
{
    printf("\n\tProcessing file '%s' ",f_name_process);
    printf("does not exist.\n");

    goto end;
}
}

```

```

processdisphed( );

/* Loop through Maestro CHN files, extract data, write to output files. */
for(count_files=0; count_files < p_number_files; count_files++)
{
    strcpy(f_name_in,p_name_array[count_files]);

    fileread( );

    if((p_ind1 & BIT0) == 0)          /* NOT output to one file */
    {
        fwrite( );
    }

    if((p_ind1 & BIT0) != 0)          /* output to one file */
    {
        printf("\n");

        fwriteone( );
    }

}

/* Close any remaining files and finish. */
end:

fcloseall( );

return 0;
}

/*****
*   Function: Process read.
*
*   Opens file with processing information.
*
*   Read in data from file.
*****/

void processread( )
{
/* Open processing file. If not found, error message and exit. */

ind1 = ind1 & (BITA - BIT1);          /* clear processing file NOT found */

if((ind1 & BIT0) != 0)                /* if default file requested */
{
    strcpy(f_name_process,"AttenCHN");
    strcat(f_name_process, ".att");
}

if((processingread = fopen(f_name_process,"r")) == NULL)
{
    ind1 = ind1 | BIT1;                /* indicate file NOT found */

    if((ind1 & BIT0) == 0)            /* if NOT default file requested */
    {
        if((ind1 & BIT3) != 0)        /* if ATT file supplied */
        {
            printf("\n");
        }

        printf("\n\tProcessing file '%s' ",f_name_process);
        printf("does not exist.\n");
    }
}
else
{

```

```

/* Read data from processing file. */

fscanf(processingread,"%d%d",&p_ind1,&p_ind2);
fscanf(processingread,"%d%d",&p_ind3,&p_ind4);
fscanf(processingread,"%d",&p_tabs);
fscanf(processingread,"%d%d",&p_low_chan,&p_high_chan);
fscanf(processingread,"%f%f",&p_low_energy,&p_high_energy);
fscanf(processingread,"%s%s",&p_output_file,p_output_type);
fscanf(processingread,"%d",&p_number_files);

p_number_chans = p_high_chan - p_low_chan + 1;

p_energy_step = (p_high_energy - p_low_energy) / (p_number_chans - 1);

for(count_files=0; count_files < p_number_files; count_files++)
{
    fscanf(processingread,"%s\n",&p_name_array[count_files]);
}

fclose(processingread);
}

ind1 = ind1 & (BITA - BIT0); /* clear default file request */

return;
}

/*****
* Function: Process disp head. *
* *
* Displays processing header information. *
*****/

void processdisphead( )
{
/* Display the results on the screen. */

printf("\nChannel numbers");
printf(" : %5d to %5d",p_low_chan,p_high_chan);
printf(" (total %d",p_number_chans);

if((p_ind3 & BIT0) == 0)
{
    printf(", not in o/p");
}
else
{
    printf("");
}

printf("\nChannel energies");

if((p_ind3 & BIT1) != 0)
{
    if((p_ind3 & BIT2) != 0)
    {
        printf(" : %5.2f to %5.2f",p_low_energy,p_high_energy);
        printf(" keV (bypass calibration)");
    }
    else
    {
        printf(" : calibrated energies from input file");
    }
}
else
{
    printf(" : not included in o/p");
}

printf("\nO/p file options: ");

```

```

if((p_ind1 & BIT0) != 0)          /* output to one file          */
{
    printf(" %s.%s",p_output_file,p_output_type);
}
else
{
    printf(" type '%s'",p_output_type);
}

if((p_ind2 & BIT0) != 0)          /* include header          */
{
    printf(", header");
}

if((p_ind2 & BIT1) != 0)          /* include .chn file names */
{
    printf(", CHN names");
}

if((p_ind3 & BIT0) != 0)          /* include channel numbers */
{
    printf(", channels");
}

if((p_ind3 & BIT1) != 0)          /* include channel energy values */
{
    printf(", energies");
}

if( ((p_ind1 & BIT0) != 0) && (p_tabs != 0) )
    /* include tab spaces between columns*/
{
    printf(", %d tab(s)",p_tabs);
}

printf("\n");

return;
}

/*****
*   Function: Process disp list
*
*   Displays processing selected list CHN files.
*****/

void processdisplist( )
{
    /* Display the selected list CHN files on the screen.          */

    printf("Listing of selected Maestro CHN files:\n\n");

    for(count_files=0; count_files < p_number_files; count_files++)
    {
        printf(" %d.\t%s\n",count_files+1,p_name_array[count_files]);
    }

    return;
}

/*****
*   Function: Process input.
*
*   Input new processing ATT file parameters.
*****/

void processinput( )
{

```

```

/*   Input new processing file.                               */
if((output_ind1 & BIT0) != 0)      /* data to one file      */
{
    printf("\n Output all data to one file (y/n)?: ");
    scanf(" %c",&answer);
    answer = toupper(answer);

    if(answer == 'Y')
    {
        p_ind1 = p_ind1 | BIT0;

        printf("\n\tOutput file name: ");
        scanf("%s",&p_output_file);
    }
    else
    {
        p_ind1 = p_ind1 & (BITA - BIT0);
    }
}

if((output_ind1 & BIT1) != 0)      /* file extension      */
{
    if( (option1 == 3) &&
        ((p_ind1 & BIT0) != 0) )   /* if data to one file */
    {
        printf("\n\t");
    }
    else
    {
        printf("\n ");
    }

    printf("Output file extension (e.g. xls): ");
    scanf("%s",&p_output_type);
}

if((output_ind1 & BIT2) != 0)      /* channel numbers     */
{
    if((p_ind3 & BIT2) != 0)        /* CHN calibrated energies bypassed */
    {
        p_ind3 = p_ind3 & (BITA - BIT1);
        /* disable 'energies to o/p' */
    }

    do
    {
        printf("\n Lowest channel number: ");
        scanf("%d",&p_low_chan);

        printf("\n Highest channel number: ");
        scanf("%d",&p_high_chan);

        if(p_low_chan >= p_high_chan)
        {
            printf("\n\t*** HIGHEST MUST BE GREATER THAN LOWEST ***\n");
        }
    }
    while(p_low_chan >= p_high_chan);
}

if((output_ind1 & BIT3) != 0)      /* channels to o/p     */
{
    printf("\n Include channels in o/p file (y/n)?: ");
    scanf(" %c",&answer);
    answer = toupper(answer);

    if(answer == 'Y')
    {
        p_ind3 = p_ind3 | BIT0;
    }
}

```

```
    }
    else
    {
        p_ind3 = p_ind3 & (BITA - BIT0);
    }
}

if((output_ind1 & BIT4) != 0)          /* energies to o/p          */
{
    printf("\n Include energies in o/p file (y/n)? : ");
    scanf(" %c",&answer);
    answer = toupper(answer);

    if(answer == 'Y')
    {
        p_ind3 = p_ind3 | BIT1;

        printf("\n Bypass calibrated energies (y/n)? : ");
        scanf(" %c",&answer);
        answer = toupper(answer);

        if(answer == 'Y')
        {
            p_ind3 = p_ind3 | BIT2;

            do
            {
                printf("\n\tLowest energy (keV): ");
                scanf("%f",&p_low_energy);

                printf("\n\tHighest energy (keV): ");
                scanf("%f",&p_high_energy);

                if(p_low_energy >= p_high_energy)
                {
                    printf("\n\t*** HIGHEST MUST BE GREATER THAN LOWEST ***\n");
                }
            }
            while(p_low_energy >= p_high_energy);
        }
        else
        {
            p_ind3 = p_ind3 & (BITA - BIT2);
        }
    }
    else
    {
        p_ind3 = p_ind3 & (BITA - BIT1);
    }
}

if((output_ind1 & BIT5) != 0)          /* header to o/p          */
{
    printf("\n Include header in o/p file (y/n)? : ");
    scanf(" %c",&answer);
    answer = toupper(answer);

    if(answer == 'Y')
    {
        p_ind2 = p_ind2 | BIT0;
    }
    else
    {
        p_ind2 = p_ind2 & (BITA - BIT0);
    }
}

if((output_ind1 & BIT6) != 0)          /* CHN NAME file to o/p   */
{
    printf("\n Include CHN file names in o/p file (y/n)? : ");
```

```

scanf(" %c",&answer);
answer = toupper(answer);

if(answer == 'Y')
{
    p_ind2 = p_ind2 | BIT1;
}
else
{
    p_ind2 = p_ind2 & (BITA - BIT1);
}
}

if((output_ind1 & BIT7) != 0)          /* tabs */
{
    if((p_ind1 & BIT0) != 0)          /* output to one file */
    {
        printf("\n Tabs between columns in o/p file (y/n)?: ");
        scanf(" %c",&answer);
        answer = toupper(answer);

        if(answer == 'Y')
        {
            printf("\n\tHow many tabs?: ");
            scanf("%d",&p_tabs);
        }
        else
        {
            p_tabs = 0;
        }
    }
}

if((output_ind2 & BIT0) != 0)          /* CHN file list */
{
    count = 0;
    count_files = 0;

    printf("\n Include all CHN files (y/n)?: ");
    scanf(" %c",&answer);
    answer = toupper(answer);

    if(answer == 'Y')
    {
        ind3 = ind3 | BIT1;          /* use all CHN files from directory */
    }
    else
    {
        ind3 = ind3 & (BITA - BIT1); /* select CHN files from directory */
        printf("\n Indicate which CHN files to include (y/n)\n\n");
    }

    done = findfirst("*.chn",&ffblk,0);

    while (!done)
    {
        count = count ++;

        if((ind3 & BIT1) == 0)      /* if selected CHN files required */
        {
            length = strlen(ffblk.ff_name) - 4;
            strncpy(f_name,ffblk.ff_name,length);
            strcpy(f_name + length,"\0");

            printf(" %d.\t%s : ",count,f_name);
            scanf(" %c",&answer);
            answer = toupper(answer);
        }

        if( ((ind3 & BIT1) != 0) || (answer == 'Y') )
            /* if all CHN files required OR */

```

```

                                /* CHN file selected */
    {
        length = strlen(ffblk.ff_name) - 4;
        strncpy(p_name_array[count_files],ffblk.ff_name,length);
        strcpy(p_name_array[count_files] + length,"\0");

        count_files = count_files ++;
    }

    done = findnext(&ffblk);
}

p_number_files = count_files;

}

output_ind1 = 0;
output_ind2 = 0;

return;
}

/*****
*   Function: Process create.
*
*   Create new processing ATT file.
*****/

void processcreate( )
{
    if((ind1 & BIT0) != 0)          /* if default file requested */
    {
        strcpy(f_name_process,"AttenCHN");
        strcat(f_name_process, ".att");
    }

    /* Create new processing file.
    */

    processingnew = fopen(f_name_process,"w+");

    fprintf(processingnew,"%d\t%d\t",p_ind1,p_ind2);
    fprintf(processingnew,"%d\t%d\n",p_ind3,p_ind4);
    fprintf(processingnew,"%d\n",p_tabs);
    fprintf(processingnew,"%d\t%d\n",p_low_chan,p_high_chan);
    fprintf(processingnew,"%f\t%f\n",p_low_energy,p_high_energy);
    fprintf(processingnew,"%s\t%s\n",p_output_file,p_output_type);
    fprintf(processingnew,"%d\n",p_number_files);

    /* Make processing file list.
    */

    if(p_number_files != 0)
    {
        for(count_files=0; count_files < p_number_files; count_files++)
        {
            fprintf(processingnew,"%s\n",p_name_array[count_files]);
        }
    }

    fclose(processingnew);

    ind1 = ind1 & (BITA - BIT0);    /* clear default file request */
    ind3 = ind3 | BIT0;            /* ind selected CHN list available */

    return;
}

```

```

/*****
*   Function: CHN disp list
*
*   Displays directory CHN files and copies the names to working memory.
*****/

void chndisplist( )
{
    /*   Display the directory CHN files on the screen.   */

    count_files = 0;
    done = findfirst("*.chn",&ffblk,0);

    printf("Directory listing of Maestro CHN files:\n\n");

    while (!done)
    {
        length = strlen(ffblk.ff_name) - 4;
        strncpy(f_name,ffblk.ff_name,length);
        strcpy(f_name + length,"\0");

        strcpy(p_name_array[count_files],f_name);

        printf("  %d.\t%s\n",count_files+1,f_name);
        done = findnext(&ffblk);

        count_files = count_files ++;
    }

    p_number_files = count_files;

    return;
}

/*****
*   Function: ATT disp list
*
*   Displays processing ATT files.
*****/

void attdisplist( )
{
    /*   Display the processing ATT files on the screen.   */

    ind1 = ind1 & (BITA - BIT2);          /* clear NO ATT file found   */

    count = 0;
    done = findfirst("*.att",&ffblk,0);

    if(done)
    {
        ind1 = ind1 | BIT2;                /* indicate NO ATT files found   */
    }
    else
    {
        printf("Processing file list:\n\n");

        while (!done)
        {
            count = count ++;
            length = strlen(ffblk.ff_name) - 4;
            strncpy(f_name,ffblk.ff_name,length);
            strcpy(f_name + length,"\0");

            printf("  %d.\t%s\n",count,f_name);
            done = findnext(&ffblk);
        }
    }
}

```

```

    return;
}

/*****
*   Function: File read.
*
*   Opens data files specified in the processing file.
*
*   Read in data from files.
*
*   Some of this manipulation is based on code from txt2ascii.c.
*****/

void fileread( )
{
    /* Maestro CHN file name from processing file. */

    f_error1[count_files] = 0;

    strcpy(f_name_out,f_name_in);
    strcpy(p_name_array[count_files],f_name_in);
    strcat(f_name_in, ".chn");

    /* Open Maestro CHN file. If not found, error message and exit. */

    if((input = fopen(f_name_in,"rb")) == NULL)
    {
        f_error1[count_files] = f_error1[count_files] | BIT0;
    }
    else
    {
        /* Read header data from Maestro CHN input file. */

        fread(&d_file_type[count_files],sizeof d_file_type[0],1,input);
        /* file type (.CHN) */
        fread(&d_mca_num[count_files],sizeof d_mca_num[0],1,input);
        /* MCA number */
        fread(&d_segment[count_files],sizeof d_segment[0],1,input);
        /* segment number */
        fread(d_acq_time_sec[count_files],sizeof(char),sizeof
d_acq_time_sec[0],input);
        /* start time seconds */
        fread(&d_realtime[count_files],sizeof d_realtime[0],1,input);
        /* real time (20 ms ticks) */
        fread(&d_livetime[count_files],sizeof d_livetime[0],1,input);
        /* live time (20 ms ticks) */
        fread(d_acq_date_day[count_files],sizeof(char),sizeof
d_acq_date_day[0],input);
        /* start date day */
        fread(d_acq_date_month[count_files],sizeof(char),sizeof
d_acq_date_month[0],input);
        /* start date month */
        fread(d_acq_date_year[count_files],sizeof(char),sizeof d_acq_date_year
[0],input);
        /* start date year */
        fread(d_acq_time_hour[count_files],sizeof(char),sizeof
d_acq_time_hour[0],input);
        /* start time hour */
        fread(d_acq_time_min[count_files],sizeof(char),sizeof
d_acq_time_min[0],input);
        /* start time minute */
        fread(&d_chan_offset[count_files],sizeof d_chan_offset[0],1,input);
        /* start channel (offset) */
        fread(&d_num_chans[count_files],sizeof d_num_chans[0],1,input);
        /* number of channels */

        if(num_chans_out == 0)

```

```

    {
        num_chans_out = d_num_chans[count_files];
    }

    if(d_num_chans[count_files] != num_chans_out)
    {
        f_error1[count_files] = f_error1[count_files] | BIT1;
    }

/* Transfer channel data from Maestro CHN input file to output array.      */
for(count_chans = 0; count_chans < d_num_chans[count_files]; count_chans++)
{
    fread(&d_chan_data[count_files][count_chans],sizeof(long),1,input);
}

/* Read trailer record information.                                          */
fread(&d_trltyp[count_files],sizeof d_trltyp[0],1,input);
/* trailer type                                                              */
fread(&d_dummy1[count_files],sizeof d_dummy1[0],1,input);
/* dummy (no information)                                                  */
fread(&d_eng1[count_files],sizeof d_eng1[0],1,input);
/* energy zero                                                              */
fread(&d_eng2[count_files],sizeof d_eng2[0],1,input);
/* energy slope                                                            */
fread(&d_eng3[count_files],sizeof d_eng3[0],1,input);
/* blank                                                                    */
fread(&d_FW1[count_files],sizeof d_FW1[0],1,input);
/* FWHM zero                                                                */
fread(&d_FW2[count_files],sizeof d_FW2[0],1,input);
/* FWHM slope                                                                */
fread(&d_FW3[count_files],sizeof d_FW3[0],1,input);
/* blank                                                                    */
fread(&d_units[count_files],sizeof(char),4,input);
/* energy units                                                            */

/* Read detector name.                                                      */
fseek(input,DETOFFSET,0);
/* set file pointer to                                                    */
/* detector name                                                            */
fread(&d_detname_length[count_files],1,1,input);
/* detector name length                                                    */
fread(&d_detname[count_files],sizeof(char),
      d_detname_length[count_files],input);
/* detector name                                                            */

/* Calculate remaining values.                                              */
c_realtime[count_files] = d_realtime[count_files] / 50;
/* real time in seconds                                                    */
c_livetime[count_files] = d_livetime[count_files] / 50;
/* live time in seconds                                                    */
c_deadtime[count_files] = (100 / c_realtime[count_files] ) *
( c_realtime[count_files] - c_livetime[count_files] );
/* average dead time                                                       */

c_high_chan_in[count_files] = d_chan_offset[count_files] +
d_num_chans[count_files] - 1;

c_high_eng_in[count_files] = ( d_eng1[count_files] +
( d_eng2[count_files] *
( d_num_chans[count_files] -1 )));

```

```

c_low_eng_out[count_files] = ( d_eng1[count_files] +
                               ( d_eng2[count_files] * p_low_chan));

c_high_eng_out[count_files] = ( d_eng1[count_files] +
                                 ( d_eng2[count_files] * p_high_chan));

fclose(input);

}

return;
}

/*****
*   Function: File write.
*
*   Write extracted data to output file.
*****/

void filewrite( )
{
/*   Prepare output file and output report file.
*/

strcpy(f_name_report,f_name_out);
strcat(f_name_report,"_info.dat");

strcat(f_name_out,".");
strcat(f_name_out,p_output_type);

/*   Check that output file does not already exist.
*/

done = findfirst(f_name_out,&ffblk,0);

if (!done)
{
printf("\nOutput file '%s' already exists.",f_name_out);
printf(" Overwrite (y/n)? ");
scanf(" %c",&answer);
answer = toupper(answer);

if(answer == 'Y')
{
ind4 = ind4 | BIT0;          /* request save output file
*/
}

printf("\n");
}
else if(count_files ==0)
{
ind4 = ind4 | BIT0;          /* request save output file
*/

printf("\n");
}
else
{
ind4 = ind4 | BIT0;          /* request save output file
*/
}

printf(" %d.\t%s\t",count_files+1,f_name_in);

if((ind4 & BIT0) == 0)          /* if output file NOT to be saved
*/
{
printf("-->\toutput file NOT created\n");
}
else if((f_error1[count_files] & BIT0) != 0)
{
printf("-->\t*** CHN FILE NOT FOUND ***\n");
}
}

```

```

else if((f_error1[count_files] & BIT1) != 0)
{
    printf("-->\t*** CHN CHANNEL COUNT ERROR ***\n");
}
else
{
    printf("-->\t%s\n",f_name_out);
    output = fopen(f_name_out,"w");
    outputreport = fopen(f_name_report,"w");

/* Information to output report file. */
    ind3 = ind3 | BIT5;          /* indicate report file */
    filereport(outputreport);

/* Header information to output file. */
    if((p_ind2 & BIT0) != 0)
    {
        filereport(output);
    }

/* .chn file name to output file. */
    if((p_ind2 & BIT1) != 0)
    {
        if((p_ind3 & BIT0) != 0)
        {
            fprintf(output,"Channel\t");
        }

        if((p_ind3 & BIT1) != 0)
        {
            if((p_ind3 & BIT2) != 0) /* if calibration energies bypassed */
            {
                fprintf(output,"Energy [keV]\t");
            }
            else
            {
                fprintf(output,"Energy [%.3s]\t",d_units[count_files]);
            }
        }

        fprintf(output,"%s\n",p_name_array[count_files]);
    }

/* Transfer channel data from output array to output file. If the CHN */
/* channel number is within the channel numbers requested in the */
/* processing file, the count is transferred to the output file. */
/* Otherwise nothing is transferred to the output file. */

    if((p_ind3 & BIT2) != 0) /* if calibration energies bypassed */
    {
        c_energy = p_low_energy;
        c_energy_step = p_energy_step;
    }
    else
    {
        c_energy = c_low_eng_out[count_files];
        c_energy_step = d_eng2[count_files];
    }

    for(count_chans = 0; count_chans < d_num_chans[count_files]; count_chans++)
    {
        if((count_chans >= p_low_chan) && (count_chans <= p_high_chan))

```

```

    {
        if((p_ind3 & BIT0) != 0)
        {
            fprintf(output,"%d\t",count_chans);
        }

        if((p_ind3 & BIT1) != 0)
        {
            fprintf(output,"%f\t",c_energy);
        }

        fprintf(output,"%ld",d_chan_data[count_files][count_chans]);

        if(count_chans != (p_high_chan) )
        {
            fprintf(output,"\n");
        }

        c_energy = c_energy + c_energy_step;
    }
}

ind4 = ind4 & (BITA - BIT0);      /* clear save output file indicator */

fclose(outputreport);

fclose(output);
}

return;
}

/*****
*   Function: File write one.
*
*   Write all extracted data to one output file.
*****/

void filewriteone( )
{
    /* Prepare output file and output report file. */

    strcpy(f_name_report,p_output_file);
    strcat(f_name_report,"_info.dat");

    strcpy(f_name_out,p_output_file);
    strcat(f_name_out,".");
    strcat(f_name_out,p_output_type);

    /* Check that output file does not already exist. */

    done = findfirst(f_name_out,&ffblk,0);

    if (!done)
    {
        printf("Output file '%s' already exists.",f_name_out);
        printf(" Overwrite (y/n)? ");
        scanf(" %c",&answer);
        answer = toupper(answer);

        if(answer == 'Y')
        {
            ind4 = ind4 | BIT0;      /* request save output file */
        }

        printf("\n");
    }
    else
    {
        ind4 = ind4 | BIT0;      /* request save output file */
    }
}

```

```

}

if((ind4 & BIT0) == 0) /* if output file NOT to be saved */
{
    printf("\tOutput file '%s' NOT created.\n",f_name_out);
}
else
{
    for(count_files=0; count_files < p_number_files; count_files++)
    {
        printf(" %d.\t%s\t",count_files+1,p_name_array[count_files]);

        if((f_error1[count_files] & BIT0) != 0)
        {
            printf("-->\t*** CHN FILE NOT FOUND ***\n");
        }
        else if((f_error1[count_files] & BIT1) != 0)
        {
            printf("-->\t*** CHN CHANNEL COUNT ERROR ***\n");
        }
        else
        {
            printf("-->\t%s\n",f_name_out);

            ind2 = ind2 | BIT0; /* indicate CHN file success */
        }
    }

    if((ind2 & BIT0) != 0)
    {
        count_files = 0; /* initial info from first CHN */
        output = fopen(f_name_out,"w");
        outputreport = fopen(f_name_report,"w");

        /* Header information (limited) to output file. */

        if((p_ind2 & BIT0) != 0)
        {
            ind3 = ind3 | BIT4; /* indicate restricted report */

            filereport(output);

            ind3 = ind3 & (BITA - BIT4); /* clear restricted report */
        }

        /* .chn file names to output file. */

        if((p_ind2 & BIT1) != 0)
        {
            if((p_ind3 & BIT0) != 0)
            {
                fprintf(output,"Channel\t");
            }

            if((p_ind3 & BIT1) != 0)
            {
                if((p_ind3 & BIT2) != 0) /* if calibration energies bypassed */
                {
                    fprintf(output,"Energy [keV]\t");
                }
                else
                {
                    fprintf(output,"Energy [%.3s]\t",d_units[count_files]);
                }
            }
        }

        for(count_files=0; count_files < p_number_files; count_files++)
        {
            if((f_error1[count_files] & (BIT0 + BIT1)) == 0)

```

```

    {
/* Information to output report file. */
        ind3 = ind3 | BIT5;          /* indicate report file */
        filereport(outputreport);

        for(count=0; count < p_tabs; count++)
        {
            fprintf(output, "\t");
        }

        fprintf(output, "%s", p_name_array[count_files]);

        if(count_files != (p_number_files - 1) )
        {
            fprintf(output, "\t");
        }
    }
    fprintf(output, "\n");
}

/* Loop through Maestro CHN files, extract data, write to output files. */
/* Transfer channel data from output array to output file. If the CHN */
/* channel number is within the channel numbers requested in the */
/* processing file, the count is transferred to the output file. */
/* Otherwise nothing is transferred to the output file. */

if((p_ind3 & BIT2) != 0)          /* if calibration energies bypassed */
{
    c_energy = p_low_energy;
    c_energy_step = p_energy_step;
}
else
{
    c_energy = c_low_eng_out[0];
    c_energy_step = d_eng2[0];
}

for(count_chans = 0; count_chans < num_chans_out; count_chans++)
{
    if((count_chans >= p_low_chan) && (count_chans <= p_high_chan))
    {
        if((p_ind3 & BIT0) != 0)
        {
            fprintf(output, "%d\t", count_chans);
        }

        if((p_ind3 & BIT1) != 0)
        {
            fprintf(output, "%f\t", c_energy);
        }

        for(count_files=0; count_files < p_number_files; count_files++)
        {
            if((f_error1[count_files] & (BIT0 + BIT1)) == 0)
            {
                for(count=0; count < p_tabs; count++)
                {
                    fprintf(output, "\t");
                }

                fprintf(output, "%ld", \
                    d_chan_data[count_files][count_chans]);

                if(count_files != (p_number_files - 1) )
                {
                    fprintf(output, "\t");
                }
            }
        }
    }
}

```

```

        }
    }
    if(count_chans != (p_high_chan) )
    {
        fprintf(output, "\n");
    }

    c_energy = c_energy + c_energy_step;
}

ind4 = ind4 & (BITA - BIT0); /* clear save output file indicator */

fclose(outputreport);

fclose(output);
}

return;
}

/*****
*   Function: File report.
*
*   Write report information to file.
*****/

void filereport(FILE *pointer)
{
    /* Title. */

    if((ind3 & BIT4) == 0) /* if NOT restricted report */
    {
        strcpy(str, p_name_array[count_files]);
    }
    else
    {
        strcpy(str, p_output_file);
    }

   strupr(str);

    fprintf(pointer, "\t\t\tATTENCHN --> %s\n\t\t\t", str);

    i = strlen(str) + 13;

    for(count = 0; count < i; count++)
    {
        fprintf(pointer, "-");
    }

    fprintf(pointer, "\n\n");

    /* File details. */

    fprintf(pointer, "INPUT ");

    if((ind3 & BIT4) == 0) /* if NOT restricted report */
    {
        strcpy(str, p_name_array[count_files]);
        strcat(str, ".chn");

        fprintf(pointer, "FILE : %s\t\t", str);
    }

    fprintf(pointer, "FILE TYPE: ");

```

```

if(d_file_type[count_files] == CHN)
{
    fprintf(pointer, ".chn\n");
}
else
{
    fprintf(pointer, "%d (not .chn ???)\n", d_file_type[count_files]);
}

if((ind3 & BIT4) == 0) /* if NOT restricted report */
{
    fprintf(pointer, "OUTPUT FILE: %s\n\n", f_name_out);

/* Detector details. */

    fprintf(pointer, "MCA NUMBER : %d\t\t\t", d_mca_num[count_files]);
    fprintf(pointer, "SEGMENT: %d\n", d_mca_num[count_files]);

    fprintf(pointer, "DETECTOR   : %.*s\n\n", d_detname_length[count_files],
                    d_detname[count_files]);

/* Acquisition details. */

    fprintf(pointer, "ACQUISITION DATE: %.*s %.*s '%.*s\t\t",
            sizeof d_acq_date_day[count_files], d_acq_date_day[count_files],
            sizeof d_acq_date_month[count_files], d_acq_date_month[count_files],
            2, d_acq_date_year[count_files]);
    fprintf(pointer, "START TIME: %.*s:%.*s:%.*s\n\n",
            sizeof d_acq_time_hour[count_files], d_acq_time_hour[count_files],
            sizeof d_acq_time_min[count_files], d_acq_time_min[count_files],
            sizeof d_acq_time_sec[count_files], d_acq_time_sec[count_files]);

    fprintf(pointer, "REAL TIME : %.2f seconds\n", c_realttime[count_files]);
    fprintf(pointer, "LIVE TIME : %.2f seconds\n", c_livetime[count_files]);
    fprintf(pointer, "DEAD TIME : %.1f %\n\n", c_deadtime[count_files]);

    fprintf(pointer, "FWHM ZERO : %e\n", d_FW1[count_files]);
    fprintf(pointer, "FWHM SLOPE: %e\n", d_FW2[count_files]);
}

fprintf(pointer, "\n\n");

/* Channel details. */

fprintf(pointer, "\t\t\t\t INPUT FILE CHANNELS\t\t\t\t OUTPUT FILE CHANNELS\n");
fprintf(pointer, "\t\t\t\t -----\t\t\t\t -----");

if((p_ind3 & BIT2) != 0) /* if calibration energies bypassed */
{
    fprintf(pointer,
            "\t\t\t\tNUMBER\t\t\t\t ENERGY [keV]\t\t\t\t NUMBER\t\t\t\t ENERGY [keV]\n");

    fprintf(pointer, "LOW CHANNEL: \t\t%5d\t\t\t %5.2f\t\t\t %5d\t\t\t %5.2f\n",
            d_chan_offset[count_files], d_eng1[count_files],
            p_low_chan, p_low_energy);

    fprintf(pointer, "HIGH CHANNEL: \t\t%5d\t\t\t %5.2f\t\t\t %5d\t\t\t %5.2f\n",
            c_high_chan_in[count_files], c_high_eng_in[count_files],
            p_high_chan, p_high_energy);
}
else
{
    fprintf(pointer,
            "\t\t\t\tNUMBER\t\t\t\t ENERGY [%.3s]\t\t\t\t NUMBER\t\t\t\t ENERGY [%.3s]\n",
            d_units[count_files], d_units[count_files]);

    fprintf(pointer, "LOW CHANNEL: \t\t%5d\t\t\t %5.2f\t\t\t %5d\t\t\t %5.2f\n",
            d_chan_offset[count_files], d_eng1[count_files],
            p_low_chan, c_low_eng_out[count_files]);
}

```

```
        fprintf(pointer,"HIGH CHANNEL: \t%5d\t\t %5.2f\t\t %5d\t\t %5.2f\n",
                c_high_chan_in[count_files],c_high_eng_in[count_files],
                p_high_chan,c_high_eng_out[count_files]);
    }

    fprintf(pointer,"TOTAL CHANNELS:\t%5d\t\t\t\t %5d\n\n",
            d_num_chans[count_files],p_number_chans);

    if((p_ind3 & BIT2) != 0)          /* if calibration energies bypassed */
    {
        fprintf(pointer,
            "\t\t\t NOTE - CALIBRATED ENERGIES BYPASSED IN OUTPUT FILE\n\n\n");
    }
    else
    {
        fprintf(pointer,"\n");
    }

    if((ind3 & BIT5) != 0)          /* if report file */
    {
        fprintf(pointer,"_____");
        fprintf(pointer,"_____ \n\n");
    }

    ind3 = ind3 & (BITA - BIT5);    /* clear report file indicator */

    return;
}
```

E.2 OTHER SOFTWARE FOR DATA ANALYSIS

A number of other programs were prepared for data analysis, not presented here. They were written as M-file functions for use with The MathWorks MatLab 6.1, release 12.1.

Table E-1 summarises the programs developed for this platform.

M-file	Program Use
MicroWedge.m	Process radiographic step wedge image data scanned by microdensitometry.
MicroSample.m	Process radiographic sample image data scanned by microdensitometry.
PGMWedge.m	Process radiographic step wedge image data scanned as PGM greyscale files. The PGM file format is described in section E.3.
PGMSample.m	Process radiographic sample image data scanned as PGM greyscale files. The PGM file format is described in section E.3.
EDXRD1EC.m	Correct transmission spectra energies after Compton shift (collected using 90° Compton scattering).
EDXRD2TM.m	Concatenate (TableCurve) fitted transmission spectra into a single attenuation correction file.
EDXRD3AC.m	Interpolate discrete transmission spectra energies to match those of EDXRD scattered spectra.
EDXRD4ES.m	Add momentum transfer and attenuation correction columns to EDXRD scattered spectra and correct for attenuation.
EDXRD5SM.m	Correct for tube current variation (wrt 8 mA) and provide total photon counts from uncorrected and corrected scattered spectra.
EDXRD7RT.m	Normalise spectra and calculate ratio between marrow region and bone region.
Compression.m	Process sample compression data from Excel XLS file.
Plot3D.m	Produce a three-dimensional plot from a text file.

Table E-1. MatLab M-files developed for data processing for this project. In all cases, the word 'sample' refers to a $15 \times 15 \times 15 \text{ mm}^3$ trabecular bone sample cube. A full explanation of EDXRD processing (using the EDXRD M-files) may be found in chapters six, seven and eight.

E.3 THE PGM IMAGE FILE FORMAT

The portable greymap (PGM) image file format was used for processing scanned radiographic image data for bone sample cube density correction (chapter five, section 5.5) and also for generating images from microdensitometry radiographic image data for bone sample cube demineralisation homogeneity assessment (chapter five, section 5.4). This format was chosen because it contains basic greyscale information in a text-type format that is easy to work with and convert to other formats.

The general PGM structure is described here, the header format shown in table E-2:

Example	Description
P2	File type identifier, being 'P2' for the PGM file type ('P5' is a variant were the grey values are stored as plain bytes).
# Free comments	Optional comments follow a '#' character, finishing at the next 'end of line' character.
36 36	The number of rows and columns of image pixels (ASCII characters in decimal).
255	Maximum grey value (ASCII characters in decimal).

Table E-2. General format of the PGM file header.

Then follows the image data in ASCII characters (decimal), each between 0 and the maximum grey value from the header. The total number of pixels must match 'rows × columns' from the header and appear in raster order. A white space character separates each item throughout the file, which may be blanks, TABs, CRs or LFs. An example PGM file follows overleaf, the image from which is shown in figure E-1:

```
P2
# Example: exmpl.pgm
30 12
15
0 0 0 0 0 0 0 0 0 0 0 0 0 0 0 0 0 0 0 0 0 0 0 0 0 0 0 0 0 0 0 0
0 7 7 7 7 7 7 0 0 0 0 0 11 11 11 11 0 0 0 0 15 0 0 0 0 0 0 0 0 15 0
0 7 0 0 0 0 0 7 0 0 0 11 0 0 0 0 11 0 0 0 15 15 0 0 0 0 0 15 15 0
0 7 0 0 0 0 0 7 0 0 11 0 0 0 0 0 11 0 0 15 15 0 0 0 0 0 15 15 0
0 7 0 0 0 0 0 7 0 0 11 0 0 0 0 0 0 0 0 15 0 15 0 0 0 15 0 15 0
0 7 0 0 0 0 0 7 0 0 11 0 0 0 0 0 0 0 0 15 0 15 0 0 0 15 0 15 0
0 7 7 7 7 7 7 0 0 0 11 0 0 0 11 11 11 11 0 0 15 0 0 15 0 15 0 0 15 0
0 7 0 0 0 0 0 0 0 0 11 0 0 0 0 0 0 11 0 0 15 0 0 15 0 15 0 0 15 0
0 7 0 0 0 0 0 0 0 0 11 0 0 0 0 0 0 11 0 0 15 0 0 15 0 15 0 0 15 0
0 7 0 0 0 0 0 0 0 0 11 0 0 0 0 0 11 0 0 0 15 0 0 0 15 0 0 0 15 0
0 7 0 0 0 0 0 0 0 0 0 11 11 11 11 0 0 0 0 15 0 0 0 15 0 0 0 15 0
0 0 0 0 0 0 0 0 0 0 0 0 0 0 0 0 0 0 0 0 0 0 0 0 0 0 0 0 0 0 0
```



Figure E-1. Image generated using the PGM file example.

REFERENCES

- Alhava E. M. (1991). Bone density measurements. *Calcified Tissue International* **49**, S21-S23.
- Alpen, E. L. (1998). Radiation biophysics, 2nd edition. (San Diego, California: Academic Press).
- An, Y. H. (2000). Mechanical properties of bone. In: Mechanical testing of bone and the bone-implant interface, ed. Yuehuei H. An and Robert A. Draughn. (Boca Raton: CRC Press LLC).
- An, Y. H., Barfield, W. R. and Draughn, R. R. (2000a). Basic concepts of mechanical property measurement and bone biomechanics. In: Mechanical testing of bone and the bone-implant interface, ed. Yuehuei H. An and Robert A. Draughn. (Boca Raton: CRC Press LLC).
- An, Y. H., Barfield, W. R. and Knets, I. (2000b). Methods of evaluation for bone dimensions, densities, contents, morphology, and structures. In: Mechanical testing of bone and the bone-implant interface, ed. Yuehuei H. An and Robert A. Draughn. (Boca Raton: CRC Press LLC).
- An, Y. H. and Bensen, C. V. (2000). General considerations of mechanical testing. In: Mechanical testing of bone and the bone-implant interface, ed. Yuehuei H. An and Robert A. Draughn. (Boca Raton: CRC Press LLC).
- An, Yuehuei H. and Draughn, Robert A. (ed.) (2000). Mechanical testing of bone and the bone-implant interface. (Boca Raton: CRC Press LLC).
- Attix, Frank H. (1986). Introduction to radiological physics and radiation dosimetry. (New York: Wiley).
- Bensen, C. V. (2000). Basic facilities and instruments for mechanical testing of bone. In: Mechanical testing of bone and the bone-implant interface, ed. Yuehuei H. An and Robert A. Draughn. (Boca Raton: CRC Press LLC).
- Bonucci, E. (2000). Basic composition and structure of bone. In: Mechanical testing of bone and the bone-implant interface, ed. Yuehuei H. An and Robert A. Draughn. (Boca Raton: CRC Press LLC).

- Burstein, A. H., Zika, J. M., Heiple, K. G. and Klein, L. (1975). Contribution of collagen and mineral to the elastic-plastic properties of bone. *The Journal of Bone and Joint Surgery* **57A**, 956-961.
- Cameron, J. R. and Sorenson, J. (1963). Measurement of bone mineral in vivo; an improved method. *Science* **142**, 230-232.
- Choi, K. and Goldstein, S. A. (1992). A comparison of the fatigue behaviour of human trabecular and cortical bone tissue. *Journal of Biomechanics* **25** (12), 1371-1381.
- Ciarelli, M. J., Goldstein, S. A., Kuhn, J. L., *et al.* (1991). Evaluation of orthogonal mechanical properties and density of human trabecular bone from the major metaphyseal regions with materials testing and computed tomography. *Journal of Orthopaedic Research* **9** (5), 674-682.
- Clarke, R. L., and Van Dyk, G. (1973) A new method for the measurement of bone mineral content using both transmitted and scattered beams of gamma rays. *Physics in Medicine and Biology* **18**, 532-539.
- Cotran, S. C., Kumar, V. and Robbins, S. L. (1994). Robbins pathologic basis of disease, 5th edition. (Philadelphia: W. B. Saunders Company).
- Crummy, L. A., Idso, J. P., Newman Jr., S. M. and Hunt, C. (1997). Method for preparation of trabecular bone matrix for histological studies using scanning electron microscopy. *Proceedings of the North Dakota Academy of Science* **51**, 188-203.
- Davis, S. and Payne, S. (1992). 101 ways to deal with a dead hedgehog: notes on the preparation of disarticulated skeletons for zoo-archaeological use. *Circaea* **8** (2), 95-104.
- Farquharson, M. J. (1996). Characterisation of bone tissue using coherently scattered x-ray photons. PhD thesis: University College, London, Department of Medical Physics and Bioengineering.
- Farquharson, M. J., Luggar, R. D. and Speller, R. D. (1997a). Multivariate calibration for quantitative analysis of EDXRD spectra from a bone phantom. *Applied Radiation and Isotopes* **48**, 1075-1082.
- Farquharson, M. J. and Speller, R. D. (1998). Trabecular bone mineral density measurements using energy dispersive x-ray diffraction (EDXRD). *Radiation Physics and Chemistry* **51**, 607-608.

- Farquharson, M. J., Speller, R. D. and Brickley, M. (1997b). Measuring bone mineral density in archaeological bone using energy dispersive low angle x-ray scattering techniques. *Journal of Archaeological Science* **24**, 765-772.
- Freemont, A. J. (1989). The histology of mineralised tissues. In: Calcified tissue, ed. D. W. L. Hukins. (Hampshire: Macmillan Press).
- Geraets, W. G., Van Der Stelt, P. F., Lips, P. and Van Ginkel, F. C. (1998). The radiographic trabecular pattern of hips in patients with hip fractures and in elderly control subjects. *Bone* **22** (2), 165-173.
- Graham, D. T. (1996). Principles of radiological physics, 3rd edition. (New York: Churchill Livingstone).
- Gunn, C. (1996). Bones and joints: a guide for students, 3rd edition. (Edinburgh: Churchill Livingstone).
- Hassager, C. and Christiansen, C. (1995). Measurement of bone mineral density. *Calcified Tissue International* **57**, 1-5.
- Hoffler, C. E., McCreadie, B. R., Smith, E. A. and Goldstein, S. A. (2000). A hierarchical approach to exploring bone mechanical properties. In: Mechanical testing of bone and the bone-implant interface, ed. Yuehuei H. An and Robert A. Draughn. (Boca Raton: CRC Press LLC).
- Hubbell, J.H., Veigele, W. J., Brigg, E. A., Brown, R. T., Cromer, D. T. and Howerton, R. J. (1975). Atomic form factors, incoherent scattering functions and photon scattering cross sections. *Journal of Physical and Chemical Reference Data*, **4** (3) 471-539.
- Huda, W., and Morin, R. L. (1996). Patient doses in bone mineral densitometry. *The British Journal of Radiology* **69**, 422-425.
- Hukins, D. W. L. (1989). Mineral deposits in tissue. In: Calcified tissue, ed. D. W. L. Hukins. (Hampshire: Macmillan Press).
- ICRP (1977). Recommendations of the International Commission on Radiological Protection, Report 26. (Oxford: Pergamon Press).
- ICRP (1991). 1990 Recommendations of the International Commission on Radiological Protection, ICRP Publication 60. (Elmsford, New York: Pergamon Press).
- ICRU (1989). ICRU report 44: Tissue substitutes in radiation dosimetry and measurement. (Bethesda: International Commission on Radiation and Units).

- JCPDS (1967). Powder diffraction file volume 9, number 9-432. In: Powder diffraction file sets 6-10 (revised), ed. L. G. Berry. (Pennsylvania: Joint Committee on Powder Diffraction Standards).
- Jiang, Y., Zhao, J., Augat, P., Ouyang, X., Lu, Y., Majumdar, S. and Genant, H. K. (1998). Trabecular bone mineral and calculated structure of human bone specimens scanned by peripheral quantitative computed tomography: relation to biomechanical properties. *Journal of Bone and Mineral Research* **13** (11), 1783-1790.
- Johns, H. E. and Cunningham, J. R. (1983). The physics of radiology, 4th edition. (Illinois: Charles C. Thomas).
- Johns, P. C. and Yaffe, M. J. (1983). Coherent scatter in diagnostic radiography. *Medical Physics* **10** (1), 40-50.
- Keller, T. S. and Liebschner, M. A. K. (2000). Tensile and compression testing of bone. In: Mechanical testing of bone and the bone-implant interface, ed. Yuehuei H. An and Robert A. Draughn. (Boca Raton: CRC Press LLC).
- Kiviranta, I., Tammi, M., Lappalainen, R., Kuusela, T. and Helminen, H. J. (1980). The rate of calcium extraction during EDTA decalcification from thin bone slices as assessed with atomic absorption spectrophotometry. *Histochemistry* **68** (2), 119-127.
- Knoll, G. F. (1989). Radiation detection and measurement, 2nd edition. (New York: Wiley).
- Koot, V. C. M., Kesselaer, S. M. M. J., Clevers, G. J., de Hooge, P., Weits, T. and van der Werken, C. (1996). The evaluation of the Singh index for measuring osteoporosis. *Journal of Bone and Joint Surgery (British Edition)*, **78-B**, 831-834.
- Kusama, T., Kai, M., Yabuuchi, E., and Bessho, Y. (1995). Dose estimates for patients receiving radiation from various instruments used for measuring bone mass and density. *Radiation Protection Dosimetry* **58** (2), 149-151.
- Leichter, I., Bivas, A., Giveon, A., Margulies, J. Y. and Weinreb, A. (1987). The relative significance of trabecular and cortical density as a diagnostic index for osteoporosis. *Physics in Medicine and Biology* **32** (9), 1167-1174.
- Linde, F. and Hvid, I. (2000). Nondestructive mechanical testing of cancellous bone. In: Mechanical testing of bone and the bone-implant interface, ed. Yuehuei H. An and Robert A. Draughn. (Boca Raton: CRC Press LLC).

- Luggar, R. D. and Gilboy, W. B. (1999). Recent developments in industrial applications of elastic scatter x-ray inspection. *Radiation Physics and Chemistry* **56**, 213-227.
- Luggar, R. D., Horrocks, J. A., Speller, R. D. and Lacey, R. J. (1996). Determination of the geometric blurring of an energy dispersive x-ray diffraction (EDXRD) system and its use in the simulation of experimentally derived diffraction profiles. *Nuclear Instruments and Methods in Physics Research A* **383**, 610-618.
- Luggar, R. D., Horrocks, J. A., Speller, R. D. and Lacey, R. J. (1997). Low angle x-ray scatter for explosives detection: a geometry optimisation. *Applied Radiation and Isotopes* **48** (2), 215-224.
- Majumdar, S., Kothari, M., Augat, P., Newitt, D. C., Link, T. M., Lin, J. C., Lang, T., Lu, Y. and Genant, H. K. (1998). High-resolution magnetic resonance imaging: three-dimensional trabecular bone architecture and biomechanical properties. *Bone* **22** (5), 445-454.
- Maquet, P. G. J. (1985). *Biomechanics of the hip*. (Berlin: Springer-Verlag Berlin Heidelberg).
- Matsumoto, C., Kushida, K., Yamazaki, K., Imose, K. and Inoue, T. (1994). Metacarpal bone mass in normal and osteoporotic Japanese women using computed x-ray densitometry. *Calcified Tissue International* **55**, 324-329.
- Mawhinney, W. H. B., Richardson, E. and Malcolm, A. J. (1984). Control of rapid nitric acid decalcification. *Journal of Clinical Pathology* **37**, 1409-1415.
- Mazess, R. B., (1982). On ageing bone loss. *Clinical orthopaedics and related research* **165**, 239-252.
- McCubbrey, D. A., Cody, D. D., Peterson, E. L., *et al.* (1995). Static and fatigue failure properties of thoracic and lumbar vertebral bodies and their relation to regional density. *Journal of Biomechanics* **28** (8), 891-899.
- NCRP (1993). Limitation to exposure to ionising radiation, NCRP Report 116. (Bethesda, MD: National Council on Radiation Protection and Measurements).
- Pacifici, R. and Avioli, L. V. (1993). Effects of ageing on bone structure and metabolism. In: *The osteoporotic syndrome*, 3rd edition, ed. L. V. Avioli. (New York: Wiley-Liss).
- Reed, G. W. (1966). The assessment of bone mineralisation from the relative transmission of ²⁴¹Am and ¹³⁷Cs radiations. *Physics in Medicine and Biology* **11**, 174.

- Royle, G. J., Farquharson, M., Speller, R. and Kidane, G. (1999). Applications of x-ray diffraction analysis in crystalline and amorphous body tissues. *Radiation Physics and Chemistry* **56**, 247-258.
- Royle, G. J. and Speller, R. D. (1995). Quantitative x-ray diffraction analysis of bone and marrow volumes in excised femoral head samples. *Physics in Medicine and Biology* **40**, 1487-1498.
- Shah, K. M., Goh, J. C., Karunanithy, R., Low, S. L., Das De, S. and Bose, K. (1995). Effect of decalcification on bone mineral content and bending strength of feline femur. *Calcified Tissue International* **56** (1), 78-82.
- Shane, E. (1988). Osteoporosis. In: *Metabolic bone and mineral disorders*, ed. S. C. Manolagas and J. M. Olefsky. (New York: Churchill Livingstone).
- Singh, M., Nagrath, A. R. and Maini, P. S. (1970). Changes in trabecular patterns of the upper end of the femur as an index of osteoporosis. *The Journal of Bone and Joint Surgery* **52A**, 457-467.
- Smyth, P. P., Adams, J. E., Whitehouse, R. W. and Taylor, C. J. (1997). Application of computer texture analysis to the Singh Index. *The British Journal of Radiology* **70**, 242-247.
- Soames, R. W. (ed.) (1995). Skeletal system. In: *Gray's anatomy: the anatomical basis of medicine and surgery*, 38th edition, ed. P. L. Williams *et al.* (New York: Churchill Livingstone).
- Speller, R. D., Royle, G. J. and Horrocks, J. A. (1989). Instrumentation and techniques in bone density measurement. *Journal of Physics E: Scientific Instruments* **22**, 202-214.
- Tortora, G. J. and Grabowski, S. R. (1996). *Principles of anatomy and physiology*, 8th edition. (New York: Harper Collins).
- Tothill, P. (1989). Methods of bone mineral measurement. *Physics in Medicine and Biology* **34** (5), 543-572.
- Van der Perre, G. and Lowet, G. (1994). Physical meaning of bone mineral content parameters and their relation to mechanical properties. *Clinical Rheumatology* **3** (Suppl. 1), 33-37.
- Whitehouse, W. J. and Dyson, E. D. (1974). Scanning electron microscope studies of trabecular bone in the proximal end of the human femur. *Journal of Anatomy* **118** (3), 417-444.

Williams, P. L. and Warwick, R. (ed.) (1980). *Gray's anatomy*, 36th edition. (New York: Churchill Livingstone).

Wong, D. M. and Sartoris, D. J. (1996). Noninvasive methods for assessment of bone density, architecture, and biomechanical properties: fundamental concepts. In: *Osteoporosis: diagnosis and treatment*, ed. D. J. Sartoris. (New York: Marcel Dekker).

Woodard, H. Q. and White, D. R. (1982). Bone models for use in radiotherapy dosimetry. *The British Journal of Radiology* **55**, 277-282.

World Health Organisation (1999). Osteoporosis: Both health organizations and individuals must act now to avoid an impending epidemic. Press release 99-58.

World Health Organisation (2002). WHO calls for strong focus on health promotion for women. Press release 2002-03.

BIBLIOGRAPHY

A list of important and useful texts encountered during the course of this work.

RADIATION PHYSICS AND DETECTION

Alpen, E. L. (1998). Radiation biophysics, 2nd edition. (San Diego, California: Academic Press).

Attix, Frank H. (1986). Introduction to radiological physics and radiation dosimetry. (New York: Wiley).

Johns, H. E. and Cunningham, J. R. (1983). The physics of radiology, 4th edition. (Illinois: Charles C. Thomas).

Knoll, G. F. (1989). Radiation detection and measurement, 2nd edition. (New York: Wiley).

ANATOMY, PHYSIOLOGY AND PATHOLOGY

An, Yuehwei H. and Draughn, Robert A. (ed.) (2000). Mechanical testing of bone and the bone-implant interface. (Boca Raton: CRC Press LLC).

Avioli, L. V. (ed.) (1993). The osteoporotic syndrome, 3rd edition. (New York: Wiley-Liss).

Cotran, S. C., Kumar, V. and Robbins, S. L. (1994). Robbins pathologic basis of disease, 5th edition. (Philadelphia: W. B. Saunders Company).

Eisenburg, R. L. and Dennis, C. A. (1995). Comprehensive radiographic pathology, 2nd edition. (St. Louis: Mosby).

Hukins, D. W. L. (ed.) (1989). Calcified tissue. (Hampshire: Macmillan Press).

Tortora, G. J. and Grabowski, S. R. (1996). Principles of anatomy and physiology, 8th edition. (New York: Harper Collins).

Williams, P. L. (ed.) (1995). Gray's anatomy: the anatomical basis of medicine and surgery, 38th edition. (New York: Churchill Livingstone).

Whitehouse, W. J. and Dyson, E. D. (1974). Scanning electron microscope studies of trabecular bone in the proximal end of the human femur. *Journal of Anatomy* **118** (3), 417-444.

BONE DENSITY MEASUREMENT

Farquharson, M. J. (1996). Characterisation of bone tissue using coherently scattered x-ray photons. PhD thesis: University College, London, Department of Medical Physics and Bioengineering.

Farquharson, M. J. and Speller, R. D. (1998). Trabecular bone mineral density measurements using energy dispersive x-ray diffraction (EDXRD). *Radiation Physics and Chemistry*. **51**, 607-608.

Speller, R. D., Royle, G. J. and Horrocks, J. A. (1989). Instrumentation and techniques in bone density measurement. *Journal of Physics E: Scientific Instruments* **22**, 202-214.

Tothill, P. (1989). Methods of bone mineral measurement. *Physics in Medicine and Biology* **34** (5), 543-572.